ONE- AND TWO-DIMENSIONAL MICHAPOSCALE GAS CHROMATOGRAPHY SYSTEMS: MATERIALS, DESIGN, AND IMPLEMENTATION

by

William Reginald Collin

A dissertation submitted in partial fulfillment
of the requirements for the degree of
Doctor of Philosophy
(Chemistry)
in the University of Michigan
2016

Doctoral Committee:

Professor Edward T. Zellers, Chair
Professor Robert T. Kennedy
Professor Katsuo Kurabayashi
Associate Professor Anne J. McNeil

DEDICATION

To my love Jeanne, the memory of my mother and the enduring support of my father.

ACKNOWLEDGEMENTS

These pages represent the culmination of many years of concerted effort, none of which would have been possible on my own.

First and foremost, I would like to thank my advisor, Professor Edward T. Zellers. Without his guidance, literally none of this dissertation would exist. I came into this program as a somewhat competent technician, and thanks to Ted's guidance, wisdom and leadership, I'm leaving as a capable scientist. Without his firm hand guiding my experimental design, writing and presentation-making, the last 5 years would have been far less productive.

I also owe a great deal to Professor Katsuo Kurabayashi, whose lab developed a key piece of technology critical to almost all of my work, the microfabricated thermal modulator. In addition, his advice and support at critical times of my career have proven invaluable. Members of his lab were critical to my studies, especially Dr. Dibyadeep Paul, who made the μTM devices I used in Chapter 4,5 and 6 and was a co-author on Chapter 3,4,5, and 6. He also mounted the μTM devices used in Chapter 3, which were made by Dr. Sung-Jin Kim. Dr. Robert Nidetz provided both excellent technical conversation and made the short microcolumns used in Chapter 3, 5 and 6 which were vital to my work.

I would also like to thank the other members of my committee, Professor Robert Kennedy and Professor Anne McNeil. As a rotation student in Professor Kennedy's lab, I got my first experience in academic research. I also use lessons learned in his separation science course on a daily basis. Professor McNeil provided insight/advice on the synthetic portion of my research which allowed me to address issues before they became problems.

Members of the Zellers Lab Group were vital to each of these chapters. Nicolas Nunovero was invaluable for electronic hardware and software for each of the chapters in this dissertation. He was always available to help troubleshoot and I enjoy working with him greatly. Drs. Gustavo Serrano and Lindsay Wright were critical to the success of the INTREPID prototype presented in Chapter 2. Dr. Hungwei Chang also contributed to Chapter 2. Amy Bondy had the synthetic hand that made Chapters 3, 4 and 6 possible. Dr. Kee Scholten was an invaluable resource for intellectually stimulating conversation, and working with him on Chapter 5 was equally rewarding. He was responsible for making the μOFRR used in Chapter 5, the CR array used for the bulk of Chapter 6 and the longer microcolumns in Chapter 3. Drs. Thitiporn Sukaew and Sun-Kyu Kim and I never shared projects, but their advice and support as senior students in the lab were greatly appreciated to a wide-eyed first-year graduate student. Dr. Chengyi Zhang synthesized nanoparticles (with Dr. Wright) and coated the CR arrays used in Chapter 6. Working with him was a joy. Helping current members Changhua Zhan, Junqi Wang and Dr. Zhijin Lin learn the skills that I could teach was fun, and their friendship is greatly appreciated. Henry also fabricated the CR array used in the microsystem of Chapter 6. Dr. Willie Steinecker for provided the manifold used in the microsystem in Appendix 3. Dr. Jonathan Bryant-Genevier brought a wealth of experience building microsystems to our conversations and troubleshooting sessions for many of my projects. Dr. Forest Bohrer fabricated many of the nanoparticles used.

Many staff members at the University of Michigan helped me. In the Environmental Health Science Department, I would like to thank Cecilia Young and Sue Crawford and Patrice Somerville. I'd like to thank George Johnston, Steve Donajkowski, Al Wilson and Jim Tice for their machining advice. Brad Richert provided technical assistance on Chapter 2. Katharine Beach fabricated devices for some of the chapters. Bruce Block designed the PCB for the μTM used in Chapters 3,5 and 6 and the C++ software used in Chapter 3. Dr. Edmund Palermo assisted with the DSC measurements in Chapter 3.

The work described in Chapter 2 was funded by the Department of Homeland Security, Science & Technology Directorate under Cooperative Agreement No. 06-G-024. Additional support was provided by Grant ECCS 1128157 from the National Science Foundation (NSF). The work described in Chapters 3-6 was funded by Grant ECCS-1307154 and/or by Grant ECCS 1128157 from the NSF, and by a generous grant from Agilent Technologies. I was supported for one semester by a Graduate Fellowship in Chemical Exposure Science from the University of Michigan Center for Occupational Health & Safety Engineering (COHSE) through Grant 1 T42 OH008455 from the National Institute for Occupational Safety and Health of the Centers for Disease Control and Prevention (NIOSH-CDCP). Travel grants from the Rackham Graduate School, which partially offset expenses associated with presenting my work at various conferences, is also gratefully acknowledged. Devices were fabricated in the Lurie Nanofabrication Facility, a member of the National Nanotechnology Infrastructure Network, which is supported by the National Science Foundation.

On a personal level, I'd like to thank my family and friends for supporting me throughout this process. My scarcity at social events was taken in stride. Stephen Wilson, Friday lunch was a happy distraction. Dr. John Gland and Dr. Paul Kennedy convinced me to go back to school. My

dad provided a sounding board and technical assistant for several of my mechanical engineering problems, no matter how weird they were. My brothers and sisters were supportive and kept me going when things got tough. Though my mom can't be here to see me finish, she was there at the start I know she would be proud of me and I wouldn't be here without her. Mom taught me how to read, and gave me a love for learning that put me where I am today. I love you and miss you. Last but certainly not least I'd like to thank Dr. Jeanne Hankett. Your love and support made me keep going when things got tough, and working with you was the highlight of my time here. Who knew I'd be sitting behind my soulmate in Separations! I'm eternally grateful for all you've done for me and look forward to what's to come.

TABLE OF CONTENTS

LIST OF FIGURES

LIST OF TABLES

LIST OF APPENDICES

ABSTRACT

This dissertation describes the development of prototype instrumentation containing gas chromatographic microanalytical systems (μGC) made from Si-microfabricated components for determining the components of complex mixtures of volatile/semi-volatile organic compounds (S/VOC). The core components are an adsorbent-packed μpreconcentrator-focuser (μPCF), a single- or dual-μcolumn separation module, and a detector comprising a single, polymer-coated μoptofluidic ring resonator (μOFRR) μsensor or an array of chemiresistor (CR) μsensors coated with various monolayer-protected Au nanoparticles (MPN). The latter produces selective response patterns that can enhance the discrimination of S/VOCs. The first prototype developed contains a single-μcolumn μGC system designed for rapid determinations of two vapor-phase markers of the explosive trinitrotoluene: 2,3-dimethyl-dinitrobenzene and 2,4-dinitrotoluene. A selective, high-volume sampler and an array of MPN-coated CRs held at elevated temperature enabled measurements of these targets at sub-parts-per-billion air concentrations in a 2-min sampling/analytical cycle among 20 interfering S/VOCs. The second prototype developed contains a dual-μcolumn microsystem designed to perform comprehensive two-dimensional gas chromatographic separations (μGC × μGC), wherein compounds separated on a first-dimension (^{1}D) μcolumn are passed through a microscale thermal modulator (μTM) and further separated on

a second-dimension (^{2}D) μcolumn. First, the μTM was fluidically integrated with ^{1}D and ^{2}D μcolumns and the separation of a 36-component VOC mixture was demonstrated using a conventional detector. Next, this μGC × μGC separation module was integrated with the μOFRR detector, and the influence of analyte volatility on the response characteristics was illustrated. Detection limits (LOD) in the low-ng range and modulated peak widths in the 100-700 ms range were achieved for a set of common environmental contaminants. The next study demonstrated the advantages of programming the minimum and maximum μTM temperatures over the course of a μGC × μGC separation to enhance analyte resolution and detectability. Then, a CR array was installed as the detector and the effects of flow rate, temperature, and analyte volatility on resolution, sensitivity, and LOD were characterized. The final study entailed the integration of a dual-adsorbent μPCF to complete the assembly of the μGC × μGC prototype and initial measurements obtained therefrom.

CHAPTER 1

INTRODUCTION

1.1 Introductory Remarks

This chapter lays the groundwork for the dissertation. The first section provides a discussion of basic gas chromatographic instrumentation. This is followed by a theoretical treatment of the parameters and variables affecting the efficiency of the separation process as well as the metrics used to evaluate performance. Drivers for miniaturizing GC components are then presented, along with a discussion of the tradeoffs of miniaturization. A critical review of the literature concerned with microfabricated GC (μGC) components and systems is then presented. Finally, the theory and practice of so-called comprehensive two-dimensional GC (GC × GC) are presented and the current state of the art in microfabricated GC × GC and related multidimensional microsystems are reviewed.

This chapter closes with a brief summary of the topics covered in subsequent chapters.

1.2 Separations of Vapor Mixtures: GC Theory

1.2.1 GC Instrumentation

Volatile and semi-volatile organic compounds (VOCs and SVOCs) with vapor pressures (p_v) sufficiently high to yield finite concentrations in air under ambient conditions.[1] Separating mixtures of (S)VOCs in order to identify and quantify their constituents is a critical aspect of many areas of research. Two examples (for brevity; dozens of such examples from wide ranging fields exist) are biomedical[2] and environmental[3] VOC samples which can indicate the health of an individual or ecosystem resepectively. A common method of separating mixtures of VOC is gas chromatography (GC), which is the focus of this dissertation.

The basic functional components of a GC are shown in Figure 1.1 and include a sample introduction system or injector, a separation column, a detector and an integration device. A supply of carrier gas entrains vapor phase sample in the injector and carries it in to the separation column where the separation takes place. GC separations are driven by differential transport of analytes through a separation column. The migration rate of each individual analyte through the column is dictated by partitioning between the mobile phase (carrier gas) and stationary phase. The detection device registers the presence of each analyte eluting from the separation column. The data is interpreted by the integration device, usually software run on a personal computer, to produce a chromatogram: a time-resolved measure of eluent concentration.

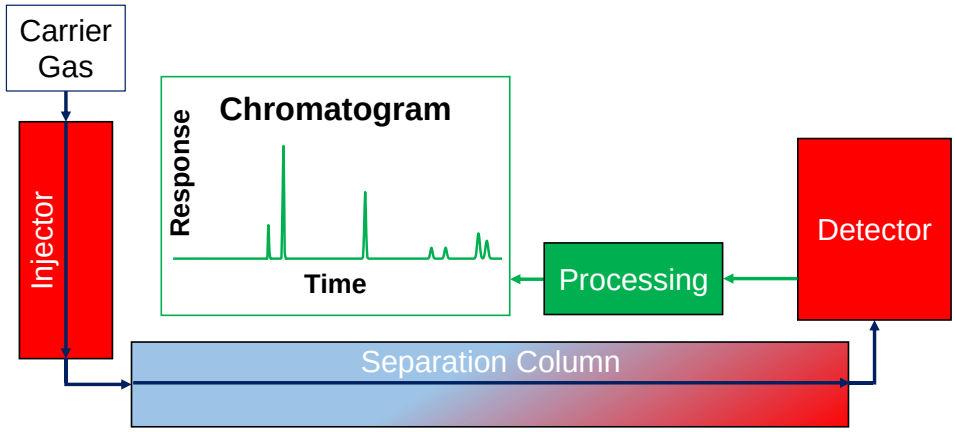

Figure 1.1. Schematic of a basic gas chromatograph. Red represents hot zones, red/blue gradient represents temperature programmable zone, green represents electronic signals, blue arrows represent carrier gas flow direction.

1.2.1.1 Injectors

Injection devices vary widely, and many exist for specific applications. Thermal desorption (TD), valve-based loops (loop) and split/splitless (S/SL) injectors are the most common, and will be the focus of the following discussion. It should be noted that this list is not exhaustive and variations on these three basic themes, combinations therof and application specific detectors exist.

In TD a sample is collected outside of the GC, from vapor phase samples, onto an adsorbent of some type packed in a sampling tube. Common adsorbents include charcoal, silica, graphitized carbon such as Carbopack and polymers such as Tenax. Increasingly, solid phase microextraction (SPME) techniques are being utilized for TD type methods, where an adsorbent fiber is used for passive sampling. The sampling tube (or SPME fiber) is then rapidly heated, desorbing the trapped analyte to be entrained into a flow of carrier gas. This method is particularly useful since a large air volume can be sampled, leading to a correspondingly large mass of trapped vapor on a relatively small volume of adsorbent, and thereby enabling the detection of low concentration analytes. Unfortunately, this method cannot be used with thermally labile compounds, since they often decompose at the high temperatures needed for desorption. In addition, the desorption volume (and

thus desorbed peak width) is limited by the rate of heating and the relatively large volume of the sampling device. This can reduce the chromatographic resolution, but can sometimes be overcome through chromatographic methods or secondary focusing downstream.[4]

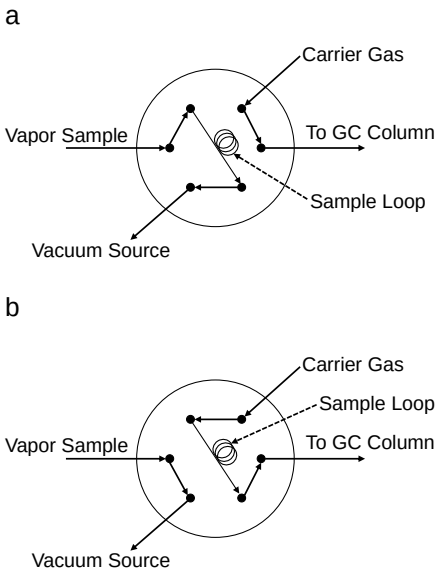

Figure 1.2. a) Sample loading position for valve/loop injection system. b) Sample inject position for valve/loop injection system.

Valve-based loop injection is used for samples that are already in the vapor phase such as air samples. A common valve/loop injection system is shown in Figure 1.2 and includes a six-port, two position valve. The entire assembly can be enclosed in a heated oven to reduce wall-adsorption of low p_v analytes. In the sample load position (Figure 1.2a), sample is drawn through the sampling loop (10-5000 μL) using a pump or vacuum supply while carrier gas supply is routed directly to the separation column. After sufficient time to completely fill the sample loop has passed, the valve is switched to re-route carrier gas flow to flush the loop onto the separation column as in Figure 1.2b.[5]

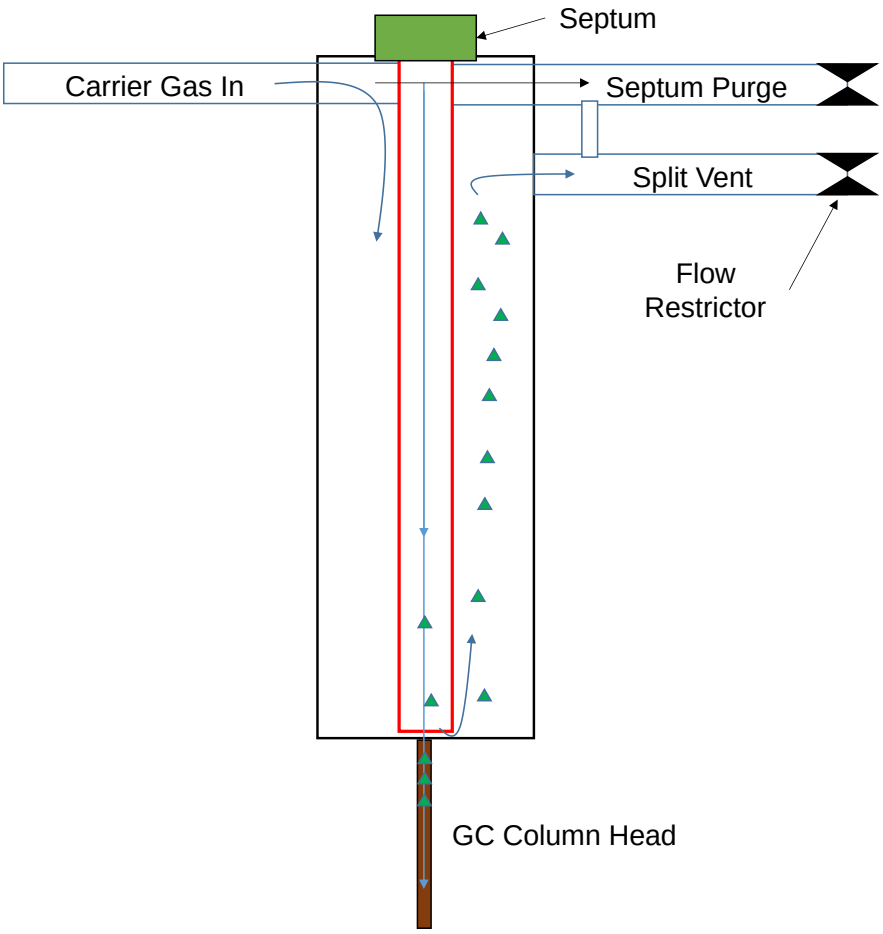

Figure 1.3. Diagram of a split/splitless injector.

By far the most common type of sample inlet for GC is the split-splitless injector.[4] This type of injector, show schematically in Figure 1.3 is used to vaporize sample for introduction to the GC separation column. The entire injector is heated, and when sample is introduced into the inner liner (outlined in red in Figure 1.3) via syringe it is instantly vaporized. In splitless mode, vaporized sample is driven onto the GC column by carrier gas entirely. This results in peaks that are broadened by dilution. If the split vent is opened (operated in split mode), a portion of the vapor is expelled from the system. The portion carried onto the column is a small fraction of the total vaporized volume, thus a split injection results in a narrower injection band than with splitless mode which leads to narrower, better resolved chromatographic peaks. The loss of a portion of the

vaporized sample of course reduces the mass that can be presented to the detector, reducing peak areas and sensitivity. This tradeoff between peak width and sensitivity must be considered when designing a method.[5]

1.2.1.2 Columns

There are two basic types of GC columns, open tubular and packed. The latter is rarely used in modern practice and will not be discussed here. In addition, several variations of open tubular columns exist (porous layer open tubular columns and support coated open tubular columns) which are not relevant to this work and thus will not be included in this discussion. It will instead focus on wall coated open tubular columns, where a thin film of liquid is spread on the inner wall of a glass, fused silica or metallic tube (capillary). These columns consisted of drawn glass tubing with a thin coating of a (usually) liquid stationary phase. Fused silica is chemically similar to the glass used in early columns and can be generally treated similarly in the coating process. By coating the outside of the fused silica with polyimide, a robust, flexible and regularly dimensioned tubing is formed. These capillaries vary greatly in length and inner diameter (id), with id typically from 100 μm to 530 μm inner diameter and with lengths typically 10-60 m.[5]

Since the separation process is driven by the reversible partitioning of analytes into the stationary phase, it is therefore the most important element of the GC column. Stationary phases are as varied as their application and are commonly polymeric.[5] Other types of stationary phase coatings also exist such as room temperature ionic liquids (RTILs)[6] and similarly viscous organic oils.[5] Common features of all stationary phase coatings include relative stability at a broad range of temperatures, chemical inertness, high viscosity and solute/solvent activity (the ability to dissolve the analytes of interest).

Each stationary phase coating type may require a different type of surface pretreatment to enable stable films to form on the inner capillary wall. This is accomplished by altering the surface chemistry to be more wettable by the stationary phase to be deposited. A common surface pretreatment for glass, fused silica or silicon is silylation.[7] Figure 1.4a shows the basic, native-state chemical structure of such a surface. In the case of silicon, exposure to the atmosphere or purposeful oxidation would render the surface very similar to that of glass/fused silica. Silazanes, cyclosiloxanes and chlorosilanes can all be used for this purpose; examples are shown in Figure 1.4b,c and d with the most common and widely applied being hexamethyldisilazane (HMDS).[8,9] Interestingly, chlorosilanes are extremely important to GC as both surface treatment agents as well as in the production of silicone polymers[8] often used for stationary phase coatings. Free hydroxyl groups on the column inner surface can react according to the scheme in Figure 1.4e, which shows the capping of surface silanols with a trialkylsilyl ether through reaction with hexaalkylsiazane. Other pretreatments include increasing the wettable surface area of the column such as wet etching with HF, HCl or salt (NaCl or $BaCO_3$) deposition.[7,10]

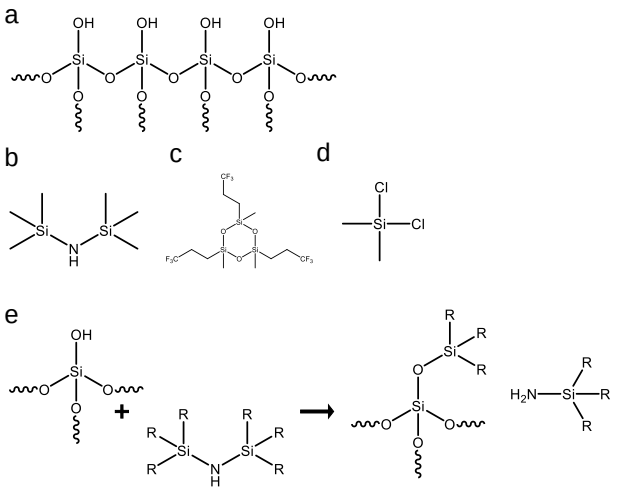

Figure 1.4. Surface pretreatment chemical structures and reactions. a) Idealized representation of the native inner surface of most GC column types; b) Hexamethyldisilazane; c) (3,3,3-trifluoropropyl)methylcyclotrisiloxane; d) dichlorodimethylsilane; e) Reaction scheme for a generic silylation of a GC column surface with a siloxane. R= organic group.

Stationary phases can be deposited onto the column walls dynamically or statically. In both processes, a solution of stationary phase in a volatile solvent is either pushed or pulled through the column. When coating dynamically, a concentrated plug is pushed through the column and a film (the thickness of which is controlled by the concentration of the coating solution) is left behind on the column wall as the solution is pushed through by partial evaporation at the meniscus of the plug. This results in a film with a thickness which is necessarily known well[7] and uniformity of the film throughout the column is also poorly controlled.[7] Static coating is a more complicated process that typically results in more uniform films of known thickness.[7] The process begins by filling the column completely with a solution of stationary phase. One end of the column is then sealed and vacuum is applied to the other, causing the solvent portion of the coating solution to evaporate and leaving a uniform coating on the capillary wall, the thickness of which can be calculated on the basis of column internal surface area and concentration of the coating solution.

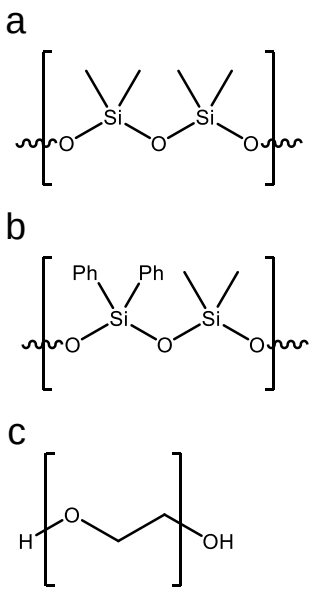

Figure 1.5. Chemical structures of common stationary phases. a) PDMS; b) 50% phenyl/50% dimethyl siloxane; c) PEG.

The most common stationary phases are siloxane polymers, the most basic structure of which is shown in Figure 1.5a along with some common functional isomers. The simplest, poly(dimethylsiloxane) (PDMS), is also among the most common. Since the methyl groups shield the backbone of the polymer, this phase is non-polar and generally separates on the basis of boiling point, though highly polar compounds elute much earlier than their boiling points would indicate. It can be coated on fused silica columns easily with or without HMDS pretreatment. Functionalization with phenyl groups (Figure 1.5b) in place of a portion (up to 50%) of the methyl positions yields another common stationary phase with slightly more polar characteristics which impart additional retention selectivity. The polymer shown in Figure 1.5c, polyethylene glycol (PEG) is an even more polar stationary phase coating, as its retention selectivity is driven by dipole-dipole interactions and hydrogen bonding ability of analytes. Pretreatment methods for the polymers in Figure 1.5 are typically tailored to the coating.

Another class of stationary phases for GC are room temperature ionic liquids (RTILs), are organic salts which have a melting point below room temperature, rendering them liquid under most GC operating conditions. Early work on these types of stationary phases was carried out decades ago,[11] though at that time their utility was limited by small operating temperature range, poor peak shape and poor retention of analytes. Recent advances by the Armstrong group[6,12] and others[13] have changed this. New phases include a wide range of anions and imidazolium or phosphatidyl[6,15] cations. In addition to an array of charge carriers, there is also a wide range of backbone structures which yield a large catalog of structures with various properties. Some of these RTILs exhibit a combination of high viscosity, low vapor pressure, solvent characteristics and thermal properties which render them useful as GC stationary phases. Most recently, Armstrong et al.[6,12] have developed a large number of these stationary phases which are excellent for separating polar compounds which have become available as commercial column.[15] The typical pretreatment process for these types of stationary phases is sodium chloride surface, roughening.[6]

Stationary phase films can be stabilized by crosslinking the polymers *in situ* or bonding them to the wall of the column. If a small portion of the stationary phase polymer contains an end group which can be crosslinked, 1% vinyl PDMS for example, then a radical initiator can be used to crosslink the film. Such films are more stable to higher temperatures, evincing less bleed (the degradation of stationary phase resulting in chromatographic artifacts) than uncrosslinked films. In addition, column longevity and retention time stability can be increased since the stationary phase film thickness and morphology is less likely to change over time in a crosslinked film. The basic reaction of a radical initiated polymer crosslinking process can be seen in Figure 1.6 and is included as a step in most polymer stationary phase coating procedures[7,16,17] as well as some RTIL

coating procedures.[12] The generation of the radical is typically accomplished using peroxides or azo compounds homolytic cleavage.

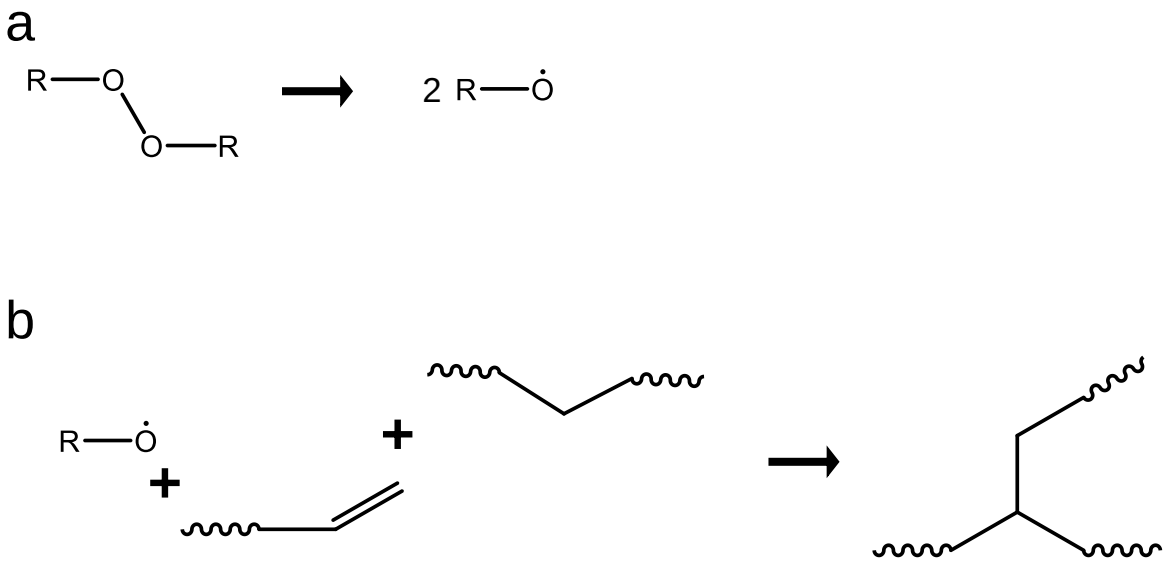

Figure 1.6. Radical crosslinking process for a generic polymer with a) hemolytic cleavage of peroxide; b) crosslinking of vinyl terminated chain at some point in another polymer chain.

1.2.1.3 Detectors

GC detectors, like columns, come in a variety of designs depending upon the application and can be universally sensitive or analyte specific. They must also respond rapidly to analyte eluting from the GC column to maintain the separation achieved. General detector types include flame ionization (FID), photionization (PID) and thermal conductivity (TCD). Detectors that provide specificity include electron capture (ECD), nitrogen phosphorous (NPD) and flame photometric types (FPD). Mass spectrometric (MS) detection can fit reasonably well into either category, since it can provide specific molecular information for a wide variety of target analytes. Each of these detector types possess unique characteristics, strengths and weaknesses which are summarized in Table 1.1. Flame ionization is by far the most common type of detection for GC,[4,5]

though MS is rapidly increasing in use as equipment becomes smaller and cheaper. Several of these GC detectors rely on the generation and measurement of gas phase ions and their measurement, with the method of generating these ions making them uniquely selective (or non-selective).

Table 1.1: Comparison of GC Detector Types

Detector	Selectivity	Operating Principle	Strengths	Weaknesses	LOD
FID	Combustible	Ionization of hydrocarbons	Cheap, general selectivity, fast response, low maintenance, sensitive	Hydrogen supply required, less sensitive to hetero compounds	100s of pg
PID	Ionizable by UV	Ionization of UV absorbers	Sensitive, fast response, no consumable gases	Lamp selection critical, UV absorber required, reaction chamber broadens peaks	10s of pg
TCD	General	Difference in thermal conductivity from carrier	Sensitive to everything, simple, easily maintained, no consumables	Not very sensitive, requires He or H_2	10s of ng
ECD	Electronegative only	Electron capture in electronegative species	Extremely sensitive, selective, no consumables	Radioactive source, not universal	100s of fg
NPD	N and P	Chemical ionization	Highly sensitive, highly selective	No sensitivity w/o N or P	1s of pg
FPD	S and P	Spectroscopic emission	Sensitive, highly selective	No sensitivity w/o S or P	10s of pg
MS	General	Ionization; mass separation	Highly sensitive, extra chemical information, structural information	Expensive, high power req., difficult operation	1s of pg

As the most commonly used detector, FID deserves special attention. A schematic of a FID is shown in Figure 1.7. Flammable analytes eluting from the GC column are burned in a hydrogen flame. This process ionizes a small portion of the combustion product, which is detected as an increase in current through the flame between two electrodes. The detector is sensitive to all hydrocarbons, with specific sensitivity increase with the number of carbons in the analyte structure. An FID can detect masses in the 100s of pg range,[4] though the sensitivity is decreased when carbon atoms are replaced with hetero atoms.[5] The FID is less sensitive than other types of detectors, excepting the TCD, so its wide acceptance is mostly related to its simplicity and good

response to most analytes. A drawback of the FID is the use of hydrogen gas, which can be dangerous if not handled properly.

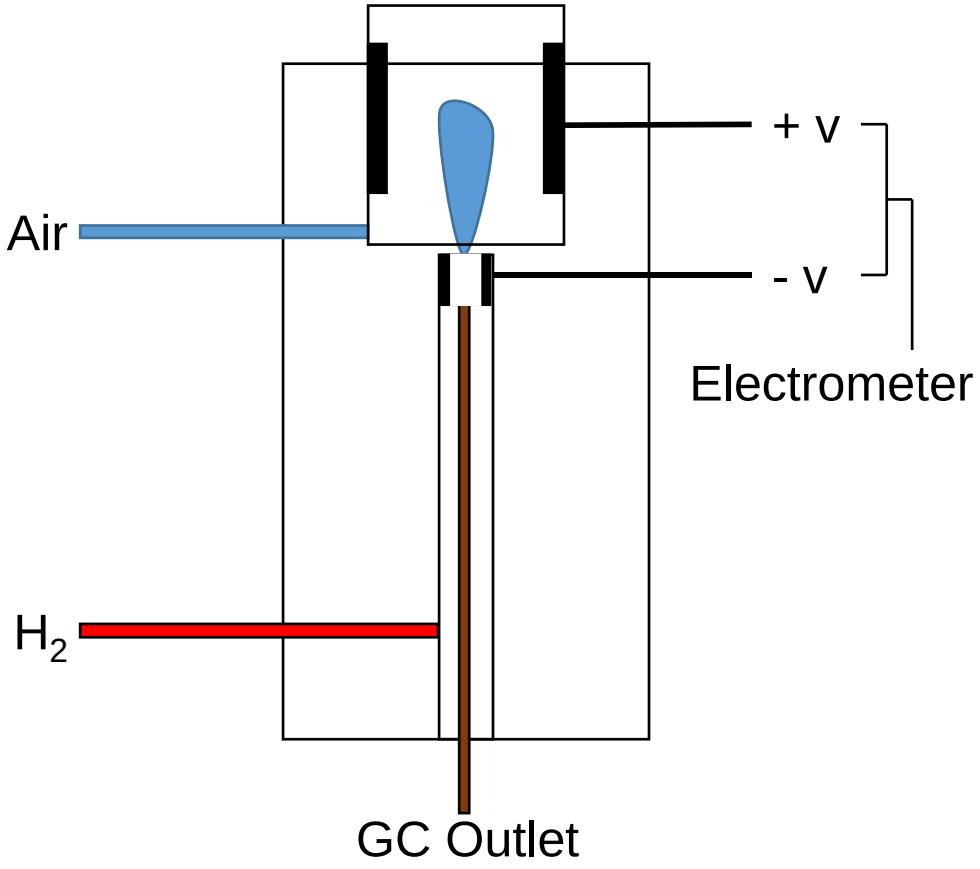

Figure 1.7. Schematic representation of a flame ionization detector.

Photoionization detectors generate ions with a high voltage UV lamp, the light from which interacts with the eluting analyte causing it to eject an electron. The resulting positive ion can be detected in a similar manner to FID. This method is highly sensitive, with detection limits in the 10s of pg[5] for highly UV active compounds such as those containing double bonds or aromatic rings. Sensitivity decreases with less UV absorbtion, for example aliphatic compounds are harder to detect than alkenes which are harder to detect than aromatics. If a high enough energy source is used, however, PIDs can be considered general detectors. Unfortunately, the reaction to produce ions requires a long path of interaction between analyte and light to be efficient enough to detect

the resulting ions. This leads to large dead volumes in the detector and broadening of chromatographic peaks.[5]

TCDs are another general-type detector. They operate by sensing the difference in temperature of a heated filament in the flow path due to the presence of analyte molecules as compared to the temperature of the filament with just carrier gas. This makes the TCD extremely useful for difficult to detect species such as permanent gases, or analytes that are too difficult to ionize in the other available types of detector. They are sensitive to any compound, so long as the thermal conductivity of the eluent is different than that of the carrier gas. They are very simple to operate and maintain, with no moving parts and no additional consumables required. The general utility comes with decreased sensitivity however, with limits of detection in the 10s of ng range.[5] The filament is housed in a flow cell with large volume relative to other detector types, which broadens chromatographic peaks. For these reasons, the use of TCD is limited to those target compounds where other methods simply won't work, or sensitivity is not an issue.

ECD is a selective detector which is extremely sensitive to analytes with electronegative groups, $-NO_2$ or –Cl for example. In these detectors a source of electrons, typically radioactive ^{63}Ni, renders the carrier gas conductive (plasma) which is detected by the current between biased electrodes. When an analyte capable of capturing free electrons elutes, the conductivity of the plasma in the detector is reduced, indicating the presence of a peak. These detectors can be extremely sensitive to certain compounds, with limits of detection in the 100s of fg for the most electronegative species such as chloro and nitro compounds. On the other hand, they are almost complete insensitive to aliphatic analytes.[5] The use of a radioactive source is also a drawback and care must be taken in its operation and venting. They are also very sensitive to the presence of oxygen as well as column bleed so care must be taken to avoid the presence of those. Furthermore,

the carrier gas itself can affect the sensitivity of the detector by attenuating the plasma generation. This can be overcome through the use of make-up gas, at the cost of diluting analyte and reducing sensitivity.[5]

The final two selective detectors respond selectively to nitrogen/phosphorous containing compounds (NPD) or sulfur/phosphorous containing compounds (FPD). They are not as commonly used and bear little mention here. NPD detectors ionize nitrogen and phosphorous compounds selectively using hot alkali metals to start a chemical reaction which is not well understood.[5] FPD relies on characteristic emission from excited-state sulfur and phosphorous in a hydrogen flame. They are both very sensitive to their selected compounds, with NPD detecting single ng quantities and FPD detecting 10s of ng.

The mass spectrometer is a widely used GC detector which detects gas phase ions generated from GC column effluent after separating them according to their mass to charge ratio (M/Z). This provides an additional degree of chemical information about the species eluting, and can be used along with retention time to identify unknown compounds, a feat not possible with any of the previously mentioned detectors. Ions are typically generated using high energy electrons generated from a heated filament to bombard eluting vapors, though other methods for ionization exist. This hard ionization method results in fragmentation of the parent ion in a reproducible pattern unique to each analtye, which aids in identification. This produces a stream of charged and uncharged species which is introduced into the mass analyzer. The uncharged species are quickly separated out; they cannot be guided by the ion optics in the mass spectrometer inlet. This leaves a stream of charged species to be separated on the basis of mass. There are a multitude of mass analyzers available, many of which have been coupled to GC columns. Figure 1.8a, b and c show three common types in schematic.

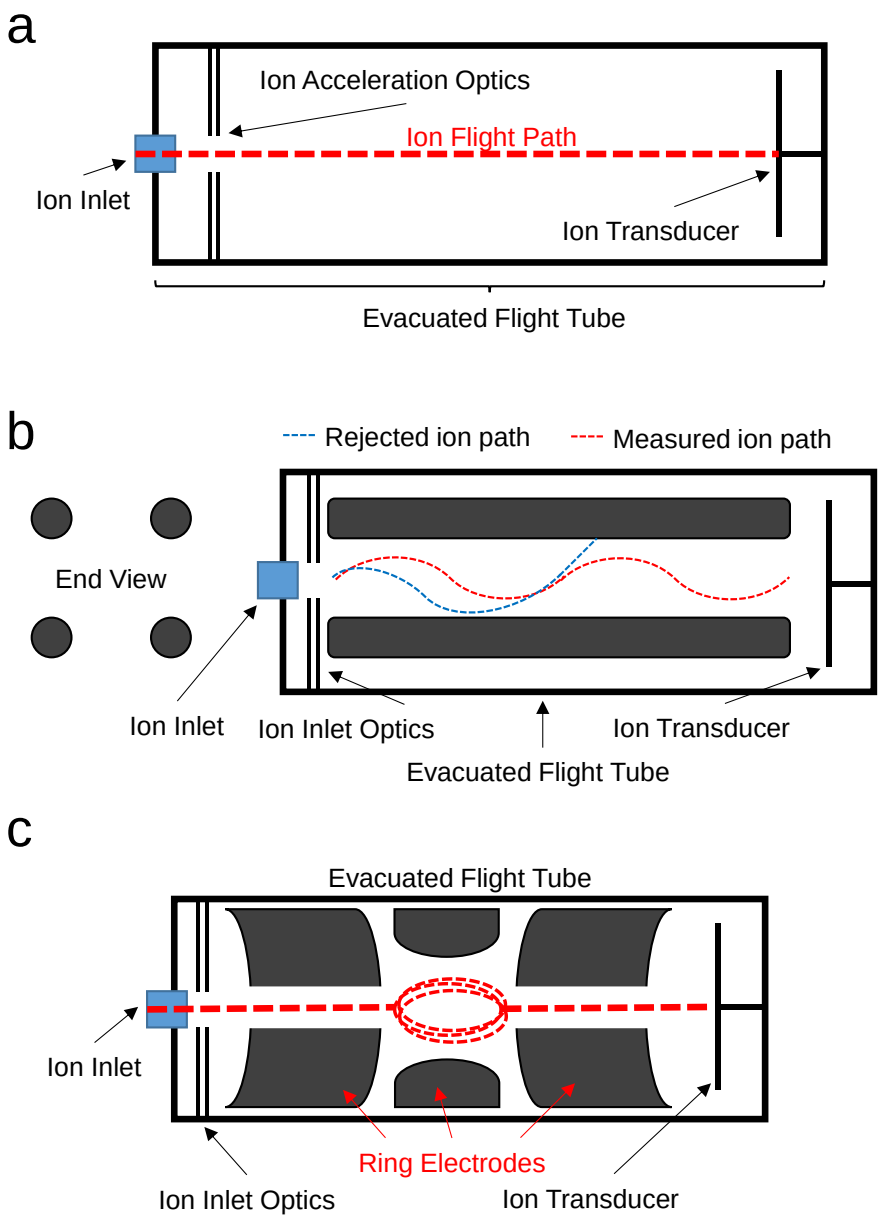

Figure 1.8. Schematic drawing of a) time of flight mass analyzer; b) quadrupole mass analyzer; c) ion trap mass analyzer.

The time of flight mass analyzer shown in Figure 1.8a pulses packets of ions into an evacuated flight tube with constant kinetic energy to be detected at the other end by an ion transducer such as an electron multiplier. The time it takes for an ion to travel from one end to the other is directly related to its mass. The quadrupole mass analyzer consists of 4 metallic poles as

shown in Figure 1.8b. It operates by alternatively attracting and repelling ions from the quadrupole elements with a high frequency RF field. The specific frequency allows ions of a certain mass to be passed through the quadrupole to be detected by the ion transducers, rejecting all others. By rapidly scanning a wide range of frequencies a wide range of ion masses can be detected, this is referred to as scan mode. If the RF field is programmed such that only a single mass can be transmitted, a single mass can be monitored which is referred to as single ion (alteranatively selected ion) monitoring (SIM) mode. The ion trap mass analyzer shown in Figure 1.8c traps ions in an electromagnetic field which is selectively varied to eject ions of a single M/Z to be detected, which can also be scanned or set to monitor a single ion. Each of these types of mass analyzers have advantages and disadvantages, which are beyond the scope of this discussion.

Generally speaking, MS detectors for GC in scan mode are less sensitive than those in SIM mode though both are quite sensitive, with limits of detection in the single pg range for SIM mode and nanograms for scan mode. The mass information provided by scanning can be invaluable for untargeted analyses or for confirmation of peak assignment. The sensitivity and selectivity provided by SIM mode is excellent for analysis of known targets. As such, mass spectrometers are generally considered the gold standard for GC detection. They are not without their drawbacks though. The instrumentation is large, expensive, tricky to operate and fragile. They often require highly trained operators to troubleshoot and develop methods. They require high power (to maintain the mass analyzers under vacuum) and sometimes additional consumables. With these problems rapidly being solved in commercial instrumentation they are becoming more and more popular as the GC detector of choice.

1.2.2 Separation Performance Metrics and the Variables Affecting Them

Measuring the performance characteristics of separations is important to the evaluation of methods and the selection of optimal conditions for analysis. Describing aspects of the chromatographic peaks is of primary importance. The most important are the retention time (t_r) or the time between injection and peak elution, maximum height of the peak (h), the area contained under the peak (A), the width of the peak at both the base and one-half of the height ($fwhm$), peak asymmetry (a) and tailing factor (TF). Figure 1.9 shows graphically these parameters [REF]. Total time elapsed for separation is also an important consideration and is often considered in choosing a chromatographic method.

The parameters of the peaks in Figure 1.9 can be used to determine a number of secondary characteristics of the separation. Column efficiency (number of theoretical plates, N), height equivalent to a theoretical plate (H), resolution (R_s), capacity factor (k), separation factor or relative retention time (α), adjusted retention time (t'_R) and peak capacity (n_c) can be calculated using Equations 1.1-1.7 respectively.[7,18]

$$N = 5.545\left(\frac{t_R}{fwhm}\right)^2 \qquad \text{(eq. 1.1)}$$

$$H = L/N \qquad \text{(eq. 1.2)}$$

Where L is the length of the GC column.

$$R_s = 1.18\left(\frac{t_{R2}-t_{R1}}{fwhm_1+fwhm_2}\right) \qquad \text{(Equation 1.3)}$$

$$k = \frac{t_R-t_M}{t_M} \qquad \text{(Equation 1.4)}$$

Where t_M is the retention time of an unretained peak and t_{R1} is the retention time of the first peak in the pair in question and t_{R2} is the retention time of the second peak.

$$\alpha = \frac{k_2}{k_1} \qquad \text{(Equation 1.5)}$$

Where k_1 and k_2 are the capacity factors of the peaks in question.

$$t'_R = t_R - t_M \qquad \text{(Equation 1.6)}$$

$$n_c = 1 + \frac{\sqrt{N}}{4R_s} \ln \frac{t_R}{t_M} \qquad \text{(Equation 1.7)}$$

Where t_R is the last eluting peak of the time window chosen and with arbitrary R_s.

Column efficiency is typically expressed in terms of *N* which hearkens back to the origins of chromatography and the use of physical plates in fractional distillation. This, along with the column length can be used to calculate *H* the height equivalent to a theoretical plate.

Resolution is a measure of the separation of two peaks from one another. It is a function of the retention times of the peaks and their widths. Figures 1.10a-d show visually the result of resolution of 1.5, 1, 0.5 and 0.25 for peaks of the same *fwhm* and *h*. Peaks with R_s values above 1.5 are considered fully resolved, between 1.5 and 0.5 partially resolved and less than 0.5 not well resolved.

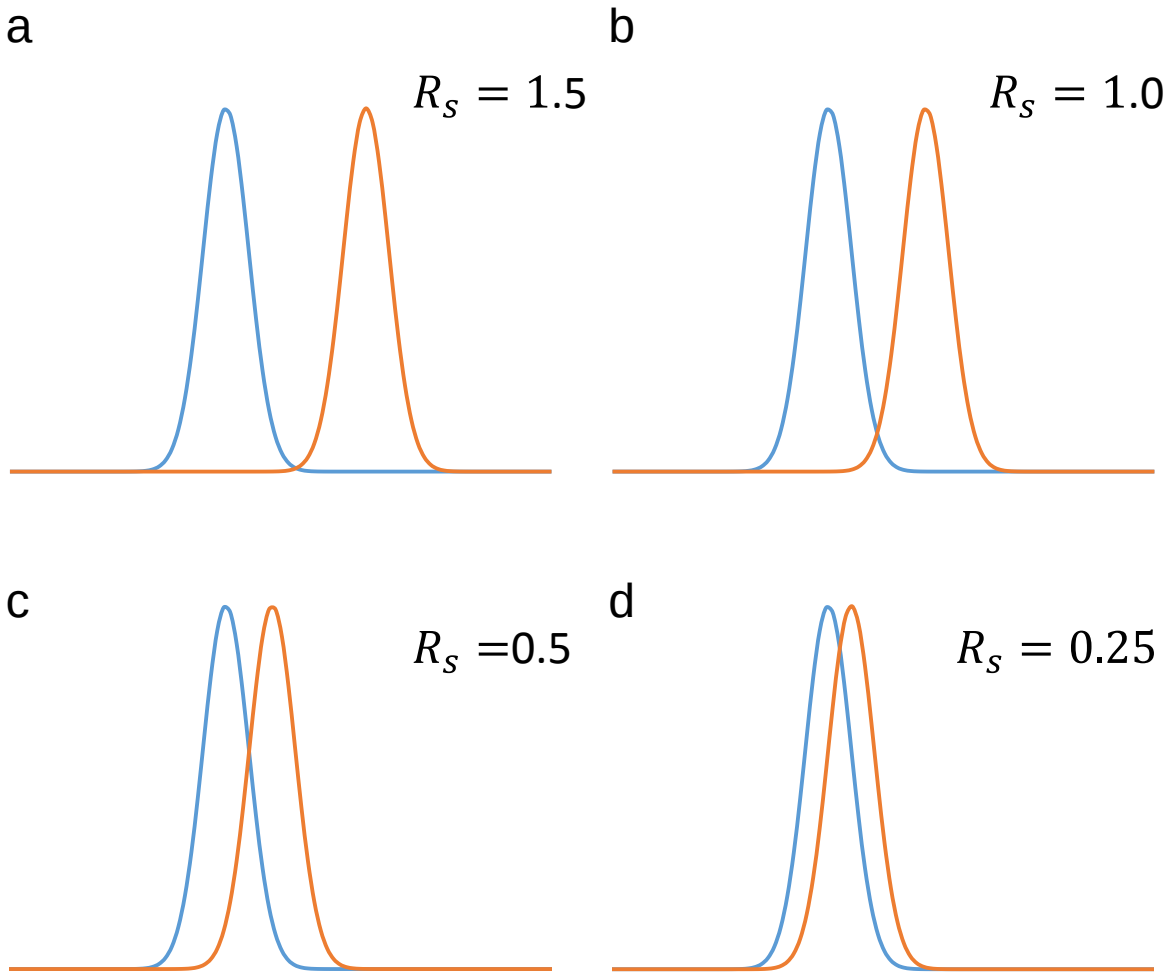

Figure 1.9. Simulated separation of two peaks with varying Rs value.

These empirical treatments of peak parameters are useful for selecting chromatographic conditions by comparison, but they don't have a physical interpretation. The physical parameters which effect the values can't be understood by examination of the equations. The van Deemter Equation shown in Equation 1.8, provides physical interpretation of the chromatographic process in terms of H and mobile phase velocity ($\bar{u}$). It describes the processes which lead to chromatographic band broadening and degradation of chromatographic separations.[5,18]

$$H = A + \frac{B}{\bar{u}} + C\bar{u} + D\bar{u}^2 \qquad \text{(Equation 1.8)}$$

The A term is referred to as the Eddy-diffusion term and applies only to liquid chromatography and GC separations using packed bed columns. The B, C and D terms in sum are equal to the height equivalent to a theoretical plate (H) and referred to as the Golay equation, the expanded form of which is shown in Equation 1.9. The B term, defined in Equation 1.10, represents the longitudinal diffusion of analyte bands in the gas phase. The C term is composed of two parts, resistance to mass transfer in the stationary phase, C_s, and resistance to mass transfer in the mobile phase, C_m which are defined in Equations 1.11 and 1.12 respectively. Not often included, though vital to interpretation of chromatograms, is the D term (Equation 1.13) which relates to band broadening outside of the GC column such as injection and detection. An explanation for each of the variables is presented in Table 1.2.[5,18]

$$H = \frac{B}{\bar{u}} + C_s\bar{u} + C_m\bar{u} + D\bar{u}^2 \quad \text{(Equation 1.9)}$$

$$B = 2D_m f_1 f_2 \quad \text{(Equation 1.10)}$$

$$C_s = \frac{2}{3}\frac{k}{(k+1)}\frac{d_f^2}{D_s} \quad \text{(Equation 1.11)}$$

$$C_m = \frac{1+6k+11k^2}{24(k+1)^2}\frac{r^2}{D_m}\frac{f_1}{f_2} \quad \text{(Equation 1.12)}$$

$$D = \frac{\Delta t^2}{L(k+1)^2} \quad \text{(Equation 1.13)}$$

With some relatively simple assumptions the Golay Equation can be effectively modeled. This allows for examination of the variables individually. The simplest form of this modelling is the calculation of H while varying $\bar{u}$. Neglecting extra-column band broadening and assuming values for D_m, D_s, r, k, d_f , f_1 and f_2 a plot of H vs. $\bar{u}$, commonly referred to as a Golay Plot, can be constructed as in Figure 1.11. The contributions of the individual terms, as well as the summation of the terms are plotted and it can be seen that at very low flow velocities longitudinal

Table 1.2. Description of variables in Equations 1.9-1.13.

Variable	Description
D_m	Solute diffusion coefficient in the mobile phase
f1	Martin-James gas compression coefficient
f2	Golay-Gidding gas compression coefficient
k	Capacity factor
df	Stationary phase film thickness
Ds	Solute diffusion coefficient in the stationary phase
r	Column inner radius
Δt	Instrumental dead time
L	Column length

diffusion is the dominant force acting on peak band width. As velocity is increased, the contribution from the B term decreases and the contribution from the linear C_m term dominates. The C_s term is finite, but not significant with the assumptions made for this simulation. The total plate height thus proceeds from an asymptotic approach to the y-axis, through a minimum, with a near-linear increase beyond the minimum. The Golay minimum is an important measure of column performance, so long as extra-column band broadening (the D term) is kept to a minimum.

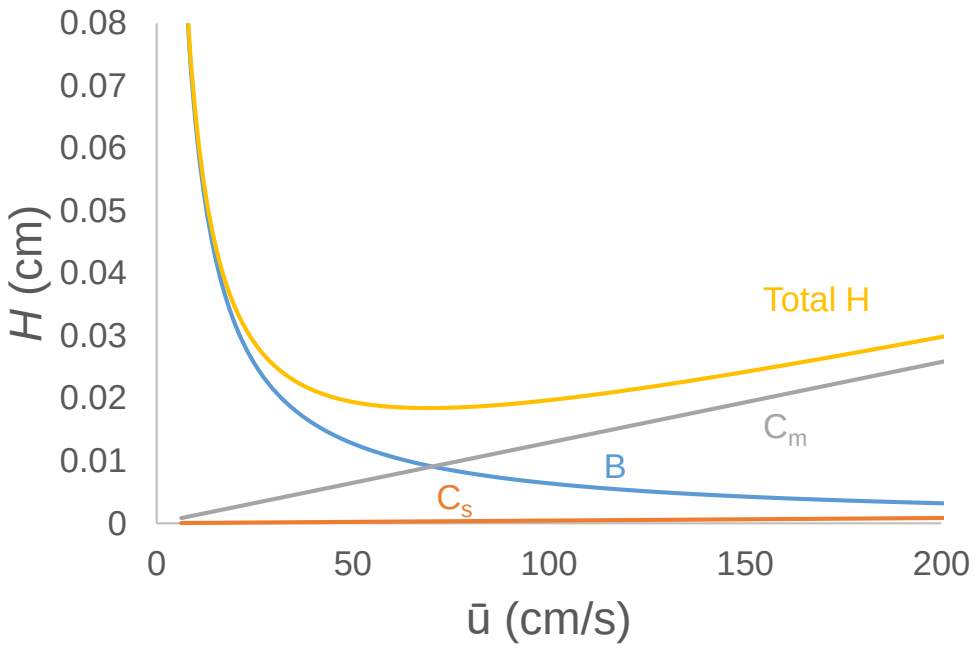

Figure 1.10. A modeled Golay Plot showing the contributions from the individual terms of the Golay Equation.

Golay plots can also be generated empirically by measuring the flow velocity of an unretained peak and *H* from sequential injections of a mixture of methane (or similarly unretained compound) and a probe compound. *H* can then be calculated via Equation 1.1 and 1.2.

The model[19] can be used to examine the effects of operating variables as well, which can provide insight to the experimental parameters chosen for evaluating columns using empirically generated Golay plots. Figure 1.12a shows the effect of varying *k* from 1-20 on the shape of the Golay plot. Figure 1.12b shows the dependence of the Golay minimum on *k*. The minimum is strongly dependent on *k*, though the effect is less pronounced for *k* values beyond 5. This provides a guide to selection of probe compounds for column evaluation. The probe should provide a *k* value above 5, but not more than 10. Values above 10 provide stable measurements of *H* but take longer for analysis and would be less ideal.

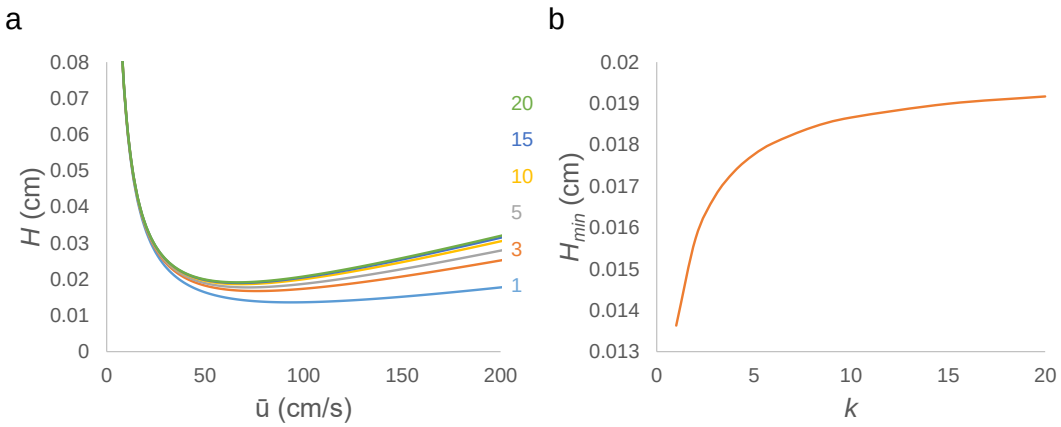

Figure 1.11. a) Golay plots with varying k. b) Plot of minimum plate heights from Golay plots with k ranging from 1-20.

The Golay equation can provide insight into column design and coating as well. Figure 1.13a shows the effect of varying column coating thickness (d_f) on the Golay plot. The minimum dramatically increases sharply beyond 0.2 µm, which equates to 0.1% of the column inner diameter for this example. H_{min} does decrease below that, but the gains in efficiency may not be worth it as

the column sample capacity would be drastically decreased. Using this rule of thumb, Figure 1.13b shows Golay plots for varying column inner diameters. As can be seen, as long as the coating thickness rule is followed, minimum plate height decreases with column inner diameter.

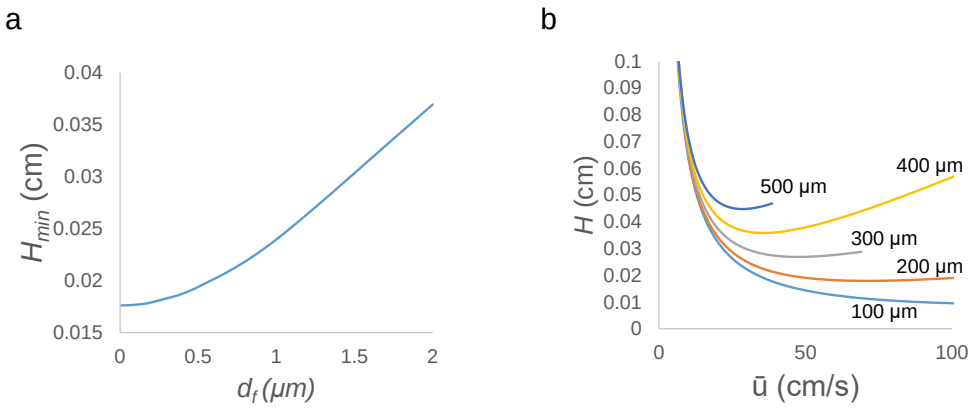

Figure 1.12. a) Dependence of H_{min} on film thickness. b) Golay plots for various column inner diameters.

Incorporating the D term of the Golay equation illustrates the importance of injection band width, especially for short columns. Figure 1.14 shows the dependence of H_{min} on an assumed injection volume, which can be estimated from the time-domain width of a peak and the flow velocity for a given column length. Clearly, narrow injection bandwidths are extremely important to achieving efficient GC separations as shown by the rapid increase in H_{min} for a given column length. The injection peak width is increasingly important as the column length decreases, as shown in Figure 1.14, with minimal effect for the 30 m column and a 7-fold increase (for the 0-5 μL range modeled) for the 0.5 m column. These factors must be considered when using Golay plots as a column comparison metric.

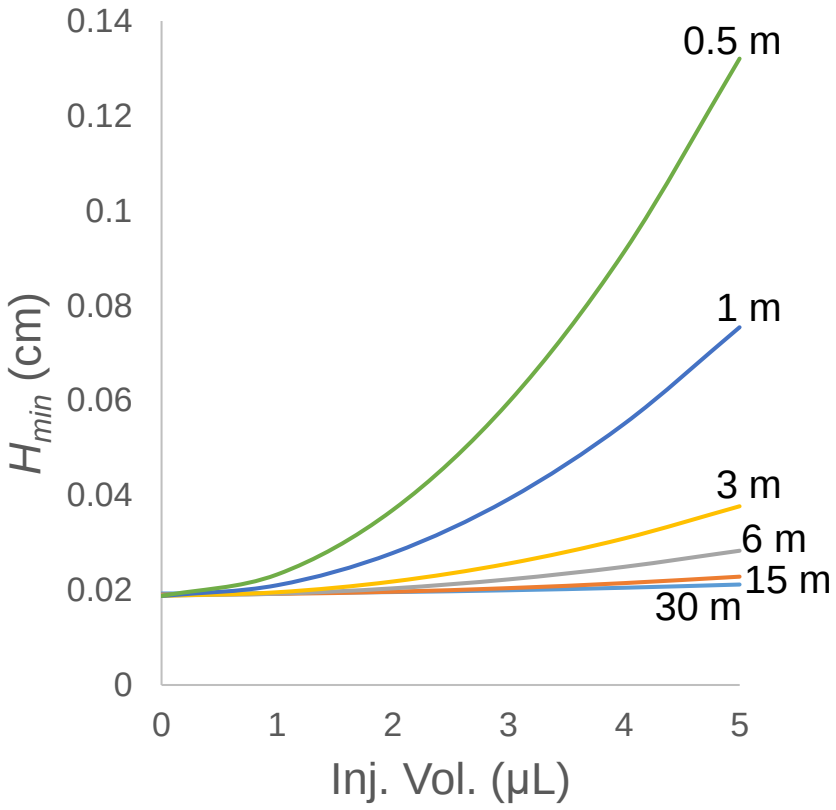

Figure 1.13. The effect of injection volume on H_{min} for a range of column lengths.

1.3 Microfabricated GC

1.3.1 Scaling Laws

The desire to make portable instrumentation is the most obvious driver for the development of microfabricated gas chromatographs (µGC). It is not, however, the only reason for the push towards smaller instrumentation. There exists a set of "scaling laws" which are generally beneficial to the chromatographic process and the production of instrumentation using micro-scale devices. Manufacturing processes typically used for the production of microelectronics in silicon have been adapted to the production of every component necessary to perform GC separations. The first report of a µGC by Terry et al. in 1979[20] aimed to make use of these manufacturing methods to take advantage of the scaling laws. The low thermal mass of the silicon enables rapid heating (or

cooling) of the components, which is attractive when considering that most GC methods include temperature programs, or at the very least, elevated temperature. Microfabrication also allows for the manufacture of columns with narrower aspects.[21]

Examining the Golay equation, and the dependence of the C term on column radius, it becomes immediately apparent that decreasing the diameter (or cross section of a non-circular column) improves efficiency and resolution. Alternatively, the *same* resolution can be achieved using a shorter column. This is essential, since column length is inherently limited by the increasing difficulty of pressure driven flow as column dimensions decrease. The possibility of incorporating multiple components in a single chip eliminates the need for bulky interconnections with large dead volumes, which can decrease sensitivity and resolution. If the correct detector type is used, one that is concentration sensitive, then the decreased dimensions require less sample mass for detection. Shrinking the components of a GC allows for portability, which in turn allows for analysis *in situ* eliminating difficulties encountered when collecting samples in the field and analyzing them in a remote laboratory. Each component of a GC has been demonstrated in microfabricated form. Microfabricated injectors, separation columns and detectors have been demonstrated as stand-alone devices and in integrated systems.

1.3.2 Microfabricated Injectors

Microfabricated injection devices fall into two general categories: valve and loop or sorbent based. The function and operation of these types of devices are similar to their bench scale counterparts. The first μGC[20] used a small sample loop and valve body incorporated on the same chip as the rest of the μGC for injection. This theme has been repeated by several others in their instrumentation.[22-25] On-chip valves are typically manufactured with a polymer membrane selectively opening and closing orifices in silicon or glass substrates. Combining several of these

valves with a sample collection channel, an analog of the 6-port, 2-position valve can be generated on-chip.[22] Often, only the microchannel sample loop is included on chip and the flow control requires valves off-chip.[25] These loop injectors can be used to inject microliter quantities of vapor phase samples onto separation columns.

Microfabricated sorbent-based injectors are much more common than valve based injectors. This type of device usually uses a small chamber or channel packed or coated with a sorbent material of the same type used in bench scale instrumentation. In addition, sorbent based injection devices have the ability to capture mass from large volumes of gas and injecting that same mass in a smaller volume. For this reason, they are often called preconcentrator/focusers and are often used in μGC to increase *system* LOD. Manginell et al.[26] have developed a mass-sensitive hotplate which captured analyte in a sol-gel on a silicon nitride platform which could be rapidly heated for injection. Zellers et al. have shown several iterations of graphitized carbon packed preconcentrator/focusers (μPCF)[27-34] with applications ranging from indoor air contamination[31] to explosives detection[32] to workplace exposure monitoring.[27] Agah and coworkers have also shown preconcentrators based on polymer coated-micropillars in a silicon chamber as well as the layer-by-layer deposition of silica nanoparticles.[35-38]

1.3.3 Microfabricated Columns

The heart of a μGC system is the separation column (μcolumn). The Bosch process for deep reactive ion etching (DRIE) of silicon has been used to define three of the sides of a rectangular or square column. This anisotropic process etches by bombardment with plasma (usually sulfur hexafluoride) normal to the surface. This is followed by the deposition of a passivation layer. These two steps are alternated until the desired depth of etch is reached. The anisotropic nature of the process is achieved because the passivation layer on horizontal surfaces

is subject to sputtering by the etchant, while vertical surfaces are not affected. Thus etching occurs only in one direction.[39] The channel can then be sealed with glass to form a tube which, after stationary phase coating, is suitable for use as a chromatographic column.[40] A cartoon of the steps in the process to make a μcolumn is shown in Figure 1.15.

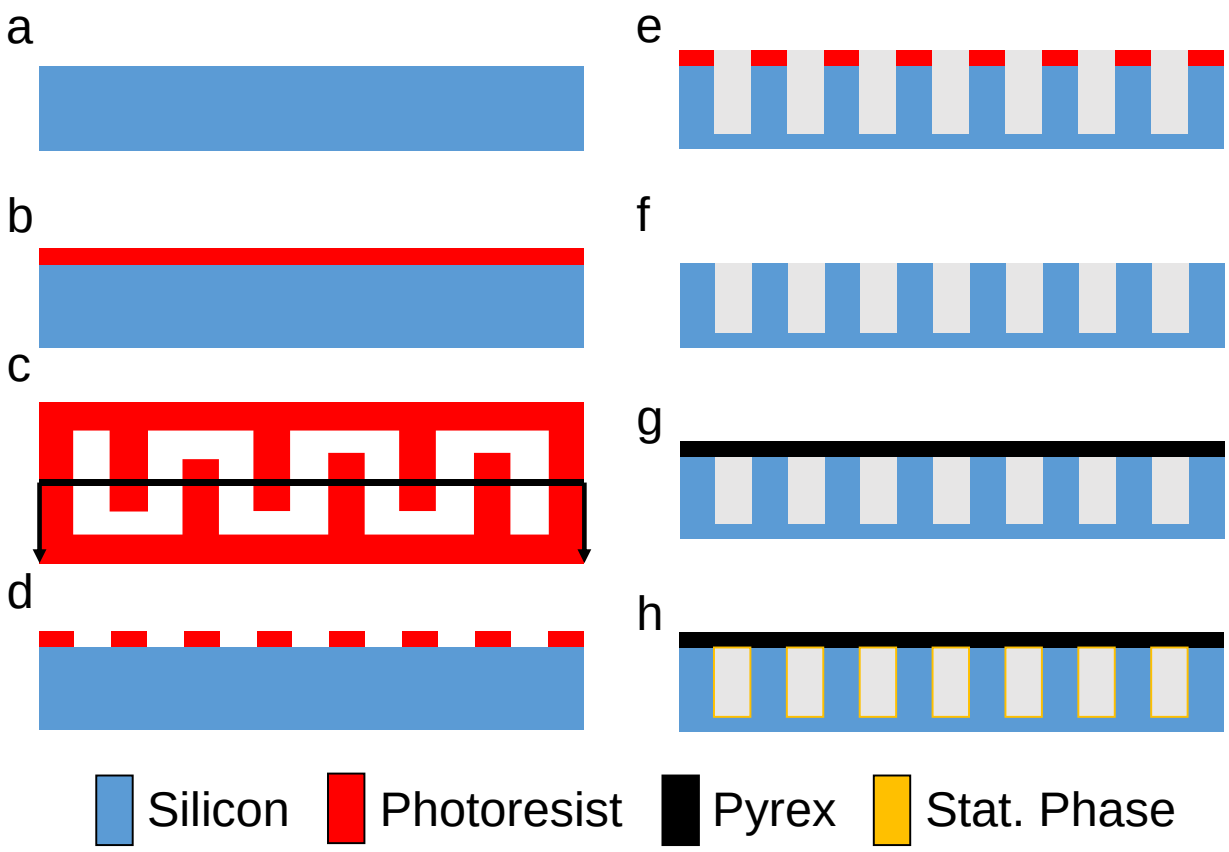

Figure 1.14. Steps in the microfabrication of GC columns. First a silicon wafer (a, edge view) is spin-coated with photoresist (b-edge view) and patterned in the desired shape (c-top view, d-edge view). DRIE forms the channels (e-edge view) and the photresist is removed (f-edge view). A Pyrex top is affixed (g-side view) and the column is coated (h-side view).

Other isotropic and anisotropic etching methods that enable the creation of round or semi-circular columns can also create μGC columns, however reports of these are less common.[41,42] The first μGC column[20] was arranged in a circular spiral with a 200 μm wide, 30 μm deep, channel sealed with Pyrex glass. It was coated with a PDMS stationary phase and generated approximately

700 theoretical plates per meter. This performance was less than stellar and work has continued on this front in many different groups around the world to try to improve the efficiency of μGC columns. At the University of Michigan, the members of the Center for Wireless Integrated Microsensing and Systems (WIMS2) developed several types of μcolumns with lengths ranging from 0.25 cm to 3 m[16,42-48] generating up to 4,900 plates per meter with a variety of stationary phases.[16] This includes work by Sacks et al on the design, fabrication and coating of silicon μcolumns,[40] nearly-round columns[42a,b] with chemical vapor deposited channel walls, and extensive investigations by Zellers et al. on stationary phase coating techniques and μcolumn performance.[16] Agah and coworkers at Virginia Tech. have recently created multichannel columns with thiolated-gold stationary phases,[49,50] semi-packed columns,[51,52] and more traditional polymer coated μcolumns.[53,54] The multicapillary columns aimed to take advantage of the GC scaling laws by minimizing the diffusion distance without sacrificing column loading capacity. Unfortunately the thiolate protected gold monolayer stationary phase used in those experiments was incredibly thin and led to loading capacity problems. They attempted to increase the mass of stationary phase in the column by including microfabricated pillars in the channels to create semi-packed columns. Other efforts include the partially buried microcolumns created by Shannon et al. at the University of Illinois which used a combination of isotropic and anisotropic methods to create nearly round columns in silica.[41] The same group examined the effect of column geometry on chromatographic performance. They determined that, of serpentine, square spiral and round spiral column geometries, serpentine columns were the most efficient in terms of plate number.[42] Though serpentine designs are also the least efficient in terms of column length per unit area, so many designs still use square or round spiral designs. Through a novel bonding method, the Shannon group was also able to produce a μcolumn fabricated entirely from silicon.[56] A unique design by

Suslick and coworkers[57] at the same institution created an entire column in PDMS, as opposed to silicon, which produced roughly 1800 plates per meter. Other groups have investigated novel coating processes such as carbon nanotubes grown *in situ*[58] and sputtered silica.[59]

From a theoretical standpoint, these rectangular channel columns behave slightly differently than the classical round open tubular columns. The C_m term of the Golay Equation must be modified to account for the change in shape. Significant theoretical work has gone into this, with treatments by Giddings,[18] Spangler,[60] and a collaboration between Ahn and Brandani.[61] Each of these successive works provided refinement to their forbears, and close agreement between theoretical and experimental data was obtained.

1.3.4 Microfabricated Detectors

Microfabricated versions of traditional GC detectors have been created and used as detectors for GC and μGC. The TCD has been used a μGC detector since the Terry report.[20] Several versions of the design incorporated on-chip μcolumns in the same manner as Terry.[54, 62-65] These simple devices still suffer from the same shortcomings as the non-microfabricated detectors as discussed previously and necessitate a carrier gas other than air for operation.[4] Sensors with reversibly-sorptive interfaces such as surface acoustic wave (SAW) devices,[66] thickness shear mode resonators (TSMR),[67] microcantilevers,[68-70] chemiresistors,[71-74] have been used in a number of μGC applications. SAW and TSMR devices measure changes in resonant frequency of a piezoelectric material as mass collects in/leaves the interface film which is typically a polymer, though, ionic liquids[75] and thiolate protected gold nanoparticles have been used with success. Stress induced response to mass deposition on the suspended beam structure of microcantilever devices have also been used as GC detectors.[69]

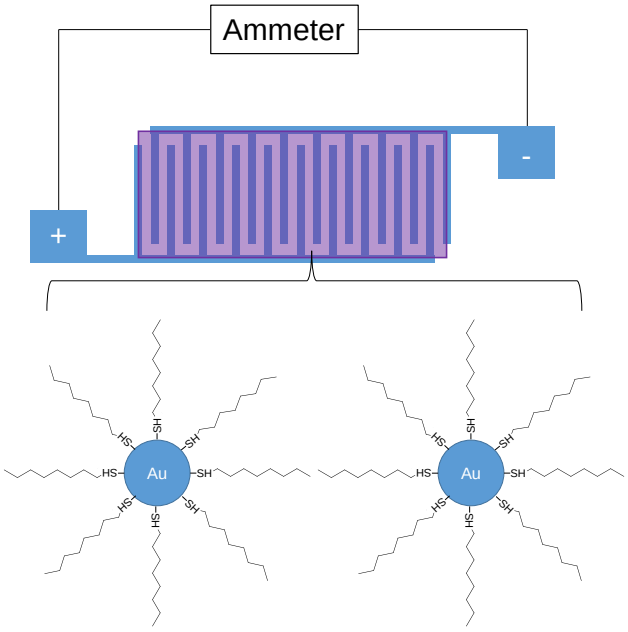

Figure 1.15. Schematic diagram of a chemiresistor array with a cartoon depiction of two octanethiol MPNs shown beneath.

Most relevant to the work presented here is the chemiresistor (CR) array detector. These devices function by sensing the change in resistance of films of thiolate monolayer protected gold nanoparticles (MPN) through cast on interdigitated gold electrodes as shown in the cartoon in Figure 1.16 which also depicts an octanethiol MPN. As vapor partitions into the film, the intercore distance increase, resulting in a commensurate increase in film resistance. Devices similar to these, with multiple different types of thiolate protecting groups have been used.[71-74] The use of an array of this type of sensor, and the differential responses afforded by that approach, enables the generation of fingerprint-like response patterns that can aid in recognition of analytes. Though not as effective as MS, this approach provides an added degree of chemical information to the GC analysis.

Other new devices have been reported recently, though this type of sensor is not widely reported yet. Early reports of Fabry-Perot sensors are promising, since they can be integrated into the μcolumn channels and are non-destructive, fast sensors.[75] A microfabricated optofluidic ring

resonator (μOFRR) device, based on macro-scale devices developed by the Fan group, has been demonstrated with PDMS and MPN stationary phases which showed fast, sensitive responses.[76-78] An optical discharge device has been reported by Gianchandani[79] which measures the optical emission induced by an electrical discharge. Agah[80] and Fan[81] have both developed microphotoionization detectors, which improve on existing PID devices by virtue of their minimized dead-volumes.

1.3.5 Microfabricated GC Systems

Systems incorporating each of the aforementioned microdevices comprise the functional analytical portion of a GC system (μGC), though other components are often necessary to form a *functional* μGC. These ancillary components are critical to the function and integration of the microcomponents, but are typically not the focus of studies as they are off-the-shelf, commercial parts. For the purposes of this discussion, a μGC is defined as a GC instrument whose salient analytical features are microfabricated. This narrows the focus of discussion, as there are many *portable* GCs that are not, strictly speaking, μGCs.

Since the first μGC, that of Terry et al.,[20] efforts at several institutions and instrument manufacturers have produced fully-functional μGCs. Kolesar et al. developed an instrument in 1994[82] which incorporated a microfabricated loop injector, μcolumn and dual detector (μTCD and CR). This instrument was used to separate and detect ammonia and nitrogen dioxide gases. The copper phthalocyanine stationary phase was deposited prior to sealing of the Si channel, a process uniquely available to μcolumns and nearly impossible in traditional capillary columns. Efforts at Sandia National Laboratory resulted in the μChemLab,[83] which incorporated several types of microinjectors, a μcolumn and a SAW detector for the detection of chemical warfare agents (CWAs). Muller et al. at the Technical University of Hamburg used a microvalve/loop injector, a

plasma polymerized μcolumn, and a μTCD for the analysis of synthetic natural gas.[84] The efforts of the Zellers group, part of the WIMS2 Center at the University of Michigan, have produced prototype instruments using μPCF devices packed with graphitized carbon, PDMS coated μcolumns and CR array detectors for measurement of indoor air contaminants,[85] vapor intrusion,[86-88] and explosive marker compounds.[89] The Gianchandani group has produced a prototype μGC, called the iGC, which incorporates micropumps as well as a microinjector, μcolumn and plasma discharge microdetector.[79] Zampolli et al. have produced a prototype which uses a cavitand sorbent packed preconcentrator μcolumn, a sorbent packed separation μcolumn and metal oxide semiconductor sensors and analyzed BTEX mixtures.[90] Most recently, the Agah group demonstrated a μGC they called Zebra.[91] This μGC incorporated several of the group's unique device designs: polymer coated micropillar preconcentrator, PDMS coated μcolumn and μTCD and was used to measure mixtures of VOCs.

1.4 Two Dimensional GC

1.4.1 Definitions, Processes and Theory

The concepts and theoretical basis for two dimensional separations were first laid out by Giddings in the 1984.[92] This work was general and dealt with many possible theoretical combinations of separation types. Some were obviously prohibited by issues with analyte compatibility issues, sample phase issues and physical coupling of separation types. A requirement for *useful* two dimensional separations is a difference in separation mechanism, or orthogonality of separations. One of these combinations was gas chromatography combined with gas chromatography, with the stipulation that the second separation must use a substantially different chemical interaction than the first.

Two dimensional gas chromatography is often used as a means to increase peak capacity and resolution as compared to traditional single dimension GC.[93] This is accomplished by performing a second separation on the effluent of a GC column with a different stationary phase than the first. This can take several forms. If only a selected portion of column effluent is subjected to a second separation, the process is referred to as "heart cut" two dimensional gas chromatography. If non-specific portions of column effluent are sampled but, importantly, not the entirety of the effluent, the process is referred to as non-comprehensive two dimensional gas chromatography. If the effluent is sampled exhaustively and subjected to a second separation, and the separation achieved in the first dimension is not degraded in the second, then the process is referred to as comprehensive two dimensional gas chromatography or GC × GC.[93-96] The first is done through a device referred to as a modulator mounted between the first and second columns.[94] The second is accomplished by using two columns with substantially different separation selectivity.[93-96] Figure 1.17 shows the workflow for a typical GC × GC experiment. The data from a single detector is parsed into individual 2D separations based on the modulation period (Pm, the time between 2D injections). These chromatograms are rotated 90° and aligned such that the X-axis represents the 1D retention time and the y-axis represents the 2D retention time. Finally, a contour plot can be generated from this rotated, aligned data.

The biggest advantage most often quoted by chromatographers advocating for the use of GC × GC is the improvement in peak capacity afforded.[93] The theory laid out by Giddings[18,92] indicates that the peak capacity for a two dimensional separation is the product of the peak capacities of the individual dimensions (Equation 1.17). There remains some controversy on this point,[97] as two GC separations will always have some degree of correlation in separation mechanism. In addition, the separation in the first dimension is often purposely degraded to enable

adequate sampling of the eluting peaks which leaves a question as to whether an optimized one dimensional separation could not achieve the same result.[97] It has been found that the critical parameter to achieve of this is the reinjection bandwidth.[97] It appears that this issue can be overcome and peak capacities near the theoretical maximum (the product of the peak capacities of the first and second dimensions) can be realized.[98]

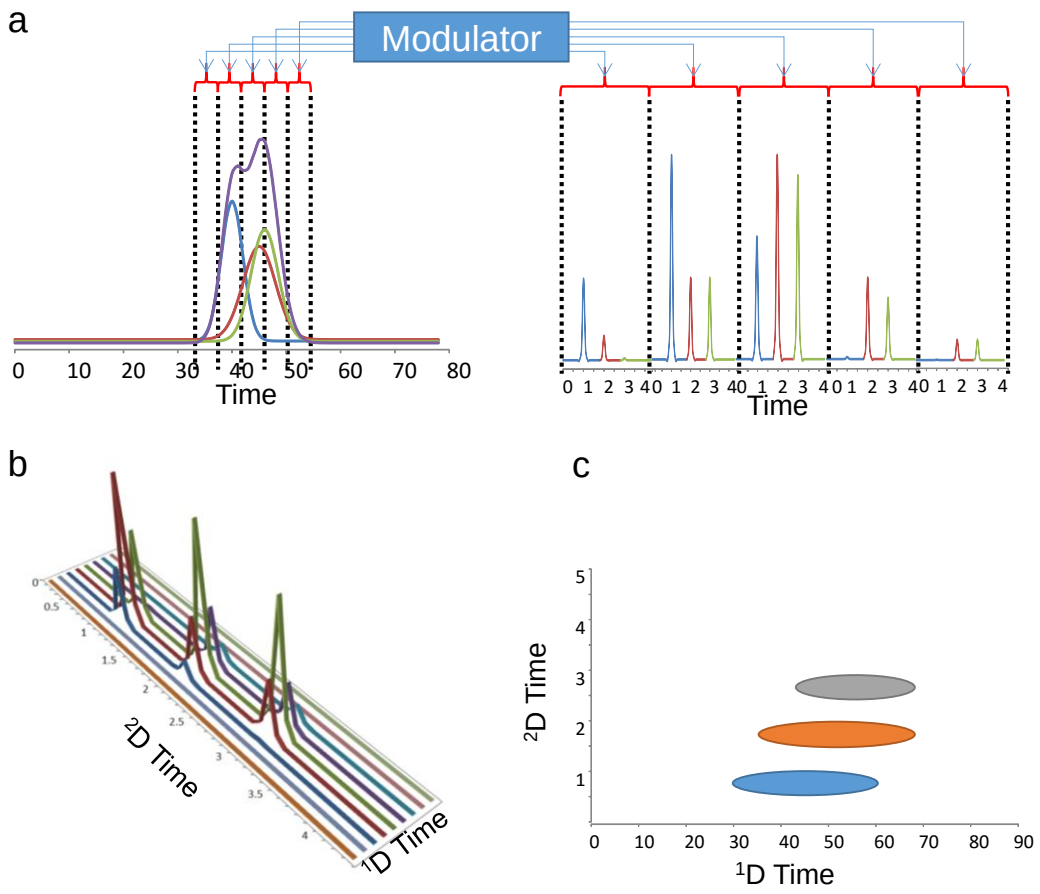

Figure 1.16. Data processing for GC × GC. Coeluting peaks (purple in a) are modulated into 2D chromatograms with a length equivalent to the Pm. These chromatograms are rotated and aligned (b) to generate a contour plot (c) if retention times in each column.

1.4.2 GC × GC Instrumentation

It wasn't until 1991 that a modulator capable of exhaustively sampling and reinjecting first column effluent was developed.[99] The invention of a method of trapping and rapidly heating a small segment of fused silica capillary by Phillips and Liu[100] was crucial to the development of the field of GC × GC. It sparked a revolution in modulator technologies, including efforts in many research groups and instrument manufacturers across the globe.

These modulators fall into two different categories: pneumatic and thermal. Pneumatic modulation accomplishes sampling and reinjection using gas pressure and valves. Diaphragm valve modulation[100] uses a 6-port valve similar to that in Figure 1.2 to direct first dimension (^{1}D) column effluent either to a second dimension (^{2}D) column or a vent line. The loss of sample when the ^{1}D column effluent is directed to the vent line precludes comprehensive separation; only ~10% of the effluent is sampled. The so-called Dean's switch operates similarly.[101] Differential flow modulation[102] modifies the design of the diaphragm valve modulator to include a sampling loop which is vented when full. This eliminates the vent line and comes closer to comprehensive GC × GC with sampling efficiencies approaching 80%.[102] Seeley and Bueno developed this idea further, and the resulting fill/flush differential flow modulator can be considered a comprehensive modulator.[103]

Thermal modulators are by far the most common type of modulation device for GC × GC. They operate by using either a thick stationary phase film[99] or extremely low temperature[104-107] to stop analyte eluting from the ^{1}D column. The modulator is then rapidly heated to remobilize the analyte, re-injecting it into the ^{2}D separation column. Several variations of thermal modulation devices exist. Most use a cryogenic fluid such as liquid nitrogen to cool a small segment of the ^{2}D

column. In early instruments, the removal of the cryogen, and subsequent return to ambient temperature, is enough to remobilize the analyte. Modern instruments however, use a heated jet of air which narrows the re-injection band.[108] Several groups and instrument manufacturers have experimented with different thermal modulator designs. A common feature in many successful thermal modulators is the use of two stages of modulation, which are rapidly alternately heated and cooled. This allows analyte that enters into the first stage of modulation during a heating cycle to be trapped, preventing any analyte from passing through the device unmodulated (a phenomenon called breakthrough).

Non-cryogenic modulators such as the the Philips modulator[99] are attractive since they require no consumable cryogen. Ledford and coworkers developed a non-cryogenic thermal modulator which uses a rotating heater to sweep a section of column, focusing and re-injecting analyte into the 2D column in the process.[110] One review[96] found that 30% of GC × GC papers published before 2003 used this type of modulator, though with the growth of cryogenic modulation, that number has certainly decreased. Another non-cryogenic modulator developed by Sacks et al. used air chilled by refrigeration to trap analyte in capillary.[106]

Cryogenic modulators occupy the top tier of thermal modulators. The longitudinally modulated cryogenic system (LMCS) developed in the Marriot lab[111] incorporates a moving sleeve continuously purged with cryogenic fluid and that moves back and forth along a section of a capillary GC column. Analyte is trapped and then released as the location of the sleeve changes. Beens et al.[112] developed a system to jet cryogen onto a segment of capillary, trapping analyte within. When the jet is turned off, the capillary spontaneously heats to the elevated ambient (oven) temperature and trapped quantity of analyte is reinjected into the ^{2}D column. Variations and modifications of this system have defined the state of the art in GC × GC separations.[107,113]

1.5 Portable/Microfabricated GC × GC

The relatively short 1D-GC columns available in extant portable μGC instruments could be greatly reduced with the addition of a second dimension of separation space. Portable instrumentation capable of performing 2D separations would be of great value for many applications, such as biomarker monitoring and fuel analysis. Several groups have demonstrated 2D separations using μcolumns and off-chip pneumatic modulators.[114] Fan et al.[115] have demonstrated multidimensional separations using multiple μcolumns and adsorbent tubes for refocusing effluent from the ^{1}D μcolumn. Thus far, there is no report of a comprehensive μGC × μGC using microcomponents for ^{1}D separation, modulation, ^{2}D separation and detection. Recently, a microfabricated thermal modulator was developed Kim and Kurabayashi[116] and tested with capillary columns[116-118] and μcolumns[119,120] in collaboration with members of the Zellers group.

1.6 Presented Research

This dissertation concerns the development of μGC and μGC × μGC systems and components with a focus on their integration with one another. The next chapter (Chapter 2) describes the development of a single-column μGC prototype for the determination of explosive marker compounds and was intended for passenger or luggage screening in airports. This results of this work were published in 2014 in *Analytical Chemistry*. Chapters 3, 4, 5 and 6 describe various aspects of the development of systems using a μTM, with the ultimate goal of producing a fully microfabricated μGC × μGC prototype. Chapter 3 deals with the integration of μcolumns with the μTM, and includes a novel RTIL stationary phase material used for the first time in μcolumns. Chapter 3 was published in *Analytical Chemistry* in 2015. Chapter 4 concerns the

implementation of temperature programming of the μTM and the attempted use of RTIL as the stationary phase coating for the μTM. The work presented in Chapter 4 is being prepared for publication. Chapters 5 and 6 build on the success of the integration of μcolumns with the μTM, adding microfabricated detector devices: the μOFRR (Chapter 5) and the CR array (Chapter 6). Chapter 6 also describes the construction of the μGC × μGC lab prototype and preliminary results obtained from this novel microsystem. The work on the μGC × μGC-μOFRR was published in *Analyst* in 2015 while the μGC × μGC-CR work is being prepared for publication.

1.7 References

1. US EPA FAQ http://www3.epa.gov/ttn/emc/facts.html#voc accessed 11/20/15
2. Ma, Hongying, et al. "Analysis of human breath samples of lung cancer patients and healthy controls with solid-phase microextraction (SPME) and flow-modulated comprehensive two-dimensional gas chromatography (GC× GC)." *Analytical Methods* 6.17 (2014): 6841-6849.
3. Prebihalo, Sarah, et al. "Determination of emerging contaminants in wastewater utilizing comprehensive two-dimensional gas-chromatography coupled with time-of-flight mass spectrometry." *Journal of Chromatography A* 1419 (2015): 109-115.
4. Skoog, D. A., Holler, F. J., & Nieman, T. A. (1998). *Principles of instrumental analysis*. Philadelphia: Saunders College Pub.
5. Grob, R. L. (2004) Theory of Gas Chromatography, in Modern Practice of Gas Chromatography, Fourth Edition (eds R. L. Grob and E. F. Barry), John Wiley & Sons, Inc., Hoboken, NJ, USA.
6. Payagala, Tharanga, et al. "Trigonal tricationic ionic liquids: a generation of gas chromatographic stationary phases." *Analytical chemistry* 81.1 (2008): 160-173. Grob, Kurt. *Making and manipulating capillary columns for gas chromatography*. Hüthig, 1986.
7. Gelest Silicon compounds: Silanes & Silicones Catalog
8. Supelco HMDS product information https://www.sigmaaldrich.com/content/dam/sigma-aldrich/docs/Supelco/Product_Information_Sheet/4750.pdf accessed 11/20/15
9. Dhanesar, Subhash C., Myra E. Coddens, and Colin F. Poole. "Influence of phase loading on the performance of whisker-walled open tubular columns coated with organic molten salts." *Journal of Chromatography A* 324 (1985): 415-421.
10. Poole, Colin F., et al. "Survey of organic molten salt phases for gas chromatography." *Journal of Chromatography A* 289 (1984): 299-320.
11. Anderson, Jared L., and Daniel W. Armstrong. "Immobilized ionic liquids as high-selectivity/high-temperature/high-stability gas chromatography stationary phases." *Analytical chemistry* 77.19 (2005): 6453-6462.
12. Zhang, Cheng, et al. "Identifying important structural features of ionic liquid stationary phases for the selective separation of nonpolar analytes by comprehensive two-dimensional gas chromatography." *Journal of Chromatography A* 1386 (2015): 89-97.
13. Pandey, Siddharth. "Analytical applications of room-temperature ionic liquids: A review of recent efforts."*Analytica Chimica Acta* 556.1 (2006): 38-45.
14. Supelco Ionic Liquid Information Page http://www.sigmaaldrich.com/analytical-chromatography/analytical-products.html?TablePage=101691909 accessed 11/20/15
15. Serrano, Gustavo, Shaelah M. Reidy, and Edward T. Zellers. "Assessing the reliability of wall-coated microfabricated gas chromatographic separation columns." *Sensors and Actuators B: Chemical* 141.1 (2009): 217-226.
16. Narayanan, Shree, Bassam Alfeeli, and Masoud Agah. "Two-port static coated micro gas chromatography column with an embedded thermal conductivity detector." *Sensors Journal, IEEE* 12.6 (2012): 1893-1900.
17. Giddings, John Calvin. *Unified separation science*. New York etc: Wiley, 1991.
18. Reidy, S., *High-performance Micro-fabricated Gas Chromatography Columns for Complex Mixture Analysis* Retrieved from Deep Blue

19. Terry, Stephen C., John H. Jerman, and James B. Angell. "A gas chromatographic air analyzer fabricated on a silicon wafer." *Electron Devices, IEEE Transactions on* 26.12 (1979): 1880-1886.
20. Matzke, Carolyn M., et al. "Microfabricated silicon gas chromatographic microchannels: fabrication and performance." *Micromachining and Microfabrication*. International Society for Optics and Photonics, 1998.
21. Lehmann, U., et al. "Micro machined gas chromatograph based on a plasma polymerised stationary phase." *Micro Total Analysis Systems 2000*. Springer Netherlands, 2000.
22. Bruns, M. W. "High speed portable gas chromatography: silicon micromachining." ErdÖl und Kohle, Erdgas, Petrochemie vereinigt mit Brennstoff-Chemie 47.3 (1994): 80-84.
23. Bessoth, Fiona G., et al. "Towards an on-chip gas chromatograph: the development of a gas injector and a dc plasma emission detector." Journal of Analytical Atomic Spectrometry 17.8 (2002): 794-799.
24. Dziuban, J. A., et al. "Portable gas chromatograph with integrated components." Sensors and Actuators A: Physical 115.2 (2004): 318-330.
25. Manginell, Ronald P., et al. "Mass-sensitive microfabricated chemical preconcentrator." Microelectromechanical Systems, Journal of 17.6 (2008): 1396-1407.
26. Lu, Chia-Jung, and Edward T. Zellers. "A dual-adsorbent preconcentrator for a portable indoor-VOC microsensor system." *Analytical Chemistry* 73.14 (2001): 3449-3457.
27. Lu, Chia Jung, and Edward T. Zellers. "Multi-adsorbent preconcentration/focusing module for portable-GC/microsensor-array analysis of complex vapor mixtures." *Analyst* 127.8 (2002): 1061-1068.W.-C. Tian, S. Pang, C.-J. Lu, E.T. Zellers, Microfabricated preconcentrator-focuser for a microscale
28. W.C. Tian, H.K.L. Chan, C.-J. Lu, S.W. Pang, E.T. Zellers, Microfabricatedmulti-stage preconcentrator-focuser for a micro gas chromatograph, J. Micro-electromech. Syst. 14 (2005) 498–507.
29. T. Sukaew, H. Chang, G. Serrano, E.T. Zellers, Multi-stage preconcen-trator/focuser module designed to enable trace level determinations oftrichloroethylene in indoor air with a microfabricated gas chromatograph, Ana-lyst 136 (2011) 1664–1674.
30. G. Serrano, T. Sukaew, E.T. Zellers, Hybrid preconcentration/focuser modulefor determinations of explosive marker compounds with a micro-scale gaschromatograph, J. Chromatogr. A 1279 (2013) 76–85.
31. T. Sukaew, E.T. Zellers, Evaluating the dynamic retention capacities of micro-fabricated vapor preconcentrators as a function of flow rate, Sens. Actuators B:Chem. 183 (2013) 163–171.
32. Bryant-Genevier, Jonathan, and Edward T. Zellers. "Toward a Microfabricated Preconcentrator-Focuser for a Wearable Micro-scale Gas Chromatograph." Journal of Chromatography A (2015).
33. B.Alfeeli,M.Agah,MEMS-based selective preconcentrationoftrace level breath analytes, IEEE Sens. J. 9 (2009) 1068–1075.
34. M. Akbar, M. Agah, A microfabricated propofoltrap for breath-based anesthesia depth monitoring, J. Microelectromech. Syst. 22 (2013) 443–451.
35. M. Akbar, D. Wang, R. Goodman, A. Hoover, G. Rice, J.R. Heflin, et al., Improved performance of micro-fabricated preconcentrators using silica nanoparticles as a surface template, J. Chromatogr. A 1322 (2013) 1–7.

36. B.Alfeeli,V. Jain, R.K. Johnson, F.L. Beyer, J.R. Heflin, M.Agah, Characterization of poly(2,6-diphenyl-p-phenylene oxide) films as adsorb
37. Method of anisotropically etching silicon United States Patent 5501893
38. Lambertus, Gordon, et al. "Design, fabrication, and evaluation of microfabricated columns for gas chromatography." Analytical chemistry 76.9 (2004): 2629-2637.
39. Agah, Masoud, and Kensall D. Wise. "Low-mass PECVD oxynitride gas chromatographic columns."*Microelectromechanical Systems, Journal of* 16.4 (2007): 853-860.
40. C.-J. Lu, W.H. Steinecker, W.-C. Tian, M.C. Oborny, J.M. Nichols, M. Agah, J.A. Potkay, H.K.L. Chan, J. Driscoll, R.D. Sacks, K.D. Wise, S.W. Pang, E.T. Zellers, Firstgeneration hybrid MEMS gas chromatograph, Lab Chip 5 (2005) 1123–1131.
41. E.T. Zellers, S. Reidy, R.A. Veeneman, R. Gordenker, W.H. Steinecker, G.R. Lambertus, H. Kim, J.A. Potkay, M.P. Rowe, Q. Zhong, C. Avery, H.K.L. Chan, R.D. Sacks, K. Najafi, K.D. Wise, An integrated micro-analytical system for complex vapor mixtures, in: Proceedings of the Transducers'07, Lyon, France, June 10–14, 2007.
42. a. M. Agah, J.A. Potkay, J.A. Driscoll, R.D. Sacks, M. Kaviany, K.D. Wise, Thermal behavior of high-performance temperature-programmed microfabricated gas chromatography columns, in: Proceedings of the Transducers'03, USA, June 8–12, 2003.
b. Potkay, Joseph, et al. "A low-power pressure-and temperature-programmable micro gas chromatography column." *Microelectromechanical Systems, Journal of* 16.5 (2007): 1071-1079.
43. M. Agah, J. Potkay, A. Elstro, G. Lambertus, R. Sacks, K.D. Wise, A high performance temperature-programmed gas chromatography column, in: Tech. Digest, North American Solid-State Sensors, Actuators, and Microsystems Workshop, Hilton Head, SC, USA, June 6–10, 2004.
44. M. Agah, J.A. Potkay, G.R. Lambertus, R.D. Sacks, K.D. Wise, High performance temperature-programmed microfabricated gas chromatography columns, IEEE J. Microelectromech. Syst. 14 (5) (2005) 1039–1050.
45. J.A. Potkay, G.R. Lambertus, R.D. Sacks, K.D. Wise, A low power pressure and temperature-programmable micro gas chromatography column, J. Microelectromech. Syst. 16 (2007) 1071–1079.
46. Shakeel, Hamza, and Masoud Agah. "Self-patterned gold-electroplated multicapillary gas separation columns with MPG stationary phases."*Microelectromechanical Systems, Journal of* 22.1 (2013): 62-70.
47. Shakeel, Hamza, et al. "Improved self-assembled thiol stationary phases in microfluidic gas separation columns." *Sensors and Actuators B: Chemical* 216 (2015): 349-357.
48. Ali, Syed, et al. "MEMS-based semi-packed gas chromatography columns." *Sensors and Actuators B: Chemical* 141.1 (2009): 309-315.
49. Shakeel, Hamza, Gary W. Rice, and Masoud Agah. "Semipacked columns with atomic layer-deposited alumina as a stationary phase." *Sensors and Actuators B: Chemical* 203 (2014): 641-646
50. Shakeel, Hamza, and Masoud Agah. "Self-patterned gold-electroplated multicapillary gas separation columns with MPG stationary phases."*Microelectromechanical Systems, Journal of* 22.1 (2013): 62-70.
51. Narayanan, Shrikanth, and Masoud Agah. "A high-performance TCD monolithically integrated with a gas separation column." *Sensors, 2012 IEEE*. IEEE, 2012.

52. Radadia, A. D., et al. "The effect of microcolumn geometry on the performance of micro-gas chromatography columns for chip scale gas analyzers." *Sensors and Actuators B: Chemical*150.1 (2010): 456-464.
53. Radadia, A. D., et al. "The fabrication of all-silicon micro gas chromatography columns using gold diffusion eutectic bonding." *Journal of Micromechanics and Microengineering* 20.1 (2010): 015002.
54. Rankin, Jacqueline M., and Kenneth S. Suslick. "The development of a disposable gas chromatography microcolumn." *Chemical Communications* 51.43 (2015): 8920-8923.
55. Stadermann, Michael, et al. "Ultrafast gas chromatography on single-wall carbon nanotube stationary phases in microfabricated channels."*Analytical chemistry* 78.16 (2006): 5639-5644.
56. Haudebourg, R., et al. "Temperature-programmed sputtered micromachined gas chromatography columns: An approach to fast separations in oilfield applications." *Analytical chemistry* 85.1 (2012): 114-120.
57. Spangler, Glenn E. "Height equivalent to a theoretical plate theory for rectangular GC columns." *Analytical Chemistry* 70.22 (1998): 4805-4816.
58. Ahn, Hyungwoong, and Stefano Brandani. "Analysis of breakthrough dynamics in rectangular channels of arbitrary aspect ratio." *AIChE journal* 51.7 (2005): 1980-1990.
59. Sun, Jianhai, et al. "Design, modeling, microfabrication and characterization of novel micro thermal conductivity detector." *Sensors and Actuators B: Chemical* 160.1 (2011): 936-941.
60. Zampolli, S., et al. "Real-time monitoring of sub-ppb concentrations of aromatic volatiles with a MEMS-enabled miniaturized gas-chromatograph." *Sensors and Actuators B: Chemical* 141.1 (2009): 322-328.
61. Rastrello, F., et al. "Thermal conductivity detector for gas-chromatography: acquisition system and experimental measurements." *Instrumentation and Measurement Technology Conference (I2MTC), 2012 IEEE International*. IEEE, 2012.
62. Kaanta, Bradley C., Hua Chen, and Xin Zhang. "A monolithically fabricated gas chromatography separation column with an integrated high sensitivity thermal conductivity detector." *Journal of Micromechanics and Microengineering* 20.5 (2010): 055016.
63. Canary Three Information Page http://www.defiant-tech.com/canarythree.php accessed 11/20/15
64. Scholten, Kee, Lindsay K. Wright, and Edward T. Zellers. "Vapor Discrimination With Single-and Multitransducer Arrays of Nanoparticle-Coated Chemiresistors and Resonators." *Sensors Journal, IEEE* 13.6 (2013): 2146-2154.
65. L. A. Pinnaduwage, D. L. Hedden, A. Gehl, V. I. Boiadjev, J. E. Hawk, R. H. Farahi, T. Thundat, E. J. Houser, S. Stepnowski, R. A. McGill, L. Deel, and R. T. Lareau, "A sensitive, handheld vapor sensor based on microcantilevers," *Rev. Sci. Instrum.*, vol. 75, no. 11, pp. 4554–4557, Nov. 2004.
66. P. J. Chapman, F. Vogt, P. Dutta, P. G. Datskos, G. L. Devault, and M. J. Sepaniak, "Facile hyphenation of gas chromatography and a microcantilever array sensor for enhanced selectivity," *Anal. Chem.*, vol. 79, no. 1, pp. 364–370, Jan. 2007.
67. M. Li, E. Myers, H. X. Tang, S. J. Aldridge, H. C. McCaig, J. J. Whiting, R. J. Simonson, N. S. Lewis, and M. L. Roukes, "Nanoelectromechanical resonator arrays for ultrafast,

gas-phase chromatographic chemical analysis," *Nano Lett.*, vol. 10, no. 10, pp. 3899–3903, Aug. 2010.
68. L. Han, X. Shi, W. Wu, F. L. Kirk, J. Luo, L. Wang, D. Mott, L. Cousineau, S. I. I. Lim, S. Lu, and C. J. Zhong, Nanoparticle structured sensing array materials and pattern recognition for VOC detection," *Sens. Actuators B Chem.*, vol. 106, no. 1, pp. 431–441, Apr. 2005.
69. Y. Joseph, A. Peic, X. Chen, J. Michl, T. Vossmeyer, and A. Yasuda, "Vapor sensitivity of networked gold nanoparticle hemiresistors: Importance of flexibility and resistivity of the interlinkage," *J. Phys. Chem. C*, vol. 111, no. 34, pp. 12855–12859, Aug. 2007.
70. Q. Zhong, W. H. Steinecker, and E. T. Zellers, "Characterization of a high-performance portable GC with a chemiresistor array detector," *Analyst*, vol. 134, no. 2, pp. 283–293, Nov. 2008.
71. E. Dovgolevsky, U. Tisch, and H. Haick, "Chemically sensitive resistors based on monolayer-capped cubic nanoparticles: Toward configurable nanoporous sensors," *Small*, vol. 5, no. 10, pp. 1158–1161, May 2009.
72. Rehman, Abdul, et al. "Differential solute gas response in ionic-liquid-based QCM arrays: elucidating design factors responsible for discriminative explosive gas sensing." *Analytical chemistry* 83.20 (2011): 7823-7833.
73. Liu, Jing, et al. "Fabry− Pérot Cavity Sensors for Multipoint On-Column Micro Gas Chromatography Detection." *Analytical chemistry* 82.11 (2010): 4370-4375.
74. Scholten, Kee, Xudong Fan, and Edward T. Zellers. "Microfabricated optofluidic ring resonator structures." *Applied physics letters* 99.14 (2011): 141108.
75. Scholten, K., et al. "Nanoparticle-coated micro-optofluidic ring resonator as a detector for microscale gas chromatographic vapor analysis." *Nanoscale*7.20 (2015): 9282-9289.
76. Collin, William R., et al. "Polymer-Coated Micro-Optofluidic Ring Resonator Detector for a Comprehensive Two-Dimensional Gas Chromatographic Microsystem: μGC× μGC–μOFRR."*Analyst* (2015).
77. Qin, Yutao, and Yogesh B. Gianchandani. "iGC2: an architecture for micro gas chromatographs utilizing integrated bi-directional pumps and multi-stage preconcentrators." *Journal of Micromechanics and Microengineering* 24.6 (2014): 065011.
78. Narayanan, Shree, Gary Rice, and Masoud Agah. "A micro-discharge photoionization detector for micro-gas chromatography." *Microchimica Acta* 181.5-6 (2014): 493-499.
79. Zhu, Hongbo, et al. "Flow-through Microfluidic Photoionization Detectors for Rapid and Highly Sensitive Vapor Detection." *Lab on a Chip* (2015).
80. Reston, Rocky R., and Edward S. Kolesar Jr. "Silicon-micromachined gas chromatography system used to separate and detect ammonia and nitrogen dioxide. I. Design, fabrication, and integration of the gas chromatography system." *Microelectromechanical Systems, Journal of* 3.4 (1994): 134-146.
81. Lewis, Patrick R., et al. "Recent advancements in the gas-phase MicroChemLab." *Sensors Journal, IEEE* 6.3 (2006): 784-795.
82. Lehmann, U., et al. "Micro machined gas chromatograph based on a plasma polymerised stationary phase." *Micro Total Analysis Systems 2000*. Springer Netherlands, 2000.
83. Lu, Chia-Jung, et al. "First-generation hybrid MEMS gas chromatograph." *Lab on a Chip* 5.10 (2005): 1123-1131.
84. Kim, S.; Chang, H.; Zellers, E.T.; *Anal. Chem.*, **2011**, 83, 7198-7206.

85. Kim, S.; Burris, D.; Chang, H.; Bryant-Genevier, J.; Zellers, E. T. , *Environ. Sci. and Technol.*, **2012**, 46, 6065-6072.
86. Kim, S.; Burris, D.; Bryant-Genevier, J.; Gorder, K.; Dettenmaier, E.; Zellers, E.T., *Environ. Sci. and Technol.*, **2012,** 46, 6073-6080.
87. Collin, W.; Serrano, G.; Wright, L.; Chang, H.; Nuñovero, N.; Zellers, E.T.; *Anal. Chem.*, 2014, 86, 655−663.
88. Zampolli, S., et al. "Real-time monitoring of sub-ppb concentrations of aromatic volatiles with a MEMS-enabled miniaturized gas-chromatograph." *Sensors and Actuators B: Chemical* 141.1 (2009): 322-328.
89. Garg, Apoorva, et al. "Zebra GC: A mini gas chromatography system for trace-level determination of hazardous air pollutants." *Sensors and Actuators B: Chemical* 212 (2015): 145-154.
90. Giddings, J. Calvin. "Two-dimensional separations: concept and promise." *Analytical chemistry* 56.12 (1984): 1258A-1270A.
91. Dimandja, Jean-Marie D. "Peer Reviewed: GC X GC." *Analytical Chemistry* 76.9 (2004): 167-A
92. Edwards, Matthew, Ahmed Mostafa, and Tadeusz Górecki. "Modulation in comprehensive two-dimensional gas chromatography: 20 years of innovation." *Analytical and bioanalytical chemistry*401.8 (2011): 2335-2349.
93. Adahchour, M., et al. "Recent developments in comprehensive two-dimensional gas chromatography (GC× GC): I. Introduction and instrumental set-up."*TrAC Trends in Analytical Chemistry* 25.5 (2006): 438-454.
94. Dallüge, Jens, Jan Beens, and A. Udo. "Comprehensive two-dimensional gas chromatography: a powerful and versatile analytical tool." *Journal of Chromatography A* 1000.1 (2003): 69-108.
95. Blumberg, Leonid M., et al. "Comparison of one-dimensional and comprehensive two-dimensional separations by gas chromatography." *Journal of Chromatography A* 1188.1 (2008): 2-16.
96. Klee, Matthew S., et al. "Evaluation of conditions of comprehensive two-dimensional gas chromatography that yield a near-theoretical maximum in peak capacity gain." *Journal of Chromatography A* 1383 (2015): 151-159.
97. Liu, Zaiyou, and John B. Phillips. "Comprehensive two-dimensional gas chromatography using an on-column thermal modulator interface." *Journal of Chromatographic Science* 29.6 (1991): 227-231.
98. Bruckner, Carsten A., Bryan J. Prazen, and Robert E. Synovec. "Comprehensive two-dimensional high-speed gas chromatography with chemometric analysis." *Analytical Chemistry* 70.14 (1998): 2796-2804.
99. Deans, D. R. "A new technique for heart cutting in gas chromatography [1]." *Chromatographia* 1.1-2 (1968): 18-22.
100. Seeley, John V., Frederick Kramp, and Christine J. Hicks. "Comprehensive two-dimensional gas chromatography via differential flow modulation."*Analytical chemistry* 72.18 (2000): 4346-4352.
101. Bueno, Pedro A., and John V. Seeley. "Flow-switching device for comprehensive two-dimensional gas chromatography." *Journal of Chromatography A*1027.1 (2004): 3-10.

102. Marriott, Philip J., and Russell M. Kinghorn. "Longitudinally modulated cryogenic system. A generally applicable approach to solute trapping and mobilization in gas chromatography." *Analytical chemistry* 69.13 (1997): 2582-2588.
103. Harynuk, James, and Tadeusz Górecki. "New liquid nitrogen cryogenic modulator for comprehensive two-dimensional gas chromatography." *Journal of Chromatography A* 1019.1 (2003): 53-63.
104. Libardoni, Mark, et al. "Design and performance evaluation of a two-stage resistively-heated thermal modulator for GC× GC." *Analytical Methods* 2.7 (2010): 936-943.
105. Edwards, Matthew, Ahmed Mostafa, and Tadeusz Górecki. "Modulation in comprehensive two-dimensional gas chromatography: 20 years of innovation." *Analytical and bioanalytical chemistry*401.8 (2011): 2335-2349.
106. Leco Product Information Page http://www.leco.com/products/separation-science/gcxgc-tofms/pegasus-4d-gcxgc-tofms Accessed 11/20/2015
107. Phillips, John B., and Edward B. Ledford. "Thermal modulation: A chemical instrumentation component of potential value in improving portability." *Field Analytical Chemistry & Technology* 1.1 (1996): 23-29.
108. Kinghorn, Russell M., and Philip J. Marriott. "Comprehensive two-dimensional gas chromatography using a Modulating Cryogenic Trap."*Journal of High Resolution Chromatography* 21.11 (1998): 620-622.
109. Adahchour, M., et al. "Recent developments in comprehensive two-dimensional gas chromatography (GC× GC): I. Introduction and instrumental set-up."*TrAC Trends in Analytical Chemistry* 25.5 (2006): 438-454.
110. Beens, Jan, et al. "Simple, non-moving modulation interface for comprehensive two-dimensional gas chromatography." *Journal of Chromatography A*919.1 (2001): 127-132.
111. Shimadzu Product Literature https://www.ssi.shimadzu.com/products/literature/Mass_spec/C146-E139A.pdf accessed 11/20/15
112. Jian, Rih-Sheng, et al. "Compact instrumentation of a μ-GC for real time analysis of sub-ppb VOC mixtures." *Microchemical Journal* 108 (2013): 161-167.
113. Liu, Jing, et al. "Smart multi-channel two-dimensional micro-gas chromatography for rapid workplace hazardous volatile organic compounds measurement." *Lab on a Chip* 13.5 (2013): 818-825.
114. Kim, Sung-Jin, et al. "Microfabricated thermal modulator for comprehensive two-dimensional micro gas chromatography: design, thermal modeling, and preliminary testing." *Lab on a Chip* 10.13 (2010): 1647-1654.
115. Kim, Sung-Jin, et al. "Evaluation of a microfabricated thermal modulator for comprehensive two-dimensional microscale gas chromatography."*Analytical chemistry* 83.14 (2011): 5556-5562.
116. Serrano, Gustavo, et al. "Comprehensive two-dimensional gas chromatographic separations with a microfabricated thermal modulator." *Analytical chemistry* 84.16 (2012): 6973-6980.
117. Collin, William R., et al. "μGC× μGC: Comprehensive Two-Dimensional Gas Chromatographic Separations with Microfabricated Components." *Analytical chemistry* 87.3 (2015): 1630-1637.

118. Collin, William R., et al. "Polymer-Coated Micro-Optofluidic Ring Resonator Detector for a Comprehensive Two-Dimensional Gas Chromatographic Microsystem: μGC× μGC–μOFRR."*Analyst* (2015).

CHAPTER 2

MICROFABRICATED GAS CHROMATOGRAPH FOR RAPID, TRACE-LEVEL DETERMINATIONS OF GAS–PHASE EXPLOSIVE MARKER COMPOUNDS

2.1 Background and Motivation

The rapid determination of trace quantities of explosives remains a critical element of security screening operations at airports and other transportation terminals. Measuring such compounds directly in the gas phase is made difficult by the complexity of normal background air contaminants also present at concentrations similar to those required for effective explosive detection.[1,2] The well-known explosive, 2,4,6-trinitrotoluene (TNT), for example, with a vapor pressure, p_v, of just 9×10^{-7} kPa at ambient temperature, produces a *saturation* concentration of < 10 ppb.[3] Although the detection of this and other explosive nitro-compounds in the gas phase is purportedly achievable with commercial instruments employing Raman spectroscopy,[4] ion mobility spectrometry,[5] mass spectrometry with direct-inlet[6] or with upstream gas chromatographic separation (GC-MS),[7] and fluorescence-based detectors,[8] each has limitations

related to the sensitivity, selectivity, size, cost, or range of detectable analytes. Thus, as with most field analytical measurements, there remains a need for smaller, less expensive and more easily operated instrumentation capable of rapid, reliable, trace-level detection of airborne explosives.

Microfabricated gas chromatographic systems (μGC) may be able to meet this need. Over the past decade, several reports have appeared on μGC systems made from micromachined-Si devices.[9-15] The inherent versatility of these microsystems has driven their development for field analysis applications where selective determination of one or more (semi)volatile organic compounds (S/VOC) is required. By use of microsensor-array detectors, crude response patterns can be obtained that add a second dimension to the analysis,[9,10,13] analogous to other hyphenated GC instrumentation. However, those microsensor array technologies that have been configured as (μ)GC detectors generally lack the inherent sensitivity to achieve the low limits of detection (LOD) required for many applications, [9,10,13,16-19] including trace-level explosives detection. This, in turn, demands preconcentration prior to separation and analysis. Although some notable alternative microsystem approaches to explosive detection have been reported recently,[20] we are not aware of any reports by other researchers on the application of integrated μGC systems to explosives detection.

In the work described here a focus is placed on the (indirect) detection of TNT. The low volatility of this compound, however, argued against its direct gas-phase detection and led us to search for more volatile surrogates that might serve as markers of TNT. Among the byproducts of manufacture found as impurities in TNT-based explosives are 2,4- and 2,6-dinitrotoluene (2,4-DNT and 2,6-DNT, respectively),[21] the p_v values of which are 5.3×10^{-5} kPa and 1.2×10^{-4} kPa, respectively. The former is found at a much higher concentration than the latter in the headspace above TNT samples, and thus it serves as a more viable marker compound.[22] The somewhat more

volatile 2,3-dimethyl-2,3-dinitrobutane (DMNB, p_v = 2.7× 10^{-4} kPa) is an officially sanctioned explosive taggant added to non-military explosive formulations (including, but not limited to TNT) to facilitate gas-phase detection.[23] Therefore, in this study, 2,4-DNT and DMNB were designated as primary markers and 2,6-DNT as a secondary marker.

As part of our effort to develop μGC instrumentation for these compounds, we recently reported on the development and optimization of a preconcentrator-focuser (PCF) module that was ultimately incorporated into the prototype described here (see below).[24] That study, which complements others concerned with the preconcentration of airborne explosives, [25-30] showed that with the proper materials, device designs, and operating conditions, the explosive markers could be rapidly captured, focused, and injected to a downstream GC column with a net transfer efficiency >85% from test atmospheres containing the markers in the presence of more than 20 relevant interferences. We also recently reported on the temperature and flow rate dependence of a microsensor array, also ultimately used in our prototype.[31] That study characterized the tradeoffs among sensitivity, detectability, and chromatographic resolution associated with variations in these critical operating parameters. We have also reported preliminary results from other work concerning various aspects of prototype development leading up to the current study.[32,33]

Here we describe the high-speed chromatographic separation of the markers from interferences with a microfabricated separation column (μcolumn), the integration of the μcolumn with the PCF and microsensor array components referred to above, and the assembly and first laboratory tests of a laptop-controlled, field-ready μGC prototype instrument, which we have dubbed INTREPID. As a preface, the main analytical features of the μGC and the application-specific variables that dictated the component and system designs, configurations, and operating conditions are summarized in the next section. Brief descriptions of all key devices are provided,

followed by a detailed description of the prototype. Then a progression of experimental results is presented characterizing and optimizing the performance of the μcolumn, various subsystems, the complete microsystem and, finally, the assembled prototype.

2.2 Overview of Analytical Subsystem Design and Operation

Figure 2.1 shows a block diagram of the primary analytical components and fluidic interconnection paths of the INTREPID μGC prototype. It shares several features with another μGC prototype we developed for another application.[13] The hybrid PCF module includes a conventional polymer membrane particulate filter that serves as a particle pre-trap, a stainless-steel tube packed with a dual-adsorbent bed that serves as a selective high-volume sampler, and a micromachined Si/Pyrex microfocuser (μF) chip with an integrated heater and an etched cavity packed with a granular adsorbent that serves as a focuser and injector.[24]

A micromachined Si/Pyrex μcolumn chip with a spiral etched channel, integrated heaters and temperature sensors, and a wall coated stationary phase provides the chromatographic separation. The SiO_x/Si chemiresistor (CR) array detector chip, which has a set of lithographically patterned interdigital metal electrodes coated with an assortment of thiolate-monolayer protected gold nanoparticle (MPN) films and a ceramic lid, yields a set of partially selective responses to eluting vapors. Fluidic interconnections are made with deactivated fused-silica capillaries. A set of commercial, solenoid-actuated three-way valves, mounted on a custom stainless-steel manifold, is used to direct airflow provided by one of two commercial, mini-diaphragm pumps. Adsorbent-packed scrubbers are used to clean the ambient-air carrier gas used during focusing and analysis.

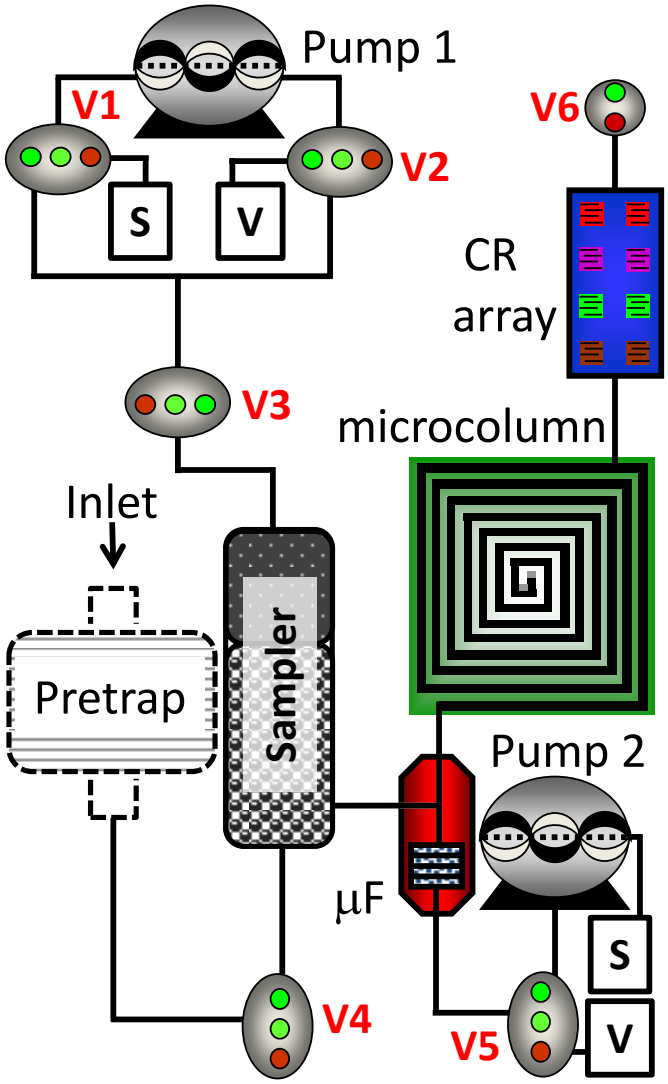

Figure 2.1. Diagram of the analytical components and fluidic pathways of the INTREPID µGC prototype. S = scrubber; V = vent port; V1-V5 = solenoid valves. See Figure A1.1 in Appendix 1 for the flow paths during sampling, focusing, and analysis modes.

The instrument was designed to proceed through three sequential operating modes (see Figure A1.1 in Appendix 1). First, the sampling mini-pump (Pump 1) would draw an air sample through the pre-trap and the manifold-mounted sampler to capture the marker compounds and the fraction of potential interfering air contaminants within a volatility range similar to that of the markers. Next, after switching the appropriate valves, Pump 1 would draw scrubbed ambient air

in the opposite direction through the sampler as it is resistively heated to desorb and transfer the captured vapors to the μF. Following another series of valve switches, a second mini-pump (Pump 2) would draw scrubbed air in and pass it through the μF as the latter is heated rapidly to backflush and inject the focused vapor mixture into the μcolumn. A rapid, temperature programmed chromatographic separation would be followed by detection with the MPN-coated CR array, which produces a response pattern for each eluting compound. The combination of selective preconcentration, chromatographic separation, and array detection was designed to enhance the accuracy and reliability of determinations of the targeted explosive marker compounds at low concentrations in the presence of interfering S/VOCs.

The ultimate performance criteria dictating the design and operating conditions of the INTREPID prototype were the speed of analysis, limits of detection (LOD), and the selectivity/reliability of the marker determinations. The inherent tradeoffs among these criteria had to be carefully assessed in establishing the final operating conditions. We found no official guidance in the literature on these criteria for explosive marker determinations at airport security checkpoints, so we adopted provisional goals of $\leq$ 2 min per analysis (including sampling, focusing, injection, separation and detection) and 1 ng as the LOD for each marker. Given these criteria and preliminary data collected on the sensitivities of the sensors in the CR array for the marker compounds,[31] we then adopted a provisional target sample volume of 1 L. This translates to an LOD of ~0.14 ppb for 2,4-DNT, 2,6-DNT, and DMNB vapors. In order to meet the 2-min analysis time criterion, the provisional duration of each mode in the analytical sequence was set as follows: 20 sec for sampling, 40 sec for focusing, and 60 sec for separation/detection.

The interferences chosen for demonstrating the selectivity of preconcentration, chromatographic separation, and array responses included a set of 15 S/VOCs from several

different functional group classes, which are common indoor air contaminants,[1,2] and members of the homologous series of n-alkanes from C_{10} to C_{16}, with p_v values similar to those of the markers (i.e., from 2.1×10^{-1} to 1.9×10^{-4} kPa, respectively), a fraction of which comprise the primary straight-chain components of JP-4 jet fuel.[34]

2.3 Experimental Methods

2.3.1 Materials

DMNB, 2,6-DNT and 2,4-DNT were purchased from Sigma-Aldrich (Milwaukee, WI) in 99% purity and were used as received. In addition, standard solutions of these marker compounds in acetonitrile/methanol (1 mg/mL) were purchased from AccuStandard (New Haven, CT). All other S/VOCs and reagents were purchased from Sigma-Aldrich or Fisher Scientific (Pittsburgh, PA) in 99% purity and used as received. The graphitized carbons, Carbopack B (C-B, 60/80 mesh, 100 m^2/g), and Carbopack Y (C-Y, 60/80 mesh, 24 m^2/g) were purchased from Supelco (Bellefonte, PA). Polydimethylsiloxane (PDMS) was obtained from Ohio Valley Specialty Chemicals (OV-1; vinyl, Marietta, OH). MPNs derived from the following thiols were synthesized by the method reported by Rowe et. al.: n-octanethiol (C8), 6-phenoxyhexane-1-thiol (OPH), 4-(phenylethynyl)-benzenethiol (DPA), and methyl-6-mercaptohexanonate (HME).[35] Average Au core diameters ranged from 3.4 (C8) to 4.7 nm (HME).

2.3.2 Primary Analytical Components

Figure 2.2 shows photographs of the interior of the INTREPID prototype (Figure 2.2a, top view) and the individual microfabricated components prior to their being installed in the instrument.

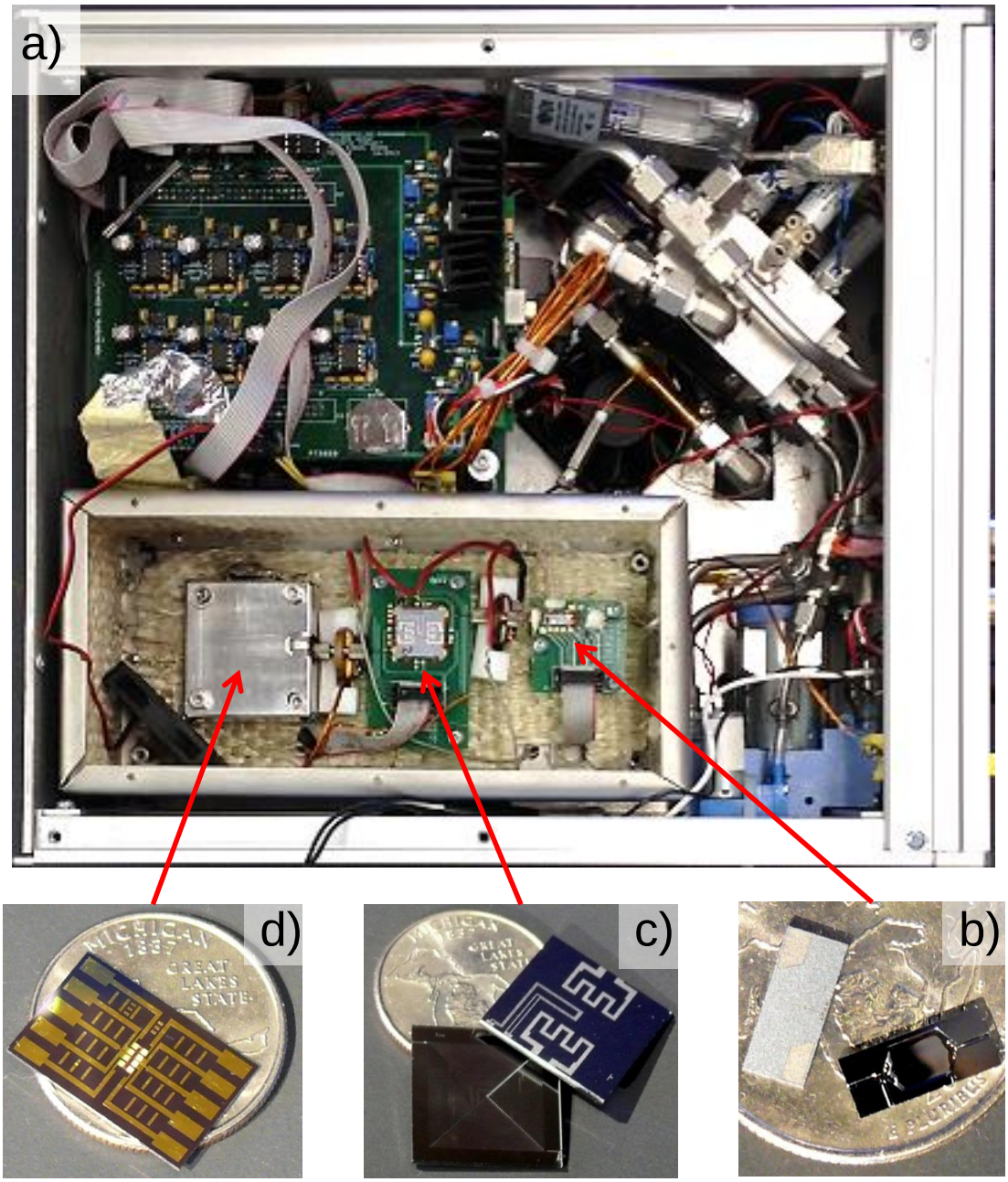

Figure 2.2. Photographs of a) the INTREPID µGC prototype; b) frontside and backside views of the µF; c) frontside and backside views of the µcolumn; and d) the CR array.

The µF, µcolumn, and CR array have been described elsewhere.[31,36,37] Therefore, detailed descriptions have been relegated to Appendix 1 and only brief descriptions are provided here. The etched-Si µF chip (Figure 2.2b) contains a 3 µL cavity packed with 2.4 mg of C-B. One side of

the cavity is connected to a split-flow channel, one arm of which connects to the sampler and the other to the μcolumn. The cavity and flow channels are sealed with Pyrex anodically bonded to the Si substrate. Two metal contact pads patterned on the backside of the substrate allow for resistive (bulk) heating of the device, the temperature of which is monitored with a thin metal resistive sensor. The etched-Si μcolumn chip (Figure 2.2c) contains a 1-m long, Pyrex-capped, spiral channel (150 × 240 μm cross-section), two thin-metal-film meander-line heaters, and a proximate resistive temperature sensor. A wall-coated PDMS stationary phase (0.15 μm thick) was deposited from solution and cross-linked in situ. Short segments of deactivated fused-silica capillary (0.25 mm i.d.) inserted into expansion sections at the inlet and outlet ports of the μF and μcolumn chips were sealed either with silicone adhesive or epoxy. The CR-array chip (2.4 cm^2, Figure 2.2d) has four pairs of interdigital metal electrodes onto which were deposited multilayer films of one of the four types of MPNs by drop casting from solution. Baseline resistances were between 1 and 10 MΩ. A slab of Macor with drilled inlet/outlet ports that accepted fused-silica capillaries (epoxied in place) was sealed above the array of electrodes using double-sided tape (internal cell volume: ~1.6 μL). Only one of each type of coated sensor was used for data generation. Each microfabricated system component was mounted on a separate (carrier) printed circuit board (PCB), and Al leads were wire bonded in place for applying voltages or measuring output signals. The μF and μcolumn were inverted prior to mounting and the PCBs had holes cut beneath the device mounting locations for heat dissipation.

The sampler was constructed from a 6-cm long, 6.35-mm i.d. thin-walled stainless-steel tube with a 6-cm long, 1.59-mm i.d. side-port tube located about 2 cm from one end. A tandem bed of 35 mg of C-B and 15 mg of C-Y (212-250 μm nominal o.d.) was used in the sampler.[24] A

Cu resistive heater coil and a fine-wire thermocouple (Omega, Stamford, CT) were used for heating to 250 ºC (15 ºC/s) during thermal desorption.

2.3.3 Prototype Assembly and Operation

The INTREPID prototype is housed in a rectangular aluminum box with a removal top panel that measures 33 (l) × 29 (w) × 13 cm (h) and weighs 5.4 kg. A machined stainless-steel block serves as the primary flow manifold. It has surface ports and threaded holes machined to accept each of the six gasket-sealed, 3-way latching solenoid valves (Lee Co., Westbrook, CT) used to direct the flow. The sampler is mounted with Swagelok® fittings to a stainless-steel tube also tapped into the manifold. A small radial fan beneath the sampler accelerates the cooling of the sampler following each thermal desorption so that the sampler reaches a temperature of ≤ 40 ºC before the next sample is collected. Pump 1, used for sampling and focusing, is a double-headed diaphragm pump (D737B, Parker Hannifin, Cleveland, OH), and Pump 2, used for injection, separation, and detection, is a smaller mini-diaphragm pump (E155, Parker Hannifin). Two large cylindrical scrubbers packed with charcoal and molecular sieves (50 and 100 g, respectively) and mounted on the outer side wall of the instrument chassis are connected to one port of each pump to remove water vapor and background S/VOCs during focusing (Pump 1) and analysis (Pump 2). The pumps are connected to the appropriate ports of the manifold via stainless-steel tubing (note: due to the net pressure drop through the sampling train, the maximum sampling flow rate (Pump 1) was 2.7 L/min).

The PCB-mounted microanalytical components (µF, µcolumn, and CR array) are secured on standoffs to the floor of a mini-oven comprising a ceramic-wool insulated 1.5-L sheet metal chamber with an adhesive-backed, resistor-embedded silicone heater pad (Watlow, St. Louis, MO) mounted to a plate on the underside of the lid, and a small circulation fan. The internal temperature

was raised to reduce adsorptive losses on interconnection surfaces that could not be heated by direct means. Fluidic interconnections among the microanalytical subsystem components were made using modified stainless-steel unions (EU.5,Valco Instrument Company, Houston, TX) that accept the 0.25-mm i.d. capillaries attached to the components. Each of the two unions was modified to fit in a small copper cradle, which was resistively heated to ~90 °C to further reduce wall adsorption. The inlet capillary of the μF was fed through a passage in the side of the chamber and connected to the side-port tube of the sampler with a 0.16 cm i.d. stainless-steel union (Valco, Houston, TX) also wrapped with a Cu wire coil. Other capillary interconnections between the manifold and the microanalytical subsystem were made with glass press-fit unions.

The electronic hardware and software used for system operation, control, and data acquisition are described in Appendix 1. Data were stored as text files as well as being displayed in real time on the laptop. Post-run data processing was performed using GRAMS 32 (ver. 6.0 Thermo Scientific, Pittsburgh, PA) and Excel (ver. 14, Office 2010, Microsoft, Redmond, WA). Projected vapor recognition rates were estimated on the basis of normalized response patterns derived from the calibrated sensitivities by means of Monte Carlo simulations coupled with extended disjoint principal components (EDPCR) classification models (see Appendix 1).

2.4 Results and Discussion

2.4.1 μColumn Separations

The 1-m channel length of the μcolumn was selected with the expectation that it would be long enough to provide sufficient peak capacity, but short enough to permit separations to be completed in ~tens of seconds at a flow rate low enough for high chromatographic efficiency. The PCB-mounted μcolumn was placed inside the oven of a bench-scale GC (Agilent 6890, Agilent

Technologies, Palo Alto, CA) and connected to the injection port and FID with deactivated capillaries. The oven was maintained at 70 °C and the μcolumn was heated to 120 °C using the integrated heaters. A mixture of all three marker compounds (0.25 mg/mL in acetone) was injected by auto-sampler through the heated injection port (0.1 μL, 1000:1 split ratio) at each of six different flow rates ranging from 0.2 to 5 mL/min. At 0.2 mL/min, which corresponds to the Golay minimum for this μcolumn,[37] the separation required 4 min; although the peaks were broad, they were fully resolved, but there was a significant amount of unused space in the chromatogram. At 5 mL/min the elution time was reduced to ~70 s and the markers were still fully resolved, but the full-width-at-half-maximum (*fwhm*) values were still quite large: 1.2, 9, and 14 s for DMNB, 2,6-DNT and 2,4-DNT, respectively. This warranted the use of temperature programming.

After a series of exploratory trials, flow and temperature programming conditions were established that permitted the separation of the three markers and four n-alkanes of similar volatility (C_{13} – C_{16}) in just 22 s at 3 mL/min, as shown in Figure 2.3. The markers eluted in < 15 s. This represents the best separation possible in the shortest period of time. The resolution (R_s) measured for the critical marker-alkane pairs were 1.5, 1.3, and 0.8 for DMNB/C_{13}, 2,6-DNT/C_{14}, and 2,4-DNT/C_{15}, respectively. The corresponding *fwhm* values for the markers were 1, 1.5, and 2.5 s, respectively. Thus, excellent chromatographic separation could be obtained at high speed using the 1-m μcolumn with on-board heaters and temperature sensors in air in the absence of significant extra-column band broadening.

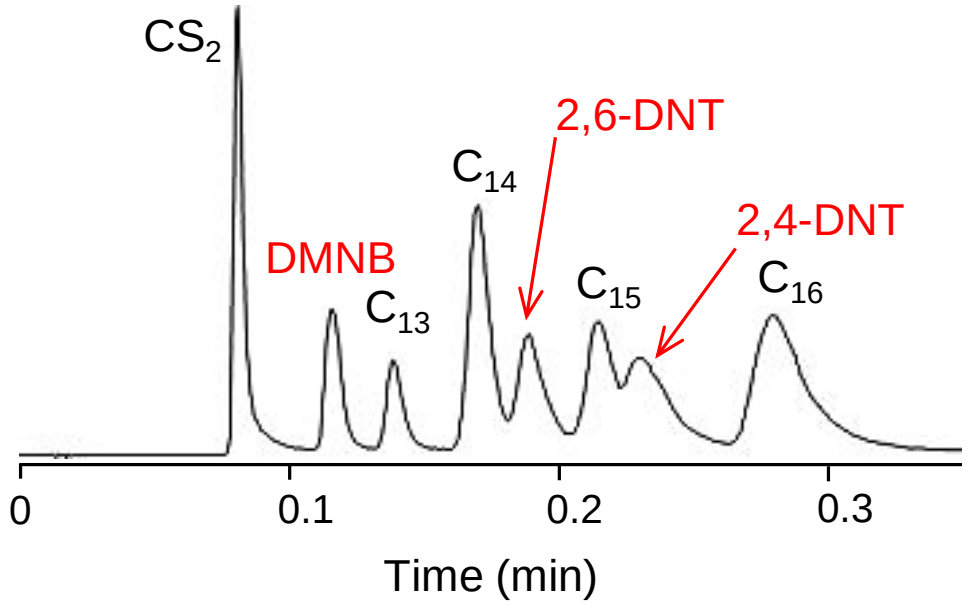

Figure 2.3. 22-s temperature programmed separation of the three explosive markers and four alkane interferences using the PDMS-coated, 1-m μcolumn connected to a bench scale GC injector and FID via deactivated capillaries. Conditions: air carrier gas, 3 mL/min; 100:1 split injection; temperature program with integrated μcolumn heaters and temperature sensor: 120 °C (initial), 4 °C/s to 140 °C, 1 °C/s to 160 °C, 4 °C/s to 180 °C, hold for 10 s.

2.4.2 Integration of μColumn and CR Array

The CR array was then connected downstream from the μcolumn with a short section of deactivated capillary inside the oven of the GC at 70°C. The upstream port of the μcolumn was connected to the GC injection port (225 ºC, 100:1 split) and the μcolumn temperature was again increased to 120 ºC with the on-board heaters. Using purified air as the carrier gas a mixture of the three markers and three n-alkanes (i.e., C_{14} – C_{16}) in CS_2 (0.5 mg/mL each) was repeatedly injected manually via syringe at each of several different flow rates. Figure 2.4 shows a representative set of chromatograms from the sensors in the CR array generated with this subsystem at a flow rate of 1.2 mL/min, which afforded the best separation. The separation required 3 min and the resolution was clearly degraded relative to that shown in Figure 2.3. The

resulting R_s values for the C_{14}/2,6-DNT and C_{15}/2,4-DNT pairs were 0.9 and 0.75, respectively. Estimated *fwhm* values were 3, 16, and 22 s, for DMNB, 2,6-DNT, and 2,4-DNT, respectively.

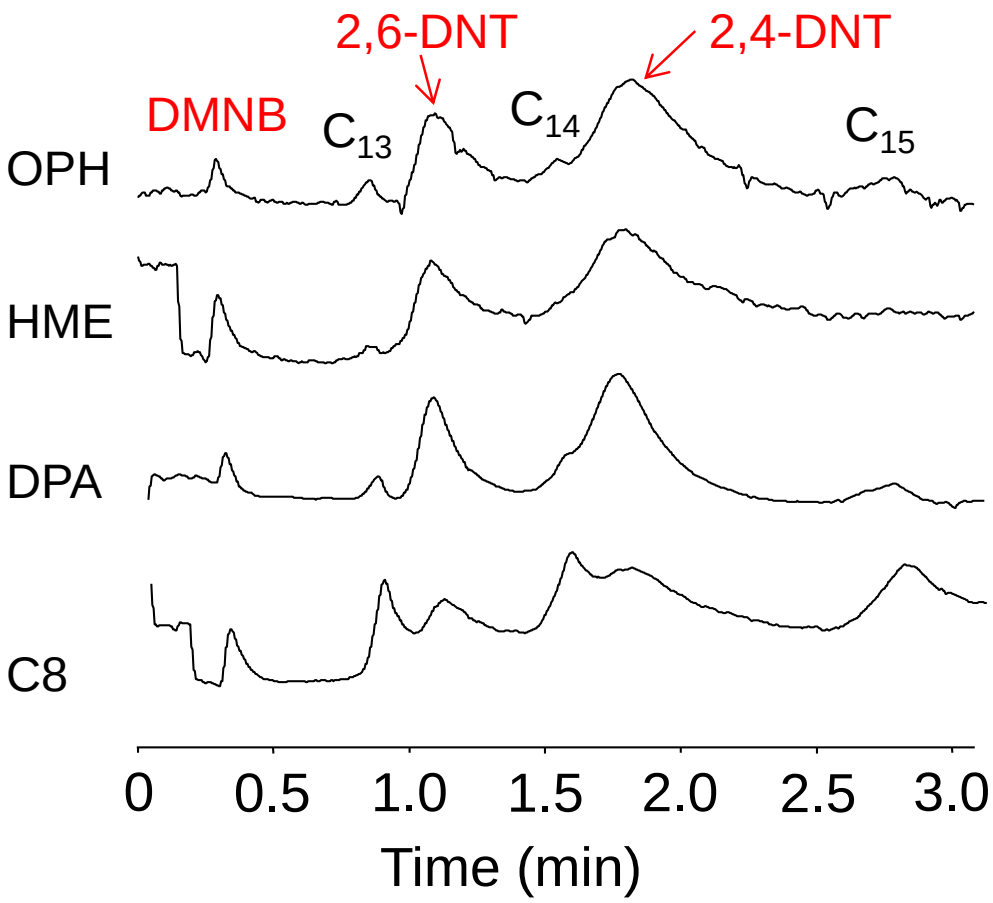

Figure 2.4. Chromatograms obtained using the microanalytical subsystem composed of a 1-m µcolumn and a CR sensor array. Conditions: µcolumn temperature = 120 °C; CR array temperature = 70 °C; 0.5 µL, 100:1 split injection; GC inlet = 225 °C; 1.2 mL/min dry-air carrier gas. Acronyms refer to the MPN coating on each sensor (see text).

The increased band broadening associated with the CR array can be attributed to the detector cell dead time, wall adsorption, and (primarily) the finite sorption/desorption rates in the MPN films on the sensors, despite operating at the detector at 70 ºC.[31] The higher sensitivity for the markers than for the n-alkane interferences, particularly for the DPA, OPH, and HME sensors,

is noteworthy, but adjustments were needed to increase the chromatographic resolution and to compensate for the band broadening associated with the CR array.

2.4.3 Integration of the μF and μColumn

We have previously reported that *fwhm* values of injection bands generated by desorption from the μF (heated to 250 ºC at 375 ºC/s for all tests) directly to an ECD at 3 mL/min were 1.3, 3.5, and 5.7 s for DMNB, 2,6-DNT and 2,4-DNT, respectively.[24] For initial tests of μF injections here, the μF and μcolumn were connected with deactivated capillary and mounted inside the GC oven, again at 70 °C, and zero-grade air was used as carrier gas. The upstream side of the μF was connected to the GC injection port (225 °C, splitless) and the μcolumn outlet was connected to the ECD. With the path to the μcolumn temporarily blocked, 0.5 μL of an acetone solution of the markers (0.25 mg/mL for DMNB and 2,6-DNT, and 0.75 mg/mL for 2,4-DNT) was injected by syringe and passed via the on-chip tee-branch through the μF adsorbent bed to mimic desorption from the sampler. The outlet port of the μF was vented and the acetone was not retained on the adsorbent at this temperature. Then, the tee-branch inlet to the μF was disconnected from the injection port and blocked with a septum, the outlet port (during focusing) of the μF was connected to the GC injection port, and the μcolumn inlet was reconnected to the μF. Prior to heating the μF and backflushing the sample into the μcolumn, the on-board heaters were used to raise the μcolumn to 120 °C and the flow rate was adjusted to 3 mL/min. As shown in Figure 2.5a (solid trace), although all three markers could be resolved under these conditions, the *fwhm* values of the peaks eluting from the μcolumn were still rather broad (i.e., 1.5, 4.3, and 9.1 s DMNB, 2,6-DNT, and 2,4-DNT, respectively), owing largely to the injection bandwidths for DMNB and 2,6-DNT, and to additional on-column broadening for 2,4-DNT.

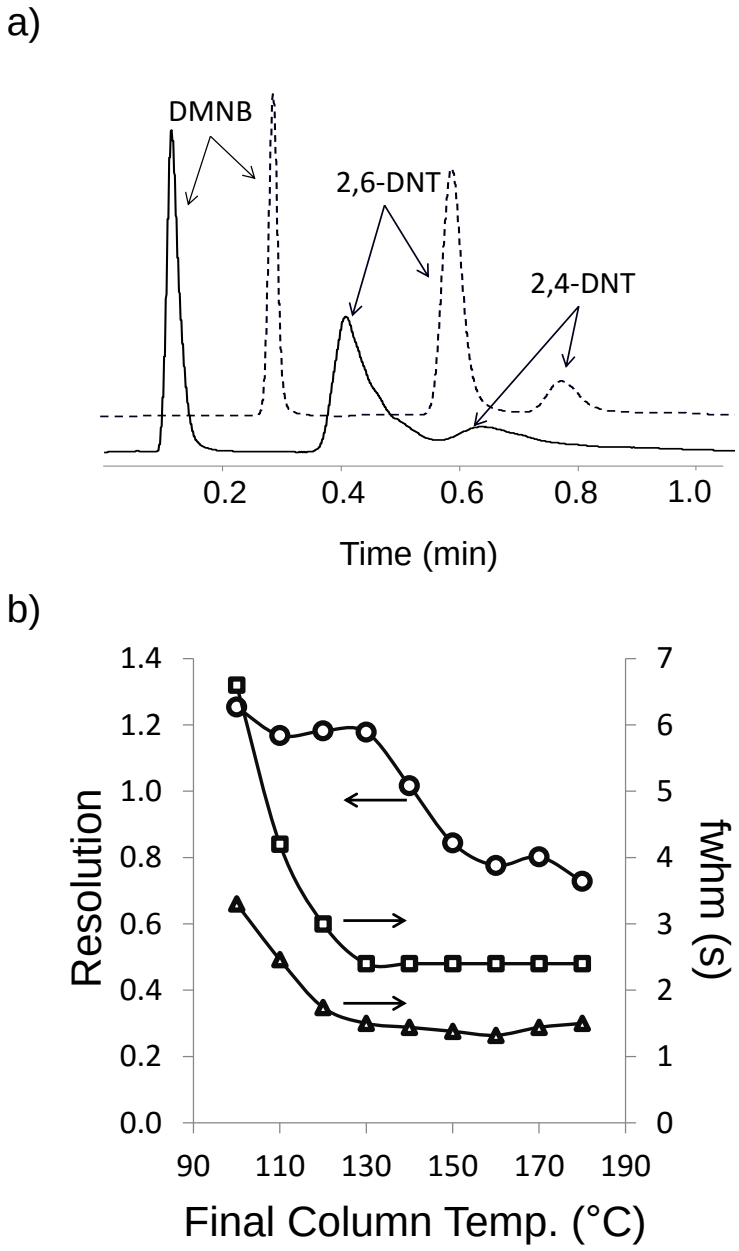

Figure 2.5: a) Isothermal (120 °C) separation of the explosive markers (solid trace) and the corresponding separation with OCF (dashed trace; 15-s hold at 70 °C, ramp at 8 °C/s to T_{max} = 120 °C; hold); b) Effect of OCF T_{max} on R_s for the 2,6-/2,4-DNT pair (diamonds) and on the *fwhm* of 2,6-DNT (triangles) and 2,4-DNT (squares) (initial 20-s hold at 70 °C in all cases). For all tests: μF injection, 3 mL/min, N_2 carrier gas, ECD.

Therefore, on-column focusing (OCF) was explored as a way of reducing both sources of band broadening. OCF entails starting the μcolumn at a temperature low enough to re-focus the

analytes at the head of the μcolumn. Fortunately, the p_v values of the DNT isomers are low enough to achieve some degree of OCF at the baseline temperature of 70 °C. The dashed-line trace in Figure 2.5a shows the effect under an initial set of conditions that entailed holding at 70 °C for 15 s followed by ramping at 8 °C/s to 120 °C. The R_s value for the 2,6-DNT/2,4-DNT pair is > 1.5, peak heights increased by 1.8 and 3.5 fold, respectively, and the peak tailing was reduced. The DMNB *fwhm* value was not greatly affected, apparently due to its higher p_v value, whereas the *fwhm* values for 2,6- and 2,4-DNT decreased to 2.1 and 3.6 sec, respectively. As a result, the overall elution time increased by only about 5 s relative to the isothermal run, despite the 15 s focusing segment.

Figure 2.5b shows the effects on the R_s value for the 2,6-/2,4-DNT pair and on the *fwhm* values of 2,6- and 2,4-DNT of holding the μcolumn at 70 °C for 20 s and then ramping at 8 °C/s to a maximum (final) temperature (T_{max}) value ranging from 100 to 180 °C (note: the 20-s hold at 70 °C improved the focusing of 2,4-DNT). DMNB peak metrics were not scrutinized at this point, since the first 20 s of the separation, in which DMNB elutes, are unchanged regardless of T_{max}. Although the *fwhm* decreased with an increase in T_{max} from 100 to 130 °C, the R_s values for 2,6- and 2,4-DNT were nearly constant due to a greater decrease in t_R of the 2,4-DNT relative to the 2,6-DNT. Above 130 °C, the *fwhm* values were constant while R_s declined further, again, due to the greater decrease in t_R for 2,4-DNT. T_{max} values > 180 °C were not explored to avoid excessive stationary phase bleed. On the basis of these data, a T_{max} of 130 °C was selected because it produces the fastest separation with the highest resolution between the DNT isomers.

2.4.4 Microsystem Testing and Calibration

The μF, μcolumn, and CR-array ensemble was then mounted inside the GC oven at 70°C, and the capillary interconnections were resistively heated to 90 °C. The marker compounds and n-alkane interferences were loaded onto the μF from solution by autosampler injection as described above, thermally desorbed/injected with backflushing into the μcolumn, and separated using the temperature program described in the preceding section (i.e., 70 °C for 20 s; ramped to 130°C at 8°C/s; hold).

The effect of flow rate from 1.2 to 3.7 mL/min was examined first. Figure A1.2 (Appendix 1) shows a series of chromatograms from a representative sensor (HME) at different flow rates for a mixture of C_{10}, C_{12}, C_{13}, C_{14}, DMNB, and 2,4-DNT (note: 2,6-DNT was omitted from this series of tests; see below). Increasing the flow rate resulted in decreases in *fwhm*, increases in R_s for the critical pair, DMNB/C_{12}, and reduced analysis time. It is clear from these traces that extra-column factors are more important than on-column factors in the overall separation. At the lower flow rates the peaks for DMNB and C_{12} severely overlap, but at ≥ 3.0 mL/min they are nearly baseline separated, as are those for the other mixture components. Although resolution continues to increase for all compounds from 3.0 to 3.7 mL/min, the peak height of DMNB decreases by ~30%. Since this leads to a commensurate increase in the LOD, and DMNB has the highest LOD of the markers (see below), sensitivity was given priority over resolution and a flow rate of 3 mL/min was adopted for further testing.

The microsystem was then calibrated under these conditions. Autosampler injections of acetone solutions containing a mixture of the three markers and the representative alkanes, C_{13} and C_{15}, were made through the GC injection port to which the μF was connected (note: as described above, the μF was temporarily disconnected from the μcolumn during loading and then

reconnected for injection, separation, and detection). The μF was then heated to inject the analyte at 3 mL/min into the μcolumn, and the temperature programmed separation proceeded using the on-board heaters and temperature sensors.

Peak areas calculated from the time-integrated voltage changes of the sensors were converted to integrated resistance changes ($\Delta R \cdot s$) and then divided by the baseline resistance, R_b. Peak maxima were similarly converted to baseline normalized resistances. Calibration curves created from peak areas or peak heights were linear. Figure A1.3 (Appendix 1) shows the peak-height calibration curves with forced-zero y intercepts. Regression analysis gave r^2 values ≥ 0.90 for the markers and $r^2 \geq 0.95$ for the n-alkanes. Sensitivities were taken as the slopes of these curves ($\Delta R \cdot R_b^{-1} \cdot ng^{-1}$) and are presented, along with the r^2 values, in Table A1.1 in Appendix 1. LODs extrapolated from these data are presented in Table 2.1.

Table 2.1. LODs for the explosive markers and C_{13}.

Sensor	LOD (ng)			
	DMNB	2,6-DNT	2,4-DNT	C_{13}
C8	6.0	1.1	2.4	24
DPA	6.5	1.6	2.5	55
OPH	2.2	0.63	1.5	12
HME	2.4	0.48	0.86	26

[a] assuming a 1-L sample volume; calculated as 3σ/sensitivity, where σ is the standard deviation of the baseline noise for each sensor and sensitivity is the forced-zero linear-regression slope of peak height vs. injected mass.

On the basis of the sensor providing the highest signal-to-noise ratio for each analyte, the LODs are 2.2 ng for DMNB, 0.5 ng for 2,6-DNT, 0.9 ng for 2,4-DNT, and 12 ng for C_{13}, and 19 ng for C_{15}. Assuming a 1-L sample volume, these correspond to concentrations of 0.30, 0.067,

0.12, and 1.6 ppb for DMNB, 2,6-DNT, 2,4-DNT, C_{13}, and C_{15}, respectively. If the least sensitive sensor in the array is used as the basis for the LODs, they increase to 6.5, 1.6, 2.5, 55, and 91 ng (or 0.90, 0.21, 0.33, 7.3, and 10 ppb), respectively. The latter would apply if all four sensors were required for discriminating the markers from interferences on the basis of their collective response patterns (see below).

The HME-coated sensor had the highest sensitivity to all of the marker compounds, consistent with HME being the most polar monolayer moiety among the MPNs in the array. As a result, the HME sensor had the lowest LODs for 2,4-DNT and 2,6-DNT. The OPH sensor had the lowest LOD for DMNB because its baseline noise level was significantly lower than that of the HME sensor. However, the HME sensor also had high sensitivity for the alkanes. This ambiphilicity can apparently be attributed to coordination of the ester moieties on neighboring thiolates, which is disrupted by polar analytes but not by non-polar alkanes. The high alkane sensitivities would be expected from the less polar OPH and C8 sensors. Due to the rigidity of the DPA moieties, the swelling of the DPA MPN film is much lower than those of the other films, leading to lower sensitivities for all analytes.[38] Note that sensitivities toward the alkanes were at least an order of magnitude lower than toward the markers, resulting in proportionally higher LODs for the former. This can be ascribed primarily to the higher alkane p_v values.

Although the response patterns derived from the calibrated sensitivities of the markers are qualitatively similar, they all differ significantly from those of the alkanes, which is evident by visual inspection of the bar charts in Figure 2.6 (C_{13} are C_{15} patterns are very similar, so only C_{13} is shown). To provide a more quantitative evaluation of discrimination on the basis of response patterns alone, a series of analyses was run using Monte Carlo simulations in conjunction with EDPCR classification models (see Appendix 1). In this approach, error is superimposed on

responses derived from the calibrated sensitivities and the resultant error-enhanced responses are combined into "test vectors" that are then classified according to their proximity to the calibrated vectors.

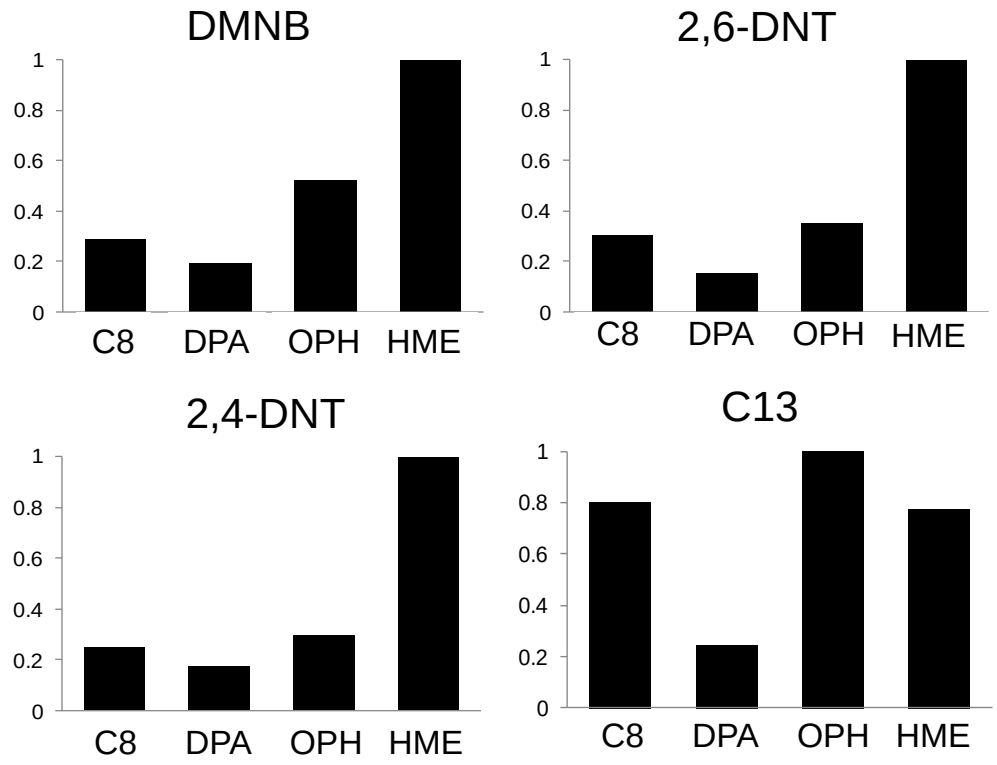

Figure 2.6: Normalized response patterns for the three marker compounds and tridecane (C_{13}; representative jet-fuel interference) derived from the calibration curves presented in Appendix 1 (Figure A1.3) generated with the INTREPID microsystem (μF, 1-m μcolumn, and CR array) .

By performing such analyses iteratively, statistical estimates of recognition rates (RR) can be generated. The RR values obtained from such analyses are presented in Table A1.2 (Appendix 1) for binary mixtures of several of the compounds under the assumption that full or partial co-elution of two peaks might arise. A recognition rate > 95% is considered acceptable. As shown, by this criterion, all of the binary marker-alkane mixture discriminations would be highly successful; that is, both mixture components were detected and the mixture could be differentiated from the individual components. In contrast, none of the markers could be differentiated from

each other in binary mixtures at an RR > 67% and the alkanes could be differentiated from each other in the mixture at a rate of only 39%. Thus, if these, or other, alkanes were to co-elute with any of the markers, the markers could still be recognized and quantified. Since near-baseline separation was achieved in this case, these results merely add confidence to the peak assignments that would otherwise be based on retention time alone.

2.4.5 Prototype Testing

As a preliminary check on the operation of the INTREPID prototype, which used another set of microsystem components, a test atmosphere containing a mixture of five common VOCs (i.e., 25 ppb each of m-xylene, ethylbenzene, cumene, *n*-C_9, and *n*-C_{10}) was analyzed repeatedly with the unheated microsystem (i.e., the mini-oven heater was turned off and the μcolumn was operated at ambient temperature). A series of nine replicate analyses was performed (6 s sampling, 40 s focusing and stabilization, 78 s separation/detection) over 2 hr. Retention time reproducibility was better than 3.6% (RSD) in all cases, averaging 1.5% (RSD) for all sensors and analytes. The average RSDs around the average peak heights and peak areas were 15% and 11%, respectively, and without the DPA sensor they were 11% and 8%, respectively (the DPA sensor gave the lowest responses in all cases). There were no trends in peak height or peak area over time. Some of this variability can be ascribed to temperature fluctuations and to fractional breakthrough of the sampler adsorbent bed at the high sampling flow rate for these relatively volatile compounds. The variation in the normalized response patterns (i.e., Euclidean distances in 4-space) ranged from 0.5 to 9% (RSD) for the five vapors (avg = 3.6%). Subsequent to these analyses, the prototype was allowed to autonomously cycle through consecutive analyses with the sampling time set to 0 s (i.e., no sample was collected) every 3 min for a total of about 3 hrs (~60 cycles) without failure.

Tests were then performed with mixtures of the two primary markers, 15 VOCs representative of indoor air contaminants, and five n-alkanes from C_9-C_{13} that comprise the primary n-alkane constituents of JP-4 jet fuel,[34] (note: as discussed in the Introduction, 2,6-DNT was removed from the set of markers at this point because of its low headspace concentration above TNT and the likelihood of its contributing relatively little to the problem of explosive detection). The list of S/VOC interferences is given in the caption of Figure 2.7. First, a CS_2 solution these 20 compounds along with the two primary markers was prepared and analyzed by conventional GC-FID. Figure 2.7a shows the reference FID chromatogram, which serves to document the complexity of the test mixture and the expected elution order on a non-polar column. Then, using a 50-mL gas-tight syringe, saturated headspace samples from three flasks containing a mixture of the 20 interferences (~5 mL), DMNB (~5mL), and 2,4-DNT (~30 mL), respectively, were collected and injected slowly into a scrubbed air stream directed past the prototype inlet in such a manner that the entire sample was collected without increasing pressure on the system. The prototype analytical sequence was initiated via the laptop controller and it proceeded through its cycle: sample at 2.7 L/min for 22 s; focus at 0.040 L/min for 40 s; switch pumps establish sensor baselines for 5 s; inject, separate, and detect at 3 mL/min for the remainder of the cycle.

Figure 2.7b shows the traces for all four CR sensors in the array. Of the 22 compounds present in the test atmosphere (see Figure 2.7a), only seven appear in the chromatograms from the prototype; the other 15 were, by design, not retained by the sampler (or μF). Compounds with p_v values less than ~ 0.2 kPa (corresponding to *n*-C_{10}) were effectively captured and focused. As shown, DMNB and 2,4-DNT were completely resolved from the n-alkane interferences, with retention times of 23 and ~50 s, respectively, although it took up to 80 s to recover the baseline. The alkanes were also well resolved, and near-baseline separation between all mixture components

was achieved. Tailing of the DMNB peaks was apparent with the more polar sensors, and was quite pronounced for 2,4-DNT with all sensors in part because of a residual contaminant eluting on the shoulder of the 2,4-DNT peak (this peak was present in blank samples run prior to the mixture analysis and is thought to be from the Tedlar bags used in the preceding experiments).

Differences in apparent 2,4-DNT retention times among the sensors are attributable to differences in desorption rates in desorption rates from the sensor films.[31] The *fwhm* values range from 1.8 to 2.0 s for DMNB and from 10 to 15 s for 2,4-DNT. The calculated values of R_s for the critical pairs are 1.6 (DMNB/C_{11}), 1.3 (DMNB/C_{12}), and 1.7 (2,4-DNT/C_{13}). The overall analytical cycle time is ~ 120 s on the basis of the 2,4-DNT peak maxima elution times. The normalized response patterns generated for DMNB, C_{13}, and 2,4-DNT from data collected from the assembled prototype provided the same degree of pattern-based discrimination as found in tests with just the microsystem. Unfortunately, quantification was compromised by several factors. First, the actual headspace concentrations of the markers were not verified. In addition, it was not possible to insure quantitative transfer to the prototype inlet. Finally, high blank values observed in screening tests after an initial injection were eventually traced to a leak in the fitting for valve V3 on the manifold, which permitted part of the focused sample to be shunted back onto the sampler during injection. Accounting for this with a rough estimate of transfer efficiency and assuming saturation and quantitative transfer of the headspace in the flask containing the markers, the LODs estimated from analyses run with the prototype were 2-fold higher than those from the microsystem reported above, on average. Given the uncertainties and likely positive biases in the estimates of injected masses, these LOD values are reasonable.

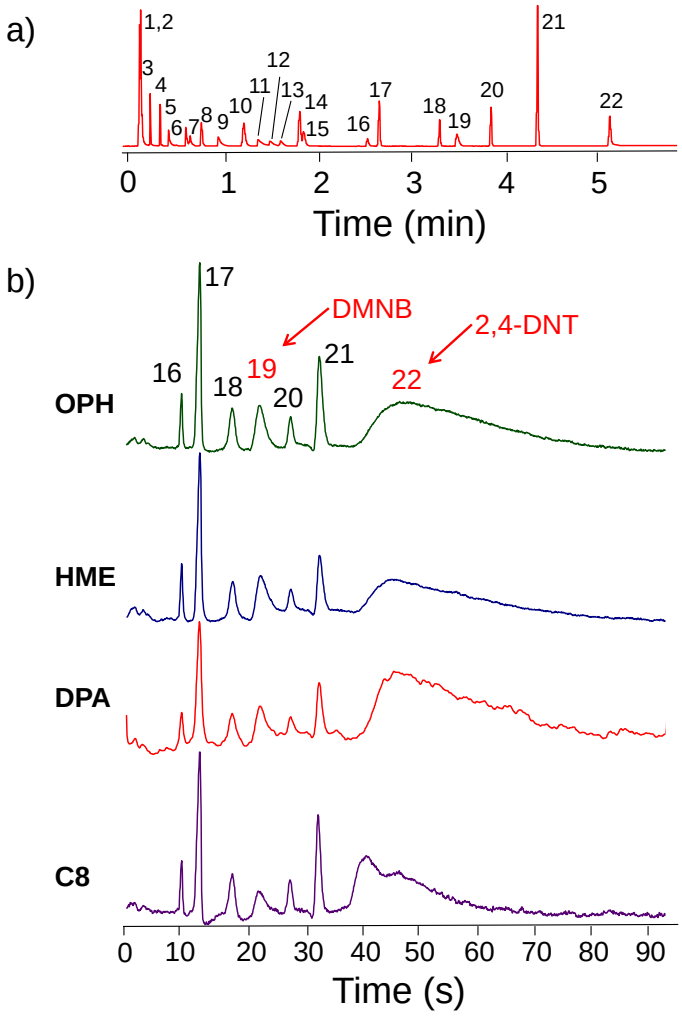

Figure 2.7. a) Reference chromatogram of a 22-component mixture (including DMNB and 2,4-DNT) obtained with a commercial 6-m long capillary column with a PDMS stationary phase (0.25 mm i.d., SPB-1, 0.25 µm thickness, Supelco) and an FID (He carrier gas, 3 mL/min); b) Chromatograms from the four CR sensors generated with the INTREPID prototype from the automated analysis of a 1-L air sample containing the 22-component mixture. Fifteen of the interferences were (intentionally) not trapped by the PCF module and therefore do not appear in the chromatograms. Compounds: 1, benzene; 2, 1-propanol; 3, *n*-heptane; 4, toluene; 5, *n*-octane; 6, hexanal; 7, 2-hexanone; 8, isoamyl alcohol; 9, *m*-xylene; 10, 2-methyl-2-hexanol; 11, 2-heptanone; 12, *n*-nonane; 13, cumene; 14, heptanal; 15, 1-hexanol; 16, octanal; 17, *n*-decane; 18, *n*-undecane; 19, DMNB; 20, *n*-dodecane; 21, *n*-tridecane; 22, 2,4-DNT. Temp prog.: 20-s hold at 70 °C, ramp at 8 °C/s to T_{max} = 120 °C; hold. See text for complete conditions.

2.5 Conclusions

On the basis of these results, we conclude that the μGC prototype described herein is suitable for automated stand-off analysis of the targeted gas-phase explosive marker compounds. Optimized for this application, the instrument relies on rapid, selective, high-volume preconcentration; rapid, temperature-programmed μcolumn separation with on-column focusing; and microsensor-array detection to unequivocally determine the explosive markers in the presence of a complex mixture of relevant background S/VOCs. An overall sampling and analytical cycle time of 2 min was achieved. On-going work is focused on documenting the accuracy and reliability of extended, autonomous operation of the INTREPID prototype through a series of mock field tests in indoor environments spiked with low- or sub-ppb concentrations of the markers.

2.6 References

1. Peng, C-Y.; Batterman, S.; J. Environ. Monit., 2000, 2, 313-324.
2. Schurmann, G.; Schafer, K.; Jahn, C.; Hoffmann, H.; Bauerfeind, M.; Fleuti, E.; Rappengluck, B., Atmospheric Environment, 2007, 41, 103-118.
3. Pella P., J. Chem. Thermodynamics, 9, 1977, 301-305.
4. RespondeR RCI Product Information Page http://www.smithsdetection.com/responder_RCI.php (accessed Jul 2013).
5. Sabre 5000 Product Information Page http://www.smithsdetection.com/sabre5000.php
6. Griffin-824 Product Information Page http://gs.flir.com/detection/chemical/mass-spec/griffin-824 (accessed Jul 2013).
7. Hapsite ER Product Information Page http://products.inficon.com/en-us/nav-products/Product/Detail/HAPSITE_ER_Identification_System?path=Products%2Fpg_ChemicalDetection%2F (accessed Jul 2013).
8. Fido-NXT Product Information Page http://gs.flir.com/products/icx-detection/explosives/fido-nxt/ (accessed Jul 2013).
9. Lu, C.J.; Steineker, W.; Tian, W.C.; Oborny, M.; Nichols, J.; Agah, M.; Potkay, J.; Chang, H.; Driscoll, J.; Sacks, R.; Wise, K.; Pang, S; Zellers, E.T., Lab Chip, 2005, 5, 1123-1131.
10. Lewis, P.; Manginell, R.; Adkins, D.; Kottenstette, R.; Wheeler, D.; Sokolowski, S.; Trudell, D.; Byrnes, J.; Okandan, M.; Bauer, J.; Manley, R.; Frye-Mason, G., IEEE Sensors, 2006, 6, 784-795.
11. Kim, H.; Steinecker, W.; Reidy, S.; Lambertus, G.; Astle, A.; Najafi, K.; Zellers, E. T.; Bernal, L. P.; Washabaugh, P. D.; Wise, K. D. Proc., 17th Intnl Conf. Solid-State Sensors, Actuators, and Microsystems, Transducers '07, Lyon, France, June 10-14, 2007, 1505-1508.
12. Zampolli, S.; Elmi, L.; Mancarella, F.; Betti, P.; Dalcanale, E.; Cardinali, G.; Severi, M., Sens. Actuator B, 2009, 141, 322-328.
13. a) Kim, S.; Chang, H.; Zellers, E.T.; Anal. Chem., 2011, 83, 7198-7206. b) Kim, S.; Burris, D.; Chang, H.; Bryant-Genevier, J.; Zellers, E. T. , Environ. Sci. and Technol., 2012, 46, 6065-6072. c) Kim, S.; Burris, D.; Bryant-Genevier, J.; Gorder, K.; Dettenmaier, E.; Zellers, E.T., Environ. Sci. and Technol., 2012, 46, 6073-6080.
14. Liu, J.; Gupta, N.; Wise, K. D.; Gianchandani, Y. B.; Fan, X., Lab Chip, 2011, 11, 3487-3492.
15. Qin, Y.; Gianchandani, Y. B., Proc., 17th Intnl Conf. Solid-State Sensors, Actuators, and Microsystems, Transducers '13, Barcelona, June 16-20, 2013, pp. 2755-2758.
16. Zhong, Q.; Steinecker, W.; Zellers, E.T., Analyst, 2009, 134, 283-293
17. Chapman, P. J.; Vogt, F.; Dutta, P.; Datskos, P. G.; Devault, G. L.; Sepaniak, M. J., Anal. Chem., 2007, 79, 364-370.
18. Li M., Myers E.B., Tang H.X., Aldridge S.J., McCaig H.C., Whiting J.J., Simonson R.J., Lewis N.S., Roukes M.L., Nano Lett., 2010, 10, 3899-903.
19. Liu, J.; Seo, J.H.; Li, Y.; Chen, D.; Kurabayashi, K.; Fan, X. Lab Chip, 2013, 13, 818-825.
20. a) Simoens, F.; Arnaud, A.; Castelein, P.; Goudon, V.; Imperinetti, P.; Lalanne Dera, J.; Meilhan, J.; Ouvier Buffet, J.L.; Pocas, S.; Maillou, T.; Hairault, L.; Gellie, P.; Barbieri S.; Sirtori, C.; Proc. SPIE 7837, Millimetre Wave and Terahertz Sensors and Technology

III, Toulouse, France, 2010, 78370B-1; b) Clavaguera, S.; Montméat, P.; Parret, F.; Pasquinet, E.; Lère-Porte, J-P.; Hairault, L., Talanta, 2010, 82, 1397.
21. Jenkins, T.; Leggett, D.; Ranney, T., CREEL, special report 99-21, available at: http://www.dtic.mil/cgi-bin/GetTRDoc?AD=ADA373402 (accessed October 2012)
22. Murrmann, R.; Jenkins, T.; Leggett, D., CREEL, Special Report 158, available at: http://www.dtic.mil/cgi-bin/GetTRDoc?AD=ADA040632 (accessed October 2012).
23. Convention on the marking of plastic explosives for the purpose of detection, available at: http://www.ciaonet.org/cbr/cbr00/video/cbr_ctd/cbr_ctd_33.html (accessed July 2013).
24. Serrano, G.; Sukaew, T.; Zellers, E.T.; J. Chrom. A, 2013, 1279, 76–85.
25. Lai, H.; Leung, A.; Magee, M.; Almirall, J.; Anal. Bioanal. Chem., 2010, 396, 2997–3007.
26. Voiculescu, I.; McGill, R.; Zaghloul, M.; Stepnowski, J.; Stepnowski, S.; Summers, H.; Nguyen, V.; Ross, S.; Walsh, K.; Marin, M., IEEE Sensors, 2006, 6,1094-1104.
27. Martin, M.; Crain, M.; Walsh, K.; McGill, R.; Houser, E.; Stepnowski, J.; Stepnowski, S.; Wu, H-D.; Ross, S., Sens. Actuators B, 2007, 126, 447-454.
28. Mohsen, Y.; Sanchez, J.; Berger, F.; Lahlou, H.; Bezverkhyy, I.; Fierro, V.; Weber, G.; Celzard, A.; Bellat, J., Sensors and Actuators B, 2013, 176, 124–131.
29. R. Ingram, J. Sikes, Proc. SPIE, 7664, 2010, 766415-1 – 766415-8.
30. Cizek, K.; Prior, C.; Thammakhet, C.; Galik, M.; Linker, K.; Tsui, R.; Cagan, A.; Wake, J.; La Belle, J.; Wang, J., Anal. Chim. Acta, 2010, 661, 117.
31. Wright, L.; Zellers, E. T.; Analyst., in press, August, 2013.
32. E.T. Zellers, G. Serrano, H. Chang, L.K. Amos, Proc., 16th Intnl Conf. Solid-State Sensors, Actuators, and Microsys., Transducers '11, Beijing, China, June 5–9, 2011, pp. 2082–2085.
33. W. Collin, G. Serrano, L. Wright, H. Chang, E. T. Zellers, Proc. 17th Intnl Conf. Solid-State Sensors, Actuators, and Microsystems, Transducers '13, Barcelona, June 16-20, 2013, pp. 2763-2766.
34. Fuels and Fuel Additives for Highway Vehicles and Their Potential Effects on Health, EPA-600/1-77-005 available at: http://nepis.epa.gov/ (accessed July 2013).
35. Rowe, M.; Plass, K.; Kim, K.; Kurdak, Ç.; Zellers, E.T.; Matzger, A., Chem. Mater., 2004, 16, 3513-3517.
36. Sukaew, T.; Chang, H.; Serrano, G.; Zellers, E. T. Analyst, 2011, 136, 1664–1674.
37. Serrano, G.; Reidy, S.; Zellers, E.T.; Sensors and Actuators B Chemical, 2009, 141, 217-226.
38. Bohrer, F.; Covington, E.; Kurdak, C.; Zellers, E. T.; Anal. Chem., 2011, 83, 3687.

CHAPTER 3

μGC × μGC: COMPREHENSIVE TWO-DIMENSIONAL GAS CHROMATOGRAPHIC SEPARATIONS WITH MICROFABRICATED COMPONENTS

3.1 Background and Motivation

The quantitative analysis of airborne volatile/semi-volatile organic compounds (S/VOC) is critical to solving numerous vexing problems, including mapping and remediating environmental pollution,[1] assessing human exposures,[2] diagnosing metabolic abnormalities,[3] combating terrorism,[4] and ensuring indoor air quality.[5] Performing such measurements directly in the field or clinic can improve the quality and quantity of data collected and can facilitate rapid interventions. Since reliable determinations of S/VOCs in complex mixtures generally require temporal/spatial separation prior to detection, gas chromatography (GC) is one of the most effective approaches to such analyses.

Advances in commercial, field-deployable GC instrumentation have led to significant improvements in performance, reliability, and portability,[6-9] and research on GC microsystems

(μGC) fabricated using Si-micromachining processing techniques[10] continues to produce innovative designs that further reduce size and power requirements.[11-18] Such microsystems represent the most promising path to realizing miniature, low-cost, ubiquitous, near-real-time air monitors for S/VOC mixtures. Yet, the inherent limitations on the maximum length and minimum diameter of μGC separation columns under pressure-driven flow place inherent constraints on peak capacity and resolution which, in turn, may limit the complexity of the mixtures that can be effectively analyzed.

Comprehensive two-dimensional gas chromatography (GC × GC) is widely viewed as the most effective method available for separating the components of highly complex S/VOC mixtures.[19,20] In GC×GC, a first-dimension (^{1}D) column is coupled through a modulator to a shorter second-dimension (^{2}D) column with retention selectivity complementary to that of the ^{1}D column. Each mixture component eluting from the ^{1}D column is re-injected in a series of narrow bands into the ^{2}D column at a rate that preserves the ^{1}D separation order. A 2-D contour plot depicting the separation in each dimension can be generated. Pneumatic[21,22] or thermal[23-26] modulators (TM) can be used, and each has advantages and limitations.[27] In the latter, a cryogenically cooled fluid is typically used to trap and focus sequential segments of each analyte peak eluting from the ^{1}D column, and then a resistive or convective heater is used to reintroduce them to the ^{2}D column.[24-26] Rapid cycling between minimum (T_{min}) and maximum (T_{max}) temperature set-points produces the desired modulation. The primary advantages of GC × GC, particularly with thermal modulation, are the higher resolution and detectability that can be realized from the taller, sharper peaks produced, relative to 1-D GC systems.[19,20,28]

In regard to μGC, adding an independent, second-dimension separation stage (i.e., μGC × μGC) is a logical approach to overcoming the limitations on analytical performance imposed by

the inherently short μcolumns. Toward that end, Kurabayashi, et al. recently reported on a microfabricated TM (μTM) that operates at much lower power levels than conventional TMs and that does not use any cryogenic fluids.[29] This μTM incorporates two, series-coupled, spiral Pyrex-on-Si microchannel stages with independent thin-metal-film meander-line heaters on each stage. It is mounted in proximity to a stacked, solid-state thermoelectric cooler (TEC). Rapid heating and cooling are possible and μTM-stage T_{min} values in the range of -20 to -35 ^{o}C and T_{max} values of 250 ^{o}C (or higher) are achievable. We have used this device to perform GC × GC separations with conventional capillary columns,[30,31] but testing to date has been performed under isothermal conditions (i.e, fixed values of T_{min}, T_{max}, and ^{1}D and ^{2}D column temperatures) that favored trapping and re-mobilization of more-volatile compounds. Less volatile analytes displayed much broader modulated peaks (*fwhm* ~seconds). Temperature programming of all components would expand the range of compounds for which effective μGC × μGC separations could be performed. Several other noteworthy efforts toward multi-dimensional μGC subsystems, all of which use pneumatic modulation or flow switching, have been reported over the past few years, as well.[32-35]

Traditionally, the ^{1}D column is coated with a nonpolar stationary phase and the ^{2}D column is coated with a more polar or polarizable phase. For the latter, room temperature ionic liquids (RTILs) have been used to good effect.[36] Several members of a relatively new class of RTILs, having trigonal tricationic core structures and a bis(trifluoromethylsulfonyl)imide (NTf_2) anion, have been explored as GC stationary phases recently by Armstrong et al.[37,38] A subset of these exhibits sub-ambient melting points, high decomposition temperatures, low bleed, and retention properties complementary to PDMS,[38] and thus are interesting prospects not only as ^{2}D μcolumn wall coatings but also as possible μTM wall coatings (note: with a discrete μTM one could potentially use different phases in the μTM and the ^{2}D μcolumn in a μGC×μGC system).

As a further step toward the realization of a field portable µGC × µGC system having fluidic and analytical components arranged as shown in the block diagram in Figure 3.1, the work described here entailed the fluidic integration and testing of wall-coated ^{1}D and ^{2}D Si-microfabricated µcolumns with a wall-coated µTM. Conventional injection methods were used along with flame ionization detection (FID). PDMS was used in the ^{1}D µcolumns and the µTM, and both a trigonal tricationic RTIL and a commercial poly(trifluoropropyl methylsiloxane) (PTFPMS, OV-215) were investigated as ^{2}D µcolumn phases.

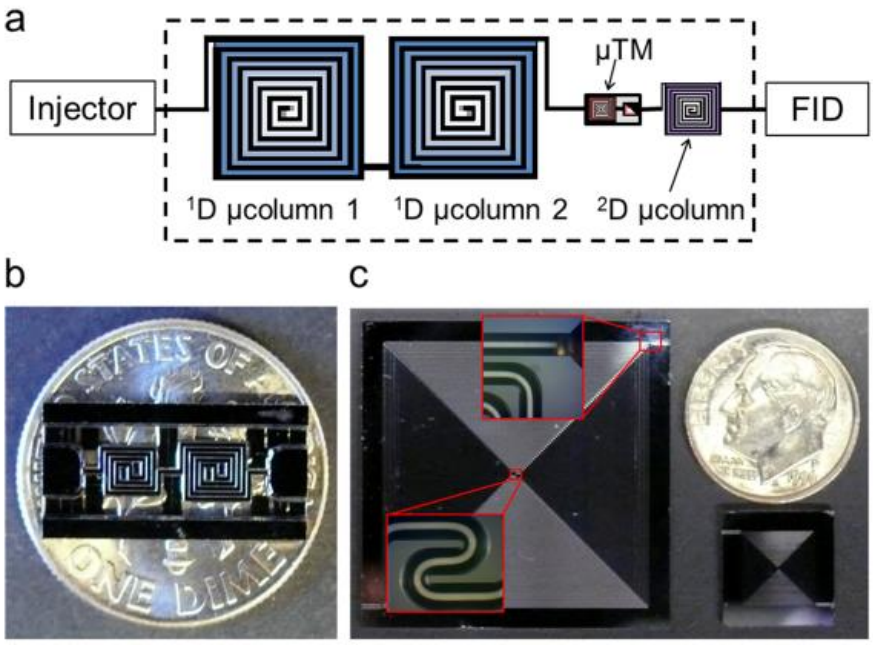

Figure 3.1. a) Block diagram of the µGC×µGC test set-up (dashed box represents the GC oven); b) the 2-stage µTM on a U. S. dime; c) 3-m ^{1}D µcolumn (left of dime) and 0.5-m ^{2}D µcolumn (below dime). Insets show enlargements of the ^{1}D µcolumn inlet and the center where the channel changes from a clockwise to an anticlockwise spiral.

After describing the deposition of the various stationary phases and characterization of the individual coated µcolumns, the results of testing the assembled subsystem with a simple mixture of alkanes under isothermal and temperature programmed conditions using the RTIL-coated ^{2}D µcolumn are presented. The separation of a more complex mixture of polar and non-polar

compounds is then demonstrated and the retention behavior of the RTIL is further evaluated. Finally, using an OV-215 coated ^{2}D µcolumn, the separation of a moderately complex mixture of 36 compounds is presented. Results are considered in terms of their impact on the design and function of a fully integrated µGC × µGC system.

3.2 Experimental Methods

3.2.1 Materials

Test compounds and starting materials for the RTIL synthesis were >98% pure (Sigma-Aldrich, Milwaukee, WI) and used without further purification. PDMS (OV-1) and PTFPMS (OV-215) were obtained from Ohio Valley Specialty Chemicals (Marietta, OH). The RTIL was synthesized by a published method[38] and characterized by standard methods, as described in Figures A2.1-A2.4, Table A2.1, and the associated text in Appendix 2. A commercial capillary column, coated with the same RTIL as that synthesized for this study and used as the stationary phase in one of the ^{2}D µcolumns, was tested for comparison (100 µm i.d., 0.5-m long, 0.08 µm SLB-IL76 phase, Supelco, Bellefonte, PA).

3.2.2 Devices

Figure 3.1b shows the microfabricated devices employed. The two-stage µTM has been described previously.[29-31] The 13×6 mm Si chip contains a single deep-reactive-ion-etched (DRIE) Si µchannel with a cross section of 250 (w) × 140 (h) µm along the length of which are two convolved square-spiral segments, 4.2 cm (stage 1) and 2.8 cm (stage 2) long, separated by a 1.0 mm long straight segment. A 100-µm thick Pyrex cap is anodically bonded to the top surface of the entire chip to seal the µchannel. Four meander-line Ti/Pt resistive heaters are patterned on the

Pyrex surface; one above each μTM stage and one each on the rim above the inlet and outlet ports. Ti/Pt RTDs are patterned beside the heaters to measure temperature.

The μTM was connected to upstream and downstream (μ)columns through 10-cm sections of deactivated fused silica capillary (250 μm i.d., upstream; 100 μm i.d., downstream) inserted into expansion ports on the chip and sealed with epoxy (Hysol 1C, Rocky Hill, CT). The device was epoxied Pyrex side up and wire-bonded to a custom carrier printed circuit board (PCB) with a hole cut out beneath the device for thermal isolation. This sub-assembly was inverted and mounted such that the Pyrex surface of the μTM was suspended directly above the TEC (Marlow, Dallas, TX). Two small slabs of Si were placed on the TEC beneath the μTM stages and two more small Si spacers were placed on the slabs. The slabs and spacers were held in thermal contact with the TEC surface with thermal grease, and the μTM was positioned with a height gauge to within ~40 μm of the spacers. The spacer and slab help to focus the cooling on the two μTM stages, while the small air gap reduces power for heating.[29] A plastic shroud through which a constant stream of dry air is passed during operation to prevent atmospheric water condensation on the device is secured around the μTM.

The basic design and fabrication of the μcolumns used here have also been described previously.[39,40] Each μcolumn consists of a DRIE-etched Si channel with an anodically bonded Pyrex cap. Thin-film Ti/Pt heaters and RTDs patterned on the back side of the Si permit temperature ramping, although this feature was not used in the current study. The ^{1}D separation stage consisted of two series-coupled 3.1 × 3.1 cm μcolumn chips with convolved square-spiral DRIE channels, 3-m long and 250 × 140 μm in cross section, wall-coated with a PDMS stationary phase. The ^{2}D separation stage consisted of a 1.2 × 1.2 cm μcolumn chip with a similarly shaped DRIE channel, 0.5-m long and 46×150 μm in cross section, wall-coated with either the RTIL or

OV-215. Fluidic connections were made through ~5-cm segments of fused silica capillary (250 μm i.d. for 3-m μcolumns, 100 μm i.d. for 0.5-m μcolumns) epoxied into expansion ports in the Si chips.

3.2.3 Stationary Phase Deposition

The ^{1}D μcolumns and μTM were statically coated individually with PDMS from a solution that also contained 1% (w/w) dicumyl peroxide as the crosslinking agent using a published procedure.[41,42] PDMS concentrations were adjusted to produce an average (nominal) wall-coating thickness of 0.20 μm for the ^{1}D μcolumns and 0.30 μm for the μTM. The PDMS in the μcolumns was cross-linked by heating at 180 °C for 1h under N_2 in a GC oven. The PDMS in the μTM was cross-linked by heating at 180 °C for 1h under N_2 using the on-chip stage heaters in order to avoid rupturing the capillary-chip union from expansion of the adhesive. An unavoidable consequence of the method is that the connecting capillaries were coated (in both the μcolumn and μTM) and crosslinked (only in the μcolumn).

Prior to (statically) coating one of the ^{2}D μcolumns with the RTIL, it was pre-treated with NaCl to promote adhesion according to a published method.[43] Details of the pretreatment and coating procedure are provided in Appendix 1, along with photomicrographs illustrating the extent of coverage (Figure A2.5). The nominal average RTIL-film thickness was 0.1 μm. Details of the procedure used for pretreatment, coating, and cross-linking of OV-215 on a separate ^{2}D μcolumn are also provided in Appendix 1.[42] The calculated average OV-215 thickness was 0.08 μm.

3.2.4 Chromatographic Efficiency

The separation efficiency of each (μ)column was determined by measuring the retention time, t_R, and the full-width-at-half-maximum (*fwhm*) of each peak as a function of average carrier

gas velocity, $\bar{u}$, using one of two probe compounds and N_2 as carrier gas. Methane hold-up times were used to determine $\bar{u}$. Peaks were approximately Gaussian and the total plate count, $N = 5.545(t_R/fwhm)^2$, and plate height, $H = L/N$, were calculated from the data for each column of length L.4.2.3 Instrumentation

3.2.5 System Integration and Testing

The two 3-m ^{1}D μcolumns were epoxied to individual carrier PCBs and wire-bonded to pads on the PCB. A cut-out in the PCB beneath each column provided a degree of thermal isolation. These μcolumns were connected in series through the attached capillaries using press-fit unions. The ^{2}D μcolumn was placed on a resistor-embedded polyimide heater pad (Omega Engineering, Inc., Stamford, CT) to which thermal grease was pre-applied. A fine wire thermocouple was inserted between them to monitor the temperature and polyimide tape was used to maintain intimate contact between the heater and μcolumn chip.

The capillaries affixed to the μTM were connected to those on the ^{1}D and ^{2}D μcolumns by means of press-fit unions, and the entire μGC × μGC subsystem was placed in the oven of a bench scale GC (Agilent 6890, Agilent Technologies, Palo Alto, CA). The outlet of the ^{2}D μcolumn was connected to the FID of the GC. Helium was used as the carrier gas. The temperature of the ^{1}D μcolumns was controlled by the GC oven. This also set the ambient temperature of the TEC, which affected the T_{min} and T_{max} of the μTM stages, respectively (discussed below). The temperature of the ^{2}D μcolumn was offset by ~20 °C above that of the oven by use of the heater pad. Note: the on-chip μcolumn heaters were not used in these experiments to avoid the need for computer control.

Test atmospheres of a mixture of C_7-C_{10} n-alkanes were generated in 10-L FlexFilm® bags (SKC Inc., Eighty Four, PA) pre-filled with N_2 into which 10 μL of neat liquid samples of each mixture component was injected and allowed to evaporate, leading to vapor concentrations in the range of 140 to 185 ppm for each alkane. A test atmosphere was similarly generated for separations run subsequently with a 16-component vapor mixture. Samples were drawn by a small diaphragm pump through a 250- or 112-μL sample loop, via a 6-port valve maintained at 30 °C, and then injected into the ^{1}D μcolumn through a 10-cm segment of capillary. For tests with the 36-component mixture, a solution containing 10 μL of each analyte in 3 mL of CS_2 was prepared, and 0.1 μL was injected directly into the GC inlet via syringe to the ^{1}D column.

A modulation period, P_m, of 5 or 6 s was used, depending on the ^{2}D retention times of the analytes. The offset between heating of the first and second stages of the μTM was 500 ms.[30,31] Operating the TEC at 8 V produced T_{min} values of -22 and -28 °C, for stage 1 and stage 2, respectively, in a 30 °C GC oven. Modulations entailed applying 100-ms voltage pulses independently to each stage heater. The voltage applied to each was ~45 V and was adjusted to achieve a T_{max} of ~210 °C at an ambient (oven) temperature of 30 °C. A constant voltage was applied independently to each μTM rim heater and adjusted to maintain the ports at 20 °C at an ambient of 30 °C. Due to a small degree of thermal crosstalk between the stages and the rims, the rim temperature increased 5-7 °C when the proximal stage was heated. Applying 4.5 V to the ^{2}D μcolumn resistive heater pad yielded a temperature of 50 °C at an oven temperature of 30 °C.

Chromatographic data were collected using ChemStation software (Rev.B.01.01, Agilent Technologies, Santa Clara, CA). A custom Visual C# program was used to control the timing of the applied voltages (via two solid-state relays), as well as to read the temperature sensors via a DAQ card (NI USB-6212, National Instruments, Austin, TX) installed on a laptop computer. The

data sampling rate from the FID was 200 Hz and it was held at 250 °C. OriginPro 9.1 (OriginLab, Northampton, MA) and GC Image (Rev 2.2, Zoex, Houston, TX) were used for chromatographic data processing and display of 2-D chromatograms, respectively.

3.3 Results and Discussion

3.3.1 (μ)Column Efficiencies

Golay plots (i.e. H vs. $\bar{u}$) for all (μ)columns are presented in Figure A2.6 of Appendix 2 and the test conditions and results are summarized in Table 3.1. Values of k' ranged from 1.1 – 4.9. The RTIL-coated μcolumn retained the probe analyte (MIBK) much more strongly than did the IL-76 capillary, which required increasing the oven temperature by 30 °C to obtain approximately the same value of k'. The maximum number of plates, N_{max}, of 3,800 plates/m calculated for the two OV-1-coated dual 3-m ^{1}D μcolumn ensemble (with each 3-m μcolumn tested individually) was ~25% lower than reported previously for similarly coated 3-m μcolumns.[39] On the basis of N_{max}, the separation efficiencies were in the order OV-1 μcolumn > OV-215 μcolumn > RTIL μcolumn ≈ IL-76 capillary.

3.3.2 Preliminary Testing with the RTIL-coated ^{2}D (μ)Column

Initial tests of the microsystem used the RTIL-coated ^{2}D μcolumn and entailed isothermal (30 °C) and temperature ramped (30-80 °C at 5 °C/min) separations of C_7 to C_{10} vapors. For the latter, the oven temperature was constrained to 80 °C to avoid overheating the ancillary electronic components on the μTM PCB. The raw μGC × μGC chromatograms are presented in Figure 3.2. For the isothermal separation (Figure 3.2a), the number of modulations per peak (i.e., the

modulation number, M_N) were 3, 2, 4, and 8 and *fwhm* values were 160, 280, 530 and 1020 ms for C_7, C_8, C_9, and C_{10}, respectively. These *fwhm* values were significantly smaller than those reported

Table 3.1. Summary of test conditions and results of Golay plots generated with the (μ)columns and stationary phases.[a]

Phase	L (m)	Probe	k'	H_{min} (mm)	$\bar{u}_{opt}$ (cm/s)	N_{max} (plates/m)
OV-1	3	C_8	4.6	0.26	7.8	3800
OV-1	3	C_8	4.9	0.26	8.8	3800
OV-215	0.5[b]	MIBK[c]	1.4	0.39	8.4	2500
RTIL	0.5[b]	MIBK	1.1	0.76	3.5	1300
IL-76[d]	0.5	MIBK	1.2	1.0	2.5	1000

[a] $k' = (t_R - t_M)/t_M$ where t_M is the methane holdup time; H_{min} and $\bar{u}_{opt}$ are from the minima in the Golay plots in Figure A2.5 in Appendix 2; [b]for both of these columns, H_{min} was calculated assuming L = 0.6 m to account for the coated interconnecting capillaries. (μ)column temperature was 30 °C except for the RTIL (60°C); commercial capillary column (0.1 mm i.d.); [d]MIBK = 4-methyl-2-pentanone.

by Kim, et al., who used the same type of μTM without a ^{2}D column installed, but a much lower carrier gas flow rate of 0.38 mL/min.[30] The insets in Figure 3.2a show enlarged views of the bases of the modulated peaks. No breakthrough was evident, but there was some tailing. The *fwhm* values for C_9 and C_{10} were relatively large owing to the low operating temperature. For C_{10}, which showed moderate tailing, the base peak widths approached the value of P_m (i.e., 5 s). Although the conditions were less than optimal, these results serve to demonstrate that the integrated microsystem was operating as intended.

The separation was then repeated with a modest oven temperature ramp from 30 to 80 °C at 5 °C/min. Figure 3.3 shows the temperature profiles for the microsystem components. The ^{1}D

μcolumn temperatures were taken as those of the GC oven. The ^{2}D μcolumn was offset ~20 °C from that of the ^{1}D μcolumn and lagged the oven temperature ramp by only 0.5 °C/min. The T_{min}

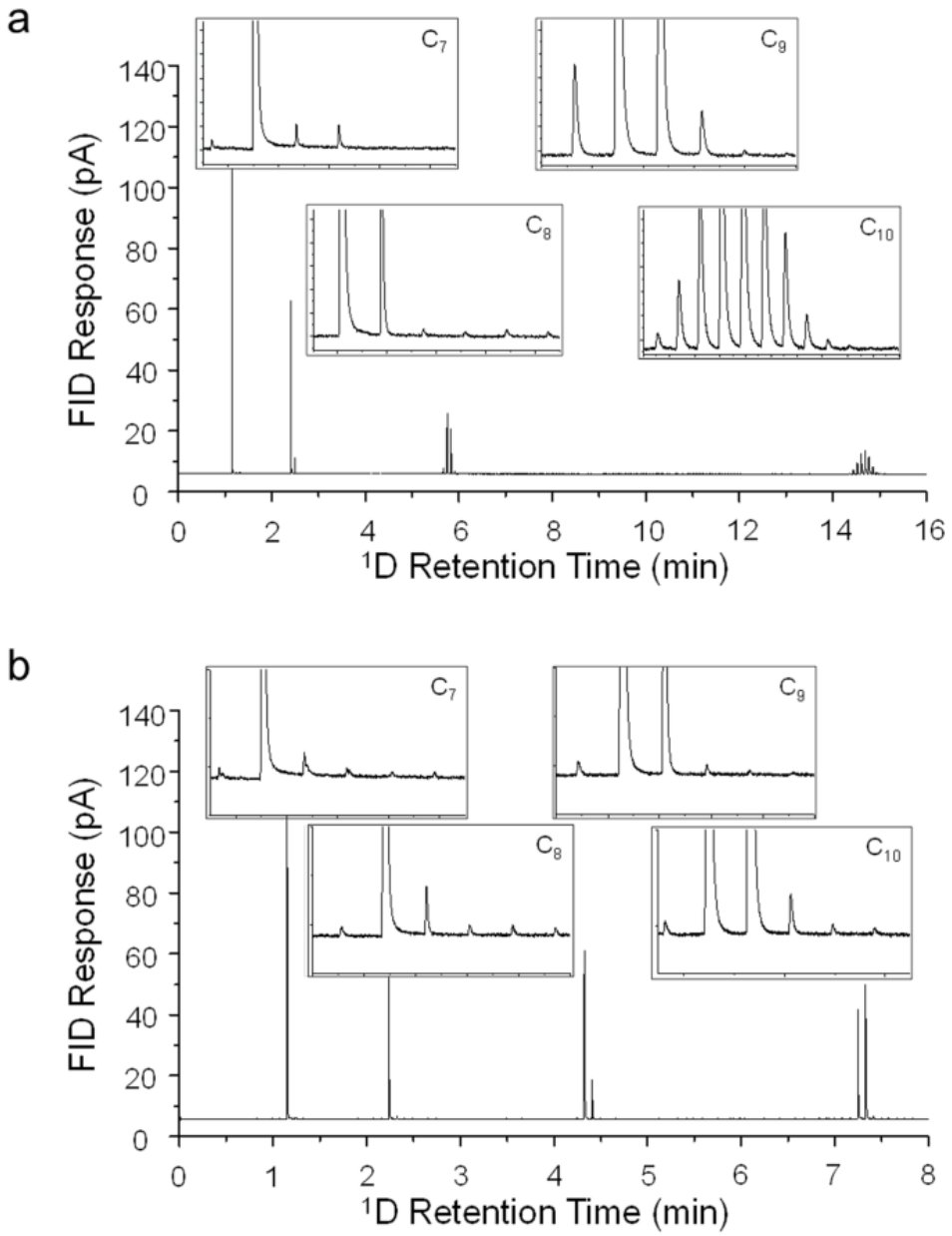

Figure 3.2. Raw chromatograms of the 2-D separations of n-alkanes C_7 through C_{10} obtained with the microsystem shown in Figure 2.1a with stationary phases of OV-1 for the ^{1}D μcolumns and the RTIL for the ^{2}D μcolumn: a) isothermal separation with the ^{1}D μcolumn at 30 °C and the ^{2}D μcolumn at 50 °C; b) temperature ramped separation (30-80 °C at 5°C/min, see Figure 3.3). Conditions: loop-injection (~ 9 ng of each analyte vapor); 1.5 mL/min of He; P_m = 5 s. All insets span a 3-pA FID response range and a 30-s time interval, except the isothermal C_{10} inset, which shows a 60-s interval.

and T_{max} values of the μTM stages also increased linearly but at rates significantly lower than that of the oven. The same was true of the average rim temperature (as noted above, the rim temperature temporarily rose 5-7 °C above the reported temperature as the adjacent stage was heated). This was not unexpected, since the large thermal mass of the TEC attenuates the effect of changes in ambient temperature on the μTM. Operation in this manner is similar to that of one version of the LMCS modulator developed by Marriott et al.,[44] wherein the T_{min} and T_{max} values were gradually increased over the course of a separation so as to maintain a T_{min} low enough for efficient trapping but high enough to efficiently remobilize the progressively less volatile eluates.

Figure 3.2b shows the raw 2-D chromatogram of the C_7-C_{10} alkane mixture for the temperature-ramped separation. Values of t_R for C_9 and C_{10} were much shorter, as expected, while those for C_7 and C_8 were about the same because they elute after only a slight change in temperature. Accordingly, values of M_N were ~2, 2, 3, and 5 and values of *fwhm* were 161, 217, 294 and 346 ms for C_7, C_8, C_9 and C_{10}, respectively. That is, the M_N and *fwhm* values for C_7 and C_8 did not change much, while those for C_9 and C_{10} decreased significantly. The reductions in M_N were due to the narrower ^{1}D peaks entering the μTM.

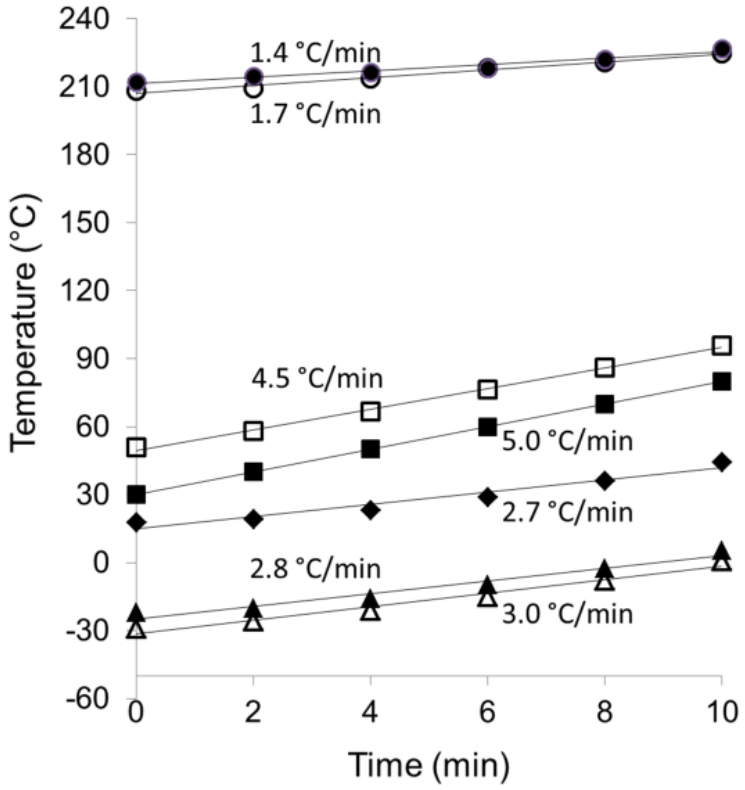

Figure 3.3. Temperature profiles of the µcolumns and µTM for the 5 °C/min oven ramp used to generate the chromatogram in Figure 2b. Legend: unfilled circles, stage-1 T_{max}; filled circles, stage-2 T_{max}; unfilled squares, ^{2}D µcolumn; filled squares, ^{1}D µcolumn (assumed to be the same as the oven); filled diamonds, rim temperature; filled triangles, stage-1 T_{min}; unfilled triangles, stage-2 T_{min}.

With temperature ramping, the *fwhm* values for the modulated C_7 peaks did not change, relative to the isothermal separation, while those for C_8, C_9, and C_{10} decreased by ~20, 45, and 65%, respectively. By running a series of additional separations with the µTM maintained at a constant baseline temperature and the ^{2}D µcolumn set at several higher (discrete, isothermal) temperatures, the influence of ramping the µTM temperature on the *fwhm* values could be separated from that of the ^{2}D µcolumn temperature. The effect of the µTM temperature ramp on the *fwhm* values of the modulated peaks was found to be negligible for C_8, moderate for C_9, and predominant for C_{10}. Although the range of this temperature ramp was very narrow, the value of

increasing the temperature of the μTM and the μcolumns as the separation proceeds is apparent. Since the increase in T_{max} was only ~14 °C, it is likely that the ~40 °C increase in T_{min} was the more important parameter affecting remobilization. Obviously, a means of heating the μTM independently would be needed to decouple it from the ambient (e.g., oven) temperature and to allow higher temperatures to be achieved without damaging the electronic components on the μTM PCB. Extending analyses to less volatile analytes would undoubtedly also require increasing the rim temperatures to avoid cold spots at the inlet and outlet of the μTM.

3.3.3 Mixture Separation with the RTIL-coated ^{2}D (μ)Column

Next, a mixture of 14 compounds spanning a range of functional group classes was separated. The temperature ramp used was the same as that in Figures 3.2b and 3.3. The resulting 2-D contour plot is shown in Figure 3.4 and the values of t_R and *fwhm* for the 14 analytes are listed in Table A2.2 in the Appendix 2. As shown, the alkanes (compounds 3, 8, 11, and 13) eluted early from the ^{2}D μcolumn, as expected, and gave sharp peak clusters, with *fwhm* values ranging from 80 (C_7) to 280 ms (C_{10}). The alkene d-limonene and the set of four aromatics (compounds 1, 6, 9, 12, 14) were all retained slightly longer than the alkanes and had *fwhm* values of 410-480 ms, with little or no tailing evident. The diether 1,4-dioxane had slightly wider modulated peaks (*fwhm* = 532 ms). Unfortunately, 2-propanol and the set of three ketones (compounds 2, 5, 7, 10) had relatively long retention times and all gave very broad modulated peaks (*fwhm* ranged from 700 to 1100 ms); in fact, 2-propanol peak wrapped around to the next modulation period. An estimate of plate height based on the peak width of 4-methyl-2-pentanone was higher than observed in the Golay plots, most likely due to operation at a velocity well beyond the Golay minimum. Values of M_N ranged from 2 (2-propanol) to 5 (C_{12}). Although benzene gave well-focused modulated peaks for this analysis, in replicate runs it would occasionally show partial breakthrough, consistent with

our previous tests of benzene with this μTM.[31] Since the value of T_{min} reached at the outset of each run was just barely sufficient to trap benzene, even a slight mis-registration in the timing of the cooling cycle of the μTM and the elution of the benzene peak from the ^{1}D μcolumn can lead to breakthrough.

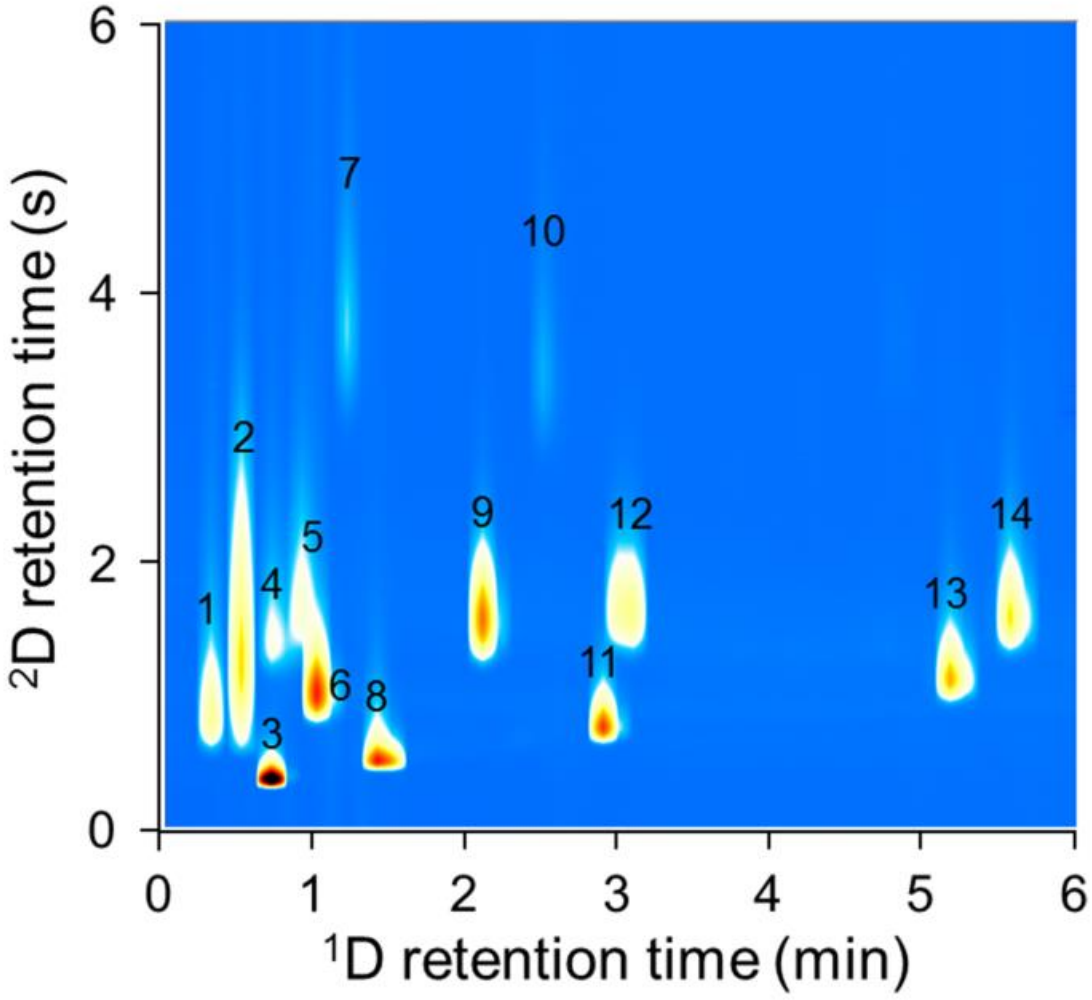

Figure 3.4. 14-compound 2-D contour plot generated with the microsystem with OV-1 coated ^{1}D μcolumns and RTIL coated ^{2}D μcolumn. Conditions: loop injection (10-20 ng of each analyte vapor); 1.5 mL/min of He; 30 °C with 5 °C/min oven ramp to 80°C; P_m = 6 s. Peak assignments: 1, benzene; 2, 2-propanol; 3, C_7; 4, 1,4-dioxane; 5, 4-methyl-2-pentanone; 6, toluene; 7, cyclopentanone; 8, C_8; 9, *m*-xylene; 10, 2-heptanone; 11, C_9; 12, cumene; 13 C_{10};, 14, *d*-limonene.

Running a similar mixture isothermally with the ^{1}D µcolumn at 33 °C and the ^{2}D µcolumn at 120 °C gave modulated *fwhm* values similar to those reported above. (Note that the increase ^{1}D t_R values for the alkanes in Figure 3.4, compared to Figure 3.2, is attributed to the insertion of a slightly longer section of 100-µm id interconnecting capillary between the µTM and the ^{2}D µcolumn and the consequent increase in pressure and decrease in velocity in the ^{1}D µcolumn.)

3.3.4 Commercial IL-76 Capillary vs. RTIL µColumn

To explore further the retention characteristics of the RTIL, a set of targeted separations was also performed after replacing the RTIL-coated ^{2}D µcolumn with the commercial IL-76 coated capillary (100 µm id, 0.5 m long), which has a slightly thinner RTIL film (0.08 µm) and yielded an N_{max} value about 30% lower than that of the RTIL µcolumn (see Table 3.1). The critical pair, C_7 and 1,4-dioxane, which co-eluted from the ^{1}D µcolumn, was selected to explore the differences in performance between the RTIL µcolumn and the IL-76 capillary column.

Representative raw chromatograms from a single modulation of this pair of compounds with the RTIL coated µcolumn and the IL-76 coated capillary column are shown in Figure 3.5a and b, respectively, for an isothermal separation (initial ^{1}D µcolumn = 30 °C; ^{2}D µcolumn = 55 °C). For C_7, the ^{2}D t_R values were about the same whereas the *fwhm* value with the µcolumn was roughly twice that with the capillary. For 1,4-dioxane, the t_R value on the µcolumn was about ~3 times longer (i.e., 3 s and 1 s, respectively) and the *fwhm* value was about ~7 times larger with the µcolumn than with the capillary (i.e., 770 ms and 115 ms, respectively).

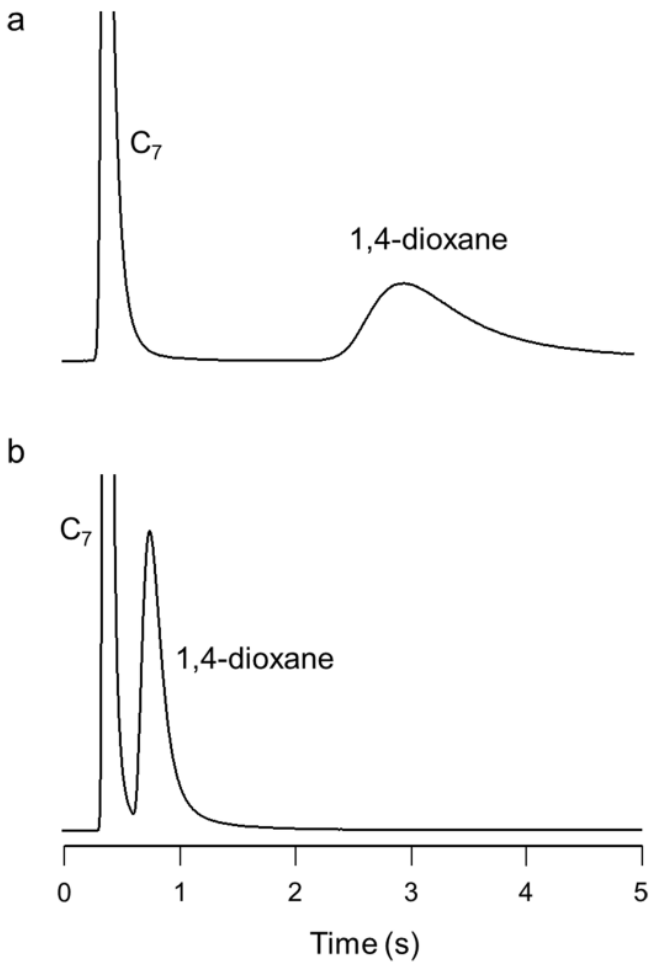

Figure 3.5. Comparison of single raw modulated chromatograms of C_7 and 1,4-dioxane using a) the RTIL-coated ^{2}D µcolumn and b) a commercial IL-76 coated ^{2}D capillary column (0.1 mm i.d., 0.5-m long). The same OV-1coated ^{1}D µcolumns were used for both a) and b). Conditions: loop injection (~ 10 ng of each analyte vapor); 1.2 mL/min of He; isothermal ^{1}D µcolumns (33 °C) and ^{2}D µcolumn (55 °C); P_m = 6 s.

These differences cannot be accounted for solely by the nominal 20% difference in RTIL film thicknesses. Although small errors in the deposition solution concentration could be contributory, we suspect that the roughness in the NaCl film in the µcolumn results in localized pooling of the RTIL during deposition on the µcolumn walls, and that this was responsible for the excessive retention of the more polar 1,4-dioxane. Since the alkane does not partition significantly into this material, there is less of an effect on its retention and band shape. Re-running this

separation at progressively higher ^{2}D µcolumn temperatures did not resolve the problem: even at 120 °C, the 1,4-dioxane peak had a *fwhm* value of 470 ms, which is too broad for effective µGC×µGC.

3.3.5 Mixture Separation with OV-215 coated ^{2}D (µ)Column

Next, the RTIL coated ^{2}D µcolumn was replaced with an OV-215 coated µcolumn of the same length and a mixture of 36 compounds was analyzed. A GC oven temperature program consisting of a 1-min hold at 30 °C followed by 5 °C/min ramp to 80 °C and a 10-min hold at 80 °C provided reasonably good separations. As before, a heater was placed in intimate contact with ^{2}D µcolumn to offset its temperature by 20 °C above that of the oven. To facilitate peak identification, compounds were added to the mixture progressively a few at a time. As such, it was possible to evaluate run-to-run retention time reproducibility for most of the peaks. Working from the contour plots, ^{1}D t_R values never varied by more than one modulation period (6 s), and ^{2}D t_R values, measured relative to that of 1-propanol, varied by < 10% (RSD) with the exceptions of C_7 (14%) and isopropanol (12%). The separation required 22 min and the range of ^{2}D t_R values was 0.1 – 4.4 s, indicating fairly good use of the 2-D space. The resolution in the 2nd dimension, which was rather low for the earliest eluting compounds (i.e., compounds 1-6), improved with increasing ^{1}D t_R values. Notably, numerous pairs of compounds that co-eluted from the 1st dimension were separated in the 2nd dimension (e.g., compounds 6 and 7, 9 and 10, 14 and 15, and 27 and 28), and the cluster consisting of compounds 19-21, which partially co-eluted in the 1st dimension were well resolved in the 2nd dimension. The excessively broad peak for benzene (compound 4) reflects µTM breakthrough, which occurred in 7 of the 13 replicates in which

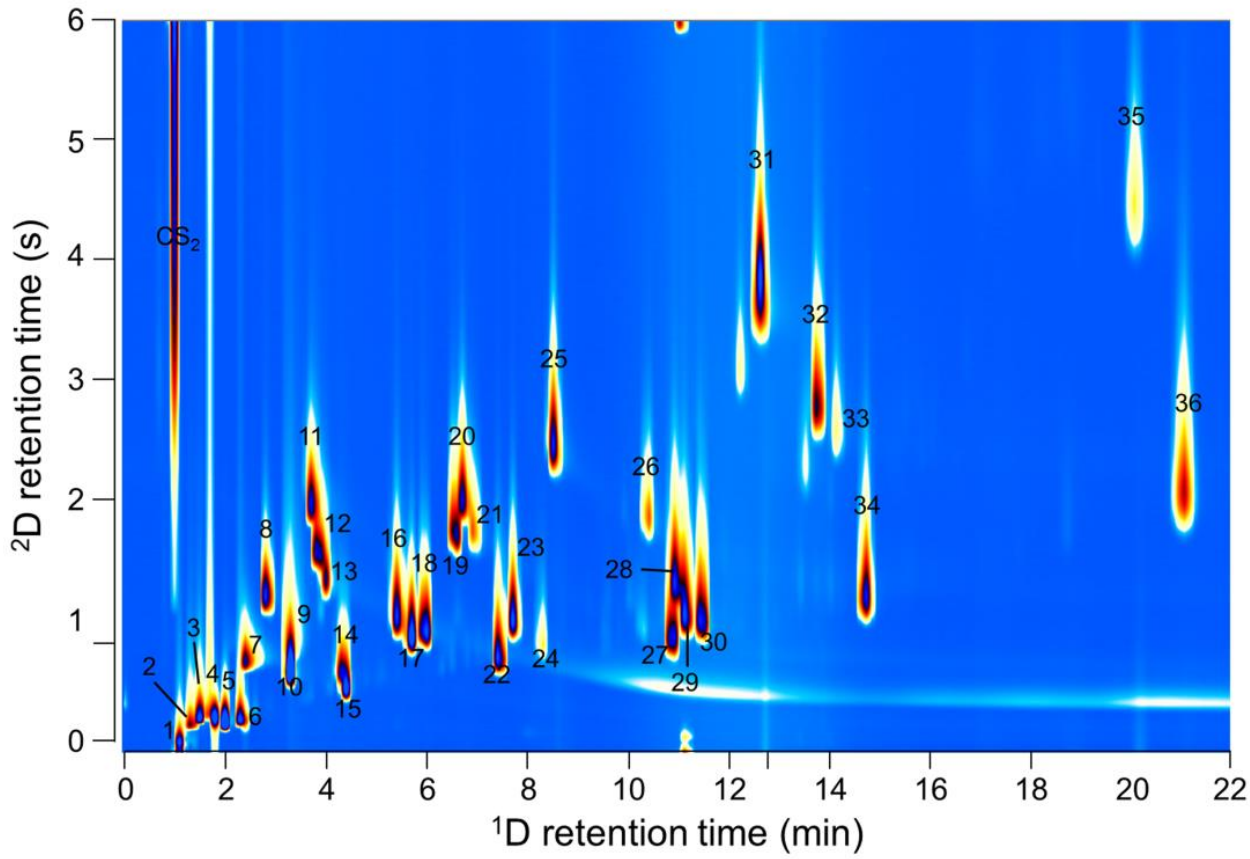

Figure 3.6. 36-compound 2-D contour plot generated with the microsystem with OV-1 coated ^{1}D µcolumns and an OV-215 coated ^{2}D µcolumn. Conditions: syringe injection (0.3 µg of each analyte in CS_2); 100:1 split; 1.5 mL/min of He; 1 min hold at 30 °C (oven), then 30-80 °C at 5 °C/min (oven), then 10 min hold at 80°C (oven); ^{2}D µcolumn offset +20 °C using resistive heater; P_m = 6 s. Peak assignments: 1, 2-propanol; 2, 1-propanol; 3, 2-butanol; 4, benzene; 5, cyclohexene; 6, C_7; 7, 1,4-dioxane; 8, 4-methyl-2-pentanone; 9, isoamyl alcohol; 10, toluene; 11, cyclopentanone; 12, 2-hexanone; 13, hexanal 14, perchloroethylene; 15, C_8; 16, 2-methyl-2-hexanol; 17, ethylbenzene; 18, m-xylene; 19, 3-heptanone; 20, 2-heptanone; 21, heptanal; 22, C_9; 23, cumene; 24, α-pinene; 25, benzaldehyde; 26, octanal; 27, dicyclopentadiene; 28, 1,2,3-trimethylbenzene; 29, $C_{10;}$ 30, *d*-limonene; 31, nitrobenzene; 32, 2-nonanone; 33, nonanal; 34, C_{11}; 35, decanal; 36, C_{12}.

benzene was analyzed. Breakthrough of compounds 1-3 was also observed in some of these replicate runs.

Values of *fwhm* ranged from 90 (compound 6, C_7) to 640 ms (compound 35, decanal) and, with the exception of the alkanes, were smaller than those obtained with the RTIL stationary phase (see Tables A2.2 and A2.3, Appendix 2); among the polar compounds *fwhm* values were 2-11 times smaller using the OV-215 ^{2}D μcolumn. For the alkanes, the temperature program used in Figure 3.6 led to slightly lower elution temperatures in most cases and, hence, similar or slightly larger (i.e., ≤ 12%) *fwhm* values. The horizontal streak at a ^{2}D t_R value of ~0.5 s is attributed to PDMS bleed from the μTM, which reached maximum intensity at ~10 min into the run. i.e., the point at which the μTM reached its highest T_{max} value of 224 °C.

The separation of mixture components into functional group bands, a so-called "structured chromatogram", is a hallmark of GC × GC. Structure can be seen in Figure 3.6, but the contour plot shown in Figure A2.7 (Appendix 2) illustrates this much more clearly; shaded ellipses were used to delineate different members of a given functional group. An interesting feature is that groups of carbonyl compounds (2-hexanone/hexanal; 2-heptanone/3-heptanone/heptanal; 2-nonanone/nonanal) eluted in a recognizable pattern with respect to each other and with a ^{1}D retention time slightly shorter than that of the n-alkane two carbons longer; the enlargement of one section of the contour plot presented in Figure A2.8 (Appendix 2) shows this pattern, which is also evident in Figure 3.6. More general patterns are evident as well. For example, the group consisting of alkenes and alkanes overlapped slightly with the group of aromatic hydrocarbons, while both were well separated from the aldehydes and ketones, which overlapped considerably due to the short ^{2}D μcolumn used and their similar polarities. The alcohols were not very distinct from either

of these two main groups, falling between the two. Notably, the ^{2}D t_R value for nitrobenzene exceeded that for all other compounds except decanal.

3.4 Conclusions

This inaugural study of μGC × μGC separations with Si-microfabricated separation and modulation components has revealed several important factors affecting the operation and performance of these microsystem components. Effective separations of moderately complex mixtures were possible using relatively short 1st and 2nd dimension μcolumns statically coated with a pair of complementary commercial siloxane polymers and a simple temperature program spanning a very modest temperature range of 50 °C. Modulated peaks had *fwhm* values between 90 and 500 ms and M_N values between 2 and 5 for compounds spanning a 700-fold vapor pressure range. Replicate analyses showed high retention-time fidelity.

The deposition of a trigonal tricationic RTIL onto the walls of the ^{2}D μcolumn was challenging and the technique is still being optimized. Our best efforts thus far yielded films that were apparently much thicker than expected. As a result, although the retention selectivity of the RTIL was quite different from that of the OV-1 ^{1}D μcolumn phase, polar analytes were retained much too strongly. On the basis of tests with a commercial capillary with the same stationary phase, refinements in the pretreatment and deposition techniques should lead to improved retention properties for this RTIL in our ^{2}D μcolumns. Extension of this approach to testing selected other trigonal tricationic RTILs with similar thermal stability is planned, followed by implementation as the stationary phase in the μTM. The expectation that one or more of such RTILs will provide low bleed rates at elevated temperatures in the μTM should allow an increase in T_{max} and a commensurate reduction in the vapor pressures of analytes that can be effectively remobilized.

Tests thus far have been performed with the entire assembly inside a conventional GC oven, utilizing bench-scale components for sample injection and detection. On-going work is directed at placing the μTM outside of the oven or using locally heated, low-thermal-mass columns to decouple the temperatures of the subsystem components. We are also exploring the use of a micromachined preconcentrator-focuser for injection and a microsensor array for detection, as further steps toward an autonomous, field portable μGC × μGC system.

3.5 References

1. Gallego, E.; Air Quality in the 21st Century, Nova Science Publishers, Hauppage, NY, 2010, 139-209.
2. de Gennaro, G.; de Gennaro, L.; Mazzone, A.; Porcelli, F.; Tutino, M.; *Atmos. Env.* 2014, 83, 119-126.
3. Petry, T.; Vitale, D.; Joachim, F.; Smith, B.; Cruse, L.; Mascarenhas, R.; Schneider, S.; Singal, M.; *Reg. Tox. and Pharm.* 2014, 69, 55-70.
4. Terzic, O.; Swahn, I.; Cretu, G.; Palit, M.; Mallard, G.; *J. Chrom. A*, 2012, 1225, 182-192.
5. Peng, C.Y.; Batterman, S.; *J. Environ. Monit.*, 2000, 2, 313-324.
6. Torion Technologies, Inc. http://torion.com/home.html (accessed 6/2014).
7. Hapsite ER Product Information Page http://products.inficon.com/en-us/nav-products/Product/Detail/HAPSITE_ER_Identification_System?path=Products%2Fpg_ChemicalDetection%2F (accessed 6/2014).
8. Defiant Technologies Homepage www.defiant-tech.com/ (accessed 6/2014).
9. APIX Technologies homepage http://apixtechnology.com/ (accessed 6/2014).
10. Terry, S.C.; Jermann, H.; Angel, J.; *IEEE Trans. Electron Dev.*, 1979, 26, 1880-1887.
11. Lu, C.J.; Steinecker, W.; Tian, W.C.; Oborny, M.; Nichols, J.; Agah, M.; Potkay, J.; Chan, H.; Driscoll, J.; Sacks, R.; Wise, K.; Pang, S.; Zellers, E.T.; *Lab Chip*, 2005, 5, 1123-1131.
12. Collin, W.; Serrano, G.; Wright, L.; Chang, H.; Nuñovero, N.; Zellers, E.T.; *Anal. Chem.*, 2014, 86, 655−663.
13. Lewis, P.; Manginell, R.; Adkins, D.; Kottenstette, R.; Wheeler, D.; Sokolowski, S.; Trudell, D.; Bymes, J.; Okandan, M.; Bauer, J.; Manley, R.; Frye-Mason, G.; *IEEE Sensors J.*, 2006, 6, 784-795.
14. Zampolli, S.; Elmi, I.; Mancarella, F.; Betti, P.; Dalcanale, E.; Cardinali, G.C.; Severi, M.; *Sens. Actuators B*, 2009, 141, 322.
15. Jian, R.; Huang, Y.; Lai, S.; Sung, L.; Lu, C.-J; *Micromech. J.*, 2013, 108, 161-167.
16. Shakeel, H.; Agah, M.; *J. Micro Electro Mech. Sys.*, 2013, 22, 62-70.
17. Reddy, K.; Liu, J.; Oo, M.; Fan, X.; *J. Micro Electro Mech. Sys.*, 2013, 22, 1174-1179.
18. Qin, Y.; Gianchandani, Y.; *Proc. Transducers '13,* Barcelona, Spain, June 16-20, 2013, 2755-2758.
19. Ong, R.C.Y.; Marriott, P.; *J. Chromatogr. Sci.*, 2002, 40, 276–291.
20. Dalluge, J.; Beens, J.; Brinkman, U.A.T.; *J. Chromatogr. A*, 2003, 1000, 69–108.
21. Seeley, J.; Micyus, N.; Bandurski, S.; Seeley, S.; McCurry, J.; *Anal. Chem.*, 2007, 79, 1840–1847.
22. Mohler, R.; Prazen, B.; Synovec, R.; *Anal. Chim. Acta*, 2006, 555, 68–74.
23. Phillips, J.; Gaines, R.; Blomberg, J.; van der Wielen, F.; Dimandja, J.M.; Green, V.; Granger, J.; Patterson, D.; Racovalis, L.; de Geus, H.J.; de Boer, J.; Haglund, P.; Lipsky, J.; Sinha, V.; Ledford, E.; *J. High Resolut. Chromatogr.*, 1999, 22, 3–10.
24. Marriott, P.; Kinghorn, R.; *Anal. Chem.*, 1997, 69, 2582–2588.
25. Harynuk J.; Gorecki, T.; *J. Chromatogr. A*, 2003, 1019, 53–63.
26. Libardoni, M.; Fix, C.; Waite, J.; Sacks, R.; *Anal. Methods*, 2010, 2, 936–943.
27. Edwards, M.; Mostafa A.; Górecki, T.; *Anal. Bioanal. Chem.*, 2011, 401, 2335–2349.

28. Blumberg, L.; David, F.; Klee, M.; Sandra, P.; *J. Chromatogr. A*, 2008, 1188, 2–16.
29. Kim, S.J.; Reidy, S.; Block, B.; Wise, K.; Zellers E.T.; Kurabayashi, K.; *Lab Chip*, 2010, 10, 1647–1654.
30. Kim, S.J.; Serrano, G.; Wise, K.; Kurabayashi, K.; Zellers, E.T.; *Anal. Chem.*, 2011, 83, 5556–5562.
31. Serrano, G.; Paul, D.; Kim, S.J.; Kurabayashi, K.; Zellers, E.T.; *Anal. Chem.*, 2012, 84, 16, 6973–6980.
32. Whiting, J.; Fix, C.; Anderson, J.; Staton, A.; Manginell, R.; Wheeler, D.; Myers, E.; Roukes, M.; and Simonson, R.; Transducers 2009, Denver, CO, USA, June 21-25, 2009, 1666-1669.
33. Lewis, A.; Hamilton, J.; Rhodes, C.; Halliday, J.; Bartle, K.; Homewood, P.; Grenfell, R.; Goody, B.; Harlinge, A.; Brewer, P.; Vargha, G.; Milton, M.; *J. Chrom. A*, 2010, 1217, 768–774.
34. Liu, J.; Seo, J.H.; Li, Y.; Chen, D.; Kurabayashi, K.; Fan, X.; *Lab Chip*, 2013, 13, 818.
35. Jian, R.S.; Huang, Y.S.; Lai, S.L.; Sung, L.Y.; Lu, C.J.; *Microchemical J.*, 2013, 108, 161–167.
36. Joshi, M.; Anderson, J.; *RSC Advances*, 2012, 2, 5470–5484.
37. Anderson, J.; Armstrong, D.; *Anal. Chem.* 2005, 77, 6453-6462.
38. Payagala, T.; Zhang, Y.; Wanigasekara, E.; Huang, K.; Breitbach, Z.; Sharma, P.; Sidisky, L.; Armstrong, D.; *Anal. Chem.*, 2009, 81, 160–173.
39. Agah, M.; Potkay, J.; Lambertus, G.; Sacks, R.; Wise, K.; *J. Micro Electro Mech. Sys.*, 2005,14, 1039-1050.
40. Lambertus, G.; Elstro, A.; Sensenig, K.; Potkay, J.; Agah, M.; Scheuering, S.; Wise, K.; Dorman, F.; Sacks, R.; *Anal. Chem.*, 2004, 76, 2629-2637.
41. Reidy, S.; Lambertus, G.; Reece, J.; Sacks, R.; *Anal. Chem.* 2006, 78, 2623-2630
42. Serrano, G.; Reidy, S.; Zellers, E.T.; *Sens. Act. B*, 2009**,** 141, 217-226.
43. de Nijs, R.; Rutten, G.; Franken, J.; Dooper, R.; Rijks, J.; *J. of High Res. Chrom. & Chrom. Comm.*, 1979, 2, 447.
44. Begnaud, F.; Debonneville, C.; Probst, J.-P.; Chaintreau, A.; Morrison, P.; Adcock, J.; Marriot, P.; *J. Sep. Sci.*, 2009, 32, 3144 – 3151.

CHAPTER 4
COMPREHENSIVE TWO-DIMENSIONAL CHROMATOGRAPHIC SEPARATIONS WITH A TEMPERATURE PROGRAMMED MICROFABRICATED THERMAL MODULATOR

4.1 Background and Motivation

Comprehensive two-dimensional gas chromatography (GC×GC) is often the most effective means of separating complex mixtures of volatile and/or semi-volatile organic compounds (S/VOCs), such as the congeners of polychlorinated biphenyls and other polyhalogenated aromatic compounds,[5,6], pesticide residues,[7,8] hydrocarbon fractions in crude oil,[9,10] fatty-acid methyl esters in biodiesel blends,[11] and trace-level VOC biomarkers of disease or metabolism in breath and urine.[12,13]

In GC×GC a first-dimension (^{1}D) column is connected through a thermal or pneumatic modulator to a short second-dimension (^{2}D) column with retention selectivity that differs from that of the ^{1}D column. [10-12] As peaks elute from the ^{1}D column they are parsed by the modulator into segments that are then injected in rapid succession into the ^{2}D column such that no mass is lost. This requires that the ^{2}D separations be completed very rapidly. If operated under the proper conditions then the total peak capacity approaches the product of the peak capacities afforded by each dimension,[13] which should exceed that provided by a one-dimensional separation column of

similar length. In any case, both the resolution and detectability of the eluting peaks can be improved.[12,13] In addition, information about analyte functionality can often be inferred from the structure of the GC×GC contour plot of ^{1}D vs. ^{2}D retention times (t_R), because analytes within the same class usually occupy segregated bands within the plot.[10-12]

Pneumatic GC × GC modulators achieve peak segmentation by injecting pulses of carrier gas or by redirecting flow at regular intervals across peaks eluting from the ^{1}D column,[14-18] Values of full width at half maximum (*fwhm*) as low as 22 ms have been achieved for peaks separated by GC × GC with state-of-the-art pneumatic modulation systems.[15] Thermal modulation (TM) entails alternately trapping ^{1}D peak segments by condensation at low temperature, typically by bathing a short section of the (typically ^{2}D) capillary column in a fluid at cryogenic temperatures, and then remobilizing each peak segment by removing the fluid, and/or applying a jet of hot air, and rapidly raising the temperature for passage of the segment to the ^{2}D column.[19-25] Values of *fwhm* as low as 20 ms[25] have also been reported by use of thermal modulation.

With TM, the trapping efficiency depends critically on the minimum modulator temperature, T_{min}, the rate at which T_{min} is recovered after each heating cycle, and the analyte vapor pressure, p_v. The efficiency of remobilization, in turn, depends on T_{max} and the rate at which T_{max} is achieved after each cooling cycle. For GC×GC separations of analyte mixtures spanning a large p_v range, there is a tradeoff between maintaining T_{min} low enough to avoid breakthrough of relatively high-p_v components and attaining a sufficiently high T_{max} at a sufficiently high rate to minimize broadening of relatively low-p_v components upon re-injection into the ^{2}D column.

The Marriott group addressed this problem effectively with their longitudinally modulated cryogenic system (LMCS), in which a moveable sleeve around a section of capillary column is cooled with a flow of cryogenic fluid.[19] As the sleeve is moved back and forth along a designated

section of one of the columns, peak segments are first immobilized by virtue of the cooling and then remobilized by virtue of the column section returning to oven temperature. By modulating the flow of cryogenic fluid to the sleeve, they were able to gradually increase T_{min} over the course of a temperature programmed separation so as to maintain the difference between T_{min} and the oven temperature constant.[21,23] This resulted in narrower and more symmetric re-injected peaks and reduced consumption of cryogen, while also avoiding breakthrough of the more volatile components of the mixtures analyzed.

Inspired by this approach, we were interested in incorporating a similar feature into the microfabricated thermal modulator (μTM) on which we have reported recently.[26-30] First described in 2010 by Kim and Kurabayashi, this μTM is cryogen-free and requires much less power to operate than conventional TMs.[26,27] It consists of a single, Pyrex-sealed Si microchannel with two thermally isolated spiral sections, or stages, each with independent thin-metal-film heaters. The μTM is mounted on a solid-state thermoelectric cooler (TEC) capable of maintaining T_{min} as low as -35 °C, and it can be heated rapidly to > 250 °C and then cooled again with modulation periods, P_m, as short as 5 s. We have used this device in GC × GC separations with conventional capillary columns,[27,28] and in μGC × μGC separations with microfabricated columns[29] and, most recently, with a polymer-coated, microfabricated optofluidic ring resonator (μOFRR) as the detector.[30]

Recognizing the constraint on the analyte volatility range over which effective μGC × μGC separations could be performed with fixed values of T_{min} and T_{max}, we first explored a passive approach to ramping these μTM temperatures by placing the device inside the GC oven during a temperature programmed separation.[29] As the oven temperature increased, T_{min} increased because of the reduction in heat dissipation from the TEC heat sink and T_{max} also increased because of the improved efficiency of heating the stages at constant applied voltage. This was marginally effective at reducing peak widths for low p_v analytes as compared to isothermal operation, but the maximum oven temperature was

limited to < 100 °C by the temperature sensitivity of the printed circuit boards (PCB) on which the μTM was mounted. Furthermore, despite cross-linking the PDMS stationary phase lining the wall of the μTM channel, loss due to bleed (i.e., decomposition) of the PDMS became notably greater at T_{max} >210 °C, which placed an additional constraint on this operating parameter.

Several commercial stationary phases are now available that have been formulated to exhibit low bleed at temperatures exceeding 350 °C. [31-33] Many of these are siloxane or silylene polymers, which also have low glass transition temperatures. Complex or proprietary procedures and/or high-temperature surface pretreatments render the incorporation of such low-bleed stationary phases into microfabricated devices difficult or impossible Recently, a relatively new class of stationary phase coatings, trigonal tricationic room temperature ionic liquids (RTILs), were shown to exhibit a combination of properties that make them attractive candidates for μTM stationary phases. These include high decomposition temperatures, low melting temperatures, low bleed rates at high temperature, high viscosities, and reasonably good retention of non-polar compounds.[34,35] Syntheses are relatively straightforward and although the surface pretreatment is tricky it does not involve high temperatures.[29,34] RTIL-coated GC columns of this type have been used as the ^{2}D column for GC × GC,[29,36] and were therefore pursued in this study as phases for our μTM.

Here, we describe an extension of our previous studies in which we demonstrate the feasibility of incorporating active temperature programming of the μTM to gradually increase T_{min} and T_{max} values over the course of a GC×GC separation. Toward this end, we used a bench scale GC, commercial ^{1}D (non-polar) and ^{2}D (polar) capillary columns, manual syringe injection, and flame ionization detection (FID). We mounted the μTM assembly on top of the GC oven and used heated interconnects to couple the μTM to the ^{1}D and ^{2}D columns. Although most experiments

used a μTM with a PDMS wall coating, we also performed preliminary tests with a room-temperature ionic liquid (RTIL) μTM wall coating, in an attempt to extend the value of T_{max}. After describing the methodology, separations of a simple mixture of alkanes are presented in which the μTM was cycled between different fixed T_{min} and T_{max} values and then was temperature programmed such that T_{min} and T_{max} were increased over the course of the run. As a practical application, the GC×GC separation of unleaded gasoline is then demonstrated. A trigonal tricationic RTIL coated μTM was then evaluated as a substituted for the PDMS stationary phase. The impact of the results on the design and function of a μTM as a simple replacement for more cumbersome and costly TMs in bench scale GC×GC is assessed.

4.2. Materials and Methods

4.2.1. Materials.

Solvents and individual test compounds were purchased from either Sigma-Aldrich (St. Louis, MO) or Fisher Scientific (Pittsburg, PA) in >98% purity. Unleaded regular gasoline was obtained from a local filling station. PDMS was obtained from Ohio Valley Specialty Chemicals (OV-1, Marietta, OH). The RTIL used, tris[2-(6-aminopropylphosphoniumhexaamido)ethyl]amine tris[bis(trifluoromethylsulfonyl)imide], was taken from an existing supply, which was synthesized by a known method.[29,34]

4.2.2. GC Instrumentation.

A bench scale GC (6890, Agilent Technologies, Palo Alto, CA) equipped with a split/splitless injector (S/SLI) and an FID was used for all experiments. Helium was used as carrier gas. Capillary columns were obtained from Agilent and Restek (Bellefonte, PA) for The PDMS-

coated ^{1}D column was from Agilent (HP-1, 30 m long, 0.250 mm i.d., 0.25 μm film thickness) and the PEG-coated ^{2}D column used for the analysis of gasoline was from Restek (Bellefonte, Pa) (RTX-Wax; 1 m long × 0.100 mm i.d. × 0.10 μm film thickness). For most experiments, the ^{2}D column was replaced with a 0.5-m long segment of uncoated 100-μm id fused silica. For all experiments, the GC oven was operated isothermally at 80 °C. The ^{2}D column was coiled and held snugly against a Kapton® encapsulated resistive-foil heater pad (Omega Engineering, Inc., Stamford, CT) with polyimide tape and wrapped with fiberglass insulation to enable heating above the oven temperature. Manual liquid injections from equal-volume-mixtures of the analytes diluted with CS_2 made using a microliter syringe through the split/splitless injection port of the GC (250 °C). The FID was maintained at 300 °C.

4.2.3. μTM Assembly.

The two-stage μTM has been described previously.[26-30] The Si chip (13×6 mm) contains a deep-reactive-ion-etched (DRIE) Si μchannel with a cross section of 250 (w) × 140 (h) μm arranged in two convolved square-spiral segments, 4.2 cm (stage 1) and 2.8 cm (stage 2) long, separated by a 1.0 mm long segment of straight channel. A 100-μm thick Pyrex cap is anodically bonded to the top surface of the entire chip to seal the μchannel. Four meander-line Ti/Pt resistive heaters are patterned on the Pyrex surface; one above each μTM stage and one above the fluidic ports on the rim of the device. Ti/Pt resistive temperature devices (RTDs) are patterned in between heater traces to measure temperature. Sections (~2 cm) of deactivated fused silica capillary (250 μm i.d., upstream; 100 μm i.d., downstream) inserted into expansion ports on the chip and sealed with epoxy (Hysol 1C, Rocky Hill, CT) provided fluidic interconnections.

The μTM used for most testing was statically coated with PDMS from a solution that also contained 1% (w/w) dicumyl peroxide as the crosslinking agent using a published procedure.[37,38]

The PDMS concentration was adjusted to produce an average (nominal) wall-coating thickness of 0.30 μm. The PDMS in the μTM was cross-linked by heating at 180 °C for 1 h under N_2 using the on-chip stage heaters in order to avoid rupturing the capillary-chip union from expansion of the adhesive. An unavoidable consequence of the method is that the connecting capillaries are coated with un-crosslinked PDMS. The RTIL μTM was also statically coated, following a NaCl surface pretreatment, as described previously.[30] The RTIL concentration was controlled to yield an average nominal wall-coating thickness of 0.07 μm. No crosslinking was performed and this method also resulted in RTIL-coated connecting capillaries.

The coated devices were epoxied, Pyrex side up, to a custom carrier PCB with a hole cut out beneath the device for thermal isolation. Aluminum wire bonds provided electrical connections off-chip. Importantly, all 4 RTDs were calibrated by measuring the resistance of the device at several temperatures using a digital multimeter.

In a departure from our previous μTM mounting schemes,[26-30] a small swatch of thermally conductive silicone material (Sil-Pad, Henkel, Chanhassen, MN) was placed against the heater trace of each stage and held there with a thin film of thermal paste. Two small, square slabs of Si were then coated on both sides with thermal paste and placed on top of each Sil-Pad swatch. The Sil-Pad provided efficient heat transfer while electrically insulating the heater traces from the Si slabs.

This sub-assembly was inverted and mounted such that the Pyrex surface of the μTM was suspended directly above the (TEC) with the top layer of thermal paste in contact with the TEC. A custom machined aluminum press was used to carefully lower this assembly in a slow, controlled manner to prevent undue torque on the device. The TEC was, in turn, mounted to a sink fabricated from stainless steel and copper pieces. Since the device was placed in close proximity to the heated

inlet and FID of the GC it was necessary to arrange a duct with a small fan to bring cool room air to the TEC heat sink. A plastic shroud through which a constant stream of dry air was passed during operation to prevent atmospheric water condensation was placed over the μTM and secured to the peripheral PCB surface.

4.2.4. Heated Interconnects.

Each of the two interconnect heaters was fashioned from a 0.5-cm i.d., 5-cm long section of thin-walled brass tubing bent at a 90 ° angle at one end and soldered to a 0.175-mm i.d., 5-cm long piece of Cu tubing. A base layer of polyimide tape was then applied, followed by a coil of NiCr heater wire, another layer of polyimide tape, and finally an insulating fiberglass sleeve (HiLec 210C, Arcade, NY). A fine wire thermocouple (Omega Engineering, Inc., Stamford, CT) was inserted between the heater and the fiberglass sleeve to monitor the temperature of the assembly. One end of a press-tight capillary connector was inserted into the open end of the brass tube and fitted with a length of deactivated fused silica capillary (250 μm i.d. for the upstream side and 100 μm i.d. for the downstream side) that was threaded through the heater tubing and extended 2-3 cm beyond the Cu end. The other end of the press-tight was used to connect to the inlet or outlet capillary epoxied to the μTM chip. A screening test was performed to confirm that the heaters were effective in minimizing any thermally induced band broadening associated with sample transfer to and from the μTM (see Table A1 and associated text in the Appendix 3).

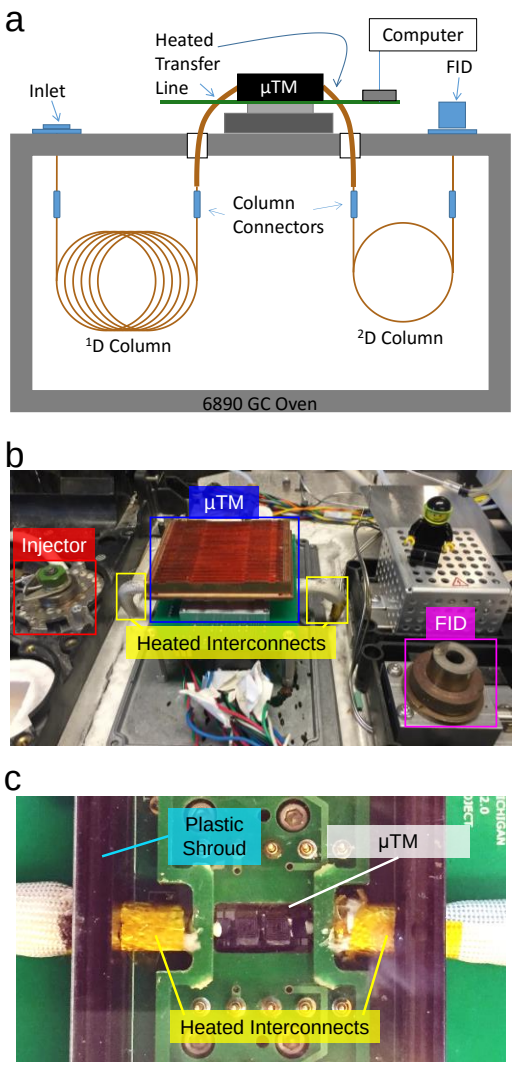

Figure 4.1. a) Diagram of the GC × GC system; b) photograph showing the inverted µTM assembly, the heated interconnects, and the placement on the top of the GC oven (LEGO figure shown for scale; cooling fan stack and heater wiring was removed for clarity); c) View of interconnect heaters at their interface with the µTM chip.

4.2.5. System Integration.

The layout diagram of the GC × GC set-up is shown in Figure 4.1a and a photograph of the µTM assembly mounted on top of the GC is shown in Figure 4.1b. Figure 4.1c provides an enlarged view of the µTM, the proximal brass end of the heated interconnect, as well as part of the plastic shroud over the µTM. The µTM assembly was oriented with the top face of the plastic

shroud facing downward, and positioned ~4 cm from the top of the GC using aluminum standoffs bolts. The Cu sections of the interconnects fit into holes drilled through the top of the GC oven at a central location. The upstream side of the ^{1}D column was connected to the split/splitless inlet of the GC and the downstream side was connected to the μTM through the heated interconnect. The downstream side of the μTM was connected through the other heated interconnect to the ^{2}D column which, in turn, was connected to the downstream FID.

4.2.6 μTM Temperature Control.

Separate programmable power supplies (Model E3647A, Agilent, Palo Alto, CA; Precision 1787B, B&K, Yorba Linda, CA) were used to apply, via solid-state relays, the voltage pulses required to control the temperature of each μTM stage. The circuit diagram is presented in Figure A3.1 of the Appendix 3. A 16-bit multi-functional DAQ card (USB-6212, National Instruments, Austin, TX) was used for signal conditioning and data acquisition. Custom software was written in LabVIEW to drive and monitor the temperature measurements and automatically execute the controlling tasks upon setup of desired set points through a computer graphical user interface (GUI). In order to explore the technical requirements and limitations of the μTM temperature control, a mathematical model was constructed and run inside a control feedback loop to simulate the performance of different controllers against the desired temperature profiles. To account for the temperature vs. voltage non-linearity, thermal responses were measured for different applied voltages. The dynamic components of the responses were fitted to a single normalized exponential curve, while the amplitude components were fitted to a second order polynomial curve. For safety reasons, with the controller architecture determined, most of the parameters of the system were estimated using the developed model, to be only finely tuned with the real device after the system was implemented. The results of this simulation are shown in Figure A3.2 of the Appendix 3.

To achieve T_{max}, a variable width pulse (55 V for the first stage and 50 V for the second stage) was periodically supplied for a very short time, initially 60 ms. By increasing the pulse width over the course of an analysis cycle, precise control of T_{max} was attained. For controlling T_{min}, a proportional-integral-derivative (PID) controller combined with a 200 Hz pulse width modulated (PWM) signal (15 V for the each stage) was found to provide the best control accuracy and temperature stability. In order to allow for a smooth transition from T_{max} to the desired T_{min}, the PID control was turned on ~0.5s after the end of each T_{max} pulse and was suspended before the next T_{max} pulse was applied.

FID data were collected using ChemStation (Agilent Technologies, Palo Alto, CA) and analyzed using OriginPro 9.1 (OriginLab, Northampton, MA). Contour plots were generated using GC Image (Zoex, Houston, TX).

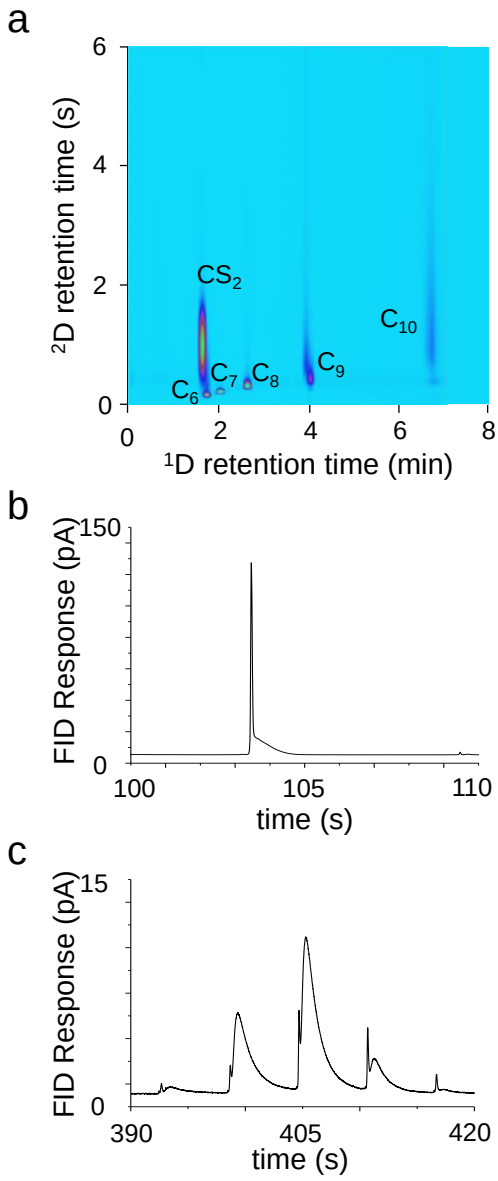

Figure 4.2. Modulated separations with (fixed) T_{min} = -25 °C and T_{max} = 100 °C. a) 2-D contour plot of the separation of C6-C10 n-alkanes; b) Raw chromatogram for C_6 peak; c) Raw chromatogram for C_{10} peak; Chromatographic conditions: 30 m (l) × 0.250 cm (id) × 0.25 µm HP-1 capillary ^{1}D column, 0.3 µm PDMS coated µTM; 0.5 m (l) × 0.170 cm (id) uncoated deactivated fused silica capillary ^{2}D column; GC oven, 80 °C; 2.0 mL/min He carrier gas.

4.3. Results and Discussion

4.3.1. Performance as a function of T_{min} and T_{max}.

Figure 4.2a shows the 2-D contour plot of C_6 - C_{10} with T_{min} and T_{max} fixed at -25 °C and 100 °C, respectively, and with P_m = 6 s. The temperature of the rim heaters of the device (T_{rim}) set to 30 °C, and they increased to 35 °C with the heating of the proximal modulator stage. Without active heating T_{rim} naturally reached a value much closer to T_{min} due to proximity to the TEC, and would have become a significant cold spot in the fluidic pathway. Unfortunately, increasing T_{rim} further led to an increase in T_{min} due to thermal cross-talk within the device. Thus, heating the rims to 30 °C represented a compromise between the two competing factors.

Efficient trapping and remobilization for C_6, C_7 and C_8, is evident from the sharp, well-defined peak profiles obtained, although careful inspection of the plot near C_6 revealed a small degree of breakthrough. Indeed, a characteristic tail in the otherwise sharp modulated C_6 peak is apparent in the raw chromatogram (Figure 4.2b). The peak profiles for C_9 and C_{10} in Figure 4.2a, in contrast, are excessively broad and diffuse due to inefficient remobilization of these less volatile compounds, as expected from the low T_{min} and T_{max} values of the µTM. This can be seen quite clearly in the raw chromatogram for C_{10} (Figure 4.2c) where the *fwhm* values of the modulated peaks are ~1.3s, tailing is quite significant, and peaks do not quite return to baseline between modulations.

Table 4.1. Peak metrics for alkane chromatograms.[a]

Cmpd.	Cold			Hot			Ramped		
	fwhm (ms)	height (pA)	area (pA-s)	*fwhm* (ms)	height (pA)	area (pA-s)	*fwhm* (ms)	height (pA)	area (pA-s)
C_6	52	120	13	610	24	16	50	280	23
C_7	44	270	13	1200	11	15	39	510	22
C_8	81	170	13	35	390	16	55	400	24
C_9	560	31	18	44	340	17	79	280	24
C_{10}	1300	7	22	67	170	18	94	190	25

[a]Peak heights and peak *fwhm* values calculated for largest modulated peak. Peak area calculated as the sum of the areas of all modulated peaks.

Under these operating conditions, the modulation number, M_N, was 1 for C_6-C_8 and it was 2 and 4 for C_9 and C_{10}, respectively. Table 4.1 presents the height and *fwhm* of the largest modulated peak for each compound in Figure 4.2a. As shown, the C_6-C_8 peaks were significantly narrower and taller than those for C_9 and C_{10}, consistent with the peak contours. The slightly larger *fwhm* for C_6, relative to that for C_7, is ascribed to partial breakthrough of C_6, which has been observed previously with this µTM design under similar operating conditions.[26,27] That notwithstanding, the results indicate that the fixed, low-temperature condition is not effective for compounds less volatile than C_8 (p_v = 1.9 kPa). For reference, Table 4.1 also presents the summed area under all modulated peaks for each compound, and shows the gradual increase in sensitivity with carbon number expected for an FID

Figure 4.3a shows the contour plot of the same n-alkanes with the µTM T_{min} and T_{max} values fixed at 0 °C and 220 °C, respectively. For this series, T_{rim} was set at 50 °C, and the T_{rim} values were observed to increase to ~55 °C at the inlet or outlet with the periodic heating of the adjacent µTM stage. The broad ^{2}D peak contours for C_6 and C_7 in Figure 4.3a are indicative of complete modulator breakthrough. The peaks eluted at slightly shorter t_R values than expected along the ^{1}D

axis and at longer t_R values than expected along the ^{2}D axis; the latter being completely unrelated to their retention on the uncoated ^{2}D column.

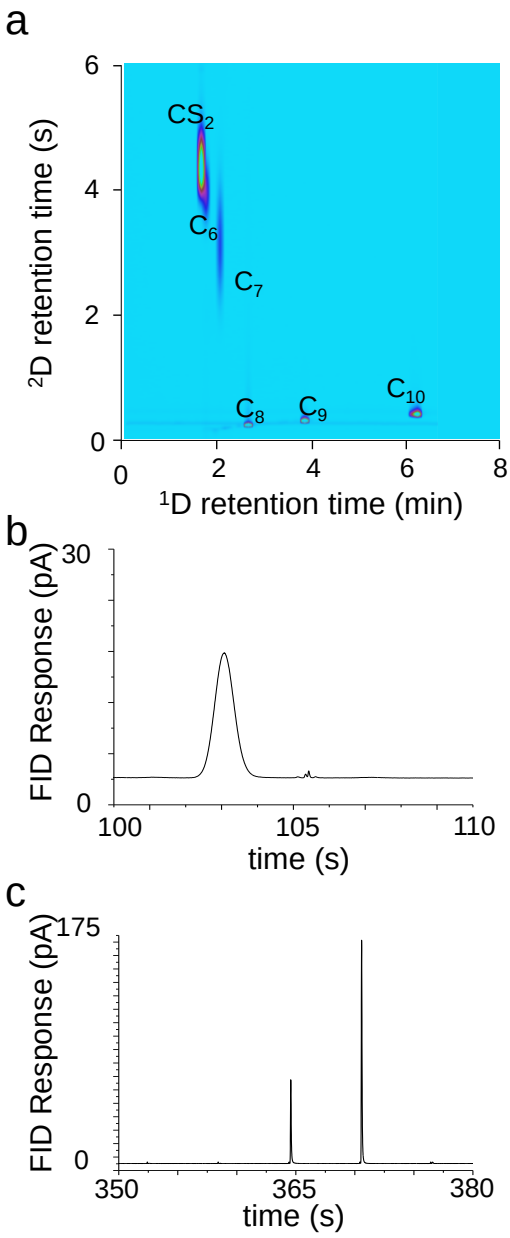

Figure 4.3. Modulated separations with (fixed) T_{min} = 0 °C and T_{max} = 220 °C. a) Alkane contour plot for fixed T_{min} = 0 °C and T_{max} = 220 °C; b) Raw chromatogram for C_6 peak; c) Raw chromatogram for C_{10} peak; Chromatographic conditions: 30 m (l) × 0.250 cm (id) × 0.25 µm HP-1 capillary ^{1}D column, 0.3 µm PDMS coated µTM; 0.5 m (l) × 0.170 cm (id) uncoated deactivated fused silica capillary ^{2}D column; GC oven, 80 °C; 2.0 mL/min He carrier gas.

The short, broad modulated peak in the raw chromatogram for C_6 in Figure 4.3b reflects the failure of the μTM to trap this compound (or C_7). The sharper profiles for C_8, C_9, and C_{10} in Figure 4.3a reflect their efficient trapping and re-injection for this range of modulator temperatures. Comparing the raw chromatogram for C_{10} in Figure 4.3c to that in Figure 4.2c further illustrates this point. Under these μTM operating conditions, the M_N values for C_6-C_9 did not change much from those under the preceding conditions, but the M_N value for C_{10} decreased from 4 to 2, due to the more efficient re-mobilization. The ^1D t_R values for C_6-C_8 did not change significantly, despite the breakthrough of C_6 and C_7, but the t_R value of C_9 decreased by about ~5 s and that for C_{10} decreased by nearly 30 s, again, due to the improvement in re-mobilization of these less volatile analytes from the μTM under these conditions. In the low-temperature case, it is likely that the low-p_v analytes such as C_{10} are not re-mobilized rapidly enough to not be re-trapped before eluting from the μTM. This accounts for the longer C_{10} t_R value.

Consistent with the chromatograms in Figure 4.3, Table 4.1 shows that the *fwhm* values for C_6 and C_7 peaks were 1-2 orders of magnitude larger, and their heights were an order of magnitude smaller, than those of the C_8-C_{10} peaks. Peak areas were comparable to those under the previous operating conditions. Note also the evidence of stationary phase bleed in Figure 3a that was absent from Figure 4.2a, i.e., the continuous horizontal line near the baseline of the contour plot.

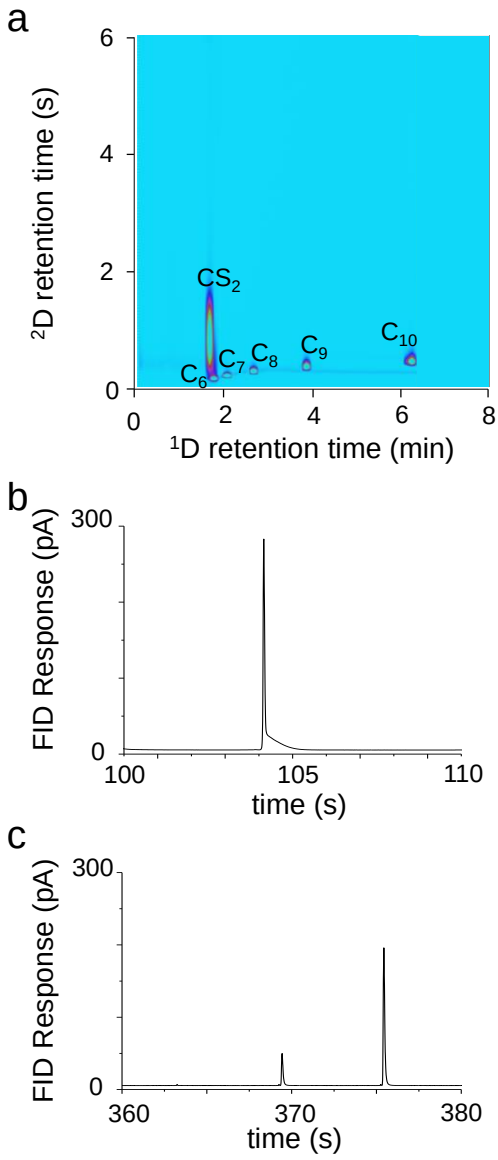

Figure 4.4. Modulated separations with ramped T_{min} and T_{max}. a) 2-D contour plot for the temperature programmed µTM using the temperature profile shown in Figure 4.5; b) Raw chromatogram for C_6 peak; c) Raw chromatogram for C_{10} peak; Chromatographic conditions: 30 m (l) × 0.250 cm (id) × 0.25 µm HP-1 capillary ^{1}D column, 0.3 µm PDMS coated µTM; 0.5 m (l) × 0.170 cm (id) uncoated deactivated fused silica capillary ^{2}D column; GC oven, 80 °C; 2.0 mL/min He carrier gas.

Figure 4.4a shows the 2-D contour plot obtained with the µTM stage temperatures programmed as shown in Figure 4.5. Initially, T_{min} and T_{max} were set at –25 and 100 °C, respectively, and held at these values for the first two minutes of the run. Then, T_{min} was increased

to -10 °C and T_{max} was increased to 150 °C linearly over the next two minutes. Finally, T_{min} was increased to 0 °C and T_{max} to 220 °C over the next six minutes,–at which point the run was concluded. Figure 4.4 only shows 8 minutes of this separation, as all alkanes eluted in this time period. The values of T_{rim} were not dynamically controlled, although they did increase with each successive change in T_{min} and T_{max}. Initially set at ~45 °C, T_{rim} increased to ~50 °C over the course of the 10-min separation. Figure 4.5 presents the thermal profile of the µTM. The programmed temperatures (yellow lines) coincide with the actual temperatures achieved (white and red lines) quite closely. Target and actual T_{max} values differed by less than ~5 °C and can be attributed to limitations on the data sampling rate of the RTDs; at 200 Hz, peak values of the heating pulses (60-220 ms) may not be captured at the heating rate, which ranges from 1,000 to 2,000 °C/s.

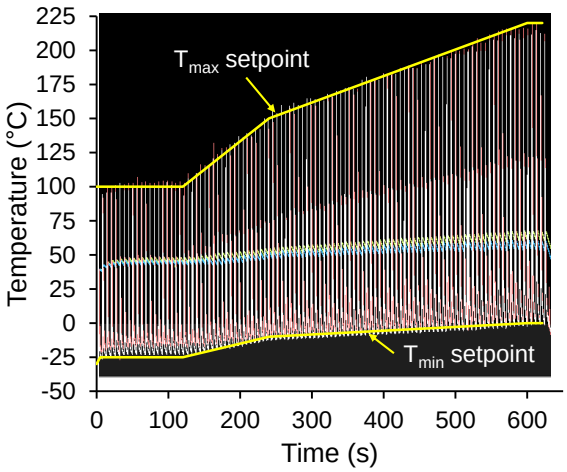

Figure 4.5. Programmed temperatures of T_{max} of µTM (dashed yellow) and T_{min} of µTM (solid yellow) overlaid on actual temperature profile achieved by the µTM. The blue line represents the temperature of the µTM rims. White and red lines represent the individual µTM stages, which reached the desired T_{min} and T_{max} with each modulation.

Figure 4.4a shows sharp peak profiles for all of the analytes. The problems with re-mobilization of C9 and C10 under fixed, low-temperature modulation conditions, and the problems with massive breakthrough of C_6 and C_7 under fixed, higher temperature modulation conditions were eliminated by ramping the µTM temperature. There was still evidence of partial

breakthrough of C_6 (Figure 4.4b), though no more than observed in the fixed, low temperature case (Figure 4.2b). The raw chromatogram of the modulated C_{10} peak in Figure 4.4c is similar to that in Figure 3c with respect to M_N, peak width, and peak height, despite both T_{min} and T_{max} being lower when C_{10} eluted than they were under the fixed, higher-temperature case. Stationary phase bleed becomes more pronounced toward the end of the separation, as the T_{max} approached 220 °C.

As shown in Table 4.1, the *fwhm* values for C_6 and C_7 were similar to those for the fixed, lower-temperature case, while those for C_8-C_{10} were 40-80% larger undoubtedly due to T_{min} and T_{max} values being lower than those in the fixed, higher-temperature case when these peaks eluted. Regardless, all *fwhm* values were <95 ms, which indicates very good overall performance. The heights of the largest modulated peaks were very similar to (or larger than) those obtained under the respective fixed-temperature cases where efficient capture and re-mobilization were obtained. The peak areas were significantly higher than in the fixed-temperature cases owing, apparently, to an error in injection volume. Taking this into account, (that is, adjusting for the difference in areas) peak heights for C_6 and C_7 in the ramped case are very similar to the cold-temperature case. C_8-C_{10} each have a slightly larger *fwhm* value than in the best fixed-temperature case, which explains the (area adjusted) taller peaks observed in the temperature-ramped case.

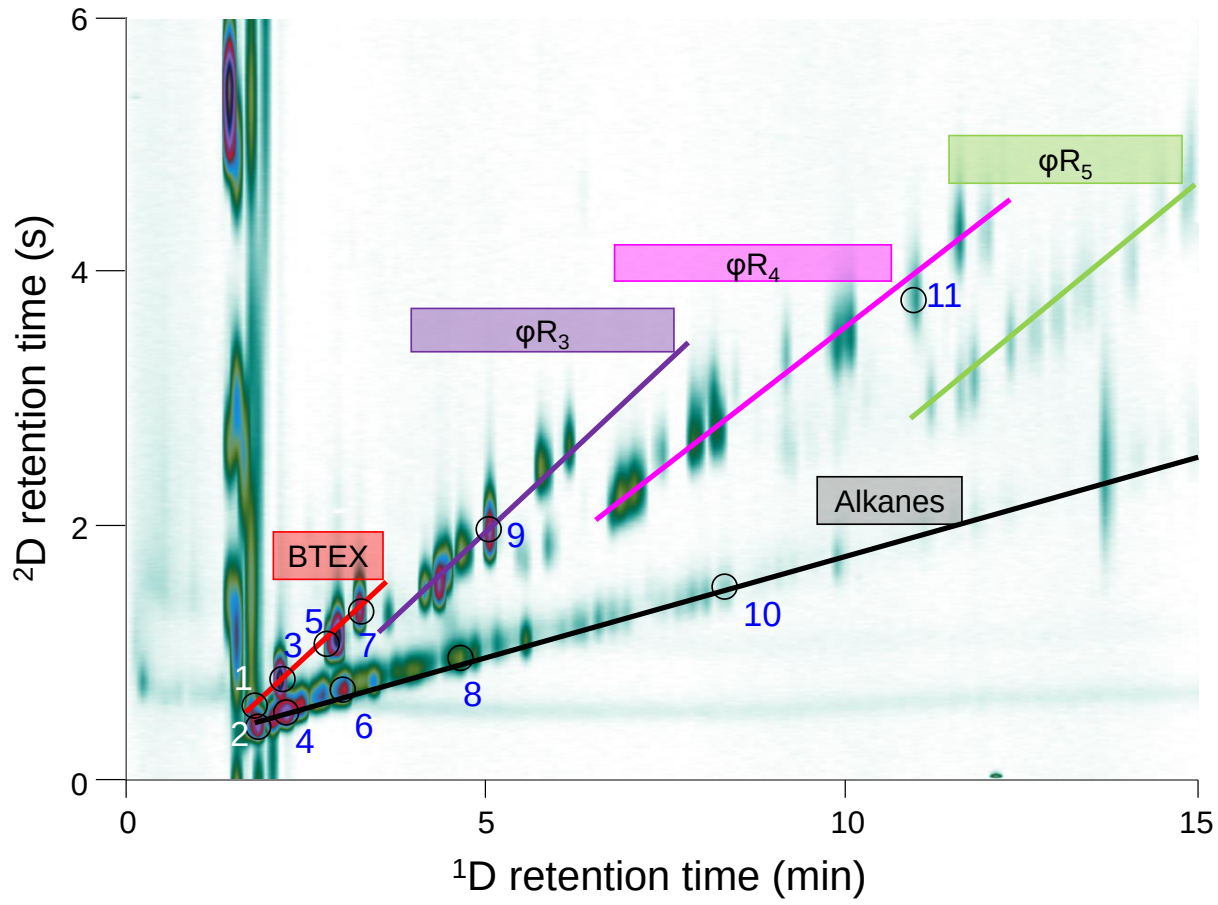

Figure 4.6. Gasoline sample analyzed using the temperature programmed µTM. Colored lines represent compound class bands: black, alkanes; red, BTEX; purple, trisubstituted aromatics; magenta, tetrasubstituted aromatics (unconfirmed); green, pentasubstituted aromatics (unconfirmed). Compounds identified by retention time matching are numbered: 1, benzene; 2, C7; 3, toluene; 4, C8; 5, ethylbenzene; 6, C9; 7, *m*-xylene; 8, C10; 9, 1,2,3-trimethylbenzene; 10, C11; 11, naphthalene. Conditions are the same as Figure 3 except the 2D column was 1 m (l) × 0.100 cm (id) × 0.1 µm (d_f) RTX-Wax capillary column heated to 90 °C.

4.3.2 Gasoline Separation with Temperature-Programmed µTM.

To further demonstrate the utility of temperature programming the µTM, a sample of unleaded gasoline was analyzed. The uncoated capillary used in lieu of a ^{2}D column in the preceding experiments was replaced with the 1-m long PEG ^{2}D column. Conditions identical to those for Figure 4.4 were established except that the separation was extended by 5 min with the

μTM T_{min} and T_{max} values were held at 0 and 210 °C, respectively, over this additional time period (note: T_{max} was not increased further to minimize bleed of the PDMS from the μTM). The ^{1}D and ^{2}D columns were held at 80 and 90 °C throughout the separation.

Figure 4.6 shows the 2-D contour plot of the gasoline sample. There are more than 100 distinguishable peaks apparent within the 15-min time period examined. Although there were likely to be additional peaks eluting at longer times,[39] no effort was made to capture or identify them, in part, because at the relatively low isothermal column temperatures employed any peaks from the small fraction of compounds in this low volatility range in gasoline would likely have been broad and difficult to detect. Temperature programming the columns would have required revising the temperature program for the μTM as well, which was deemed to be beyond the scope of this initial proof-of-concept study

Figure 4.6 displays the type of structure that is the hallmark of GC × GC. Colored lines have been superimposed to assist in visualizing the strata. Retention times and *fwhm* values for the selected compounds that were identified by retention time matching with known standards analyzed separately under the same conditions are shown in Table 4.2. The relative locations of the designated strata as well as the specific compounds in Figure 4.6 are quite similar to those reported by Pedroso et al. for GC × GC separation of gasoline with similar ^{1}D and ^{2}D column lengths and stationary phases (see Figure 4.1a in ref. 39). On the basis of our own retention time matching experiments and the assignments reported in that study, we have assigned functional group classifications to all of the bands in Figure 4.6.

Table 4.2. Peak metrics for GC x GC contour plot of unleaded regular gasoline in Figure 4.6.[a]

Compound	$^1D\ t_R$ (min)	$^2D\ t_R$ (s)	*fwhm* (ms)
benzene	1.7	0.46	300[b]
C_7	1.8	0.43	140
toluene	2.1	0.79	170
C_8	2.2	0.54	150
ethylbenzene	3.0	1.08	200
C_9	3.0	0.72	170
m-xylene	3.3	1.35	220
C_{10}	4.6	0.96	190
1,2,3-TMB	5.1	1.08	270
C_{11}	8.4	1.51	270
naphthalene	11.0	3.81	460

[a]Peak height values calculated for largest modulated peak. [b]Partial coelution with an unidentified, untrapped compound renders this *fwhm* value larger than expected.

Other features of this chromatogram, such as the broad peak at t_R = 14 min straddling the alkane stratum, and unmodulated peaks eluting before benzene, could not be identified. Since the gasoline sample contained up to 15% ethanol, we speculate that it elutes near top left corner of the separation space, again, similar to the results observed by Pedroso et al.

In comparing results in Figure 4.6 to those in Figure 4a for those compounds common to both analyses, it is seen that the *fwhm* values for the former are much larger due to the addition of a 1-m coated ^2D column compared to operation with 0.5-m uncoated fused silica capillary. Still, *fwhm* values remained < 500 ms even for analytes with vapor pressures estimated to be < 0.01 kPa. This is more than sufficient to produce high quality GC × GC separations even with unoptimized ^1D separation conditions. Partial coelution of benzene with another component produced a *fwhm*

value significantly higher than for the neighboring peaks. Consistent with expectations, among the alkanes and aromatic compounds in Table 4.2 with similar $^{1}D\ t_R$ values, those with larger $^{2}D\ t_R$ values were broader.

4.3.3 RTIL Stationary Phase.

In order to access a higher temperature range for the μTM, the problem of stationary phase bleed must be solved. We attempted to do this using a RTIL stationary phase coating in the μTM, which has been shown to be more thermally stable than PDMS.[34] Indeed, under conditions similar to those used in Figure 3 (which showed significant bleed), no bleed is evident when using the RTIL coated μTM.

The trapping efficiency of the RTIL coated μTM was evaluated by analyzing samples containing homologous series of alkanes (C_7-C_{10}), aldehydes (C_5-C_8) and aromatics (benzene, toluene, ethylbenzene, and 1,2,3-trimethylbenzene) at two different levels of injection mass: 1 ng and 50 ng of each compound The results for the set of n-alkanes are shown in Figure 4.7. Those for the other sets of compounds are shown in Figure A3.3 in Appendix 3. Immediately evident is the breakthrough of C_7-C_9 in Figure 4.7a obtained at the higher injection mass level. This was a common result for the other compound classes as well. For the aromatic compounds at 50 ng, breakthrough was evident for all compounds except 1,2,3-TMB and octanal. This is indicative of insufficient retention of the lighter, which was unexpected since RTIL columns have regularly been used in commercial systems.[38] This was investigated with the 1 ng injections shown in Figure 4.7b for the alkane set and Figure A3.3 of Appendix 3 for the all three sets. At the lower injection mass level, breakthrough was still observed for C_7-C_9 alkanes; it was significant for C_7 and moderate for C_8 and C_9. Similar trends were observed among the compounds in the other sets, where some degree of breakthrough was apparent for every compound except 1,2,3-TMB and

octanal. Similar results were obtained with a thicker stationary phase coating in the µTM, indicating that the lack of capacity is not entirely due to the phase ratio.

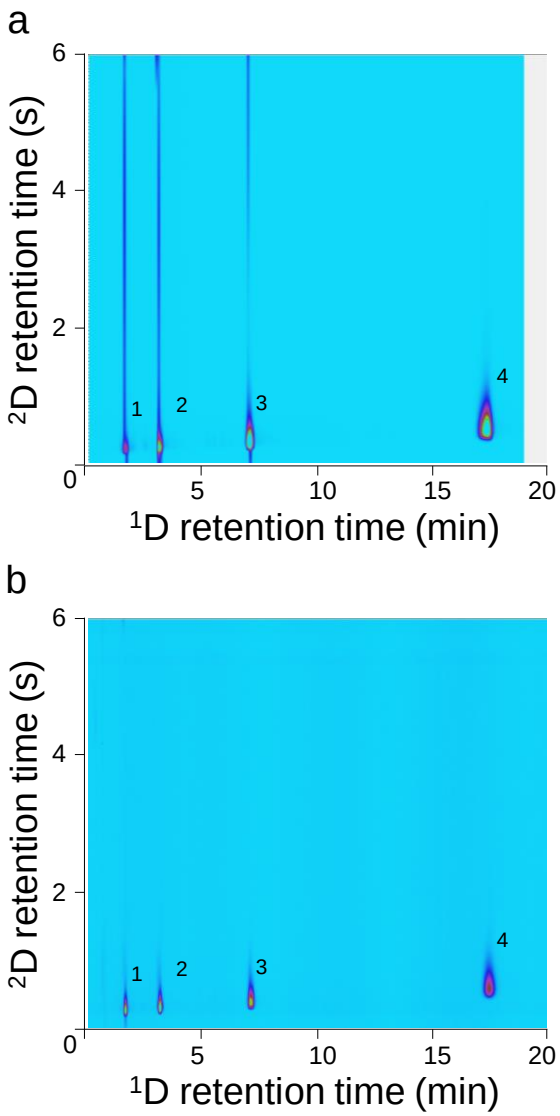

Figure 4.7. Alkane separation using RTIL coated µTM. Conditions: µTM, 0.07 µm thick RTIL; T_{min} = -30 °C; T_{max} = 230 °C; P_m = 6 s; ^{1}D column, 6 m PDMS 0.2µm film thickness; ^{2}D = uncoated fused silica capillary; FID detection. Panel a) 50 ng injection; b) 1 ng injection.

4.4 Conclusions

This study showed the adaptation of a conventional benchtop GC to a fully functional GC × GC instrument that uses a µTM. This type of modulator requires no additional consumables

beyond those required for conventional GC operation, and it is relatively simple to operate. The effectiveness of computer controlled temperature programming was demonstrated, which represents an important step towards the utilization of this technology for the analysis of very complex mixtures. The challenge of conveying analyte outside the heated zone of the GC oven for modulation was overcome with the use of small, simple interconnect heaters which were very effective at reducing wall adsorption in the intervening capillary. Two different temperature control schemes were implemented to effect the desired modulation temperature ramping; PID for minimum temperature control during the times between modulator pulses, and PWM for control of the maximum temperature of the modulation event. These advances allowed for the GC × GC separation of the components of unleaded gasoline, which is the most complex mixture separation yet demonstrated using a μTM device. Temperature programming of 1D and 2D separation columns has the potential for yielding further increases in complexity of the sample.

The mixed results using the RTIL coated μTM indicate the need for further exploration of this class of stationary phases in this application. While the lack of bleed is very promising and is among the more compelling reasons to consider RTILs for this purpose, the lack of trapping observed is disappointing.

4.5 References

1. Dimitriou-Christidis, P.; Bonvin, A.; Samanipour, S.; Hollender, J.; Rutler, R.; Westphale, J.; Gros, J.; Arey, J., *Environ. Sci. Technol.*, 49, 2015, 7914-7925.
2. Prebihalo, S.; Brockman, A.; Cochran, J.; Dorman, F., *J. Chrom. A*, 1419, 2015, 109-115.
3. Nolvachai, Y.; Kulsing, C.; Marriot, P., *Crit. Rev. Environ. Sci. Technol.*, 45, 2015, 2135-2173.
4. Weng, N.; Wan, S.; Wang, H.; Zhang, S.; Zhu, G.; Liu, J.; Cai, D.; Yang, Y., *J. Chrom. A.*, 1398, 2015, 94-107.
5. Duhamel, C.; Cardinael, P.; Peulon-Agasse, V.; Firor, R.; Pascaud, L.; Semard-Jousset, G.; Giusti, P.; Livadaris, V., *J. Chrom. A.*, 1387, 2015, 95-103.
6. Kanateva, A.; Kurganov, A.; Yakubenko, E., "*Petroleum Chemistry*, 54, 2014, 459-465.
7. Seeley, J.; Seeley, K.; Libby, E.; McCurry, J., *J. Chrom. Sci.*, 45, 2007, 650-656.
8. Ma, H.; Li, X.; Chen, J.; Wang, H.; Cheng, T.; Chen, K.; Xu, S.; *Anal. Methods*, 6, 2014, 6841-6849.
9. Weinert, C.; Egert, B.; Kulling, S.; *J. Chrom. A.*, 1405, 2015, 156-167.
10. Eiserbeck, C.; Nelson, R.; Reddy, C.; Grice, K.; "Advances in Comprehensive Two-Dimensional Gas Chromatography (GC × GC)" in Principles and Practice of Analytical Techniques in Geosciences Edited by K. Glice, Royal Society of Chemistry, 2015, 324-365.
11. Edwards, M.; Mostafa, A.; Gorecki, T.; *Anal. Bioanal. Chem.*, 401, 2011, 2335-2349
12. Dimandja, J., *Anal. Chem.*, 76, 2004, 167A-174A
13. Blumberg, L.; David, F.; Klee, M.; Sandra, P.; *J. Chromatogr. A*, 2008, 1188, 2–16.
14. Adachour, M.; Beens, J.; Vreuls, R.; Brinkman, U.; *Trends in Anal. Chem.*, 25, 540-553, 2006.
15. Mohler, R.; Prazen, B.; Synovec, R.; *Anal. Chim. Acta*, 2006, 555, 68–74.
16. Seeley, J.; Micyus, N.; Bandurski, S.; Seeley, S.; McCurry, J.; *Anal. Chem.*, 2007, 79, 1840–1847.
17. Poliak, M.; Kochman, M.; Amirav, A.; *J. Chrom. A.*, 1186, 2008, 189-195.
18. Tranchida, P.; Salivo, S.; Franchina, F.; Mondello, L.; *Anal. Chem.* 87, 2015, 2925-2930.
19. Marriot, P.; Kinghorn, R.; *Anal. Chem.*, 69, 1997, 2582-2588.
20. Phillips, J.; Gaines, R.; Blomberg, J.; van der Wielen, F.; Dimandja, J.M.; Green, V.; Granger, J.; Patterson, D.; Racovalis, L.; de Geus, H.J.; de Boer, J.; Haglund, P.; Lipsky, J.; Sinha, V.; Ledford, E.; *J. High Resolut. Chromatogr.*, 1999, 22, 3–10.
21. Haglund, P.; Harju, M.; Danielsson, C.; Marriot, P.; *J. Chrom. A.* 962, 2002, 127-134.
22. Harynuk J.; Gorecki, T.; *J. Chromatogr. A*, 2003, 1019, 53–63.
23. Begnaud, F.; Debonneville, C.; Probst, J.-P.; Chaintreau, A.; Morrison, P.; Adcock, J.; Marriot, P.; *J. Sep. Sci.*, 32, 2009, 3144-3151.
24. Libardoni, M.; Fix, C.; Waite, J.; Sacks, R.; *Anal. Methods*, 2010, 2, 936–943.
25. Fitz, B.; Wilson, R.; Parsons, B.; Hoggard, J.; Synovec, R.; *J. Chrom. A.*, 1266, 2012, 116-123.
26. Kim, S.J.; Reidy, S.; Block, B.; Wise, K.; Zellers, E.T.; Kurabayashi, K.; *Lab Chip*, 10, 2010, 1647-1654.
27. Kim, S.J.; Serrano, G.; Wise, K.; Kurabayashi, K.; Zellers, E.T.; *Anal. Chem.*, 83, 2011, 5556-5562.

28. Serrano, G.; Paul, D.; Kim, S.J.; Kurabayashi, K.; Zellers, E.T., *Anal. Chem.*, 84, 2012, 6973-6980.
29. Collin, W.R.; Bondy, A.; Paul, D.; Kurabayashi, K.; Zellers, E.T., *Anal. Chem.*, 87, 2015, 1630-1637.
30. Collin, W.R.; Scholten, K; Fan, X.; Paul, D.; Kurabayashi, K.; Zellers, E.T., *Analyst*, 141, 2015, 261-269.
31. Sigma-Aldrich Product Information Page http://www.sigmaaldrich.com/analytical-chromatography/gas-chromatography/columns/slb-gc-capillary/story.html (accessed 1-7-16)
32. Agilent Webinar Transcript http://www.agilent.com/cs/library/eseminars/public/Low%20Bleed%20Stationary%20Phase%20for%20GC.pdf (accessed 1-7-16)
33. Restek Product Information Page http://www.restek.com/Landing-Pages/Content/gen_B004 (accessed 1-7-16)
34. Payagala, T.; Zhang, Y.; Wanigasekara, E.; Huang, K.; Breitbach, Z.; Sharma, P.; Sidisky, L.; Armstrong, D.; *Anal. Chem.*, 2009, 81, 160–173.
35. Sharma, P.; Payagala, T.; WAnigasekara, E.; Wijeratne, A.; Huang, J.; Armstrong, D., *Chem. Mater.*, 2008, 20, 4182-4184.
36. Joshi, M.; Anderson, J.; *RSC Advances,* 2012, 2, 5470–5484.39
37. Reidy, S.; Lambertus, G.; Reece, J.; Sacks, R.; *Anal. Chem.* 2006, 78, 2623-2630.
38. Serrano, G.; Reidy, S.; Zellers, E.T.; *Sens. Act. B,* 2009, 141, 217-226.
39. Pedroso, M.P.; de Godoy, L.A.F.; Ferreira, E.C.; Poppi, R.J.; Augusto, F., *J. Chrom. A,* 2008, 1201, 176-182.
40. Delmonte, P.; Fardin-Kia, A.; Rader, J.; *Anal. Chem.*, 85, 2012, 1517-1524.

CHAPTER 5

POLYMER-COATED MICRO-OPTOFLUIDIC RING RESONATOR DETECTOR FOR A COMPREHENSIVE TWO-DIMENSIONAL GAS CHROMATOGRAPHIC MICROSYSTEM: μGC × μGC– μOFRR

Adapted from W.R. Collin et al., "Polymer-Coated Micro-Optofluidic Ring Resonator Detector for a Comprehensive Two-Dimensional Gas Chromatographic Microsystem: μGC × μGC–μOFRR," *Analyst,* 2015, Accepted Manuscript, DOI: 10.1039/C5AN01570G with permission from The Royal Society of Chemistry.

5.1 Background and Motivation

Research over the past decade or so on Si-microfabricated gas chromatographic microsystems (μGC) has led to several improvements in design and operation that have moved us closer to low-cost, low-power instrumentation capable of analyzing the components of airborne volatile organic compound (VOC) mixtures at low concentrations in near-real time.[1-10] Such air monitoring capabilities are not possible with stand-alone sensors or sensor arrays.[11] Unfortunately, the maximum lengths and minimum diameters of μGC separation columns are subject to practical constraints which, in turn, limit the complexity of VOC mixtures that can be reliably analyzed by such microsystems.

Microscale comprehensive two-dimensional gas chromatography (μGC × μGC), implemented using Si and/or glass micromachined components, represents one promising approach to overcome these limitations. As in bench scale GC × GC systems,[12,13] in μGC × μGC a first-dimension (^{1}D) μcolumn is connected through a (micro-scale) thermal or pneumatic modulator to a shorter second-dimension (^{2}D) μcolumn that has retention properties differing from those of the ^{1}D μcolumn. As the peak from each mixture component elutes from the ^{1}D μcolumn it is re-injected piecewise into the ^{2}D μcolumn at a rate high enough to maintain the ^{1}D elution sequence. Ideally, then, the peak capacity is increased significantly over that provided by a one-dimensional separation column of similar length, and both the resolution and detectability of the eluting peaks can be improved.[12,13]

Thermal modulation, which offers certain advantages over pneumatic modulation, entails continuous, rapid thermal cycling of the mid-point modulation device during the course of an analysis: cooling to trap peak segments from the ^{1}D μcolumn and then heating to remobilize/reinject them into the ^{2}D μcolum.[14,15] Kim et al. developed the first microfabricated thermal modulator (μTM).[16] It contained a series of two spiral, Pyrex-capped, deep-reactive-ion-etched (DRIE) Si microchannel sections (stages) with independent thin-metal-film heaters. Mounted just above a compact stack of thermoelectric coolers (TEC), this μTM could be heated to ≥ 250 °C and then cooled to ≤ –20 °C in rapid succession. By virtue of the focusing effect exerted on the eluting analytes, the modulated peak segments could be compressed, leading to commensurate improvements in resolution and detectability.

Recently, this type of device was used to perform GC × GC separations with conventional capillary columns[17,18] and μGC × μGC separations with microfabricated ^{1}D and ^{2}D columns,[19] but in all cases using a conventional, bench-scale flame ionization detector (FID). Due to nature of the

modulation process, the short length of the ^{2}D μcolumn, and the relatively high linear velocity of the carrier gas, the peaks generated at the outlet of the separation module can be very narrow. Therefore, a detector with a low dead volume and short response time, such as an FID, is required. For ultimate application in field or clinical settings, a more compact, portable detector is needed.

Whiting, et al., were the first to describe a GC × GC separation using microfabricated separation and detection components.[20] High-aspect-ratio DRIE-Si separation columns were used with a conventional high-pressure, pneumatic modulation system to separate a 4-VOC mixture in just a few seconds; an array of polymer coated cantilever sensors was used for detection. Other multi-dimensional separation subsystems made using microfabricated columns and various sample manipulation and sensing technologies have been reported recently that embody alternative approaches to enhancing peak capacity in GC microsystems.[21,22] However, there has yet to be a report of a μGC × μGC system in which all critical components were microfabricated.

We recently introduced the microfabricated optofluidic ring resonator (μOFRR) sensor and demonstrated it as a μGC detector.[23] It was modeled after the OFRR sensors developed by Fan et al. from thinned glass capillaries.[24] The μOFRR sensing structure consists of a hollow, wide-bore, vertical SiO_x cylinder with an expanded midsection grown, and subsequently etched free, from a Si mold. Resonant whispering gallery modes (WGM) are generated in the cylinder wall by coupling to a tunable laser with an optical fiber taper placed beside the μOFRR cylinder. The evanescent field of the WGM extends into the interior of the cylinder, and a shift in resonant wavelength, λ_{WGM}, will occur from changes in the optical properties (e.g., the refractive index, *RI*) at the inner surface according to the following expression:[24] $\Delta\lambda_{WGM} = 2\pi r \Delta n_{eff}/m$, where r is the radius of the μOFRR, m is an integer specifying the mode number, and n_{eff} is the effective *RI* that takes into account the mode distribution in the air, wall, surface layer and the interior fluid.

Transient shifts in λ_{WGM} result from swelling and *RI* changes of a thin polymer film lining the cylinder due to reversible sorption of vapor passing through the cylinder. Initial tests of a PDMS-coated μOFRR connected downstream from a single μGC column showed remarkably fast responses and low detection limits under typical operating conditions.[23] These results suggested that this device might have sufficiently high sensitivity and sufficiently rapid response times to serve as the detector for μGC × μGC analyses.

Here, we report on preliminary performance characterization tests of a μGC × μGC separation module with a polymer-coated μOFRR sensor installed as the detector. Figure 3.1 shows a block diagram of the analytical components *all of which were microfabricated*. After describing the materials and methods employed, results are presented from a series of μGC × μGC−μOFRR analyses of three VOC mixtures under different isothermal conditions. The factors affecting the responses from the μOFRR sensor are explored. The inherent tradeoff between resolution and sensitivity attributable to the volatility of the analytes is highlighted, and it is shown that adequately rapid responses are achievable for most analytes. The prospects of using μOFRRs and μOFRR arrays in portable μGC × μGC instrumentation are considered.

5.2 Experimental Methods

5.2.1 Materials

The test compounds 1,4-dioxane (DOX), 4-methyl-2-pentanone (PON), toluene (TOL), cyclopentanone (CPN), hexanal (HAL), *n*-heptane (C_7), *n*-octane (C_8), *n*-nonane (C_9), *n*-decane (C_{10}), ethylbenzene (ETB), *m*-xylene (XYL), and cumene (CUM) as well as all other solvents used were >98% pure (Sigma-Aldrich, Milwaukee, WI) and used without further purification. The PDMS (OV-1) and poly(trifluoropropylmethyl)siloxane (PTFPMS, OV-215) polymers used as

stationary phases or sensor coatings were obtained from Ohio Valley Specialty Chemicals (Marietta, OH).

5.2.2 Device Descriptions and Preparations

The μTM fabrication, mounting configuration, and operation have been described previously.[16-19] Briefly, the Si chip (1.3 × 0.6 cm; Figure 3.1) contains a Pyrex-sealed DRIE-Si μchannel (250 × 140 μm cross section) arranged in two thermally isolated convolved square-spiral segments, 4.2 cm (upstream) and 2.8 cm (downstream) long, separated by a 1.0 mm segment. Each stage, as well as each rim, has a Ti/Pt meander-line heater patterned on the Pyrex channel cap. RTDs are patterned in close proximity to the heaters to measure the temperature of each location. Two nominally identical μTM devices were used in the course of this study.

Fluidic connections between the μTM and upstream/downstream μcolumns were made through ~5-cm sections of deactivated fused silica capillary (250 μm i.d., upstream; 100 μm i.d., downstream) inserted into expansion ports on the chip and sealed with epoxy (Hysol 1C, Rocky Hill, CT). The device was wire-bonded, heater side up, to a custom printed circuit board (PCB) Two small Si spacer chips were positioned under the heaters and held in place with photoresist. The assembly was inverted and then carefully placed on two additional Si chips positioned on the top surface of the TEC, with the thermal grease ensuring thermal contact. A plastic enclosure was then secured around the μTM through which a blanketing stream of dry air was passed during operation to prevent atmospheric water condensation on the device.

Each μcolumn consisted of a DRIE-Si convolved square spiral channel with an anodically bonded Pyrex cap, the basic design and fabrication of which have also been described previously.[25-27] The ^{1}D separation stage assembled for this study consisted of two 3-m-long, series-coupled μcolumns (3.1 × 3.1 cm chips, 250 × 140 μm channel cross-section) wall-coated

with a PDMS stationary phase (Figure 4.1). The ^{2}D separation stage consisted of a single 0.5-m-long µcolumn (1.2 × 1.2 cm chip, 46 × 150 µm cross-section) wall-coated with OV-215 (Figure 4.1). Fluidic connections to the µTM were made through ~5-cm segments of fused silica capillary (250 µm i.d. for 3-m µcolumns, 100 µm i.d. for 0.5-m µcolumns) epoxied into expansion ports in the Si chips, and attached through fused silica press-fit connectors.

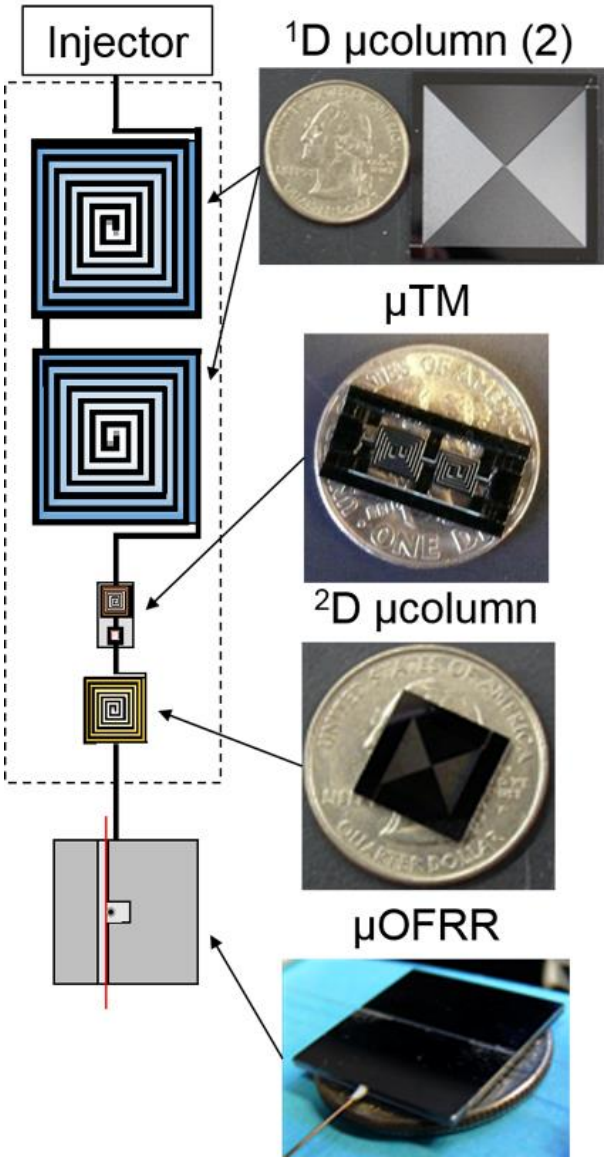

Figure 5.1. Illustration depicting the four separate microcomponents of the µGC × µGC–µOFRR subsystem and their interconnection. Photographs to the right show the µcolumns and µOFRR with US quarters for scale, and the µTM with a US dime for scale.

The μOFRR structure and fabrication have been described in detail.[23,28] The μOFRR cylinder is 250 μm i.d. and has a 1.2-μm thick SiO_x wall. The internal cavity of the cylinder extends completely through the center of the 2 × 2 cm, 520-μm thick Si chip. The μOFRR resonator protrudes vertically 80 μm from an annular trench etched into the substrate and has a 30 μm tall toroidal expansion region at the midsection, with a maximum diameter ≅ 300 μm. Backside DRIE was used to create both a tapered expansion port along the underside of the chip for capillary insertion, and a narrower microfluidic channel connecting the capillary port and the μOFRR inlet aperture. A final front-side DRIE step created an optical-fiber alignment channel running laterally across the surface tangential to the μOFRR cylinder.[23]

A PDMS stationary phase was deposited and cross-linked separately on the inner walls of the ^{1}D μcolumns and the μTM by known methods,[16,27] producing estimated PDMS film thicknesses of 0.20 and 0.30 μm, respectively. A 0.08 μm thick film of OV-215 was deposited on the wall of the ^{2}D μcolumn and cross linked by the same methods, following pretreatment with (3,3,3-trifluoropropyl)methylcyclotrisiloxane to promote adhesion by the OV-215.[19] To coat the inner wall of the μOFRR, the resonator cavity was filled with a toluene solution of PDMS and the solvent was evaporated by placing the device in a vacuum chamber for 10 min. The PDMS film thickness was estimated from the solution concentration to be ~0.3 μm assuming uniform deposition on the cavity. Following PDMS deposition, the backside fluidic channel was sealed with a 2 × 2 cm Pyrex coverplate using UV curable glue (NOA 81, Norland Optical, Cranbury, NJ). A short section of fused-silica capillary (250 μm i.d.) was then inserted into the tapered expansion port and sealed with epoxy to provide fluidic connection to the upstream μcolumns.

5.2.3 System Integration

The two 3-m ^{1}D μcolumns were bonded to individual carrier PCBs with epoxy and connected using a press-fit union. A polyimide thin-metal-film heater pad (Omega Engineering, Inc., Stamford, CT) was affixed to the ^{2}D μcolumn with thermal grease and polyimide tape, with a fine-wire thermocouple inserted between them to monitor temperature. The μTM was connected between the ^{1}D and ^{2}D μcolumns using press-fit unions.

The μGC × μGC subsystem was placed inside the oven of a bench scale GC (Agilent 6890, Agilent Technologies, Palo Alto, CA). The temperature of the oven determined the temperature of the ^{1}D μcolumns as well as the ambient of the TEC. The temperature of the ^{2}D μcolumn was further controlled by the heater pad and was set higher than that of the oven. The outlet capillary of the ^{2}D μcolumn was fed through the wall of the oven and connected to the μOFRR or connected directly to the FID with a press-fit union to generate reference chromatograms under the same conditions as used with the μOFRR. The FID is considered to have no dead volume and to provide virtually instantaneous responses to eluting analytes.

An optical fiber (SMF-28, Corning Inc., Corning, NY) was drawn over a hydrogen flame and a 1.4-cm segment was tapered down to an outer diameter of ~1 μm. The fiber was positioned in the on-chip alignment channel using a Vernier micrometer such that the thinnest part of the fiber contacted the expanded section of the μOFRR. The fiber was secured in place using a UV curable adhesive applied on the far left and right sides of the chip. This assembly, as well as a photodiode (InGaAs PIN, Marktech Optoelectronics, Latham, NY) and a fiber splice (Fiberlok II, 3M, Saint Paul, MN), were mounted on the 3D-printed mounting fixture depicted in Figure 4.2. One end of the optical fiber terminated at the photodiode and the other was inserted into the fiber splice for

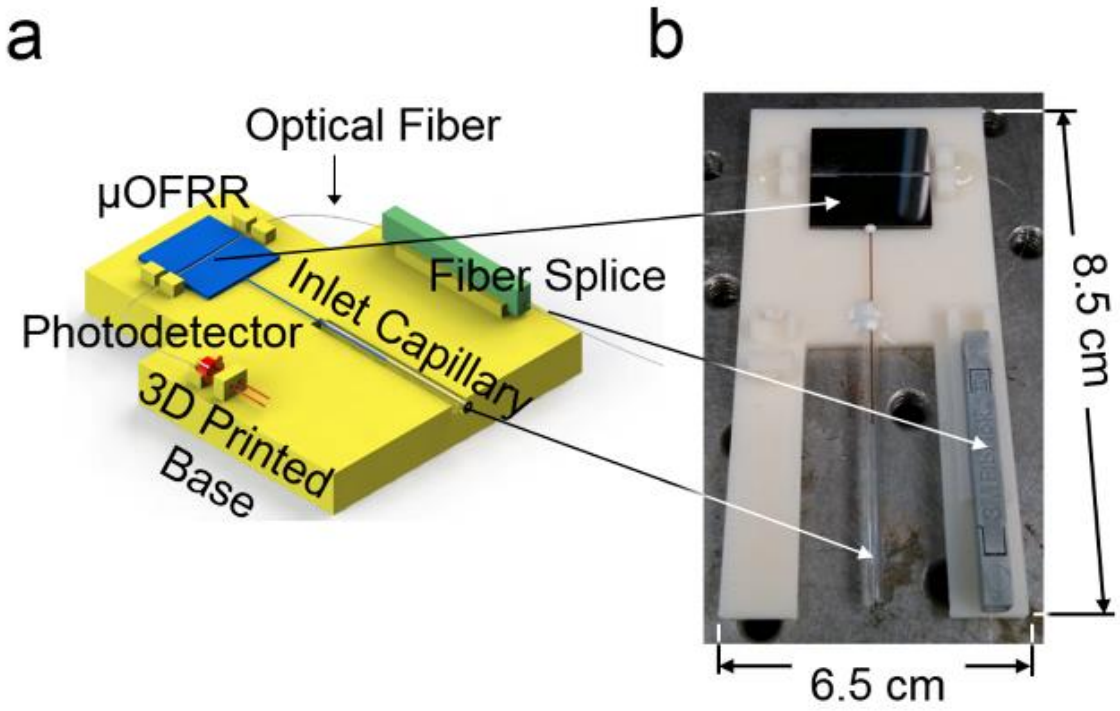

Figure 5.2. a) Diagram of the 3-D-printed mounting fixture for the μOFRR sensor, photodetector and fiber splice; b) photograph of the assembly with the photodetector removed.

easy connection to the external laser. This arrangement provided a stable, robust platform for the sensor and allowed for interconnecting the fluidics without needing to worry about the optics.

The entire μOFRR assembly was placed inside a small custom-made chamber equipped with a thermocouple and resistive heater which was maintained at 25 °C. The optical source was a 1550-nm fiber-coupled laser (CQF939/251, Philips, Amsterdam, NE); both the laser and the photodiode were connected to a DAQ card and controlled by custom-developed LabVIEW software. Two separate μOFRRs were used in the study: after completing the analysis of the *n*-

alkane mixture, an optical fiber broke on the first device and it was replaced with a second, nominally identical device for subsequent tests.

5.2.4 System Testing

A test atmosphere of a mixture of C_7-C_{10} vapors was generated in a 10-L FlexFilm® bag (SKC Inc., Eighty Four, PA) pre-filled with N_2 into which liquid samples of each mixture component were injected and allowed to evaporate. The injected volumes were ~ 40 μL corresponding to nominal vapor concentrations ranging of ~250 to 1300 parts-per-million (ppm) by volume. Test atmospheres of 7- and 11-component VOC mixtures were generated similarly, but more precisely, for subsequent analyses. The 7-VOC mixture contained 1,4-dioxane, 4-methyl-2-pentanone, toluene, C_8, ethylbenzene, 3-heptanone, and C_9. The 11-VOC mixture contained the same 7 components in addition to cyclopentanone, hexanal, *m*-xylene, and cumene. For these test atmospheres, 40.0 μL of each neat liquid was injected, except for cyclopentanone, hexanal, and 3-heptanone, for which 80.0 μL was injected. The resulting concentrations ranged from 550 to 2200 ppm. The VOC air concentrations were verified post-hoc by a single point calibration of each compound with the FID reference detector. For all analyses, samples were drawn by a small diaphragm pump through a 100-μL sample loop via a 6-port valve maintained at 30 °C, and then injected into the ^{1}D μcolumn through a 10-cm segment of deactivated fused-silica capillary for (modulated) separation and detection.

The μTM was operated as described previously;[18,19] temperature was modulated between a minimum, T_{min}, of about –20 °C and a maximum, T_{max}, of 180°C, with a 500 ms offset between heating of the first and second stages. A modulation period, P_m, of 7 s was used for the *n*-alkane tests and a P_m of 5 s was used for the other vapor mixtures. The longer P_m was used in an effort to

reach a lower T_{min} by increasing the μTM cooling time. The shorter P_m was used to increase the modulation rate.

A custom Visual C# program was used to control the timing of the applied voltages and to read the temperature sensors of the μTM via a DAQ card (NI USB-6212, National Instruments, Austin, TX). For the μOFRR, the laser was swept over a wavelength range of 330 pm at a rate between 26 and 56 hertz, while the output of the photodiode was monitored. Resonant wavelength was defined as the wavelength at the output minimum and was calculated and recorded in real time by a peak finding algorithm in the LabVIEW software. OriginPro 9.1 (OriginLab, Northampton, MA) and GC Image (Rev 2.2, Zoex, Houston, TX) were used for chromatographic data processing and display of 2-D chromatograms, respectively. The FID was operated at 250 °C with a data sampling rate of 200 Hz. Chromatographic data were collected by ChemStation software (Rev.B.01.01, Agilent Technologies, Santa Clara, CA).

5.3 Results and Discussion

5.3.1 Alkane Mixture

The raw μGC × μGC–μOFRR chromatogram showing the isothermal separation and detection of C_7-C_{10} is presented in Figure 3.3. The total elution time was ~25 min due to the low column temperatures and low flow rate. In all cases, vapor exposure resulted in λ_{WGM} shifting to longer wavelengths, which indicates an increase in the effective *RI* of the PDMS film. Since the difference between any of the *n*-alkane *RI* values (Table 4.1) and that of the PDMS (n = 1.404) is small, and C_7 and C_8 have *RI* values *lower* than that of PDMS, evidently film swelling dominates the net responses. This follows from the nominal PDMS film thickness of 300 nm being much less than the penetration depth of the evanescent field of the 1550-nm WGM. In this so-called

"thin-film" regime,[23,29] any polymer swelling would increase the fraction of the probed interior volume occupied by the polymer. The observation of reversible red shifts λ_{WGM} is consistent with previous reports on polymer-coated (μ)OFRR sensors. [23,24]

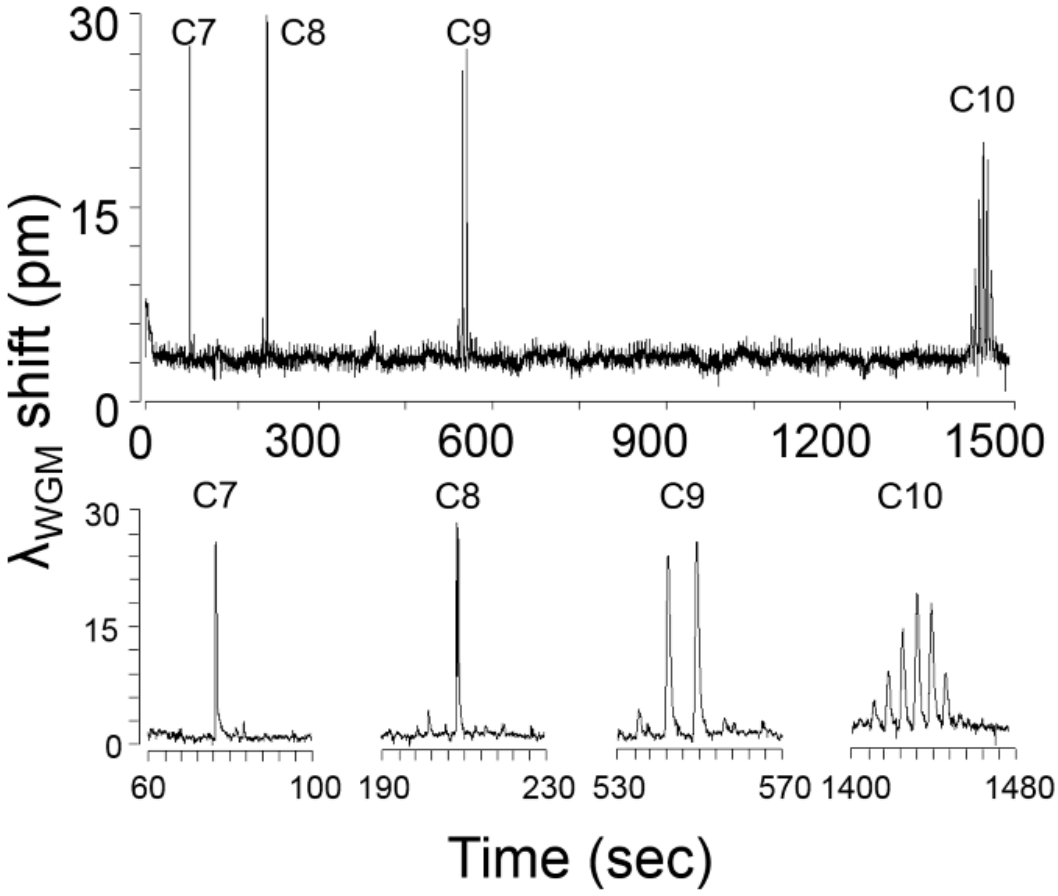

Figure 5.3. Raw μGC × μGC–μOFRR chromatogram of C_7-C_{10}. Enlarged views of the modulated peaks for each analyte are shown beneath the full trace. Conditions: ^{1}D μcolumns (oven), 30 °C; ^{2}D μcolumn, 50 °C; μOFRR, 25 °C; P_m , 7 sec; He carrier gas, 1.5 mL/min.

Table 5.1. Physical properties and modulated peak widths (*fwhm*) for *n*-alkanes detected with the μOFRR.

Compound	RI[a]	p_v[b] (kPa)	*fwhm* (sec)
n-heptane	1.386	6.0	0.34
n-octane	1.394	1.6	0.56
n-nonane	1.406	0.46	1.0
n-decane	1.409	0.12	2.0

[a] @ 25 °C, ref. 33. [b] @ 25 °C, ref. 3

The modulation number, M_N, is the number of modulations per peak, and it is one variable affected by the operating conditions of any μGC × μGC separation. It is primarily a function of the width of the peak eluting from the ^{1}D μcolumn and the selected P_m value, but can also be affected by the detector response speed. Early eluting peaks are invariably narrower and hence have lower M_N values. For effective μGC × μGC analyses it is generally recommended to adjust conditions to get M_N values of 3-4 for as many peaks as possible.[30] Higher M_N values provide diminishing returns, and temperature programming is typically used to decrease the retention time (t_R) and peak width of less-volatile mixture components. The M_N values for the *n*-alkanes increased from 1 for C_7, to 6 for C_{10} (see enlarged traces in Figure 3). Peak shapes were relatively symmetric, though some tailing was evident in all cases. For C_{10}, the baseline was barely recovered between successive modulated peaks.

Table 4.1 presents the values of the full-width-at-half-maximum (*fwhm*) of the largest modulated peak for each alkane. This variable is a function of the efficiency of remobilization from the μTM, the retention time on the ^{2}D μcolumn, and the kinetics of sorption and desorption into and out of the PDMS interface film in the μOFRR. All of these factors are affected by the vapor pressure (p_v) of each analyte, primarily through its influence on the desorption rates from the PDMS films in the μTM and the μOFRR, and to a lesser extent through its contribution to

chromatographic band broadening in the (polar) ^{2}D µcolumn. Consistent with the expected trend, the *fwhm* values increased from 340 msec for C_7, to 2000 msec for C_{10}.

A rough estimate of the sensitivity of the µOFRR to each alkane was determined by summing the areas of all modulated peaks (in pm-sec) and dividing by the injected mass (in ng). The latter was taken as the product of the test atmosphere concentration and the sample loop volume, but since the volumes of injected compounds used to establish the test atmosphere were not carefully measured, and there was no independent verification of the resulting air concentrations, we present only relative values here. The relative sensitivities increased from C_7 to C_{10}, with ratios of 1:2.5:5.6:13, respectively, in fairly good agreement the corresponding ratios of partition coefficients in PDMS among these alkanes reported in the literature.[31,32]

These results illustrate a phenomenon common to VOC sensors relying on reversible physisorption: peak width and sensitivity both increase with decreasing analyte p_v value. Since the resolution between two peaks is inversely proportional to the average peak width, there is an inherent tradeoff between peak-area sensitivity and chromatographic resolution.[1]

5.3.2 VOC Mixtures

Figure 4.4 shows the raw µGC × µGC chromatograms with the µOFRR and the FID for the 7-VOC mixture comprising compounds from several different functional group classes (see Figure 3.4 caption for operating conditions). Compounds 1-3 had M_N values of 1 with both detectors, while for compounds 4-7 the second modulated peak is more apparent with the FID than with the µOFRR. This is due to differences in detector sensitivity and response speed: the faster, more sensitive FID captured the smaller modulated peaks in the two cases where they were not apparent from the µOFRR trace. Note that peak 1 (1,4-dioxane) in the FID trace suffered from breakthrough in the modulator and, therefore, appears broad and truncated, whereas for the

μOFRR run it was captured and remobilized efficiently. As shown, the t_R values aligned precisely between the two runs with the two detectors. This, notwithstanding the differences in relative magnitudes of the pair of peaks for those compounds with M_N = 2, separated by the 5-sec modulation period, that occurred because of slight differences in the onset of μTM heating relative to the elution of a peak from the ^{1}D μcolumn.

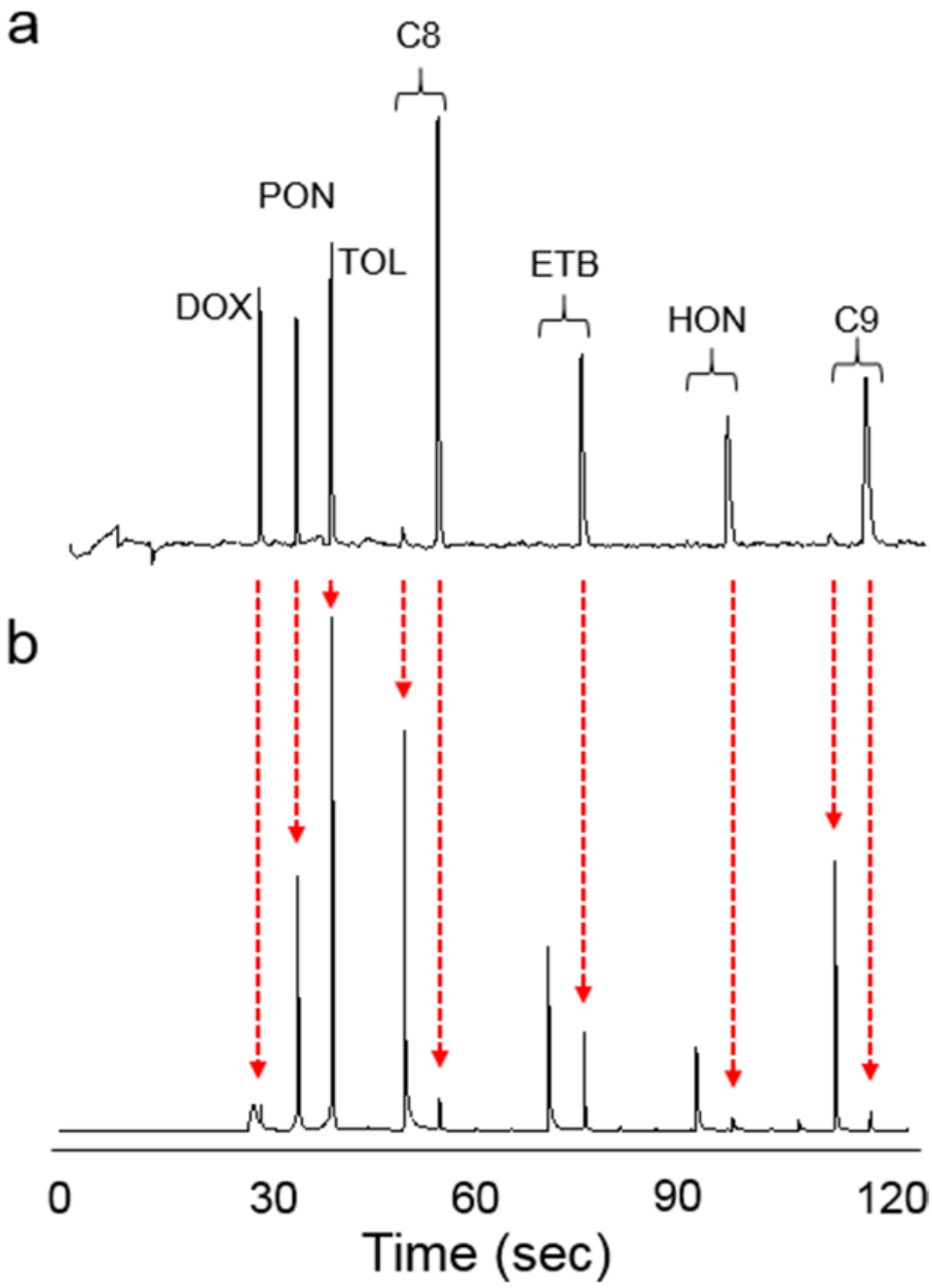

Figure 5.4. Raw chromatograms of the 7-VOC mixture with a) µGC × µGC–µOFRR and b) µGC × µGC–FID. Vertical, dashed red arrows show the time registration of the corresponding peaks between the two runs. Conditions: ^{1}D µcolumns, 50 °C; ^{2}D µcolumn, 80 °C; µOFRR, 25 °C; P_m, 5 sec; He carrier gas, 2.5 mL/min.

Figure 4.5a shows the inverse proportionality between p_v and *fwhm* for the 7-VOC mixture with both the μOFRR and the reference FID. All *fwhm* values from the μOFFR were larger than the corresponding *fwhm* values with the FID, and the slope of the line for the μOFRR in Figure 4.5a is ~5.5 times larger than that for the FID. The (shallower) slope of the FID curve reflects the influence of upstream (i.e., non-detector) factors on the peak width. Specific values of p_v, *fwhm*, and the *fwhm* ratios are listed in Table 4.2. The trends in *fwhm* values with the μOFRR are consistent those observed for the *n*-alkanes in Table 4.1.

In Figure 4.5b, the largest modulated peaks from the μOFRR and FID are superimposed for 4-methyl-2-pentanone and C_9. The ordinate scales were adjusted to so that the two peak heights matched (note: the *fwhm* is independent of the magnitude of the peak, as long as the peak shape is approximately Gaussian). For the more volatile 4-methyl-2-pentanone (p_v = 2.63 kPa) the *fwhm* value of the μOFRR peak was 150 msec, just 15% larger than the 130-msec *fwhm* value of the FID peak. For the less volatile C_9 (p_v = 0.46 kPa), the *fwhm* of the μOFRR peak was 690 msec, nearly 4 times larger than the180-msec *fwhm* of the FID peak. These data depict quite clearly the extent to which analyte volatility affects the response speed of the μOFRR. The smallest *fwhm* value observed with the μOFRR was 120 msec, for 1,4-dioxane. Unfortunately, as noted above, this compound did not yield a Gaussian peak with the FID so no comparison could be made. Regardless, these data demonstrate that the μOFRR is capable of resolving very narrow peaks for compounds of relatively high volatility.

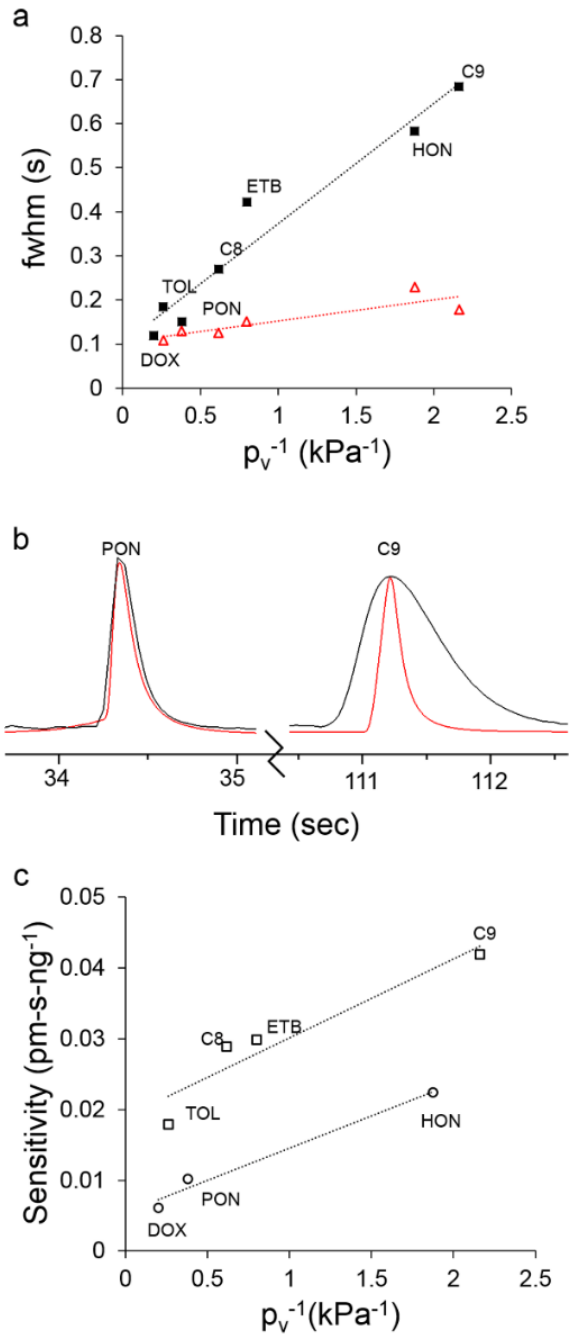

Figure 5.5. a) Plot of analyte p_v^{-1} vs. *fwhm* of the largest modulated peak for the 7-VOC mixture with the µOFRR (filled squares) and FID (unfilled triangles), and the corresponding best-fit regression lines (note: the 1,4-dioxane peak is missing from the FID data due to µTM breakthrough); b) Superimposed chromatograms from the µOFRR (black) and FID (red) for 4-methyl-2-pentanone (left, p_v = 2.63 kPa) and C_9 (right; p_v = 0.46 kPa); c) Plot of analyte p_v^{-1} vs. peak-area sensitivity (sum of all modulated peaks) for the 7-VOC mixture with the µOFRR, and the corresponding best-fit regression lines for the polar (circles) and non-polar (squares) compounds. For conditions, see Figure 4.4.

Table 5.2 Physical properties and µGC × µGC performance metrics for the two VOC mixtures.

			7-VOC Mixture[a]					11-VOC Mixture[b]			
			fwhm (sec)					*fwhm* (sec)			
Compound	RI[c]	p_v[d] (kPa)	µOFRR	FID	ratio	sensitivity (pm-sec/ng)	LOD[e] (ng)	µOFRR	FID	ratio	sensitivity (pm-sec/ng)
1,4-dioxane	1.422	4.97	0.12	na[f]	na	0.006	15	0.22	0.17	1.3	0.007
toluene	1.494	3.84	0.19	0.11	1.7	0.018	8	0.32	0.15	2.1	0.021
4-methyl-2-pentanone	1.400	2.63	0.15	0.13	1.2	0.010	12	0.60	na	na	0.010
n-octane	1.394	1.62	0.27	0.13	2.1	0.029	7	0.48	0.16	3.0	0.027
cyclopentanone	1.437	1.50	-[g]	-	-	-	-	0.49	0.34	1.4	0.008
ethylbenzene	1.493	1.25	0.42	0.15	2.8	0.030	11	0.79	0.22	3.6	0.037
hexanal	1.404	1.20	-	-	-	-	-	0.45	0.31	1.5	0.003
m-xylene	1.494	1.11	-	-	-	-	-	0.78	0.25	3.1	0.030
cumene	1.491	0.60	-	-	-	-	-	1.30	0.33	3.9	0.040
3-heptanone	1.406	0.53	0.59	0.23	2.6	0.022	19	1.01	0.51	2.0	0.017
n-nonane	1.406	0.46	0.69	0.18	3.8	0.042	16	1.24	0.24	5.2	0.041

[a] He flow rate = 2.5 mL/min; [b] He flow rate = 1.5 mL/min; [c] @ 25 °C, ref. 33; [d] @ 25 °C, ref. 34; [e] LOD calculated as 3 × (mass injected) /(signal-to-noise ratio) of tallest modulated peak; [f] µTM breakthrough; [g] data not collected.

Figure 4.5c shows the inverse proportionality between p_v and peak-area sensitivity for the 7-VOC mixture with the μOFRR. The systematic differences in sensitivities between the non-polar and polar subsets can be ascribed to differences in vapor-PDMS affinity (i.e., partition coefficient). Of course, peak-height sensitivity, from which limits of detection (LOD) are derived, is generally increased significantly by thermal modulation; but small shifts in the timing of the modulation relative to the elution of the peak can lead to large changes in the distribution of heights among the modulated peaks for a given analyte. This reduces the reliability of LOD estimates when using manual initiation of injections and modulator heating as we did in this study. Regardless, LODs were calculated on the basis of the responses obtained, just to get rough estimates of detectability. These ranged from 7 ng (C_8) to 15 ng (C_9) for the nonpolar compounds and 12 ng (4-methyl-2-pentanone) to 18 ng (3-heptanone) for the polar compounds. Thus, sensitive detection is easily achievable using the μGC × μGC–μOFRR.

The 11-VOC mixture analyses were performed under the same conditions as the 7-VOC analyses, with the exception that the He carrier gas flow rate was decreased to 1.5 mL/min to increase the time spent by the analytes on the ^{2}D μcolumn. The values of *fwhm* and sensitivity for each compound are presented in Table 4.2, for comparison with the corresponding values measured with the 7-VOC set at the higher flow rate. Sensitivities were quite similar for the compounds common to both data sets, whereas *fwhm* values for the 11-VOC set were approximately twice those for the 7-VOC set, and the μOFRR:FID *fwhm* ratios were also larger, both because of the lower flow rate. Interestingly, the *fwhm* ratios for the polar analytes were consistently lower than those of the non-polar analytes of similar vapor pressure; undoubtedly due

to the lower extent of partitioning of the former into the PDMS interface film. Nonetheless, all 11 compounds were well resolved and eluted in ~ 3 min.

The 2-D contour plots in Figure 4.6a and b, generated from the 11-VOC separations with the μOFRR and FID, respectively, show that the two detectors yielded comparable performance. Several of the peak contours from the μOFRR are broader along the y axis, reflecting the larger *fwhm* values from that detector, and the μOFRR contours from several of the later eluting compounds are narrower along the x axis, reflecting the smaller M_N values. Features appearing on the far left side of Figure 3.6a are artifacts from the initial temperature stabilization of the laser source, which did not affect the analysis. The small peak to the right of 4-methyl-2-pentanone in both plots was traced to a residual impurity in the bag used to prepare the test atmosphere. Both plots show the expected longer ^{2}D t_R values for the polar compounds, as well as reasonably good use of the available chromatographic space. Notably, the ^{2}D separation markedly improved the resolution of the cluster of peaks with ^{1}D t_R values in the range of 50-65 sec, many of which would otherwise partially overlap (i.e., with only a ^{1}D separation).

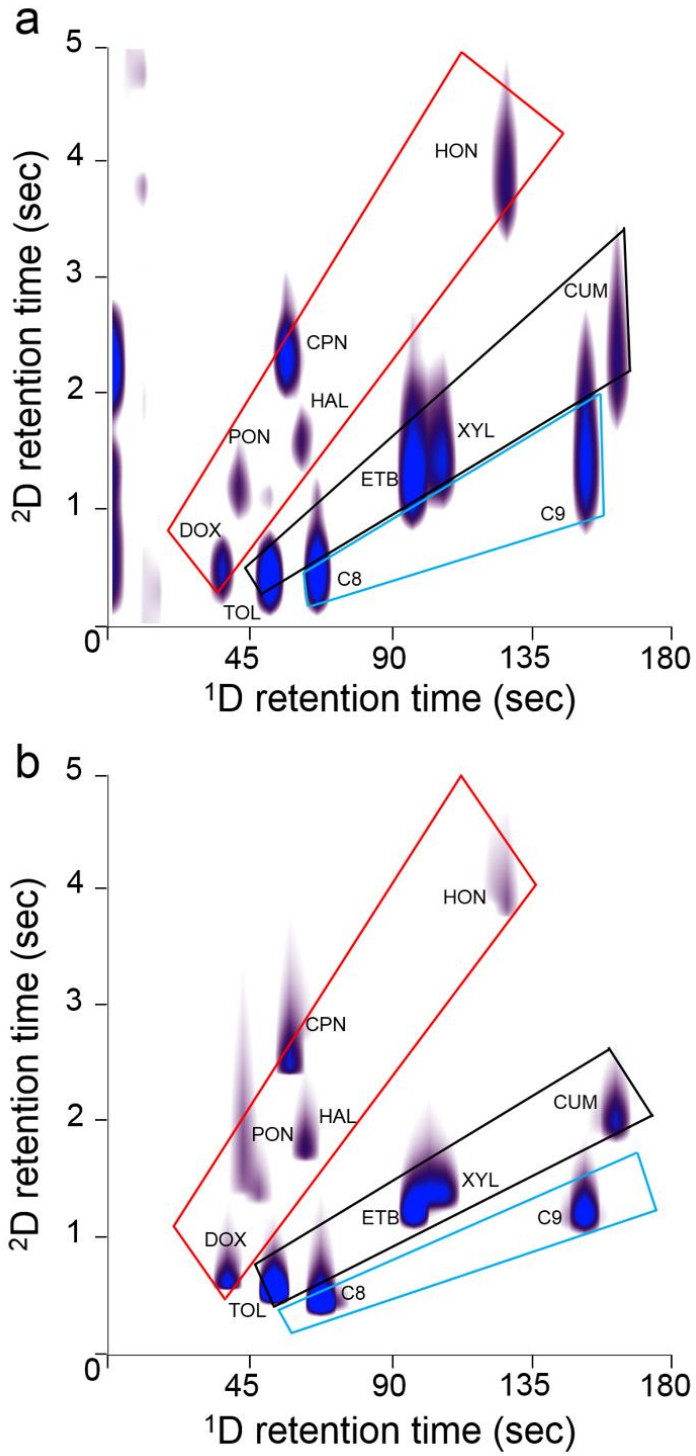

Figure 5.6. 2-D contour plots of the 11-VOC mixture with a) µOFRR detection and b) FID. Overlayed boxes are visual guides to the structure of each chromatogram: alkanes (blue), aromatics (black), and oxygenates (red) occupy the segregated zones indicated. Conditions: ^{1}D µcolumns, 50 °C; ^{2}D µcolumn, 80 °C; P_m, 5 sec; He carrier gas, 1.5 mL/min.

One hallmark of GC × GC is the "structure" of the contour plot, in which the peaks from members of different functional group classes align along segregated zones. Given the simplicity of the 11-VOC mixture, there are only three such zones, one each for alkanes, aromatics, and "oxygenates" (i.e., ketones, aldehydes, ethers). As shown, both plots exhibit similar structural zones, but the boundaries are a bit sharper with the FID, due to higher degree of resolution afforded by this detector. Still, the μOFRR plot retains all of the key aspects of the FID plot. (Note: in both plots the ^{2}D t_R values for C_{10} and cumene are shorter than expected due to a common phenomenon called "wraparound", which occurs when analyte t_R values are longer than the P_m and they elute, not during the modulation period in which they should, but in the next period. Thus, although the C_{10} and cumene ^{2}D t_R values appear to be between 1 and 3 sec, they are actually between 6 and 9 sec).

5.4 Conclusions

From the results of this preliminary study, we conclude that the PDMS-coated μOFRR can, indeed, serve as an effective detector for μGC × μGC, and that the thermally modulated μGC×μGC–μOFRR represents a promising new technology for analyzing airborne VOC mixtures. This is the first instance of comprehensive two-dimensional gas chromatographic analysis using a subsystem in which all core analytical components were microfabricated.

Perhaps the most prominent finding from this study was the critical dependence of the μOFRR response time on the analyte p_v value, through its influence on the rate of desorption of a vapor from the polymer interface film on the μOFRR cylinder. This is a feature common to all VOC sensors employing sorptive interfaces, but it takes on more significance with μGC × μGC because of the narrowness of the modulated peaks that need to be resolved. For the most volatile

VOCs tested here the *fwhm* values of the μOFRR peaks were comparable to those of an (ideal) FID, but for the least volatile compounds tested here they were several-fold larger.

Although the μOFRR peak widths were sufficiently narrow to permit effective separations, their dependence on p_v^{-1} represents a potentially limiting factor for this application. Using thinner polymer films or operating a slightly elevated temperature would reduce this problem, but both would be accompanied by losses in sensitivity. Ramping the temperature of the μOFRR over the course of an analysis would be a better solution, and its feasibility to address this issue is currently being explored.

The LODs we estimated from the response data were in the low-ng range, indicating a useful level of detectability among all analytes tested; however, the use of manual coordination of injection and modulation functions rendered the LODs quite variable. We believe this can be easily addressed by automatically synchronizing injection and modulation triggers and thereby generating more reproducible modulated-peak intensity profiles.

We are currently working on incorporating a micro-preconcentrator/focuser to complete the microsystem, and to permit autonomous air monitoring in the field. The integration of the μOFRR with embedded optical fiber waveguide and miniaturized ancillary components, demonstrated here, constitutes an enabling step toward such a fieldable unit. Although scrubbed ambient air could be used as the carrier gas with this microsystem,[1,3,5,23] the inevitable loss of chromatographic efficiency incurred at the relativelyseparation flow rates employed here argues strongly for retaining He as the carrier gas. This option is facilitated by the availability of small He canisters and regulators. On-going efforts are being directed toward the use of nanoparticle interface films instead of polymer films,[35] and the development of μOFRR arrays that can provide response patterns for analyte identification.

5.5 References

1. C.-J. Lu, W. H. Steinecker, W.-C. Tian, M. C. Oborny, J. M. Nichols, M. Agah, J. A. Potkay, H. K. Chan, J. Driscoll, R. D. Sacks, *Lab Chip*, 2005, **5**, 1123-1131.
2. P. R. Lewis, R. P. Manginell, D. R. Adkins, R. J. Kottenstette, D. R. Wheeler, S. S. Sokolowski, D. E. Trudell, J. E. Byrnes, M. Okandan, J. M. Bauer, *IEEE Sensors J.*, 2006, **6**, 784-795.
3. S. K. Kim, H. Chang, E. T. Zellers, *Anal. Chem.*, 2011, **83**, 7198-7206.
4. R. P. Manginell, J. M. Bauer, M. W. Moorman, L. J. Sanchez, J. M. Anderson, J. J. Whiting, D. A. Porter, D. Copic, K. E. Achyuthan, *Sensors*, 2011, **11**, 6517-6532.
5. W. R. Collin, G. Serrano, L. K. Wright, H. Chang, N. Nuñovero, E. T. Zellers, *Anal. Chem.*, 2013, **86**, 655-663.
6. R.-S. Jian, Y.-S. Huang, S.-L. Lai, L.-Y. Sung, C.-J. Lu, *Microchem. J.*, 2013, **108**, 161-167.
7. L. K. Wright, E. T. Zellers, *Analyst*, 2013, **138**, 6860.
8. Y. Qin, Y. Gianchandani, *J. Microelectromech. Sys.*, 2014, **23**, 980-990.
9. A. Garg, M. Akbar, E. Vejerano, S. Narayanan, L. Nazhandali, L. Marr, M. Agah, *Sens. Acuators B*, 2014**, 212**, 145-154.
10. H. Zhu, R. Nidetz, M. Zhou, J. Lee, S. Buggaveeti, K. Kurabayashi, X. Fan, *Lab Chip*, Lab on a Chip **15**, 3021-3029 (2015)
11. C. Jin, P. Kurzawski, A. Hierlemann, E. T. Zellers, *Anal. Chem.*, 2008, **80**, 227-236.
12. T. Górecki, J. Harynuk, O. Panić, *J. Sep. Sci.*, 2004, **27**, 359-379.
13. J. Dallüge, J. Beens, U. A. T. Brinkman, *J. Chrom. A.*, 2003, **1000**, 69-108.
14. J. B. Phillips, R. B. Gaines, J. Blomberg, F. W. van der Wielen, J. M. Dimandja, V. Green, J. Granger, D. Patterson, L. Racovalis, H. J. de Geus, *J. Hi. Res. Chrom.*, 1999, **22**, 3-10.
15. M. Libardoni, C. Fix, J. H. Waite, R. Sacks, *Anal. Meth.*, 2010, **2**, 936-943.
16. S.-J. Kim, S. M. Reidy, B. P. Block, K. D. Wise, E. T. Zellers, K. Kurabayashi, *Lab Chip*, 2010, **10**, 1647-1654.
17. S.-J. Kim, G. Serrano, K. D. Wise, K. Kurabayashi, E. T. Zellers, *Anal. Chem.*, 2011, **83**, 5556-5562.
18. G. Serrano, D. Paul, S.-J. Kim, K. Kurabayashi , E. T. Zellers, *Anal. Chem.*, 2012, **84**, 6973-6980.
19. W.R. Collin, A. Bondy, D. Paul, K. Kurabayashi, E. T. Zellers, *Anal. Chem.*, 2015, **87**, 1630-1637.
20. J. J. Whiting, C. S. Fix, J. M. Anderson, A. W. Staton, R. P. Manginell, D. R. Wheeler, E. B. Myers, M. L. Roukes , R. Simonson, *Proc. Solid-State Sensors, Actuators and Microsystems Conference*, 2009, 1666-1669, Jun. 21-25, Denver, CO.
21. B.-X. Chen, T.-Y. Hung, R.-S. Jian, C.-J. Lu, *Lab Chip*, 2013, **13**, 1333
22. J. Liu, J.-H. Seo, Y. Li, D. Chen, K. Kurabayashi, X. Fan, *Lab Chip*, 2013, 13, 818-825.
23. K. Scholten, X. Fan, E. T. Zellers, *Lab Chip*, 2014, **14**, 3873-3880.
24. S. I. Shopova, I. M. White, Y. Sun, H. Zhu, X. Fan, G. Frye-Mason, A. Thompson, S.-J. Ja, *Anal. Chem.*, 2008, **80**, 2232-2238.
25. M. Agah, J. A. Potkay, G. Lambertus, R. Sacks, K. D. Wise, *J. Microelectromech. Sys.*, 2005, **14**, 1039-1050.

26. G. Lambertus, A. Elstro, K. Sensenig, J. Potkay, M. Agah, S. Scheuering, K. Wise, F. Dorman, R. Sacks, *Anal. Chem.*, 2004, **76**, 2629-2637.
27. S. Reidy, G. Lambertus, J. Reece, R. Sacks, *Anal. Chem.* 2006, **78**, 2623-2630.
28. K. Scholten, X. Fan, E. T. Zellers, *Appl. Phys. Lett.*, 2011, **99(14)**, 141108.
29. A. M. Kummer, A. Hierlemann, H. Baltes, *Anal. Chem.*, 2004, **76**, 2470-2477.
30. J. Beens, H. Boelens, R. Tijssen, J. Blomberg, *J. Hi. Res. Chrom.*, 1998, **21**, 47-54.
31. P. A. Martos, A. Saraullo, J. Pawliszyn, *Anal. Chem.*, 1997, **69**, 402-408.
32. A. Hierlemann, A. J. Ricco, K. Bodenhöfer, A. Dominik, W. Göpel, *Anal. Chem.*, 2000, **72**, 3696-3708.
33. G. Baysinger in *CRC Handbook of Chemistry and Physics*, National Institute of Standards and Technology, 2014.
34. J. L. a. W. G. Mallard in *NIST Chemistry WebBook, NIST Standard Reference Database Number 69*, National Institute of Standards and Technology, Gaithersburg MD, 20899.
35. K. W. Scholten, W. R. Collin, X. Fan, and E. T. Zellers, *Nanoscale*, 7, 9282-9289, 2015 .

CHAPTER 6

A COMPREHENSIVE TWO-DIMENSIONAL GAS CHROMATOGRAPHIC MICROSYSTEM WITH MICROFABRICATED PRECONCENTRATION/INJECTION, SEPARATION, AND CHEMIRESISTOR ARRAY DETECTION: μGC × μGC– μCR

6.1 Background and Motivation

The timely analysis of complex mixtures of airborne volatile organic compounds (VOCs) is vital to many areas of interest. Point of care biomarker measurement,[1] workplace exposure,[2] analysis of water supplies[3] and soils[4] for contamination, detection of chemical warfare agents[5] and explosives[6] are applications where in-field measurements would be far more useful than collecting samples and sending them to a lab for analysis. Extant portable instruments capable of multi-VOC determinations are often bulky, expensive and complex.[5] Smaller, simpler instruments cannot distinguish target analytes from interferences.

Microfabricated gas chromatographic (μGC) instrumentation is a promising technology that combines small size with multi-VOC analytical capabilities. Several groups are working towards fieldable instruments.[6-10] Unfortunately, μGC separation columns are limited in length (relative to capillary GC columns) by both the fabrication processes as well as the difficulty

associated with pushing gas flow through long columns. This limits the resolution and peak capacity (the number of compounds able to be separated in a given time period) achievable.

One promising approach to overcoming the inherent limitations related to short columns used in μGC is comprehensive two dimensional μGC (μGC × μGC). In μGC × μGC, effluent from a first-dimension (^{1}D) GC μcolumn is quantitatively trapped and re-injected into a second dimension (^{2}D) μcolumn with a different (complementary) stationary phase coating,[11] by means of a pneumatic or thermal modulation device.[12] Very few efforts to create portable μGC × μGC instrumentation have been reported. A few groups have demonstrated multidimensional separations with microfabricated components.[13-15] The first such report came from an effort at Sandia National Laboratory.[13] Pneumatic modulation with μcolumns and a tuning fork resonator sensor was used in the 2D separation of 5 compounds. Chen et al. used stop flow modulation and a valve to direct effluent from the ^{1}D μcolumn to one of three ^{2}D separation columns, with detection via FID. Liu et al.[15] have demonstrated multidimensional separations using multiple μcolumns and adsorbent tubes for refocusing effluent from the ^{1}D μcolumn. In that work, the use of long sample collection periods allows for long (and thus higher resolution) ^{2}D separations, but this is done at the expense of ^{1}D separation resolution.

Collaboration between the Zellers group and the Kurabayashi group yielded a microfabricated thermal modulator (μTM) that has been tested with conventional capillary columns[16-18] and μcolumns[19] with conventional (FID) detection, as well as with μcolumns and a microsensor as the detector.[20] However, there has yet to be a report of a complete, stand-alone μGC × μGC.

Detectors for μGC × μGC must exhibit fast response to capture the elution of very narrow modulated peaks, which are typically <1 s wide (*fwhm*). In Chapter 5 we described the

implementation of a micro optofluidic ring resonator (μOFRR) detector as one such detector and the effect of sorptive interfaces on *fwhm* values.[20] Here we describe an analogous study using a detector comprising a CR array that employs films of monolayer protected gold nanoparticles (MPNs) as interface layers for the detection of VOCs. Several reports of these MPN-coated CR arrays as GC and μGC detectors have appeared in recent years.[6,8,21] In practice, films of MPNs are coated onto interdigitated gold electrodes, voltage is applied and the resistance of the film is measured. Upon exposure to vapors, the film swells and causes an increase in resistance. Differential responses from an array of such sensors with different MPN ligand types can be combined to form a pattern unique to each analyte, which can aid in recognition/discrimination. Each film type sorbs eluting vapor to a different extent, yielding differential responses to that vapor which is unique for each compound.

Sampling and injection in μGC is most often accomplished using adsorbent packed sampling devices which can quantitatively capture analyte from a large volume sample. Such sorbent based injectors capture mass from large volumes of gas and then inject that mass into the separation module in a smaller volume. Zellers et al. have used graphitized carbon packed preconcentrator/focusers (μPCF).[22-24] Agah and coworkers have also shown preconcentrators based on polymer coated-micropillars in a silicon chamber as well as the layer-by-layer deposition of silica nanoparticles.[25,26] Common to all of these devices is the ability to rapidly heat the device to thermally desorb analyte and inject it into the separation device.

We report here for the first time the integration of microfabricated PCF, separation module and sensor along with ancillary electronic components to create the first standalone μGC × μGC microsystem. First, a new generation of CR devices is described and characterized with a single upstream μcolumn. Next, the μTM is used to evaluate the utility of the CR as a detector for very

narrow peaks (without a ^{2}D separation) and investigate the effects of flow rate and temperature of the sensor in terms of *fwhm*, sensitivity and LOD. Then, a 20 compound separation is performed using the μGC × μGC subsystem. Next, the assembly of a complete μGC × μGC-μCR array is described. Finally, a "proof-of-function" experiment is presented showing preliminary results in a complex mixture analysis.

6.2 Materials and Methods

6.2.1 Materials.

Volatile organic compounds (VOC) were >98% pure (Sigma-Aldrich, Milwaukee, WI) and used without further purification. Carbopack X and Carbopack B (Sigma-Aldrich, Milwaukee, WI) was sieved to 210 - 250 μm prior to use. JR-507 Slow Reducer was obtained from PPG (Pittsburgh. PA). Vapor phase samples were prepared by injecting the appropriate amount of liquid VOC into the sample bags (SKC, Eighty-four, PA) which had been filled with a known volume of scrubbed, dry nitrogen. MPNs for CR (octanethiol and 6-phenoxyhexanethiol) array coating were taken from existing stocks prepared by the method reported by Rowe et al.[27] Room temperature ionic liquid (Tris[2-(6-aminopropylphosphoniumhexaamido)ethyl]amine tris[bis(trifluoromethylsulfonyl)imide]) was taken from existing stocks prepared according to the method reported by Payagala et al.[28] used in Chapter 3.

6.2.2 Microfabricated Devices

The two-stage μTM has been described extensively in previous publications[16-20] as well as Chapters 3, 4 and 5. Briefly, the 1.3 × 0.6 cm Si chip contains deep-reactive-ion-etched (DRIE) Si μchannel with a cross section of 0.250 (w) × 0.140 (h) mm arranged in two convolved square-spiral stages, 4.2 cm (stage 1) and 2.8 cm (stage 2) long, separated by a 1.0 mm long straight

segment which provides thermal isolation. A Pyrex cap (100-μm thick) is anodically bonded to the top surface of the chip to seal the μchannel. Four serpentine Ti/Pt resistive heaters are patterned on the Pyrex surface; above each μTM stage and each rim above the inlet and outlet ports. RTDs are patterned (in Ti/Pt) in close proximity to the heaters to measure temperature.

The μTM was connected to ^{1}D and ^{2}D (μ)columns through 10-cm (^{1}D) and 5 cm (^{2}D) sections of deactivated fused silica capillary (250 μm i.d., ^{1}D; 100 μm i.d., ^{2}D) inserted into on-chip expansion ports and sealed with epoxy (Hysol 1C, Rocky Hill, CT). The device was then epoxied with the Pyrex side up to a custom carrier printed circuit board (PCB) with a hole cut out beneath the device for thermal isolation. Then, electrical connections were made using aluminum wire-bonds. Two small Si-on-glass spacers with trenches to isolate the edge of the chip from the stages were placed directly on top of the μTM, one directly over each stage heater and held in place using photoresist. The photoresist was then allowed to dry overnight at room temperature. Next, two riser slabs fabricated from Si are placed on the spacers using thermal paste for adhesion. This sub-assembly is inverted and mounted such that the Pyrex surface of the μTM is suspended directly above the 4-tier TEC (Marlow, Dallas, TX). The slabs and spacers are held in contact with the TEC surface with thermal grease which increases heat conduction from the device to the TEC. The μTM is positioned within ~40 μm of the spacers, with the remaining gap being filled by thermal paste. A plastic shroud allows a stream of dry air to be passed over the device during operation to prevent atmospheric water from condensing/freezing on the μTM surface.

The μPCF parameters used were recently described and evaluated by Bryant-Genevier et al.[29] as the sampling/injection device intended for a belt-mounted μGC, though the actual device used differed slightly. It consists of dual DRIE-etched Si cavities (4.7 and 2.9 μL) with a Pyrex lid. On the back side of the Si chip, heaters and resistive thermal devices (RTDs) were patterned

in Ti-Pt which allowed for rapid, controlled, heating of the device for desorption. The cavities were packed with Carbopack X and Carbopack B which are suited to the analyte volatility range targeted by this microsystem.

The design and fabrication of the μcolumns used here have also been described previously.[30,31] Each μcolumn consists of a Si channel (DRIE-etched) with a Pyrex cap anodically bonded atop to form the fourth wall. Though thin-film Ti/Pt heaters and RTDs are patterned on the back side of the Si which would permit temperature ramping, that feature was not used herein. The ^{1}D separation column consisted of two separate, series-coupled 3.1 × 3.1 cm μcolumn chips with convolved square-spiral, DRIE etched channels. Each μcolumn is 3-m long with a 250 × 140 μm cross section. The 1.2 × 1.2 cm μcolumn chip ^{2}D separation column consisted of a similarly shaped DRIE channel, though in this case it was 0.5-m long and 46×150 μm in cross section. Segments of fused silica capillary (250 μm i.d. for 3-m μcolumns, 100 μm i.d. for 0.5-m μcolumns) epoxied into expansion ports in the Si chips allowed for fluidic interconnection to the GC inlet (upstream of the ^{1}D μcolumn), the μTM (between the 1D column and 2D column) and the CR array or FID (downstream of the ^{2}D column).

The μCR array consisted of a series of 10 sets of Au/Cr interdigitatal gold electrodes deposited via a standard lift-off method onto a glass substrate. Each IDE contained 27 pairs of electrodes that were 4 μm wide and were spaced 4 μm apart with and overlap of 210 μm and adjacent sets were spaced 500 μm apart. An RTD on the top side and meander-line heater on the back side were also included in the fabrication, though neither was used herein. Octanethiol (C8) and 6-phenoxyhexanethiol (OPH) monolayer protected gold nanoparticles (MPNs) films were coated onto 5 sensors each in the array. A Si lid with a 140 μm deep × 350 μm wide DRIE running the length of the lid down the center directly above the array. This was placed with the aid of a

microscope, and held in place with double-sided tape (UHB, 3M, St. Paul, MN). Following placement, a bead of Hysol 1-C epoxy (Henkel) ensured a leak free seal. Uncoated fused silica capillary (250 μm id) was epoxied into expansion ports in the Si lid to provide fluidic interconnection to the ^{2}D μcolumn.

6.2.3 Stationary Phase Deposition

The ^{1}D μcolumns and μTM were statically coated separately with PDMS from a solution that also contained 1% (w/w) dicumyl peroxide as the crosslinking agent according to published procedures.[32,33] PDMS concentrations were adjusted to produce an average (nominal) wall-coating thickness of 0.20 μm for the ^{1}D μcolumns and 0.30 μm for the μTM. The PDMS in the μcolumns was cross-linked by heating at 180 °C for 1h under N_2 in a GC oven. The PDMS in the μTM was cross-linked by heating at 180 °C 1h under a static head of N_2 using the stage heaters on-chip to avoid cracking the capillary-chip union from expansion of the adhesive. A consequence of this method is that the connecting capillaries were coated (μcolumn and μTM) and crosslinked (μcolumn). Prior to (statically) coating one of the ^{2}D μcolumns with the RTIL, it was pre-treated with NaCl to roughen the surface and improve adhesion according to a published method.[10] The nominal average RTIL-film thickness was 0.05 μm. An alternative stationary phase coating for the ^{2}D μcolumn, OV-215 (Ohio Valley Specialty), deposited as described in Chapter 3 to a film thickness of 0.08 μm.

6.2.4 μGC × μGC-CR Integration

Images of each device are shown in the sub-system diagram shown in Figure 6.1a. For initial experiments, samples were drawn through a 100 μL sample loop connected to a six-port gas sampling valve connected to the inlet of a bench scale 6890 GC (Agilent Technologies, Palo Alto,

CA). He carrier gas was used in all experiments. In some experiments, no second dimension column was used and the μTM was connected to either the μCR array or the FID of the GC via deactivated fused silica capillary. The ^{1}D μcolumns, μTM and ^{2}D μcolumn were housed in the GC oven and held at 30 °C. The ^{2}D μcolumn was heated above the oven temperature with a small thin-film heater held in close contact with the Si side of the chip with thermal paste. A thermocouple was placed between the heater and the μcolumn chip to monitor the temperature. On-chip heaters were not used in these experiments to simplify the control software and power needed. The μCR array was held in a small metal enclosure heated with a silicone-embedded resistive metal heater. This was controlled with a standalone temperature controller and thermocouple (Omega Engineering, Stamford, CT) placed in close proximity to the μCR and operated at either 30 °C or 40 °C just outside of the GC oven with connection to the 2D μcolumn were made a hole in the side wall of the oven. Data from 8 sensors were collected, but due to similarity in responses and for the sake of brevity, only a single sensor of each MPN type is presented. FID and μCR data had to be collected separately to separate any sensor induced effects on peak metrics from chromatographic effects. The head pressure was adjusted such that peak retention times were conserved despite the change in pressure drop between the two detectors.

6.2.5 Standalone Microsystem Integration

Figure 6.1b shows the assembled microsystem, which builds on the previous section with the addition of a μPCF. Other (non-microfabricated) components include a valve manifold (VGC Chromatography, Dayton, OH) with small 3-way latching valves (Lee Company, Westbrook, CT) and a small vacuum pump (KNF, Trenton, NJ) two device interface boards (custom built in house) and a data acquisition board (NI USB-6212, National Instruments, Austin, TX). Two separate personal computers were used: one solely for μTM control and one for control of the other

components and sensor readout. Data were collected using routines written in LabView. An GC was used for carrier gas (He) supply, though the manifold can accept small gas cylinders for more portable use. Additonal heated zones include the capillary between the ^{1}D µcolumn and the µTM, the capillary between the µTM and ^{2}D µcolumn and the capillary between the ^{2}D µcolumn and the µCR array. This was necessary to mitigate cold spots in the flow path to the extent possible. The first heated zone was constructed using a short section of stainless steel reinforced polyimide tubing (Microlumen) with the stainless steel reinforcement acting as a resistive heater after applying DC current to achieve a temperature of 80 °C. The other two heated zones consisted of 1/4" stainless steel tubing first wrapped with polyimide tape, then wrapped with Ni-Cr wire and finally another layer of polyimide tape. DC current was applied to heat the assembly to 100 °C. The temperatures of the zones were measured with a fine wire thermocouple (Omega). These additional heaters are not shown in Figure 6.1b for clarity.

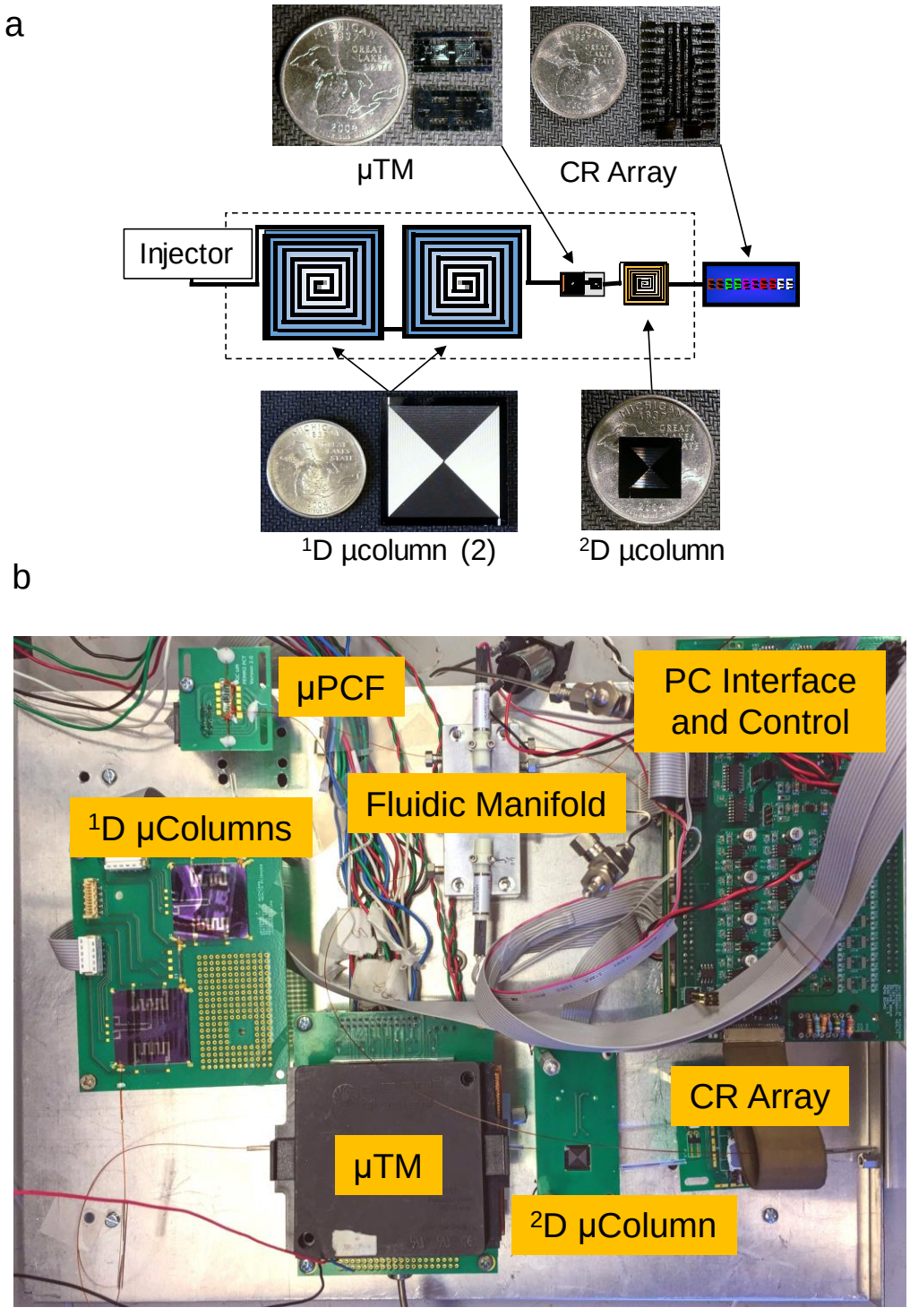

Figure 6.1: a) Diagram of the system with a photograph of the devices; b) Photograph of the assembled microsystem.

6.3 Results and Discussion

6.3.1 μGC CR Array Evaluation

Initially, the CR array was evaluated in a single dimension separation (that is, with the μTM in line but turned off and no ^{2}D μcolumn) and with FID in a separate run for reference. A mixture of 6 VOCs was separated: C_7, toluene (TOL), C_8, ethylbenzene (ETB), C_9 and C_{10}. The μCR array was held at 30 °C the 6-VOC experiments and three different flow rates (1.5, 2 and 3 mL/min) were tested. The 6-VOC chromatograms in Figure 6.2a shows the fidelity achieved in terms of fwhm, analyte retention time and, generally, peak shape for the 3 mL/min case. Note the signal to noise ratios for the C8 and OPH sensors is much lower than that achieved with FID. This is consistent with previous observations, as limits of detection (LOD) for this type of sensor are generally about three orders of magnitude higher than FID.[6,8] Figure 6.2b compares *fwhm* for the three detectors: C8-CR, OPH-CR and FID based on a single injection at 3 mL/min. It was not possible to measure *fwhm* values for the CR array and FID simultaneously, so the small discrepancies noted can be attributed to slight differences in experimental conditions. Connecting to the FID after the μTM required a slightly different pressure than with the μCR array to drive the 3 mL/min flow rate, so the small fluctuations in *fwhm* are not surprising. This is noted at the other flow rates as well. The C8-CR *fwhm* values were generally lower than those from the OPH-CR, with only a few exceptions. This was could not be explained as a difference in pressure, as with the FID results, because the data were collected concurrently during the same experiment. The discrepancies in fwhm are likely associated with baseline fluctuations for the CR, which can *appear* to broaden the eluting peaks in some cases if periodic noise coincides with the tail of a peak. Peak *fwhm* values were within 10 % of one another (CR to FID and CR to CR) for all flow rates (data not shown), excepting C_{10} at 2 mL/min C_7 at 3 mL/min. From these experiments, it is

clear that the new generation of μCR array provides detection that, while not as sensitive as FID, is certainly able to keep up with the peak widths observed in single dimensional separations.

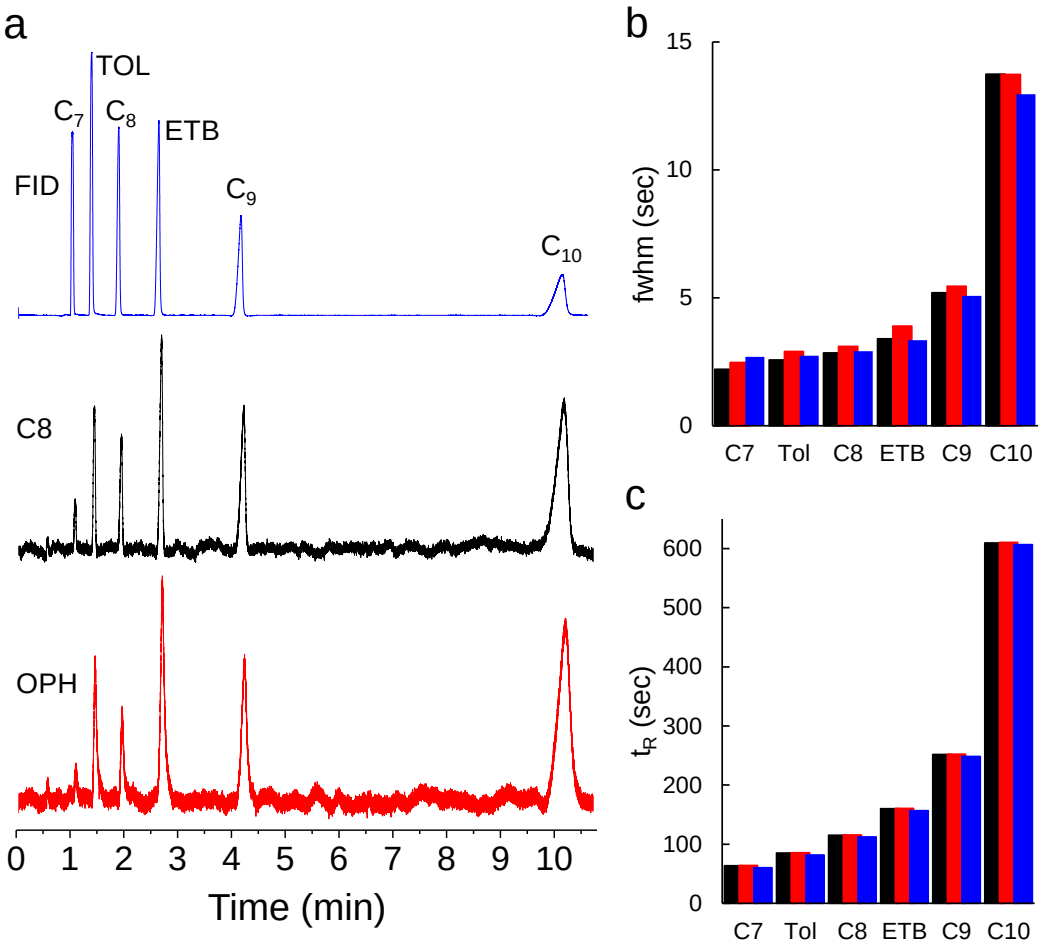

Figure 6.2. a) One dimensional chromatographic separation with FID (blue), C8-CR (black) and OPH-CR (red) detection. b) Comparison of fwhm values for C8-CR (black), OPH-CR (red) and FID (blue). c) Comparison of retention times for C8-CR (black), OPH-CR (red) and FID (blue). Conditions: 3 mL/min He carrier gas; 30 °C CR oven; 30 °C separation oven.

6.3.2 μGC with Modulation: CR Array Evaluation

Next, the μCR array response characteristics were evaluated with modulated peaks of the same 6-VOC mixture. The μTM was connected to the μCR array with uncoated capillary. Figure

6.3 shows the raw chromatograms obtained at 3 mL/min and an array temperature of 30 °C. FID data were again obtained in a separate run.

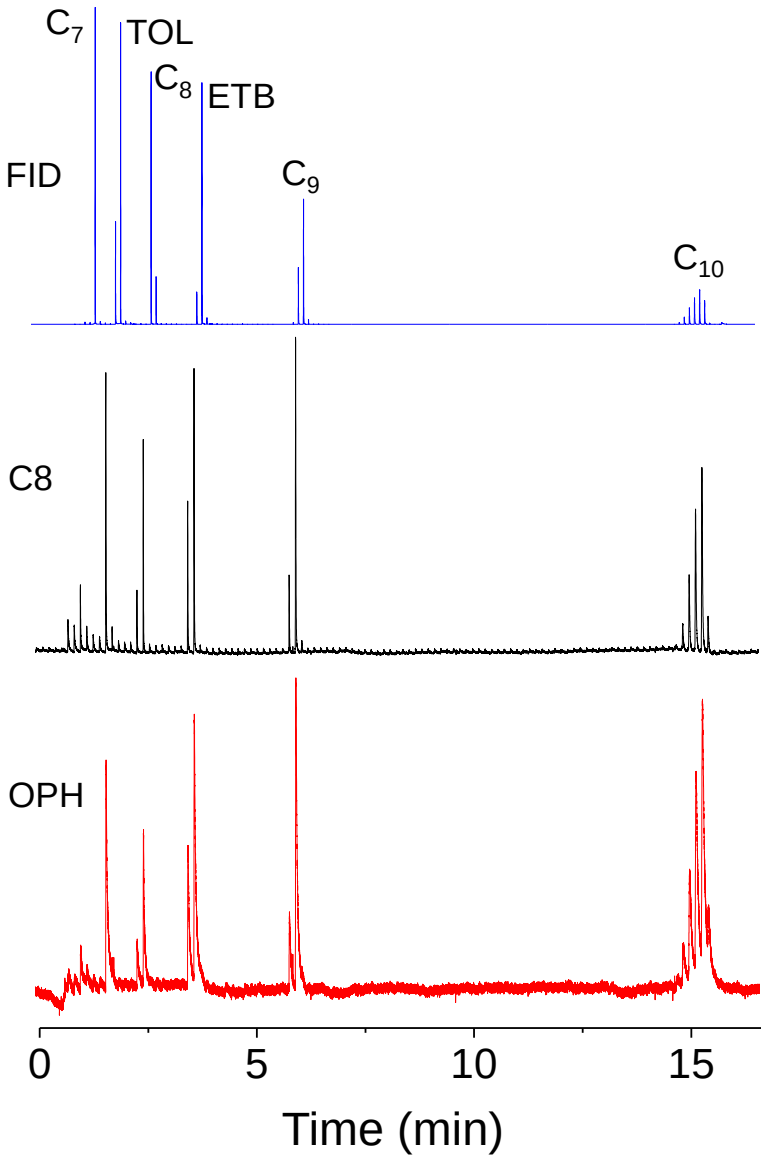

Figure 6.3. Typical µGC × µGC chromatograms obtained using FID (blue), C8-CR (black) and OPH-CR (red) detection. Conditons: 1.5 mL/min He carrier gas; 30 °C CR oven; 30 °C separation oven; 6 s Pm.

Immediately evident is the fact that the OPH-CR generates peaks which are much broader than either the C8-CR or the FID. This is in contrast to the 1D-µGC experiments, which showed little difference between any of the detectors in terms of fwhm. It appears that with the narrow

peaks generated by the μTM, band broadening imparted by the CR array becomes significant. Peak modulation numbers (M_n, the number of peaks per compound in the modulated chromatogram) are maintained from C8-CR to OPH-CR and ranged from 1-5. This is not strictly true when comparing the CRs to the FID as sensitivity differences between the two detectors causes the very smallest modulated peaks visible in FID are not detected on the CR array.

Figure 6.4 shows the results of integration for C_{10} with two different detector temperatures and three different flow rates. C_{10} was chosen as the focus of this discussion because the M_N did not drastically change. This is critical since sensitivity and LOD is strongly dependent on M_N. The timing of modulations could not be controlled well enough with the current circuitry to ensure eluting peaks are modulated the same from run to run, small variations occur depending on the exact timing of the heating/cooling cycle. A further complicating factor is the change in M_N due to differing flow rates and narrowing of ^{1}D peaks.

Peak fwhm values for the C8-CR and for the OPH-CR are presented in Figure 6.4a and b respectively as a function of both temperature and flow rate. FID fwhm values were roughly half of C8-CR fwhm values which in turn were roughly half of those of the OPH-CR. This broadening is associated with the finite time needed to sorb into the MPN films, a common feature of sorption-based detectors.[6,20,34] The fact that the C8-CR fwhm values are smaller than the OPH-CR values indicates even slower mass transfer for this process. Increased flow rate decreases CR peak fwhm values, since the peak inevitably spends less time in the sensing region with higher flow rate. Temperature increases cause faster mass transfer, which also serves to decrease fwhm values. These trends in fwhm values with varying flow rate and temperature mirror those observed in previous studies.[34]

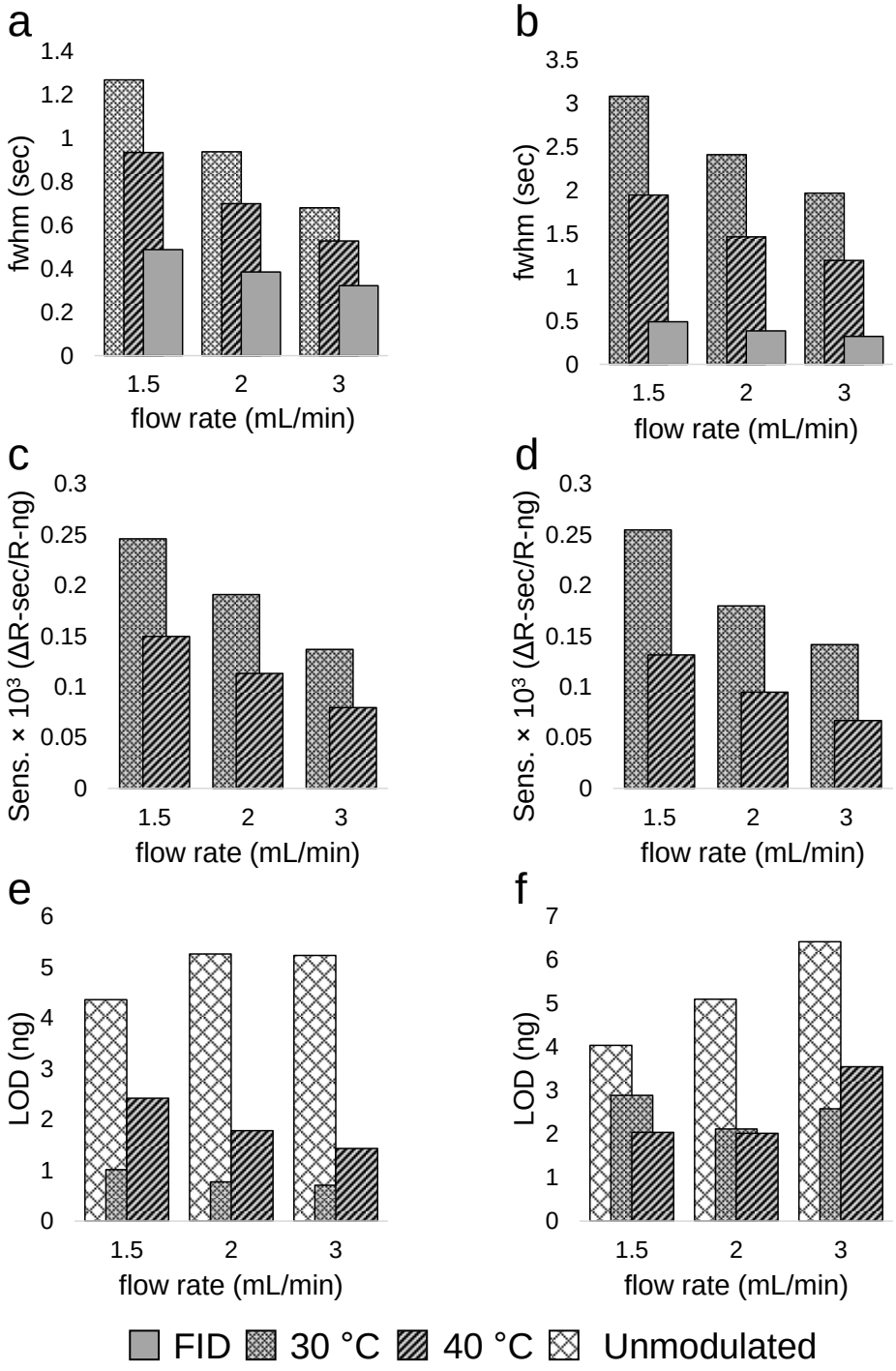

Figure 6.4. a,b) Representative charts of fwhm vs. flow rate for C10 on C8-CR (a) and OPH-CR (b) at different temperatures with FID for reference. c,d) Representative charts of sensitivity vs. flow rate for C10 on C8-CR (c) and OPH-CR (d) at different temperatures. e,f) Representative charts of LOD vs flow rate with no modulation; All data shown is for C10.

The sensor sensitivities were also dependent upon flow rate and temperature. Sensitivites for both types of CR were similar and highest at low flow rate and temperature. The OPH-CR sensitivity for C_7 at 3 mL/min and 40 °C was the lowest, while the most sensitive was the OPH-CR at 1.5 mL/min and 30 °C (the C8-CR at 1.5 mL/min and 30 °C was a close second). Figure 6.5a shows a plot of sensitivity versus inverse p_v for the 1.5 mL/min, 30 °C. The linearity of Figure 6.5a was conserved at the other flow rates and temperatures.[20] The aromatic compounds showed slightly increased sensitivity, though R^2 values were <0.90 in all cases. OPH-CR sensitivities did not follow this trend, likely due to pi-pi interactions in the film with the aromatic analytes. A regression line through the alkane compounds, shown in Figure 6.5b, which do not interact with the pi electrons of OPH, is linear. The increased sensitivity to the aromatic analytes relative to alkane analytes of similar p_v is expected.

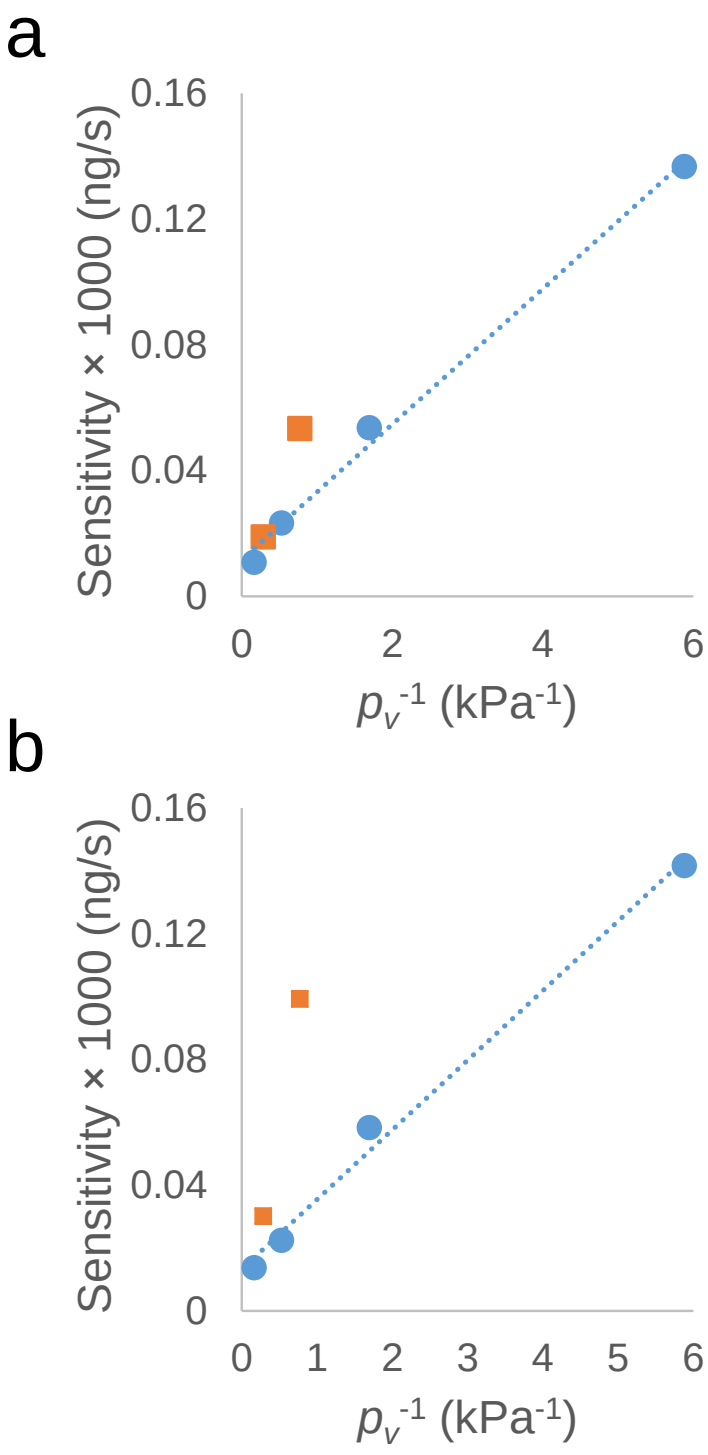

Figure 6.5. a) C8-CR sensitivity versus inverse vapor pressure at 3 mL/min and 30 °C. b) OPH-CR sensitivity versus inverse vapor pressure at 3 mL/min and 30 °C. Circles: alkanes; squares: aromatics.

Limits of detection for were as low as 0.52 ng for C9 on the C8-CR at 30 °C and 2 mL/min and as high as 22 ng for C7 on the OPH-CR at 40 °C and 3 mL/min. These values are affected by both CR conditions *and* μTM conditions, which makes direct comparison difficult. Increasing temperature is known to produce narrower, but shorter peaks,[34] which would act to increase the LOD. Increasing flow rate has the same effect, however it also reduces the modulation number via narrower ^{1}D peaks entering the μTM. This would have the effect of decreasing the LOD, since taller peaks would result. In addition, the timing of the μTM is not currently synced with the injection, which adds uncertainty to both the modulation number and the amount of a peak in any individual modulation, which would have an uncertain effect on LOD. As such, any study of LOD in terms of temperature and flow rate would be unable to separate μTM effects from CR effects.

That said, C_{10} had a relatively stable modulation number for all flow rates and temperatures so some trends could be identified. Figures 6.4e and f show the LOD values calculated for each sensor type at each flow rate and temperature as well as without modulation. For the C8-CR, these results agree with expectations; unmodulated peaks give the highest LODs at every flow rate and LOD decreases with increasing flow rate. The lower temperature at each flow rate had the lowest the LOD, though at 30 °C LOD reductions due to flow rate were less significant. The OPH-CR was a bit more unstable, modulated peaks still gave lower LOD than unmodulated, however at 3 mL/min LODs increased relative to the 2 mL/min case, likely due to a shift in modulation timing that reduced the size of the modulated peaks. The results of these experiments allow for the selection of "ideal" operating parameters which reflect the tradeoffs that must be made between resolution, sensitivity and speed. A good trade-off is achieved operating the sensor at 2 mL/min and 40 °C.

6.3.3 µGC × µGC-CR

Next, the RTIL coated µcolumn was inserted in between the µTM and CR and a 20 component VOC mixture was analyzed. This mixture included analytes of interest for exposure monitoring applications[34] (compounds 3, 4, 6, 7, 12 and 13) as well as potential breath biomarkers of disease (compounds 9, 14 and 19).[1,35] The 2-D contour plot is shown in Figure 6.5. Separations that would have been difficult, if not impossible, on a single 6-m column were easily done with the µGC × µGC. For example, compounds 4-7 would not have been separated in 1D-µGC. Compounds 2/3 and13/14 would be completely overlapped. The added dimension of separation allowed for easy separation of these analytes from one another. Values of fwhm ranged from 0.31 to 1.5 s. These are larger than those measured for the 6 compound mixture, which can be attributed to broadening on the ^{2}D µcolumn. The wide range of ^{2}D t_Rs indicates efficient use of the available separation space. As expected, the composite response from the two differently coated CR sensors produced responses patterns that were unique for each analyte, which could be used for identification purposes (inset).

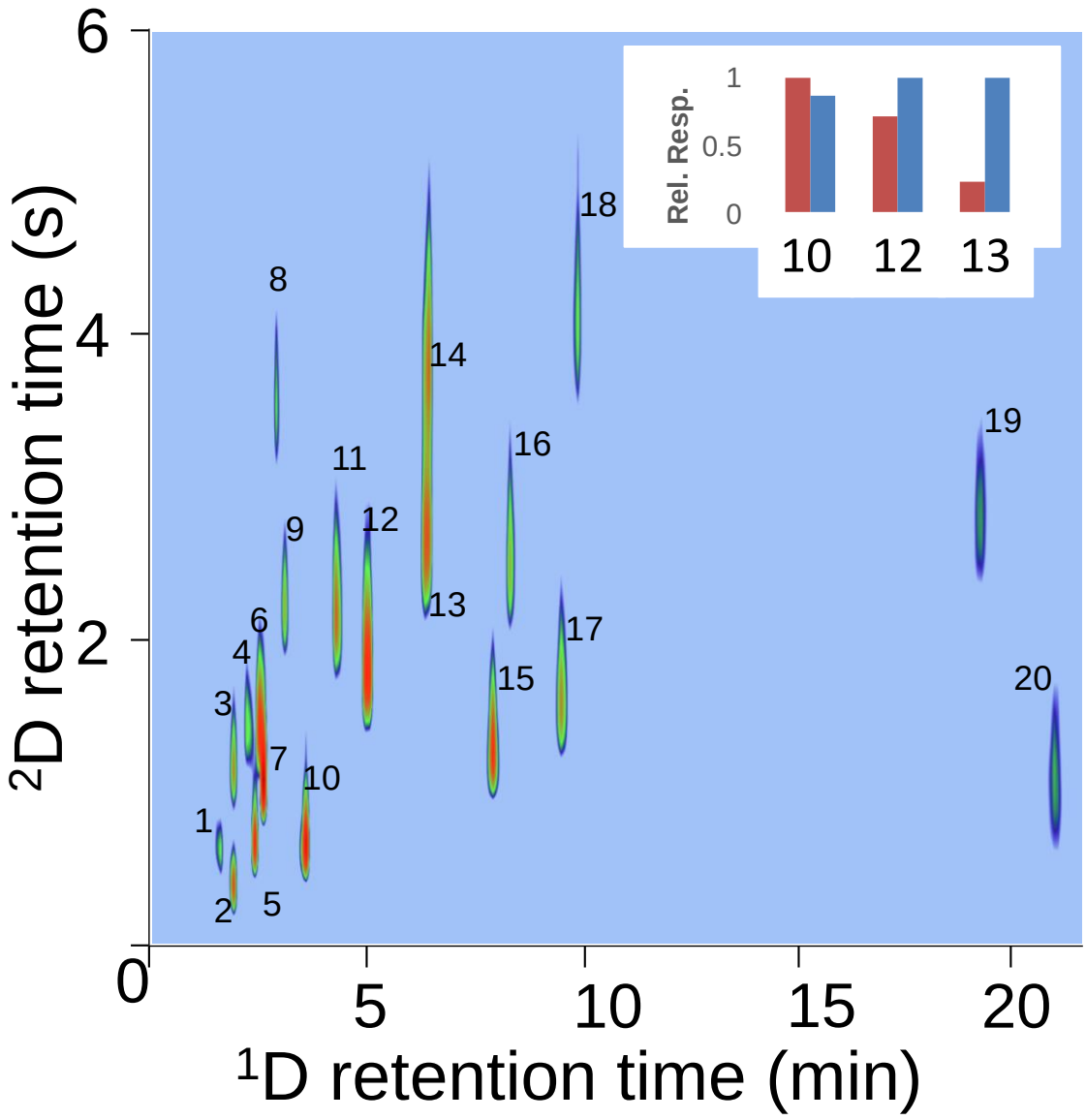

Figure 6.6. Contour plot showing the separation of 20 compounds. A C8-CR was used for detection. Compounds: 1) fluorobenzene; 2) heptane; 3) 1,4-dioxane; 4) 1,1,2-trichloroethane; 5) 1-chloropentane; 6)4-methyl-2-pentanone; 7) toluene; 8) cyclopentanone; 9) 2-hexanone; 10) octane; 11) chlorobenzene; 12) ethylbenzene; 13) o-xylene; 14) 3-heptanone; 15) nonane; 16) cumene; 17) (+)α-pinene; 18) 2-chlorotoluene. Conditions: ~0.1 ug injection from a static test atmosphere; 1.5 mL/min He carrier gas; isothermal 30 °C 1D µcolumns; isothermal 50 °C 2D RTIL coated µcolumn; 6 s modulation period; µCR held at 30 °C. Inset: response patterns generated for compounds 10, 12 and 13 using C8 and OPH CR sensitivities.

6.3.4 μGC × μGC-CR Microsystem

The assembled microsystem was tested using a specialty industrial paint thinner and a newly coated μCR array. This mixture was chosen because the MSDS indicated a mixture of polar and non-polar solvents and a moderate vapor pressure range. Most importantly, it contains several compounds which are common potential health hazards which would be challenging to separate in a 1D separation. For this experiment, 10 μL of the solvent was injected into an aluminized gas sampling bag (Supelco) containing 9L of nitrogen. A 1.5 mL sample of this was loaded onto the μPCF, which equates to a total mass of roughly 140 ng of the mixture. The sampler was then rapidly heated (25-225 °C in 3 s) and held at 225 °C for 30 s to ensure complete desorption. This transferred the preconcentrated sample into the separation module. The 1D and 2D μcolumns were temperature programmed.

The resulting 2-D contour plot is shown in Figure 6.8. For simplicity, only the results using the C8-CR are shown. Several peaks were identified on the basis of peak matching with known standards from previous experiments using the same mixture and FID detection (data not shown). The fwhm values of these peaks ranged from 150 ms to 2.4 s. Broad peaks for polar compounds were expected based on previous work.[19] Of note are the separations that would have been extremely difficult in a single dimension, namely the separation of the aromatic and keto compounds, some of which have known adverse health effects, from the relatively innocuous ligroin mixture.[30] This highlights the utility of μGC × μGC in such an application. Identification and quantitation of those compounds would be hindered by co-elution. Although quantitation was not the goal of this proof-of-function experiment, careful calibration would enable the quantitation of those peaks, free of alkane interferences.

6.4 Conclusions

Separations by μGC × μGC require a detector capable of measuring extremely narrow peaks. The μCR tested produced peaks significantly narrower than modulation periods typically used in μGC × μGC, making it a promising detector for future microsystems. The initial μCR tested utilized two different MPN films, C8 and OPH that yielded peaks significantly broader than those from the FID under similar conditions. The vapor pressure dependence of sorption based sensors affected their responses. This was surprising in light of the close agreement in the 1-D μGC separations. The analysis of a mixture which included targets of exposure assessment and breath biomarker analysis highlight the utility of a portable instrument for these applications.

While far from a complete characterization of the first microsystem, the proof-of-function experiment conducted shows the obvious utility of the breadboard instrument constructed. The separation of a moderately complex mixture, rapidly and with little coelution, is a promising result. A complete characterization of the microsystem would include quantitative results, as well as more complex separations.

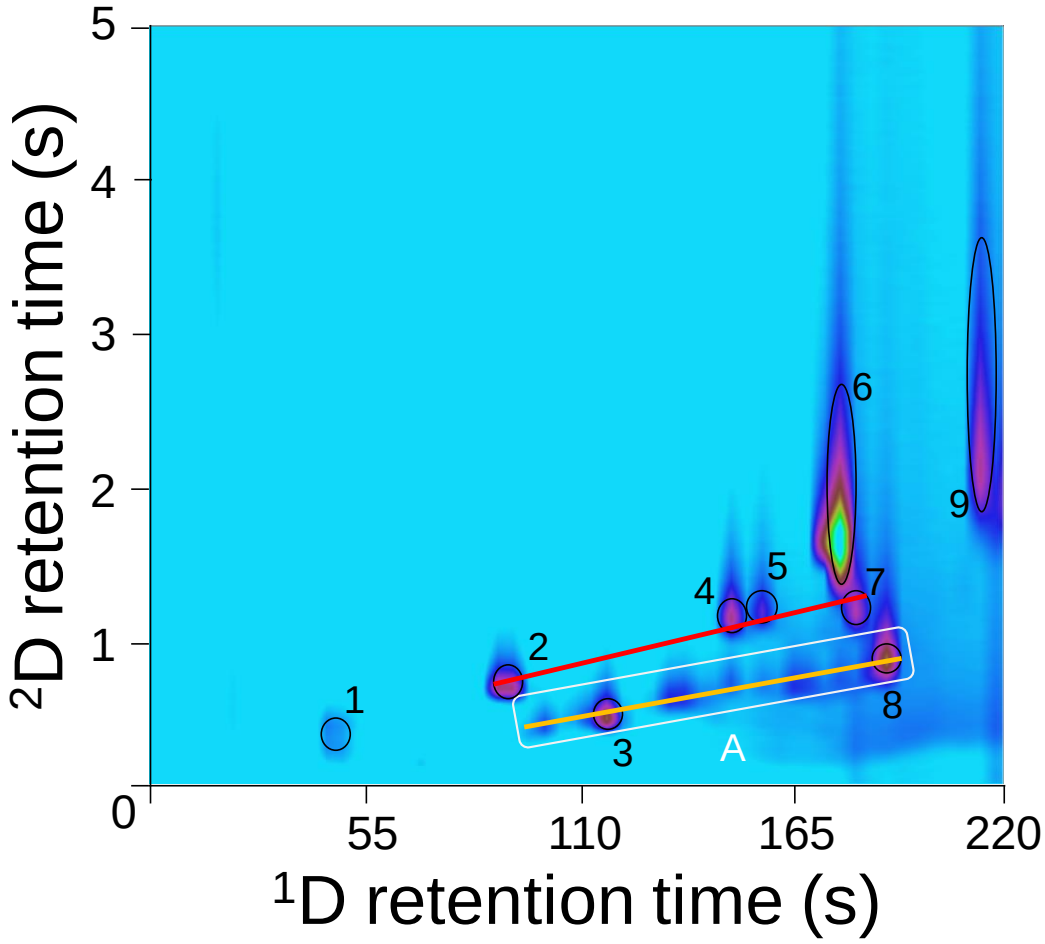

Figure 6.7. Chromatogram of a specialty paint thinner generated using microsystem. Compounds: 1) butanone; 2) toluene; 3) octane; 4) ethylbenzene; 5) *m*-xylene; 6) 2-heptanone; 7) *o*-xylene; 8) nonane; 9) ethyl 3-ethoxypropionate. The white box labeled A encompasses the hydrocarbon mixture known as ligroin. Conditions: ^{1}D and ^{2}D column program: 0-150 s, 30 to 50 °C; 150-180 s, 50 to 140 °C; 180 to 270 s, 140 to 150 °C. T_{min} and T_{max} values gradually increased throughout the run; from 0 – 120 s T_{min} was -30 °C and T_{max} was 100 °C, from 120 to 180 s T_{min} increased from -30 °C to 0 °C and T_{max} increased from 100 °C to 210 °C. The final condition was held from 180 -270 s. ^{1}D and ^{2}D µcolumns temperature programmed (see text); µTM temperature programmed (see text); He carrier gas 2 mL/min; 5 s P_m; 136 ng sample injected. The heavy lines indicate structure; orange corresponds to alkane compounds and red corresponds to aromatics.

6.5 References

REFERENCES

36. Phillips, Michael, et al. "Detection of lung cancer using weighted digital analysis of breath biomarkers." *Clinica Chimica Acta* 393.2 (2008): 76-84.
37. Brinke, J. Ten, et al. "Development of new volatile organic compound (VOC) exposure metrics and their relationship to “sick building syndrome” symptoms." *Indoor Air* 8.3 (1998): 140-152.
38. Lara-Gonzalo, Azucena, et al. "Critical comparison of automated purge and trap and solid-phase microextraction for routine determination of volatile organic compounds in drinking waters by GC–MS." *Talanta* 74.5 (2008): 1455-1462.
39. Llompart, Maria, Ken Li, and Merv Fingas. "Headspace solid phase microextraction (HSSPME) for the determination of volatile and semivolatile pollutants in soils." *Talanta* 48.2 (1999): 451-459.
40. Sekiguchi, Hiroyuki, et al. "On-site determination of nerve and mustard gases using a field-portable gas chromatograph-mass spectrometer." *Forensic toxicology* 24.1 (2006): 17-22.
41. Collin, William R., et al. "Microfabricated gas chromatograph for rapid, trace-level determinations of gas-phase explosive marker compounds."*Analytical chemistry* 86.1 (2013): 655-663.
42. Zampolli, S., et al. "Real-time monitoring of sub-ppb concentrations of aromatic volatiles with a MEMS-enabled miniaturized gas-chromatograph." *Sensors and Actuators B: Chemical* 141.1 (2009): 322-328.
43. Kim, S.; Burris, D.; Bryant-Genevier, J.; Gorder, K.; Dettenmaier, E.; Zellers, E.T., *Environ. Sci. and Technol.*, **2012,** 46, 6073-6080.
44. Qin, Yutao, and Yogesh B. Gianchandani. "iGC2: an architecture for micro gas chromatographs utilizing integrated bi-directional pumps and multi-stage preconcentrators." *Journal of Micromechanics and Microengineering* 24.6 (2014): 065011.
45. Garg, Apoorva, et al. "Zebra GC: A mini gas chromatography system for trace-level determination of hazardous air pollutants." *Sensors and Actuators B: Chemical* 212 (2015): 145-154.
46. Dimandja, Jean-Marie D. "Peer Reviewed: GC X GC." *Analytical Chemistry* 76.9 (2004): 167-A
47. Edwards, Matthew, Ahmed Mostafa, and Tadeusz Górecki. "Modulation in comprehensive two-dimensional gas chromatography: 20 years of innovation." *Analytical and bioanalytical chemistry*401.8 (2011): 2335-2349.
48. Whiting, Joshua J., et al. "High-speed two-dimensional gas chromatography using microfabricated GC columns combined with nanoelectromechanical mass sensors." *Solid-State Sensors, Actuators and Microsystems Conference, 2009. TRANSDUCERS 2009. International*. IEEE, 2009.
49. Chen, Bo-Xun, et al. "A multidimensional micro gas chromatograph employing a parallel separation multi-column chip and stop-flow μGC× μGCs configuration." *Lab on a Chip* 13.7 (2013): 1333-1341.
50. Liu, Jing, et al. "Smart multi-channel two-dimensional micro-gas chromatography for rapid workplace hazardous volatile organic compounds measurement." *Lab on a Chip* 13.5 (2013): 818-825.

51. Kim, S.J.; Reidy, S.; Block, B.; Wise, K.; Zellers E.T.; Kurabayashi, K.; *Lab Chip*, 2010, 10, 1647–1654.
52. Kim, S.J.; Serrano, G.; Wise, K.; Kurabayashi, K.; Zellers, E.T.; *Anal. Chem.*, 2011, 83, 5556–5562.
53. Serrano, G.; Paul, D.; Kim, S.J.; Kurabayashi, K.; Zellers, E.T.; *Anal. Chem.*, 2012, 84, 16, 6973–6980.
54. Collin, William R., et al. "μGC× μGC: Comprehensive Two-Dimensional Gas Chromatographic Separations with Microfabricated Components." *Analytical chemistry* 87.3 (2015): 1630-1637.
55. Collin, William R., et al. "Polymer-Coated Micro-Optofluidic Ring Resonator Detector for a Comprehensive Two-Dimensional Gas Chromatographic Microsystem: μGC× μGC–μOFRR."*Analyst* (2015).
56. Cai, Qing-Yun, and Edward T. Zellers. "Dual-chemiresistor GC detector employing monolayer-protected metal nanocluster interfaces." *Analytical chemistry* 74.14 (2002): 3533-3539.
57. Lu, Chia-Jung, and Edward T. Zellers. "A dual-adsorbent preconcentrator for a portable indoor-VOC microsensor system." *Analytical Chemistry* 73.14 (2001): 3449-3457.
58. Lu, Chia Jung, and Edward T. Zellers. "Multi-adsorbent preconcentration/focusing module for portable-GC/microsensor-array analysis of complex vapor mixtures." *Analyst* 127.8 (2002): 1061-1068.W.-C. Tian, S. Pang, C.-J. Lu, E.T. Zellers, Microfabricated preconcentrator-focuser for a microscale
59. W.C. Tian, H.K.L. Chan, C.-J. Lu, S.W. Pang, E.T. Zellers, Microfabricatedmulti-stage preconcentrator-focuser for a micro gas chromatograph, J. Micro-electromech. Syst. 14 (2005) 498–507.
60. M. Akbar, D. Wang, R. Goodman, A. Hoover, G. Rice, J.R. Heflin, et al., Improved performance of micro-fabricated preconcentrators using silica nanoparticles as a surface template, J. Chromatogr. A 1322 (2013) 1–7.
61. B.Alfeeli,V. Jain, R.K. Johnson, F.L. Beyer, J.R. Heflin, M.Agah, Characterization of poly(2,6-diphenyl-p-phenylene oxide) films as adsorb
62. Rowe, M.; Plass, K.; Kim, K.; Kurdak, Ç.; Zellers, E. T.; Matzger, A. Chem. Mater. 2004, 16, 3513−3517.
63. Payagala, Tharanga, et al. "Trigonal tricationic ionic liquids: a generation of gas chromatographic stationary phases." *Analytical chemistry* 81.1 (2008): 160-173.
64. Bryant-Genevier, Jonathan, and Edward T. Zellers. "Toward a Microfabricated Preconcentrator-Focuser for a Wearable Micro-scale Gas Chromatograph." Journal of Chromatography A (2015).
65. M. Agah, J.A. Potkay, G.R. Lambertus, R.D. Sacks, K.D. Wise, High performance temperature-programmed microfabricated gas chromatography columns, IEEE J. Microelectromech. Syst. 14 (5) (2005) 1039–1050.
66. J.A. Potkay, G.R. Lambertus, R.D. Sacks, K.D. Wise, A low power pressure and temperature-programmable micro gas chromatography column, J. Microelectromech. Syst. 16 (2007) 1071–1079.
67. Reidy, Shaelah, et al. "High-performance, static-coated silicon microfabricated columns for gas chromatography." *Analytical chemistry* 78.8 (2006): 2623-2630.
68. Serrano, Gustavo, Shaelah M. Reidy, and Edward T. Zellers. "Assessing the reliability of wall-coated microfabricated gas chromatographic separation columns." *Sensors and Actuators B: Chemical* 141.1 (2009): 217-226.

69. Wright, L. K., and E. T. Zellers. "A nanoparticle-coated chemiresistor array as a microscale gas chromatograph detector for explosive marker compounds: flow rate and temperature effects."*Analyst* 138.22 (2013): 6860-6868.
70. NIOSH Pocket Guide to Chemical Hazards http://www.cdc.gov/niosh/npg/ accessed 11/21/15
71. Banday, Khalid Muzaffar, et al. "Use of urine volatile organic compounds to discriminate tuberculosis patients from healthy subjects."*Analytical chemistry* 83.14 (2011): 5526-5534.

CHAPTER 7

CONCLUSIONS AND FUTURE DIRECTIONS

7.1 Conclusions

The body of research presented in this dissertation entailed several aspects of the design, assembly, characterization, and optimization of μGC and μGC × μGC systems and their components for analyzing mixtures of S/VOCs relevant to homeland security, environmental contamination monitoring, and biomedical diagnostics. This chapter summarizes the major achievements and conclusions reached, the impacts of the accomplishments, the lessons learned, and the directions that future efforts in this area might take.

The first chapter provided a review of the underlying principles and theory relevant to the components and systems developed here. It also provided a critical analysis of the metrics of μGC system performance.

The second chapter presented a prototype microfabricated gas chromatograph (μGC) adapted specifically for the rapid determination of selected gas-phase marker compounds of the explosive 2,4,6-trinitrotoluene (TNT) at sub-parts-per-billion (ppb) air concentrations in complex mixtures. This project was purely application driven. That is to say a problem was identified, and the instrument was built to solve it. In Chapter 2, components including Si-microfabricated

focuser, separation column, and sensor array, were integrated with a high-volume sampler of conventional construction to reduce analysis time and limits of detection (LOD). The markers selected as targets of the analysis were 2,4-dinitrotoluene (2,4-DNT; a persistent impurity of TNT) and 2,3-dimethyl-2,3-dinitrobutane (DMNB; a taggant), with 2,6-dinitrotoluene (2,6-DNT; a less prominent impurity) also included in numerous tests. Through the use of selective preconcentration, on-column focusing, temperature-programmed chromatographic separation, and sensor array detection/recognition, determinations of the primary markers in the presence of 20 (or more) interferences in ~ 2 min under laptop control is demonstrated. LODs are estimated to be 2.2, 0.48, and 0.86 ng for DMNB, 2,6-DNT, and 2,4-DNT, respectively, which correspond to 0.30, 0.067, and 0.12 ppb for a 1-L air sample. This chapter highlighted and, to some extent, solved problems unique to the analysis of extremely-low volatility analytes. First and foremost is the need to adequately heat interconnections to prevent wall-adsorption of analyte, which broadens chromatographic peaks. Broader peaks are more difficult to distinguish from closely eluting interferences, so elimination of all possible sources of broadening is desirable. Mitigation of broadening that does occur was accomplished through on-column focusing, adding another tool to the chromatographic toolbox for use in μGC.

The third chapter dealt with the development and characterization of a microanalytical subsystem comprising Si-microfabricated first- and second-dimension separation columns and a Si-micromachined thermal modulator (μTM) for comprehensive two-dimensional (i.e., μGC × μGC) separations. The first separation dimension consisted of two series coupled 3.1 × 3.1 cm μcolumn chips with etched channels 3-m long and 250 × 140 μm in cross section, wall-coated with a PDMS stationary phase. The second separation dimension consisted of a 1.2 × 1.2 cm μcolumn chip with an etched channel 0.5-m long and 46 × 150 μm in cross section wall-coated with either

a trigonal tricationic room-temperature ionic liquid (RTIL) or a commercial poly(trifluoropropylmethyl siloxane) (OV-215) stationary phase. This represents the first successful use of RTIL as the stationary phase coating in a μcolumn. The development of this new material (done in the Armstrong Group at the University of Texas and Supelco) and the method for coating it (and materials like it) is a valuable endeavor because the stationary phases currently used in μGC lag behind those available for capillary GC in terms of versatility. Solving this shortcoming is necessary since, ideally, any extant capillary GC method could be translated to μGC. The μTM consisted of a Si chip containing two series coupled, square spiral channels 4.2 and 2.8 cm long and 250 × 140 μm in cross section wall-coated with PDMS. This μTM uses no cryogen, instead it uses a ~20 W thermoelectric cooler. The experiments used conventional injection methods and flame ionization detection. Temperature-ramped separations of a simple alkane mixture using the RTIL-coated ^{2}D μcolumn produced reasonably good peak shapes and modulation numbers; however, strong retention of polar compounds on the RTIL-coated ^{2}D μcolumn led to excessively broad peaks with low ^{2}D resolution. Substituting OV-215 as the ^{2}D μcolumn stationary phase markedly improved the performance. A structured 22-min chromatogram of a 36-component mixture spanning a vapor pressure range of 0.027 to 13 kPa was generated with modulated peak *fwhm* values ranging from 90 to 643 ms and modulation numbers of 1-6. This was the first report a μGC × μGC system where all key separative processes occurred in/on silicon chips.

Chapter 4 departed slightly from the microsystem focus of the preceding and next chapters to investigate aspects of the μTM. The effect of dynamically programming the minimum and maximum temperatures (T_{min} and T_{max}) was investigated. With constant T_{min} and T_{max} values of -25 and 100 °C respectively, extremely broad peaks were observed for low vapor pressure (p_v)

compounds while high p_v compounds were effectively trapped. Alternatively, constant T_{min} and T_{max} values of 0 and 220 °C yielded complete breakthrough of high p_v compounds and excellent trapping and remobilization of low p_v compounds. By dynamically changing T_{min} and T_{max} throughout the separation, it was shown that peak width could be kept to a minimum and breakthrough could be minimized for all p_v compounds tested, with peak *fwhm* values <100 ms for all compounds tested (note: no stationary phase coating was used in the second column for this experiment). This step forward required the mounting of the μTM outside of the GC oven, which had not been done previously and necessitated an interconnection heater. The lessons learned from heating components in Chapter 2 were used in the design of this interconnect. Using capillary GC columns similar to those used for commercial bench scale applications, the components of a sample of gasoline were separated in 15 minutes. Through the use of the temperature programmed μTM, peak *fwhm* values ranged from 145 ms to 460 ms. This represented the most complex mixture yet separated using the μTM. In an effort to fully take advantage of the new thermal programming options, specifically the higher range of temperatures now accessible, the RTIL used in Chapter 3 was coated on the μTM. This switch was made in an effort to eliminate stationary phase bleed noted in the PDMS coated μTM, as the RTIL had previously been shown to be more stable at high temperature. This hypothesis proved accurate, unfortunately the retention characteristics of the RTIL limited its utility. Significant breakthrough was evident several analytes in each of three compound classes: alkanes, aromatics and aldehydes.

The final two chapters take the microanalytical system used in Chapter 3 and attempt to push it a further step towards a complete, stand-alone microsystem. In Chapter 5 the first results from a micro-analytical subsystem that integrates a detector comprising a polymer-coated micro-optofluidic ring resonator (μOFRR) chip with a microfabricated separation module capable of

performing thermally modulated comprehensive two-dimensional gas chromatographic separations (μGC × μGC) of volatile organic compound (VOC) mixtures was presented. The μOFRR (2 × 2 cm) chip consists of a hollow, contoured SiO_x cylinder (250 μm i.d.; 1.2 μm wall thickness) grown from a Si substrate, and integrated optical and fluidic interconnection features. Whispering gallery mode (WGM) resonances were generated within the μOFRR wall by coupling to a 1550-nm tunable laser and photodetector via an optical fiber taper. Shifts in the WGM wavelength caused by reversible sorption of eluting vapors from the ^{2}D microsystem PDMS film lining the μOFRR cylinder were monitored. Isothermal separations of a simple alkane mixture using on the microsystem confirmed that efficient μGC × μGC–μOFRR analyses could be performed and that responses were dominated by film-swelling. The modulated peak width and the sensitivity to the VOCs were inversely proportional to the vapor pressure of the analyte, as revealed by tests with more diverse (7 and 11 component) VOC mixtures. Modulated peaks as narrow as 120 ms were comparable to previous results using FID. Limits of detection in the low-ng range were achieved, which is in the same range as results obtained with CR devices in Chapter 2. Structured contour plots, the hallmark of GC × GC separations, generated with the μOFRR were comparable to FID. This study further highlighted the need to know fully the effect of vapor pressure on peak dynamics, and the need for a way to mitigate the dependence as much as possible.

Chapter 6 is very similar to Chapter 5, though a CR array was used in place of the μOFRR. A newly designed CR array was tested using octanethiol (C8) and 6-phenoxyhexanethiol (OPH) as interface layers. The CR array was first evaluated in terms of *fwhm* and t_R fidelity without thermal modulation on a mixture of 6 compounds, including alkanes and aromatics to evaluate the efficacy of the new sensor design. Close agreement between the CR array results and FID for these experiments were promising for the ultimate use as a detector for μGC × μGC separations.

Modulated separations were then performed and, in contrast to the single dimension separations, the FID consistently yielded peaks ~2X narrower than the C8-coated CR and ~4X narrower than the OPH-coated CR. Sensitivities were generally inversely related to p_v, though deviations were observed for the aromatic compounds, especially for the OPH-coated CR which afforded pi-pi interactions with the aromatic analytes. Sensitivities were maximized at low flow rate and lower temperature. Limits of detection ranged from as low as 0.5 ng (C9 on C8-coated CR) to as high as 22 ng (C7 on OPH-coated CR). Due to the nature of the modulation process, the effects of temperature and flow rate on LOD were volatile, the exact peak height being strongly dependent on the timing of the modulation. A moderately complex separation of VOCs chosen from targets of biomarker and exposure assessment was performed using the microsystem with excellent use of two dimensional space and resolution. Structured separation was achieved for compounds eluting early in the chromatogram and somewhat degraded near the end where chromatographic conditions were less than ideal for the low-volatility compounds. Finally, a stand-alone microsystem was assembled and a preliminary test was presented. The results of these experiments further highlighted the need for tight temperature control of all aspects of the chromatographic instrument, as any band broadening associated with narrow μGC × μGC peaks can drastically degrade separations.

7.2 Future Directions

The preceding chapters have shown the development of μGC and μGC × μGC technology that should enable its use in many areas where benchtop GC analysis is unwieldy, inconvenient or prohibited by time. The 1D-μGC prototype demonstrated that even very low-volatility compounds can be analyzed via μGC *in situ* for homeland security applications. Though we only targeted markers of TNT, the instrument could be refined further to capture and analyze a wide range of

compounds. The difficulty of transferring these high-boiling compounds was recognized and alternative methods for overcoming this issue would include more localized heating of interconnects to form a continuously heated path for analyte. Such a heating system could be made with traditional machining techniques and existing off-the-shelf heaters.

The μGC × μGC has the potential to solve an even greater number of analytical problems if remaining issues can be resolved. First and foremost, and similarly to the single dimension case mentioned, it is absolutely vital to find an improved method to prevent the adhesion of analyte *in between* analytical components. This is especially critical for μGC × μGC, since the peak widths are so narrow that even modest increases degrade performance significantly and gains made by the addition of a second dimension are lost. The second critical shortcoming that must be overcome before the extant μTM can have the impact that it is surely capable of is increasing the range of volatility that it can effectively trap and release. There are two aspects to this problem. The first is the minimum temperature, which as Chapter 4 showed is critical to trapping of volatile compounds. Commercial consumable free instruments reach minimum modulation temperatures of -80 °C and cryogenic systems reach even lower temperatures.

Currently the μTM can only reach -25 °C. This may be sufficient for portable applications, however if the μTM is to be used in a benchtop GC, this is certainly insufficient. The minimum temperature is partly limited by the air cooling of the thermoelectric cooler (TEC), which uses a heatsink and a fan to lower the temperature of the back-side of the TEC. More efficient cooling using liquid heatsink chillers would be more efficient and possibly enable even lower TEC temperatures to be achieved. The maximum temperature of the μTM is a further hindrance. Currently, the PDMS stationary phase coating is limited to roughly 210 °C, beyond that stationary phase bleed increases prohibitively. Attempts to use an RTIL were successful in preventing bleed

at higher μTM temperatures, though the trapping ability left something to be desired. This does not close the door on this possibility though, as there is a massive library of other possible RTILs that could find utility as sorptive, bleed-free μTM coatings. Solving these problems would enable a consumable-free device that would enable many laboratories that ordinarily could not do GC × GC separations to do so cheaply and easily.

In conclusion, if these problems can be solved the door is opened to many applications where an on-site, high peak capacity instrument with the ability to quickly separate complex mixtures are needed. This would include, but not be limited to breath sampling in clinics, crude oil analysis at well sites, exposure assessment, food contaminant analysis (pesticides) and food origin authentication. Essentially, any application where samples must be collected in the field for analysis in a lab could benefit from this powerful tool. The potential for a cheap, simple, low-maintenance modulation device would enable the technique to find new applications by virtue of accessibility. The μTM, as demonstrated in Chapter 4, has that potential.

APPENDIX 1
SUPPORTING INFORMATION FOR CHAPTER 2

A1.1 Flow paths during each operating mode of the INTREPID prototype

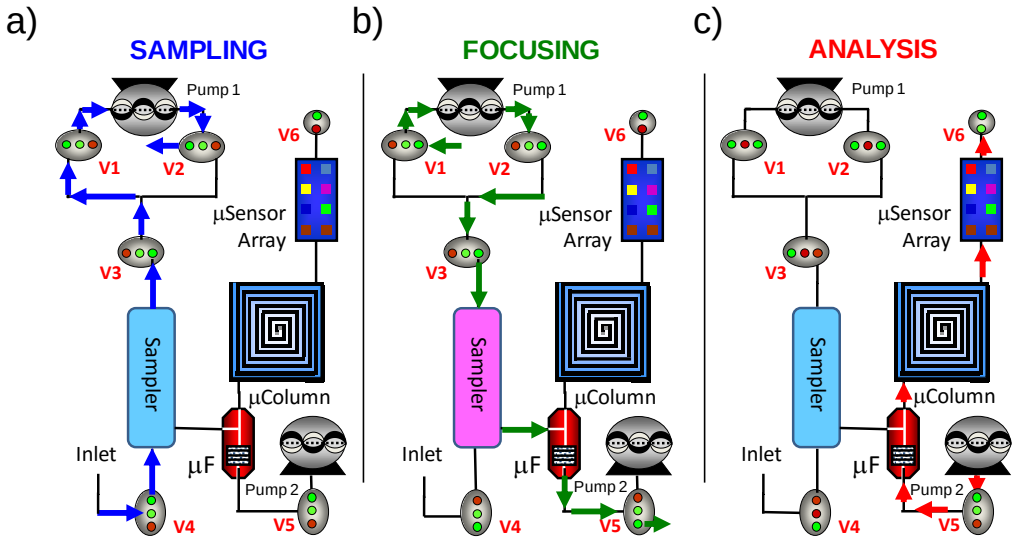

Figure A1.1. Schematic diagrams showing the three operational modes and the corresponding sample flow paths of the INTREPID prototype.

A1.2 Descriptions of the components of the INTREPID prototype

The µF chip (Figure 2.2b) contains a hexagonal deep-reactive-ion-etched (DRIE)-Si cavity (3.2 × 3.5 mm) with tapered inlet/outlet sections, a side-port channel for adsorbent loading (2.4 mg of C-B sieved to a size range of 212-250 µm), and narrow DRIE-Si pillars near the inlet and

outlet ports for retaining the adsorbent. One of the two etched flow channels connecting the cavity to the edge of the chip has a tee branch through which vapors desorbed from the sampler are passed to the μF. The entire chip is capped with an anodically-bonded Pyrex cover plate. Evaporated Cr/Au heater contacts and a Ti/Pt resistive temperature device (RTD) are used for heating and monitoring temperature during thermal desorption/injection, which entails heating to 225 °C in < 0.6 s for all testing performed in this study. Short segments of deactivated fused silica capillary were inserted into the three fluidic ports at the edge of chip and sealed with high-temperature silicone adhesive (Duraseal® 1531, Cotronics, Brooklyn, NY).

The 1.8 × 1.8 cm^2 μcolumn chip (Figure 2.2c) contains a 1-m long convolved square spiral DRIE-Si channel with a rectangular cross-section (150 × 240 μm) capped with an anodically bonded Pyrex cover plate, and two meander-line Au/Cr integrated heaters and Ti/Pt temperature sensors for rapid temperature programming. Deactivated fused silica capillary segments (0.25 mm i.d., ~10-cm long) were inserted into expansion sections at the inlet and outlet ports at opposing edges of the chip and sealed with epoxy (Hysol Epoxy Patch 1C, Rocky Hill, CT). The μcolumn channel was statically coated with a 0.15-mm thick PDMS stationary phase (OV-1, Ohio Valley Specialty Chemical, Marietta, OH) from solution and cross-linked using dicumyl peroxide.

The 2.0 × 1.2 cm CR-array chip (Figure 2.2d) has two rows of four Au/Cr interdigital electrodes (IDEs) patterned on a thermal-SiO_x/Si substrate. Each IDE has 24 electrode pairs with the following dimensions: 5 μm widths/spaces, 450 μm length, and 410 μm overlap. The array was cleaned by sequential immersion in acetone and 2-propanol with sonication and dried in air. Solutions of each type of MPN (~5 mg/mL; toluene for C8, DPA, and OPH; methylene chloride for HME) were prepared and adjacent sensors were coated with the same type of MPN by drop casting from solutions with a 0.5 μL syringe to create multilayer films with baseline resistances

between 1-10 MΩ. The array was enclosed beneath a Macor block using a VHB-tape gasket (3M, St. Paul, MN), resulting in a detector cell volume of ~1.6 μL. Inlet/outlet ports drilled into the Macor lid were fitted with deactivated fused-silica capillaries and sealed with epoxy.

A1.3 Electronic Hardware and Software

A custom pneumatic-control PCB connected to a digital I/O card (USB-6501, National Instruments, Austin, TX) was used to actuate the pumps, valves, fans, interconnection heaters, and sampler heaters. A second PCB connected to a 16-bit multi-functional DAQ card (USB-6218, National Instruments) provided control of the μF and μcolumn heaters as well as the readout of the thermistors on the PCBs and RTDs on the devices. This PCB also carried circuitry for sensor response amplification, signal filtering, and sensor signal readout. A 3 VDC bias was applied from an on-board coin battery to each of the eight MPN-coated CRs through a matched reference resistor. The change in voltage measured across each CR was recorded by the DAQ card at 20 Hz after amplification of the signal difference between baseline and measured values. The relative resistance change of each CR was calculated as a function of this measured voltage and instrumental settings. A USB hub connected the PCBs to a laptop computer running a control program written in LabVIEW (Ver. 8.5, National Instruments, Austin, TX). Additional components of INTREPID included a power supply and a mini-oven temperature controller with a digital meter, which were embedded together in a separate external unit.

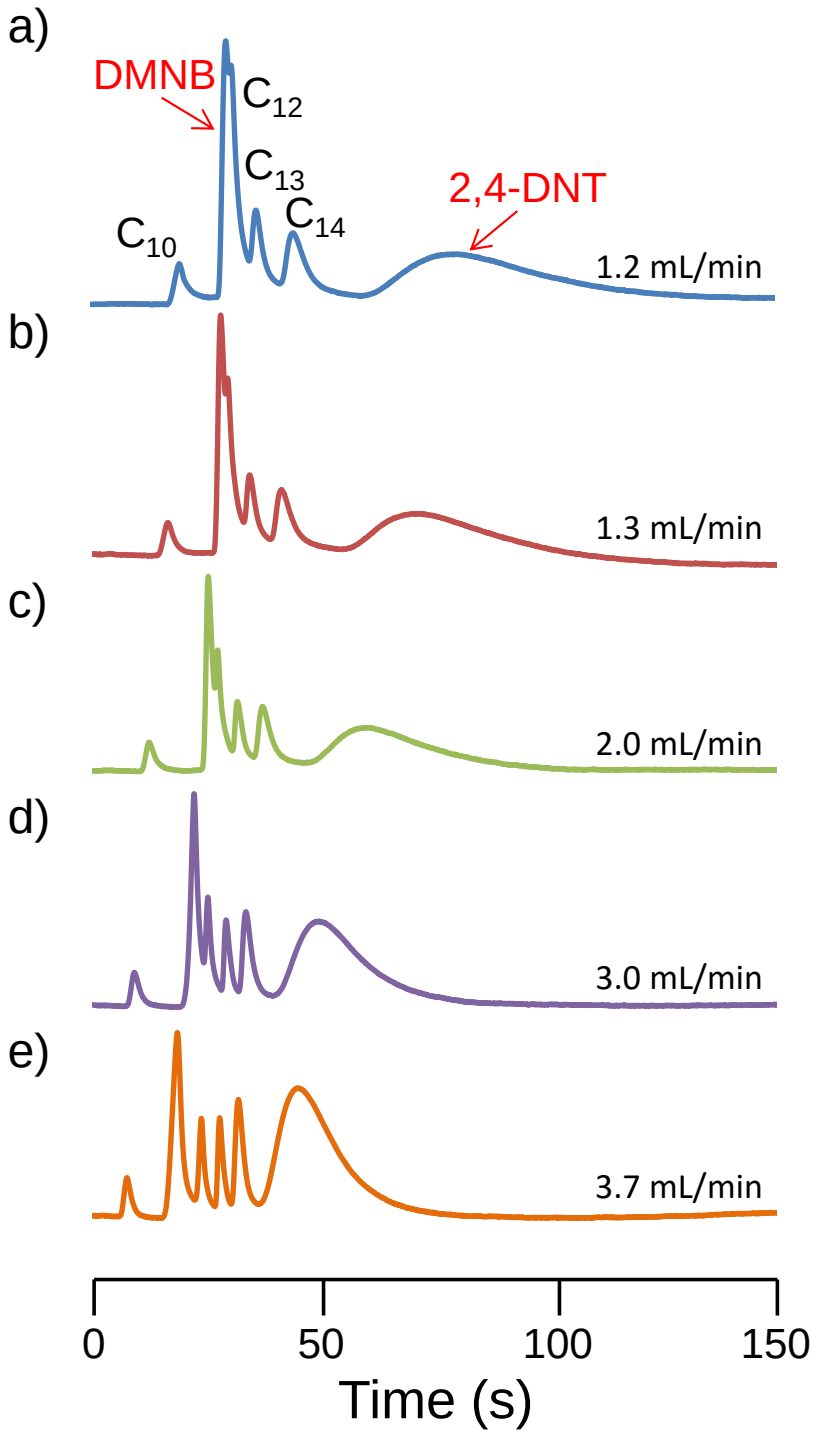

Figure A1.2. Chromatograms obtained with the INTREPID microsystem (i.e., µF, µcolumn, and MPN-coated CR array; HME sensor output shown) at the following flow rates: a) 1.2; b) 1.3; c) 2.0; d) 3.0; and e) 3.7 mL/min. Baseline oven (microsystem) temperature: 70°C; µcolumn temperature program: 70 °C for 20 s, ramp at 8 °C/s for 7.5 s, hold at 130 °C. Baseline GC oven temp: 70 °C. (Note: the data at 3.0 ml/min were presented in ref. 31 and are included here for completeness).

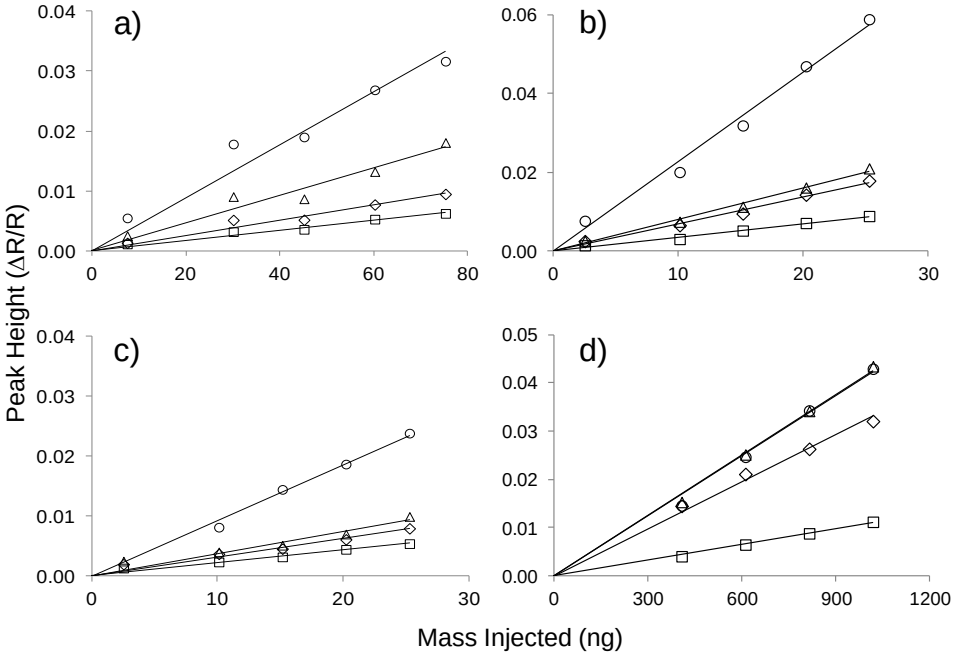

Figure A1.3. Calibration curves generated using the INTREPID microsystem for a) DMNB; b) 2,6-DNT; c) 2,4-DNT; d) C_{13}. Legend: C8, diamonds; DPA, squares; OPH, triangles; HME, circles. The ranges of injected masses were as follows: 7.5-75 ng for DMNB; 2.5-25 ng for 2,6- and 2,4-DNT; and 450-1000 ng of C_{13}. Temp program for the μcolumn: 70 °C for 20 s, ramp at 8 °C/s for 7.5 s, hold at 130 °C. Baseline GC oven temp: 70 °C.

Table A1.1. Calibration curve slopes and LODs obtained using the microanalytical subsystem.

Cmpd	C8		DPA		OPH		HME	
	Slope[a]	LOD[b]	Slope	LOD	Slope	LOD	Slope	LOD
DMNB	0.13 (0.94)	6.0	0.09 (0.95)	6.6	0.23 (0.93)	2.2	0.44 (0.93)	2.4
2,6-DNT	0.69 (0.99)	1.1	0.35 (0.98)	1.6	0.80 (0.99)	0.63	2.3 (0.99)	0.48
2,4-DNT	0.31 (0.92)	2.4	0.22 (0.94)	2.5	0.37 (0.90)	1.4	1.3 (0.91)	0.86
C_{13}	0.033 (0.97)	24	0.011 (0.99)	55	0.042 (0.99)	12	0.041 (0.99)	26

[a] *Slope of peak height based calibration curve.* [b] *LOD in ng. Parenthetical values indicate r^2 for the curve.*

A1.4 Discrimination of Markers from Interferences via CR-array Response Patterns

Although good chromatographic resolution was achieved in the tests performed, the use of sensor array response patterns can enhance the reliability of analyte determinations that would otherwise be based on retention time alone. In addition, if any overlaps were to occur due to changes in analytical conditions, the response patterns could be used to determine the identities of the components of composite peaks comprising, say, a binary mixture of two analytes.

To express the diversity of the array response patterns for the markers and interferences in more quantitative terms they were assessed using Monte Carlo (MC) simulations coupled with extended disjoint principal components regression (EDPCR) classification models. Various pairs of analytes were selected and each MC-EDPCR analysis entailed a determination of whether the binary mixture could be differentiated from the individual compounds comprising the mixture. Using the experimental sensitivity values, synthetic MPN-CR responses to each vapor were generated by randomly selecting a vapor concentration within the range of 5-10×LOD, where the LOD was dictated by the least sensitive sensor in the array to ensure that all sensors were contributing to the response patterns. The response from each sensor was calculated from the calibration-curve regression equation and then error was introduced by adding to it a value obtained by multiplying that response value by a factor derived from randomly sampling a Gaussian distribution with a mean of zero and a standard deviation of 0.05, corresponding to an average random sensitivity error (ε) of 5% of the response. The error enhanced responses from each sensor were combined and then the location of the resulting response vector was projected onto the principal component corresponding to the original calibrations for each vapor via EDPCR.

Assuming linear additivity, the 'calibrated'response vectors for the binary mixture over the range of concentrations of interest (i.e., 5-10×LOD) were established and error enhanced responses to each binary mixture were generated iteratively as with the individual vapors. The identity assigned to this synthetic response vector was determined by its proximity (Euclidean distance) to the calibrated vectors for the mixture or either of the individual components. This procedure was performed iteratively (i.e., 500 samples) to yield a statistically precise estimate of recognition rate (RR) for each case considered (i.e., compound 1, compound 2, or the mixture). Details of this methodology as applied to sensor-array evaluations can be found elsewhere.[S1-S3]

Note that error is superimposed on each sensor response separately. The results of these analyses were logged in a recognition matrix that indicates the number and nature of correct and incorrect assignments of identity. Since the ability to differentiate a mixture from its components is more difficult than differentiating the individual vapors from each other (i.e, where mixtures are not considered), we have focused on the former problem. The results are summarized in Table A1.2 in terms of the recognition rate (RR, %) of the mixtures considered.

An RR value of 95% indicates a high sufficiently degree of discrimination. As shown, very low RR values were found for the C_{13}+C_{15} and 2,6-DNT+2,4-DNT mixtures, as expected from the structural similarities of the mixture components. High RR values were found for the other pairs.

Table A1.2. Recognition rates (RR, %) for EDPCR analyses of binary mixtures of marker compounds and/or interferences.[a]

Vapor Mixture	RR (%)
DMNB + C_{13}	96.0
2,6-DNT + C_{13}	98.2
2,6-DNT + C_{15}	98.8
2,4-DNT + C_{15}	99.6
C_{13} + C_{15}	39.0
2,6-DNT + 2,4-DNT	46.6

[a]Based on MC-EDPCR analysis (500 iterations) with 5% superimposed error at 5-10× LOD. Sensitivities are defined as $\Delta R/R \cdot 10^3$/ng and LODs are in ng (see Table 2.1).

A1.5 LabVIEW program for control and data acquisition

The LabVIEW program used to control the INTREPID prototype has all of the essential elements required for 1) autonomous operation of all fluidic, thermal, and analytical components for single or multiple cycles, 2) display of instrument status, and 3) display of the responses from the array (i.e., real-time chromatograms). The software was developed and configured to afford the least cumbersome and fastest approach to determinations of the target analytes. It has a menu-driven, user-adjustable, graphic-user-interface (GUI) for setting the operating parameters, acquiring chromatographic data from all sensors, and displaying results.

More specifically, this program provides proportional-integral-derivative (PID) temperature control of the heated devices (sampler, heated interconnects, μF, μcolumn), on-off control for valve switching and pump and fan activation, and sensor response readout. User-defined pump, valve, and heater actuation timing and temperature settings, and the μcolumn temperature program are entered at the start of a run through GUI on the laptop computer for

automatic operation. Manual operation of any mode, as well as autonomous operation for any number of complete sampling and analytical cycles, are both possible. To allow continuous unattended operation, as well as manual operation, an event-based code structure was used, in which a precisely timed main loop runs acquisition and control tasks in background, while a secondary loop waits for user inputs or programmed sequences and then commands task states in the main loop. Additional advantages of this structure are the possibility to drive controls independently and to customize the operation sequences of the instrument after the development stage. A copy of this code was debugged with the INTREPID circuit boards and then successfully implemented in the assembled prototype.

One of the important functionalities is a μF initial temperature control, which allows the temperature of the μF to be set at a slightly elevated level via its integrated heater, rather than being controlled solely by the mini-oven of the prototype. This function employs a PID control routine that generates a PWM signal at 50Hz. The PID control routine was integrated with the basic on/off heating control. It deactivates itself automatically when the on/off control is activated, which results in fast heating and also rapid adjustment of baseline temperature. It enables the μF to be heated to 70-80 °C, for example, while the μcolumn remains unheated or independently heated to a different temperature.

Acquisition channels and corresponding graphs were included for monitoring the sampler and mini-oven temperatures. Sampler and capillary interconnection temperatures are acquired using thermocouples while the temperatures of the device carrier boards are measured using IC resistive temperature devices (RTD). A closed-loop control for the heating of the sampler was implemented in order to achieve a heating rate that would permit reaching 250 ºC in 15 sec. A pair

of digital outputs from the DAQ switches on/off two voltages, one of 17 V to achieve fast initial heating, and one of 9 V for reducing ripple.

A set of manual controls for turning on and off valves and pumps independently was incorporated into the LabVIEW front panel control GUI. As well, a set of controls for programming automation of the instrument was added in the form of a time table. A routine executes the programmed sequences by triggering corresponding controls accordingly. It allows an "Auto" mode for one time execution of the sequence and "Continuous" mode for a loop execution. Figure A1.3 provides a screenshot of the control panel relevant to these functions. In order to allow integration of generated code into an executable stand-alone program, a set of controls was added for setting up workspace variables like RTD calibration parameters, heating temperatures for sampler and μfocuser, and valve default states.

In summary, the LabVIEW code was developed and integrated into a final, coherent program with user definable settings, where appropriate, that permits single analyses or a continuous series of analyses (the number of which would be user-selected) to be run automatically prior to subsequent user intervention.

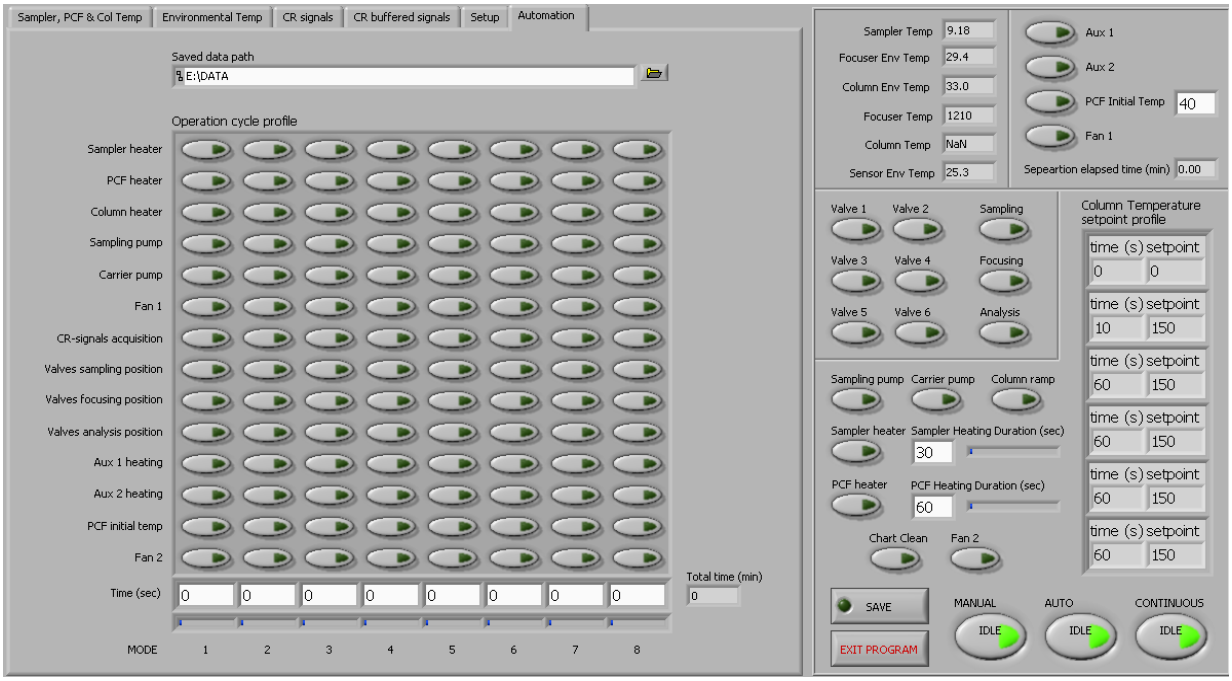

Figure A1.3. Screenshot of Labview controls for automated and manual operation.

A1.6 References

1. Jin, C.; Kurzawski, P.; Hierlemann, A.; and Zellers, E.T. *Anal. Chem.* **2008,** 80, 227.
2. Park, J.; Groves, W.A.; and Zellers, E.T. *Anal. Chem.* **1999**,71, 3877.
3. Hsieh, M.-D.; and Zellers, E.T. *Anal. Chem.* **2004,** 76, 1885.

APPENDIX 2
SUPPORTING INFORMATION FOR CHAPTER 3

A2.1 Structure of the RTIL

The structure of the trigonal tricationic room-temperature ionic liquid (RTIL) that was synthesized and used as the ^{2}D µcolumn stationary phase is shown in, Figure A2.1. [1]

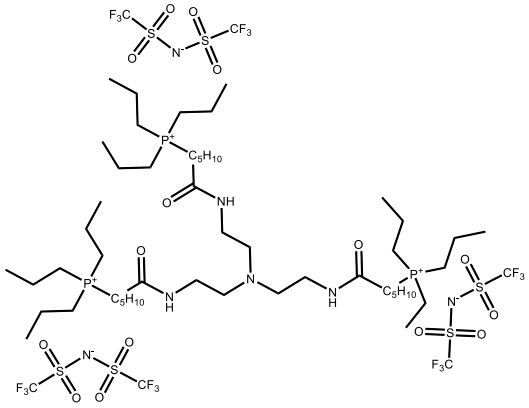

Figure A2.1. Structure of Tris[2-(6-aminopropylphosphoniumhexaamido)ethyl]amine tris[bis(trifluoromethylsulfonyl)imide] (RTIL).

A2.2 Elemental analysis

Analyses for C, H, N, and F were performed by Atlantic Microlab Inc. (Norcross, GA). Duplicate measurements of C, H, and N were performed. Table A2.1 shows the results. Experimental values agree closely with theoretical values.

Table A2.1 Elemental analysis of the RTIL (values are % mass).

Element	Theor.	Measured		Error[a]
C	38.93	38.5	38.5	-0.4
H	6.19	6.16	6.04	-0.09
N	5.57	5.32	5.28	-0.27
F	19.44	19.7	--[b]	+0.3

[a] difference of average measurement from theoretical; [b] duplicate was not collected.

A2.3 ^{1}H NMR analysis

The ^{1}H NMR spectrum of the RTIL in DMSO-d6 was collected on a Varian MR400 spectrometer (400 MHz). Chemical shifts (δ, ppm) are relative to tetramethylsilane (TMS). Chemical shifts and integrated intensities are consistent with those reported in the literature; [1] peaks due to residual water and other minor impurities are also apparent (Figure A2.2).

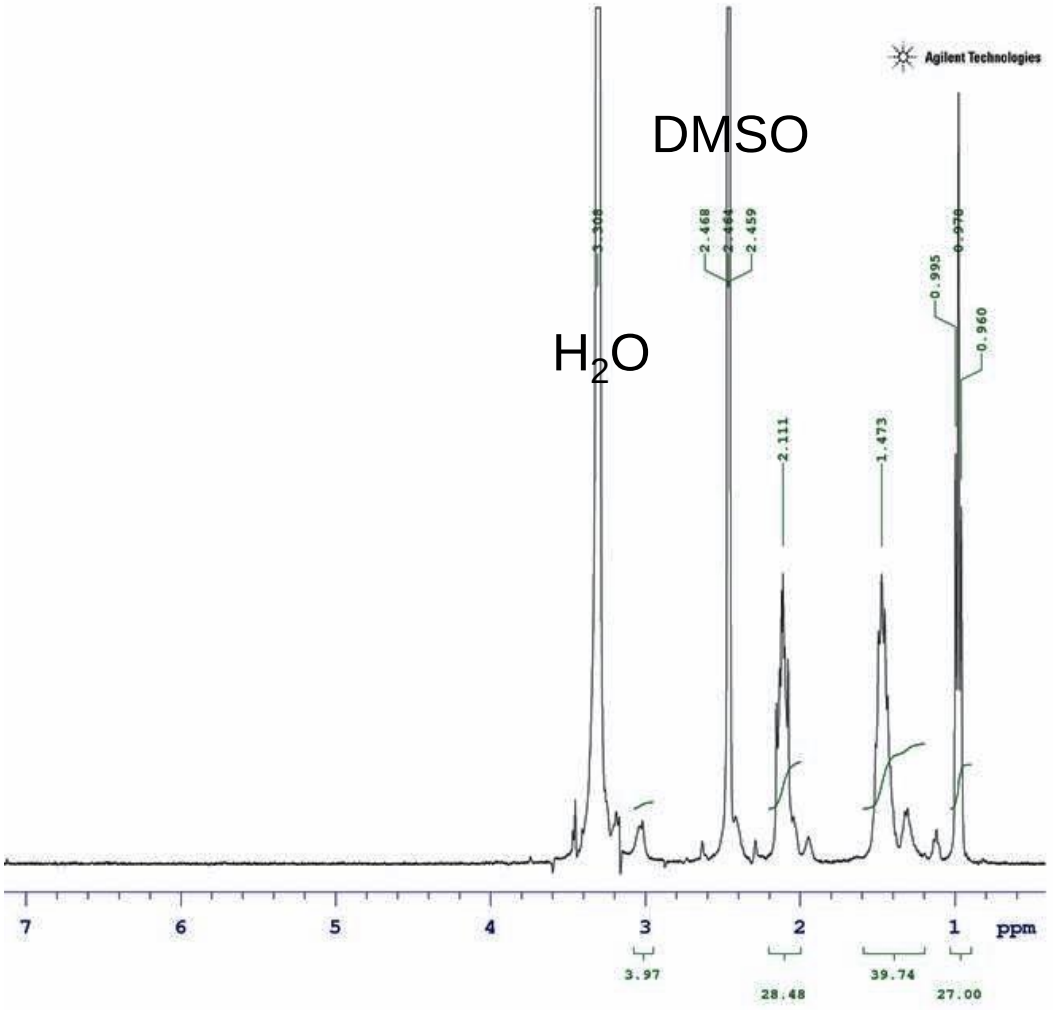

Figure A2.2. ^{1}H NMR (400 MHz, DMSO): δ(ppm) = 3.06 (br s, 4H), 2.11 (m, 28H), 1.47 (m, 40H), 0.98 (t, 27H). Multiplicities are reported as follows: singlet (s), triplet (t), multiplet (m), broad (b). All NMR spectra were recorded at room temperature.

A2.4 Phase transitions

Differential scanning calorimetry (DSC) was performed on a 13-mg sample of the RTIL crimp-sealed in an aluminum pan using a TA Instruments DSC Q2000. Scans were performed using the following non-isothermal protocol: pre-melting (equilibrate at -90 °C for 5 min); heating scan (linear ramp from -90 to 40°C @ 10°C/min); cooling scan (linear ramp from 40 to -90°C at

10 °C/min); repeat heating and cooling scans for a total of 10 scans. Figure A2.3 presents the results. Phase transition temperature of -27 °C is close to the literature value of -31 °C. [1]

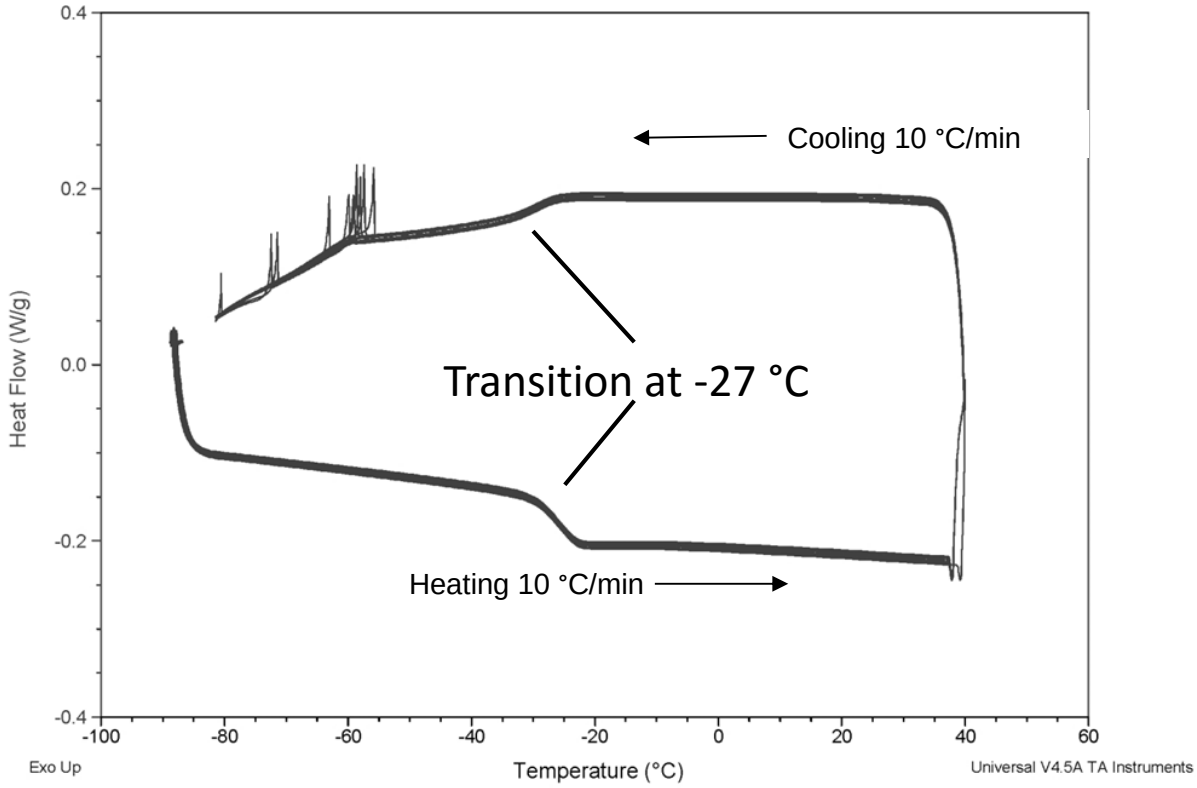

Figure A2.3. DSC thermogram for the RTIL. The solid-to-liquid phase transition occurs between -25.3°C and -28.8°C. 10 scans overlaid.

A2.5 Thermal stability

Thermogravimetric analysis (TGA) was used to determine the thermal stability of the RTIL using a Perkin Elmer Pyris 1 instrument. Samples (~ 10 mg) were heated in platinum pans from 30 to 600°C at 10°C/min in both N_2 and air sheath gases. Results are presented in Figure A2.4 as mass loss vs. temperature. Values of 1% and 5% mass loss under N_2 were 290 and 370 °C respectively. These were 2.1% higher and 4.9% lower than the values reported in literature.[1] Values

of mass loss in air are similar to those in N_2, confirming the high-temperature air stability of this RTIL.

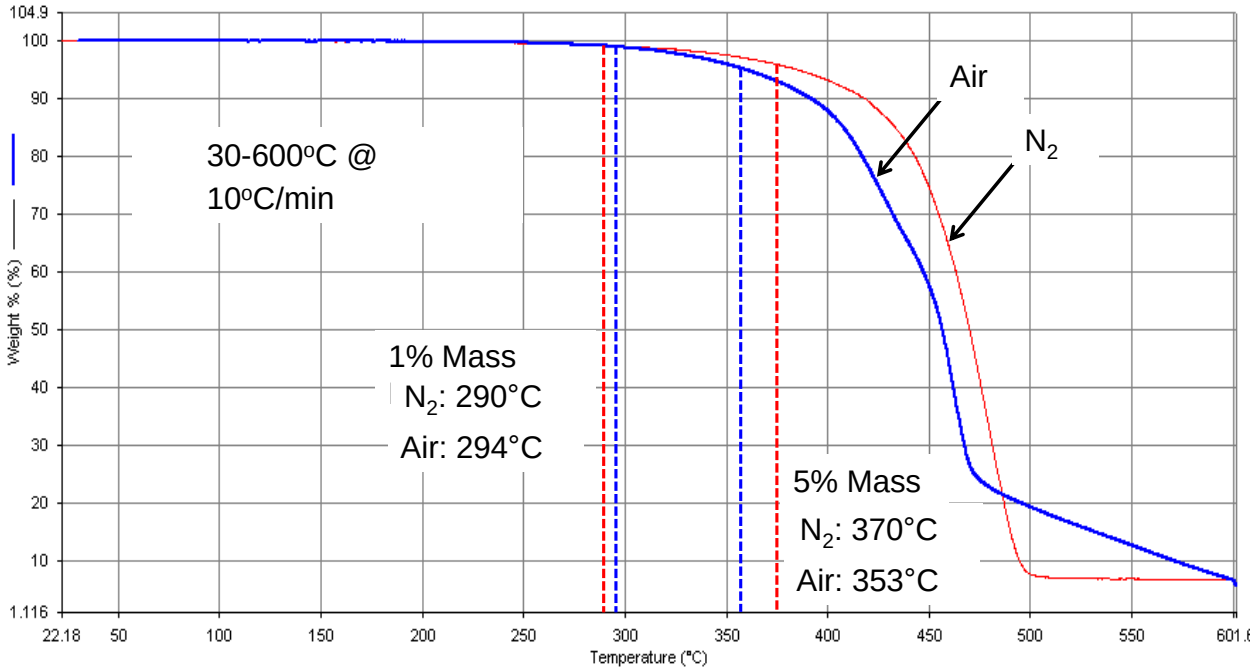

Figure A2.4. TGA curves for the RTIL heated at 10 °C/min with a sheath gas of N_2 (red curve) and air (blue curve).

A2.6 RTIL and OV-215 deposition on the ^{2}D µcolumns

In preparation for pretreating the 0.5-m ^{2}D µcolumn prior to RTIL coating, a colloidal suspension of NaCl was prepared by rapidly dispensing 3 mL of saturated NaCl in methanol into 8 mL of 1,1,1-trichloroethane (TCA). After rinsing the µcolumn with dichloromethane and methanol, the suspension was passed through the µcolumn at 2-3 cm/s under a positive pressure of N_2, leaving a thin layer of the salt on the inner walls. After drying under N_2, a rough, (visually) uniform film of NaCl remained on the walls. The µcolumn was then statically coated with the

RTIL from a dichloromethane solution (8 mg/mL) to yield a nominal average RTIL-film thickness of 0.1 μm.

A second pretreatment using cyanopropyltetramethyldisiloxane (CPTMS) was attempted according to a published method.[2] First, the μcolumn was rinsed sequentially with dichloromethane and methanol, and then dried under N_2. Then, a 20% solution of aqueous HCl was passed through the μcolumn for 30 min at 0.1 mL/min, followed by rinsing with 1 mL of methanol and drying with N_2. Next, 1 mL of 10 % CPTMS in methanol was passed though the μcolumn. After drying under N_2 for 30 min, the ends of the μcolumn were sealed with silicone septa and it was heated at 300 °C for 24 hr. The μcolumn was then rinsed with 1 mL each of methanol, dichloromethane, and diethyl ether, and dried under N_2.

In preparation for coating with OV-215, the ^{2}D μcolumn was pretreated with (3,3,3-trifluoropropyl)methylcyclotrisiloxane (TFPCMS) according to a published method.[3] First, the μcolumn was rinsed sequentially with dichloromethane and methanol, and then dried under N_2. Then, a 20% solution of aqueous HCl was passed through the μcolumn for 30 min at 0.1 mL/min, followed by rinsing with 1 mL of methanol and drying with N_2. Next, 1 mL of 1% TFPCMS in dichloromethane was passed though the μcolumn. After drying under N_2 for 30 min, the ends of the μcolumn were sealed with silicone septa and it was heated at 300 °C for 24 hr. The μcolumn was then rinsed with 1 mL each of methanol, dichloromethane, and diethyl ether, and dried under N_2. The OV-215 was then deposited statically from a 0.35% (w/w) solution in 4:1 diethyl ether: ethyl acetate that also contained 1% (w/w) dicumyl peroxide. Crosslinking at 180 °C for 1 hr in a GC oven produced a wall coating of OV-215 with an average (nominal) thickness of 0.08 μm.

Figure A2.5a shows a portion of an uncoated μcolumn for reference. Figure A2.5b shows the corresponding portion of a second μcolumn that was statically coated with the RTIL after

pretreatment with CPTMS. This method should have produced a polar surface which could be wetted by the RTIL; however, as evidenced by the droplets of RTIL Figure A2.5b, this was unsuccessful. Figure A2.5c shows the NaCl/RTIL coated µcolumn. The surface roughness on the channel walls I attributed to the NaCl crystals. The absence of droplets implies good RTIL wetting of the NaCl surface. Figure A2.5d shows portions of the OV-215 coated µcolumn; the hazy appearance of the channel is taken as evidence of a uniform coating.

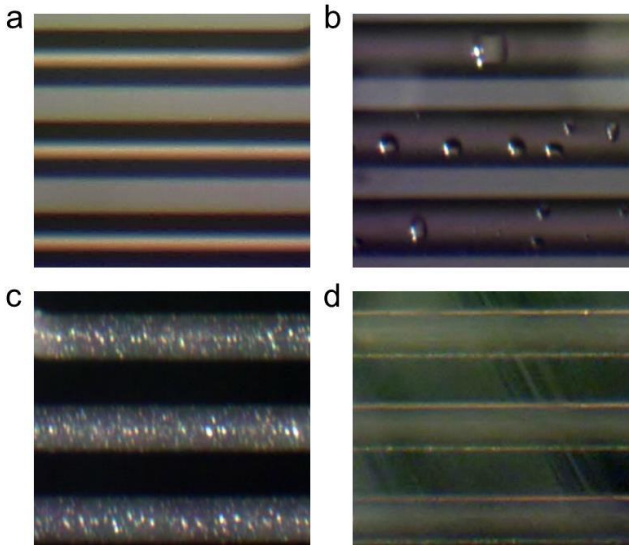

Figure A2.5: Optical micrographs of µcolumns (20X magnification); a) an uncoated 0.5 m µcolumn; b) the CPTMS pretreated 0.5 m µcolumn with RTIL droplets; c) the NaCl/RTIL coated 0.5 m µcolumn; d) the OV-215 coated 0.5 m µcolumn.

A2.7 Golay plots of the (µ)columns

The µcolumns used in this study were first characterized through the construction of Golay plots. The µcolumns were placed in a GC oven and attached to the split/splitless inlet and the FID detector. A small amount of the headspace of a vial containing the probe compound and methane (see Figure 3.1 in the main text for probe compounds) was injected via gas-tight syringe. From the resulting FID chromatogram, probe compound retention time (t_r) and *fwhm* (w_h) were used to calculate the height equivalent to one theoretical plate (H) using the following equations:

$$H = N/L$$

$$N = 5.45 \times \left(\frac{t_r}{w_h}\right)^2$$

The retention time of methane was used to calculate the average flow velocity (ū) which was plotted against *H* to yield the Golay plots in Figure A2.6.

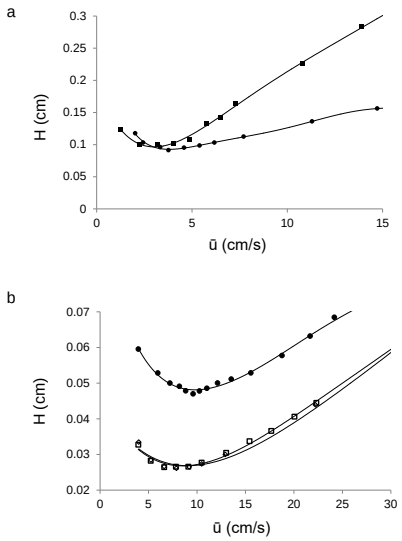

Figure A2.6. Golay plots for (μ)columns used in this work. a) 0.5 m commercially coated, SLB-IL76, 100 μm id capillary (squares) and 0.5 m μcolumn (46 × 150 μm cross section) coated with RTIL (circles); b) 3 m μcolumns (150 × 240 μm cross section) wall-coated with PDMS (unfilled squares and diamonds) and 0.5 m μcolumn (46 × 150 μm cross section) wall-coated with OV-215 (circles). See Table 3.1 in main text for conditions and results.

A2.9 Analyte Lists

Tables A2.2 and A2.3 provide descriptive information about the compounds separated in the contour plots presented in Figures 3.4 and 3.6, respectively, in the main text.

Table A2.2. Retention times and peak widths for compounds in Figure 3.4.

No.	Analyte	$^1D\ t_r$ (min)	^2D *fwhm* (msec)
1	benzene	0.3	480
2	isopropanol	0.5	1100

3	C_7	0.7	80
4	1,4-dioxane	0.7	532
5	MIBK	0.9	700
6	toluene	1.0	330
7	cyclopentanone	1.2	1010
8	C_8	1.4	120
9	*m*-xylene	2.1	450
10	2-heptanone	2.5	990
11	C_9	2.9	185
12	cumene	3.1	450
13	C_{10}	5.2	280
14	*d*-limonene	5.6	410

Table A2.3 pv, retention times, and fwhm values for cmpds. in Figure 3.6 of the main text.

	Analyte	p_v (kPa)	^1D t_R (min)	^2D *fwhm* (ms)		Analyte	p_v (kPa)	^1D t_R (min)	^2D *fwhm* (ms)
1	2-propanol	5.8	1	100	19	3-heptanone	0.53	6.5	270
2	1-propanol	2.7	1.3	110	20	2-heptanone	0.51	6.7	300
3	2-butanol	2.4	1.4	100	21	heptanal	0.47	6.9	300
4	benzene	12.7	1.7	110	22	C_9	0.59	7.4	210
5	cyclohexene	11.9	1.9	90	23	cumene	0.60	7.6	240
6	C_7	6.1	2.3	90	24	a-pinene	0.53	8.3	240
7	1,4-dioxane	5.3	2.3	150	25	benzaldehyde	0.17	8.4	340
8	MIBK	2.6	2.8	230	26	octanal	0.27	10.3	310
9	isoamyl alcohol	0.5	3.2	380	27	dicyclopentadiene	0.31	10.8	260
10	toluene	3.5	3.2	160	28	mesitylene	0.20	10.9	280
11	cyclopentanone	1.5	3.6	310	29	C_{10}	0.17	11.1	270
12	2-hexanone	0.5	3.8	250	30	*d*-limonene	0.21	11.4	270
13	hexanal	1.5	3.9	240	31	nitrobenzene	0.035	12.5	480
14	perchloroethylene	2.5	4.2	170	32	2-nonanone	0.080	13.7	400
15	C_8	1.9	4.3	150	33	nonanal	0.035	14.1	400
16	2-me-2-hexanol	0.3	5.3	280	34	C_{11}	0.055	14.6	300
17	ethylbenzene	1.3	5.6	210	35	decanal	0.027	19.9	640
18	*m*-xylene	1.1	5.9	210	36	C_{12}	0.028	20.9	490

A2.10 Structured chromatogram

Figure A2.7 shows the peak apex plot associated with Figure 3.6 in the main text. Figure A2.8 shows an enlarged view of one region of Figure 3.6, highlighting the repeating pattern evident for ketones/aldehydes/alkanes. See text for discussion of these figures.

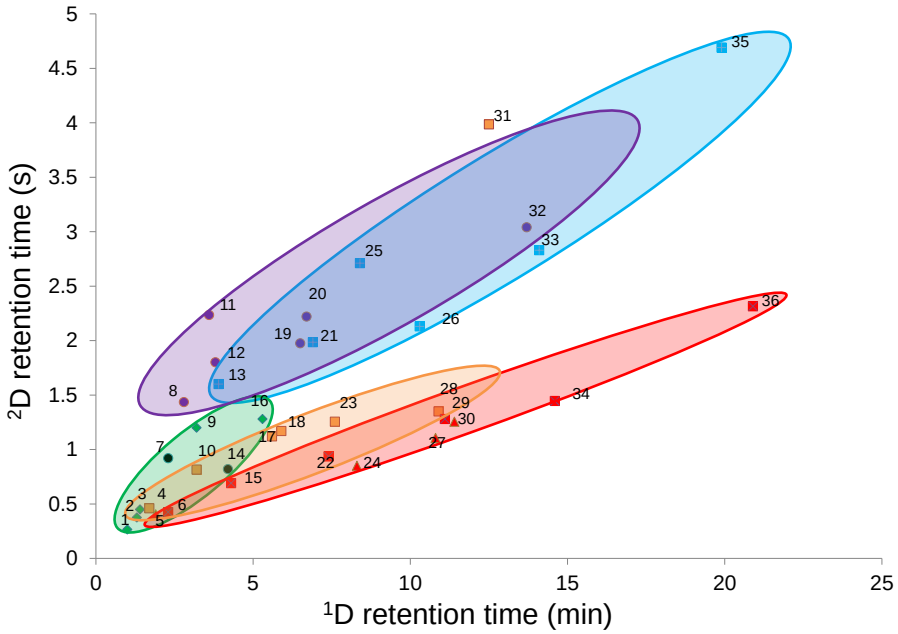

Figure A2.7: Structured chromatogram generated from the 2D chromatogram in Figure 3.6 of the main text. See Table A2.3 for peak identification.

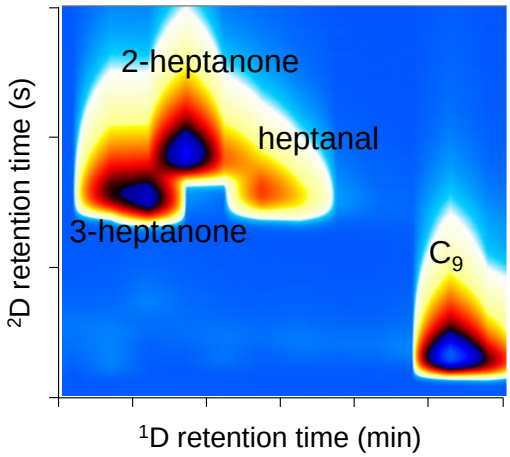

Figure A2.8: Expanded region of Figure 3.6 in the main text showing the elution pattern of ketones/aldehydes in relation to the alkane 2 carbons longer.

A2.11 References

1. Payagala, T; Zhang, Y; Wanigasekara, E; Huang, K; Breitbachm Z; Sharma, P; Sidisky, L; Armstrong, D; *Anal. Chem.,* 2009, 81, 160-173.
2. Grob, Kurt Making and manipulating capillary columns for gas chromatography A. Hüthig, 1986.
3. Serrano, G.; Reidy, S.; Zellers, E.T.; *Sens. and Act. B, Chem.,* 2009**,** 141, 217-226.

APPENDIX 3
SUPPORTING INFORMATION FOR CHAPTER 4

A3.1 µTM Control and Simulation

Figure A3.1 shows the schematic diagram of the control hardware and Figure A3.2 shows simulated data of the operation of a single µTM stage.

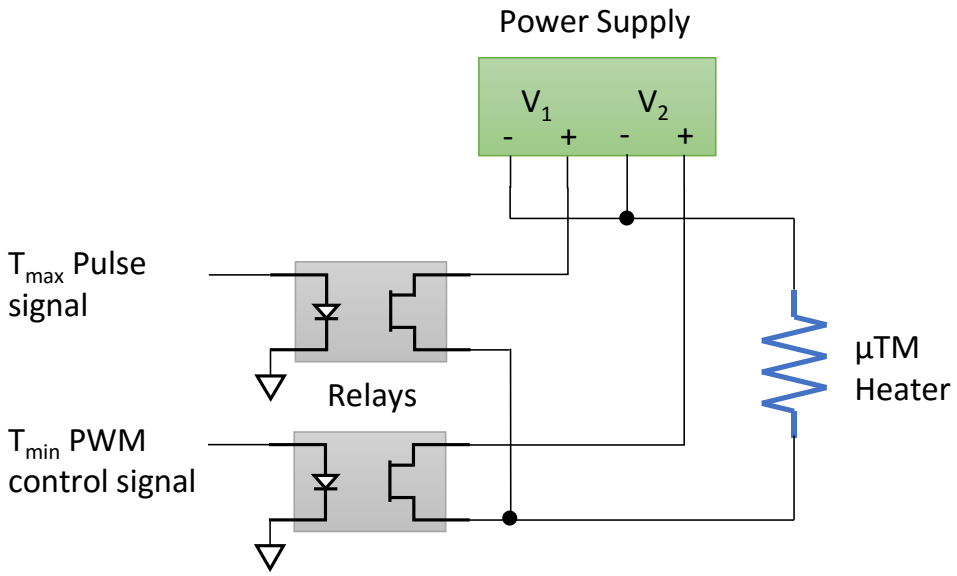

Figure A3.1. Schematic diagram of the actuation circuitry for operating the heater of one (representative) µTM stage, where two parallel relay circuits provide independent programmable power for controlling the µTM T_{max} and T_{min} values. The circuit for T_{max} allows for a rapid rise to the set-point T_{max} value by applying a single pulse for each modulation event, the width of which was increased as demanded by the temperature program. The circuit for T_{mim} allowed this temperature to be ramped through the entire separation period using a PID feedback control loop driving a PWM wave. A similar set-up is used for the second µTM stage heater which was actuated 500 ms after the first one for every modulation event.

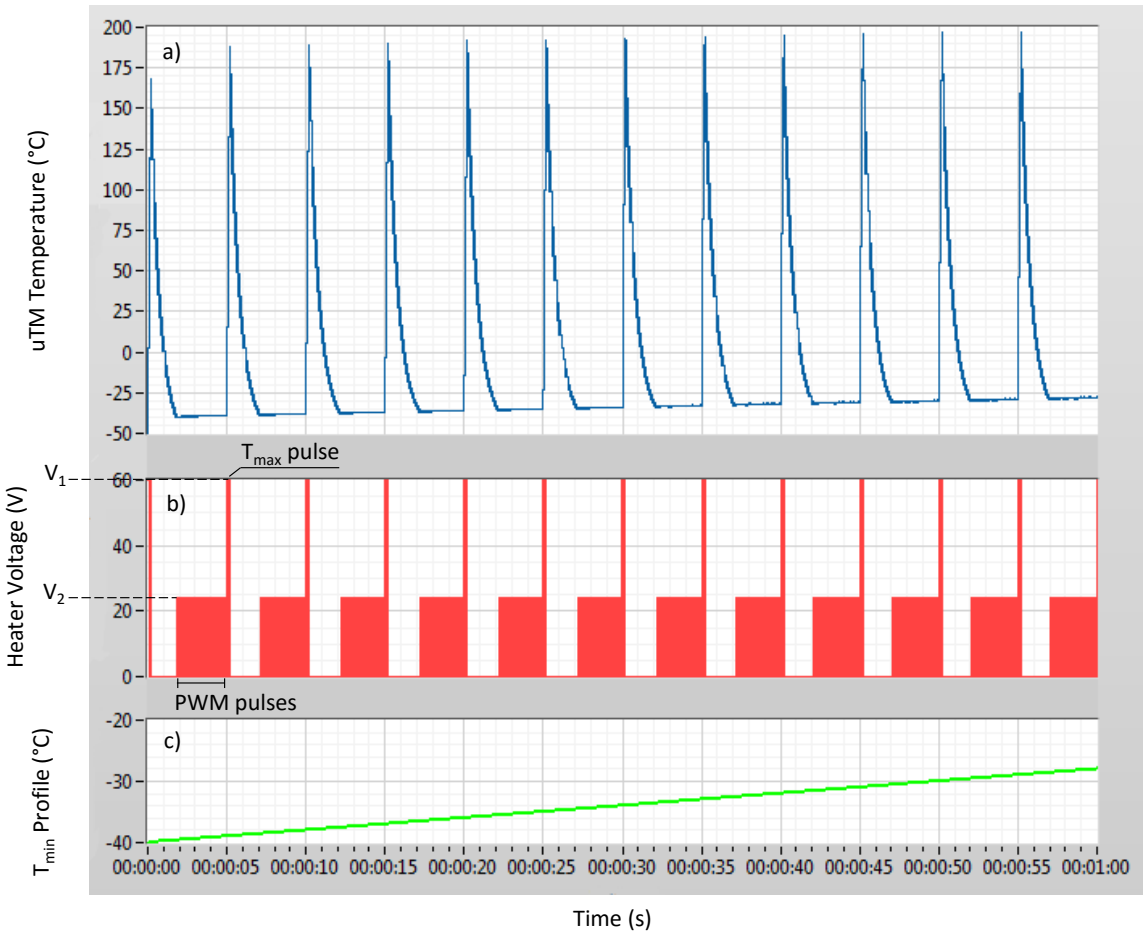

Figure A3.2. Simulated results of the µTM temperature control protocol, using the developed LabVIEW code and the open-loop thermal model of a µTM stage: a) µTM control output following the programmed temperature; b) voltage applied to the integrated heater, showing the periodic sequence of single T_{max} pulses, preceded by a short delay, and the PWM wave for controlling T_{min}; c) T_{min} ramp set-point profile at 12°C/min starting at -40°C.

A3.2 Heated Interconnect Validation

Table A3.1. Peak fwhm values for various compounds with interconnect heater on/off.

Compound	p_v [a] (kPa)	fwhm (off) (sec)	fwhm (on) (sec)
C_6	21	0.54	0.55
benzene	12	0.60	0.61
C_7	6.1	0.61	0.62
toluene	3.5	0.73	0.73
C_8	1.9	0.81	0.81
ethylbenzene	1.3	1.01	1.01
C_9	0.59	1.03	1.02
m-xylene	1.1	1.27	1.25
C_{10}	0.17	2.33	2.28
1,2,3-TMB	0.19	2.32	2.26
C_{11}	0.052	4.58	4.35
napthalene	0.034	6.27	5.90

[a]Values from Ref. *1.

Heated interconnects were installed between the ^{1}D column and the μTM and between the μTM and the ^{2}D column to minimize peak broadening that might be incurred by mounting the μTM externally and thus exposing vital areas to the cool lab air. The heated interconnects were tested by comparing the *fwhm* of a series of test compounds ranging in vapor pressure from 0.03 kPa to 20.8 kPa injected into the system with the interconnect heaters both on and off. In both cases, the temperatures of both stages and both rims of the μTM were set to 100 °C and the device was not modulated. The ^{1}D columns was held in the GC oven at 80 °C In lieu of a ^{2}D column, a segment of uncoated fused silica capillary was used. The flow rate of the He carrier gas was set at roughly 2 mL/min and the GC oven was held at 80 °C.

Table A3.1 shows *fwhm* values. For the more volatile compounds (p_v >~1) little change in *fwhm* was noted between the two conditions. In fact, a slight increase was noted in some cases when the heater was on. This increase was minor and likely due to random fluctuation. The peak width reduction noted for lower volatility compounds with the interconnect heaters on ranged from tens to hundreds of ms, which is significant in light of the extremely narrow peaks generated by the µTM.

A3.3 RTIL µTM Characterization

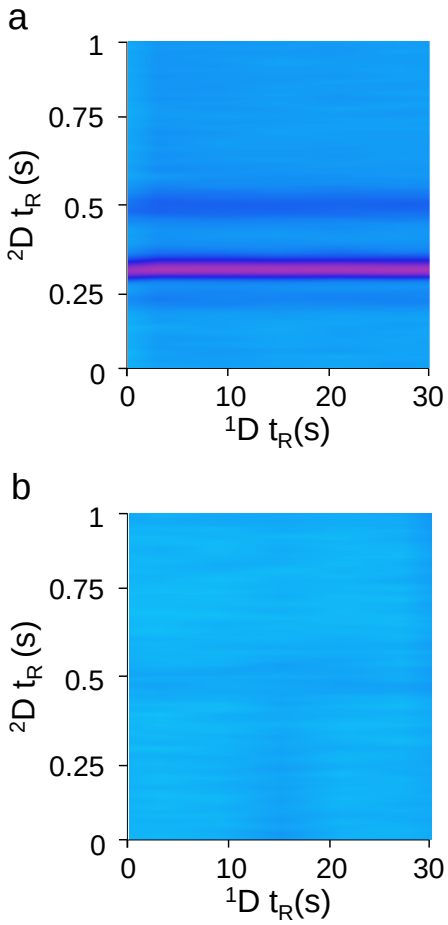

Figure A3.3. Contour plots showing the first 30 seconds of a separation using a) PDMS coated µTM and b) RTIL coated µTM. Modulator conditions: 1.5 mL/min He carrier gas; T_{min} = -25 °C; T_{max} = 220 °C (a) and 230 °C (b). P_m was 6 seconds, however only the first 1 second is shown (where bleed would be evident).

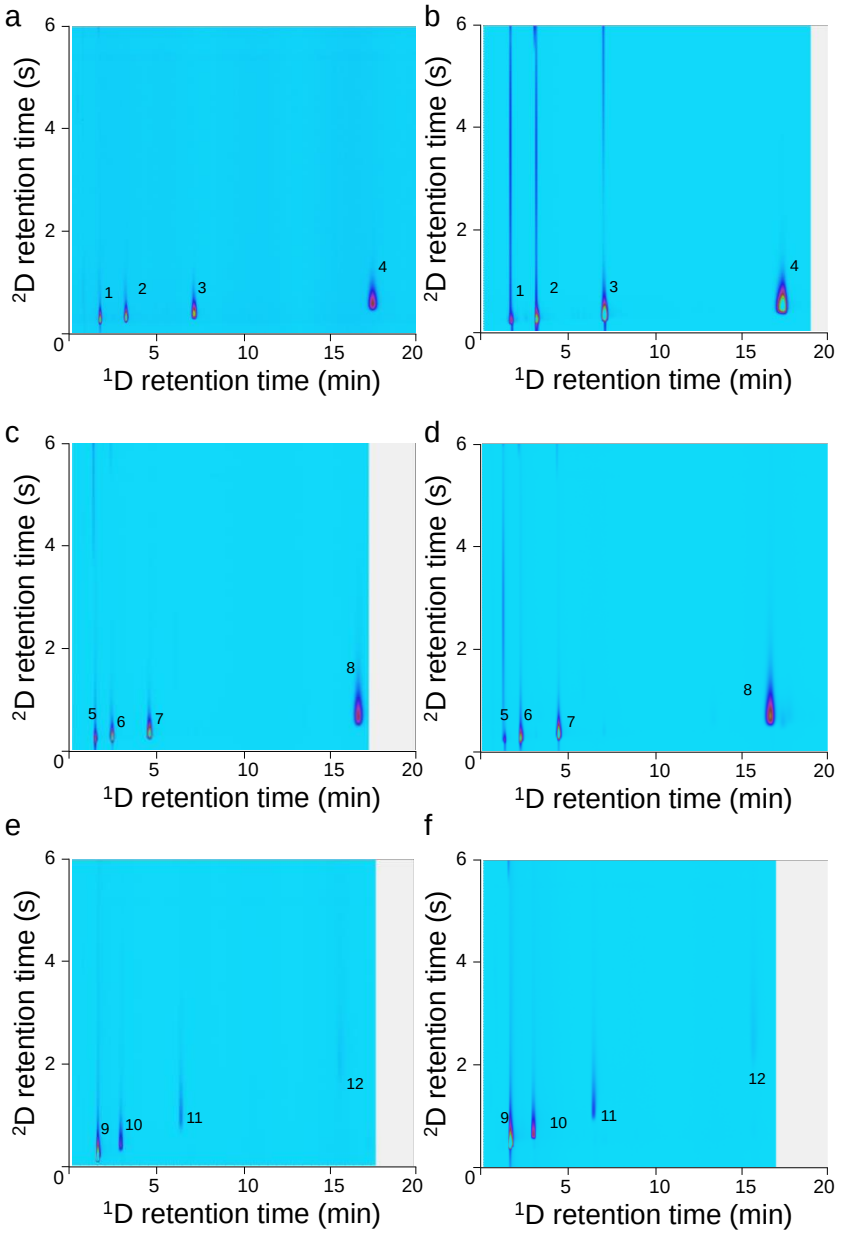

Figure A3.4. Figure 8. a,b) Homologous alkane, b,c) aromatic and e,f) aldehyde separations using RTIL coated µTM. Conditions: µTM : 0.07 µm thick RTIL; Tmin = -30 °C; Tmax = 230 °C; P_m = 6 s; ^{1}D column, 6 m PDMS 0.2µm film thickness; ^{2}D = uncoated fused silica capillary; FID detection. Panel a,c,e) Approximately 1 ng injection; b,d,f) Approximately 50 ng injection. 1-4: C7-C10 n-alkanes; 5-8: benzene, toluene, ethylbenzene, 1,2,3-TMB; 9-12: C5-C8 n-aldehydes.

References

1. J. L. a. W. G. Mallard in *NIST Chemistry WebBook, NIST Standard Reference Database Number 69,* National Institute of Standards and Technology, Gaithersburg MD, 20899.